





This is to certify that the  
 dissertation entitled  
 Phase Transformations in Thin Films of  
 TiNi Thermoelastic Alloys  
 presented by  
 Liuwen Chang  
 has been accepted towards fulfillment  
 of the requirements for  
Ph.D. degree in Materials Science



Major professor

Date 4/1/93

**LIBRARY  
Michigan State  
University**

**PLACE IN RETURN BOX to remove this checkout from your record.  
TO AVOID FINES return on or before date due.**

DATE DUE	DATE DUE	DATE DUE
FEB 6 1998 - 107	_____	_____
JUL 01 2000	_____	_____
_____	_____	_____
_____	_____	_____
_____	_____	_____
_____	_____	_____
_____	_____	_____

MSU Is An Affirmative Action/Equal Opportunity Institution

c:\crl\data\due.pm3-p.

**PHASE TRANSFORMATIONS IN THIN FILMS OF TiNi  
THERMOELASTIC ALLOYS**

**By**

**Liuwen Chang**

**A DISSERTATION**

**Submitted to  
Michigan State University  
in partial fulfillment of the requirements  
for the degree of**

**DOCTOR OF PHILOSOPHY**

**Department of Materials Science and Mechanics**

**1993**

## ABSTRACT

### PHASE TRANSFORMATIONS IN THIN FILMS OF TiNi THERMOELASTIC ALLOYS

By

Liuwen Chang

The objective of this research is to investigate the microstructure and thermoelastic transformation characteristics in sputter-deposited TiNi thin films with emphasis on the relationship between processing parameters, structure, and properties as they compared with similar bulk alloys.  $Ti_x(NiCu)_{1-x}$  films were fabricated by triode magnetron sputtering from either a single  $Ti_{50}Ni_{45}Cu_5$  alloy target or alternating  $Ti_{50}Ni_{45}Cu_5$  and pure titanium targets. Energy dispersive X-ray microanalyses showed the resulting films with Ti-layer to alloy-layer thickness ratio of 0, 1/16 and 1/9 had titanium content of approximately 47.4, 49.2 and 51.0 at% respectively. The 2.6 % titanium depletion found in the films deposited from the alloy target resulted from preferential resputtering of Ti. The sputtering yield ratio,  $Y_{Ti}/Y_{Ni}$ , in amorphous TiNi alloys varied from 1.75 to 9 with the bombarding particle energies of 500 eV to 50 eV, according to results of ion beam assisted deposition study. The as-sputtered binary and ternary films were amorphous with substrate temperature  $T_s < 500$  K. The crystallization behavior of Ti(NiCu) films was studied by differential scanning calorimetry and X-ray diffraction. Results showed the amorphous films underwent polymorphic reaction with crystallization temperatures of about 40 K lower than those of binary alloys. The microstructures and thermoelastic transformation characteristics of annealed Ti(NiCu) films were examined using transmission electron microscopy, X-ray diffraction, differential scanning calorimetry and electrical resistivity measurement. Generally speaking, the microstructures of the Ti(NiCu) films annealed at 823 and 923 K coincided with the prediction made from the extrapolation

of high temperature ternary phase diagram. However, the features of thermoelastic transformations were complicate. Two kinds of two-step transformations, an  $B2 \leftrightarrow R \leftrightarrow$  monoclinic martensite ( $M_M$ ) one and a  $B2 \leftrightarrow$  orthorhombic martensite  $\leftrightarrow M_M$  one, were first found in a 47.4 at%-Ti film and a 51.0 %-Ti film, with about 5 at% Cu, respectively. On the other hand, a near equiatomic Ti(NiCu) film (49.2 at%-Ti) underwent a simple B2-to-monoclinic martensitic transformation. In addition, retained austenite were found in 49.2 %-Ti and 51.0 %-Ti films, and its volume fraction directly corresponded to the vacuum condition during anneal, i.e., lower vacuum resulted in more retained austenite. Detailed crystallographic data and self-accommodation mechanism for orthorhombic martensite were obtained by electron microscopy.

## **ACKNOWLEDGMENTS**

**I am deeply indebted to Dr. David S. Grummon, my major professor, for his advice, interest and continuous support throughout the course of this research.**

**Sincere appreciation is extended to my guidance committee members: Dr. Kalinath Mukherjee, Dr. William P. Pratt Jr. and Dr. Martin A. Crimp.**

**I would like to give special thanks to Reza Loloee and Vivion Shull in Department of Physics and Astronomy, Dr. Karen L. Klomparens in Center of Electron Optics, Michael J. Rich in Composite Materials Center as well as to Dr. Rai Hwang in Department of Chemistry at Michigan State University, and Dr. John Mansfield at the University of Michigan for their assistance in accessing various experimental instruments.**

**Appreciation is also expressed to the National Science Foundation (under Grant #MSS8821755 ) and the Ford Motor Company for the financial support of this research.**

**Finally, I am very grateful to my wife Tzuei-Shiang for her understanding during all those days when it seemed I would rather stay in my laboratory than at home.**

## TABLE OF CONTENTS

<b>LIST OF TABLES</b>	<b>vii</b>
<b>LIST OF FIGURES</b>	<b>viii</b>
<b>1. INTRODUCTION</b>	<b>1</b>
<b>2. LITERATURE REVIEW</b>	<b>5</b>
<b>2.1. General Aspects of Martensitic Transformation</b>	<b>6</b>
<b>2.1.1. Thermoelastic Transformation, Shape Memory Effect and Superelastic Effect</b>	<b>6</b>
<b>2.1.2. Crystallography of Martensitic Transformation</b>	<b>9</b>
<b>2.2. Diffusional Transformations in Near-Equiatomic TiNi and Ti(NiCu) Alloys</b>	<b>12</b>
<b>2.3. Thermoelastic Transformations in TiNi-Based Alloys</b>	<b>14</b>
<b>2.3.1. Thermoelastic Transformations in TiNi Alloys</b>	<b>14</b>
<b>2.3.2. The Effects of Copper Addition on Martensitic Transformation</b>	<b>18</b>
<b>2.4. Crystallization Behavior of Ti-Ni Alloys</b>	<b>20</b>
<b>2.5. Thin Film Processing</b>	<b>21</b>
<b>2.5.1. Thin Film Deposition by Sputtering</b>	<b>21</b>
<b>2.5.2. Ion Beam Assisted Deposition</b>	<b>25</b>
<b>2.6. Current Research on TiNi Thin Films</b>	<b>29</b>
<b>3. EXPERIMENTAL METHODS</b>	<b>35</b>
<b>3.1. Materials</b>	<b>35</b>
<b>3.2. Deposition Equipment</b>	<b>37</b>
<b>3.2.1. Magnetron Sputter-deposition Apparatus</b>	<b>37</b>
<b>3.2.2. Ion Beam Assisted Deposition Apparatus</b>	<b>40</b>
<b>3.2.3. Modified IBAD Arrangement</b>	<b>41</b>
<b>3.3. Deposition Procedures</b>	<b>42</b>
<b>3.3.1. Magnetron Sputter-Deposition</b>	<b>42</b>
<b>3.3.2. Ion Beam Assisted Deposition</b>	<b>44</b>
<b>3.3.3. Modified IBAD</b>	<b>46</b>
<b>3.4. Crystallization Behavior of As-Sputtered Ti(NiCu) Thin Films</b>	<b>47</b>
<b>3.4.1. Crystallization Temperature and Enthalpy</b>	<b>47</b>
<b>3.4.2. X-ray Diffraction</b>	<b>49</b>
<b>3.5. Heat Treatment</b>	<b>50</b>
<b>3.6. Composition Analyses</b>	<b>50</b>

3.7. Thickness Measurement	52
3.8. Microstructure Evaluation	53
3.8.1. X-ray Diffraction	53
3.8.2. Scanning Electron Microscopy	53
3.8.3. Transmission Electron Microscopy	53
3.9. Martensitic Transformations in Ti(NiCu) Thin Films	54
3.9.1. Differential Scanning Calorimetry	54
3.9.2. Electrical Resistivity Measurement	54
3.9.3. X-ray Diffraction	55
3.9.4. Transmission Electron Microscopy	55
4. RESULTS AND DISCUSSION	57
4.1. Fabrication of TiNi Thin Films	57
4.1.1. Structural Characterization of Sputter-Deposited Films	58
4.1.2. Composition of Sputter-Deposited Films	62
4.1.3. Crystallization Behavior of Ti(NiCu) Thin Films	70
4.2. Microstructure Evaluation	74
4.2.1. SL Films	74
4.2.2. PML-16 Films	78
4.2.3. PML-9 Films	81
4.2.4. Further Discussion	84
4.3. Thermoelastic Transformation Characteristics	87
4.3.1. Transformations in SL Films	87
4.3.2. Transformations in PML-16 Films	96
4.3.3. Transformations in PML-9 Films	106
4.3.4. Additional Discussion: Thin Films and TEM Foils versus Bulk Alloys	123
5. CONCLUSIONS	126
BIBLIOGRAPHY	233

## LIST OF TABLES

<b>Table</b>		<b>Page</b>
3-1:	Deposition parameters for magnetron sputter-deposited films.	133
3-2:	Deposition parameters for ion beam sputter ion beam assisted deposited films fabricated for direct TEM observation.	134
3-3:	Deposition parameters for ion beam sputter ion beam assisted deposited films.	134
4-1:	Comparison of d-spacing values of the precipitates shown in Figure 4-5 and the TiN phase [129].	135
4-2:	Compositions of target alloy and magnetron sputter-deposited films.	135
4-3:	DSC data for magnetron sputter-deposited Ti(NiCu) films.	136
4-4:	Transformation data for PML-16 films.	136
4-5:	Crystallographic data for Type-I twinning.	137
4-6:	Transformation data for PML-9 films.	138
4-7:	Summary of transformation data for PML films.	139
4-8:	Crystallographic data for orthorhombic martensite in the cubic basis.	140

## LIST OF FIGURES

Figure	Page
1-1: Schematic drawing of the shape memory effect: (a) austenite single crystal; (b) martensite consisting of two variants; (c) variant coalescence on loading; and(d) martensite reverting to austenite on heating.	142
2-1: Two dimensional schematic drawing of the martensitic transformation: (a) crystal structures of austenite and martensite respectively; (b) lattice deformation transforming austenite lattice to martensite lattice; (c) lattice invariant shear maintaining an undistorted habit plane; and (d) rigid body rotation maintaining a continuous interface.	143
2-2: Section through a martensite plate, showing the banded structure of relative amounts $x$ of twin 2 and $(1-x)$ of twin 1. The plane of paper is perpendicular to the twin planes [25].	144
2-3: Equilibrium phase diagram for Ti-Ni alloys [29].	144
2-4: Isothermal cross section through the Ti-Ni-O phase diagram at 1200 K [42].	145
2-5: Isothermal cross sections through the Ti-Ni-Cu phase diagram (a) at 1073 K and (b) at 1143 K [44].	146
2-6: Electrical resistance as a function of temperature showing a two-step transformation in a Ti(NiFe) alloy [50].	147
2-7: $(\bar{1}11)B2$ stereographic projection showing R-phase variants A, B, C and D and twinning relations between them [53].	147

<b>2-8:</b>	<b>Self-accommodation morphology of R-phase (above) and corresponding schematic variant-combination (bottom) [53].</b>	<b>148</b>
<b>2-9:</b>	<b>Self-accommodation morphology of monoclinic martensite (above), and a sub-micro model depicting crystallographic relationships between variants in the triangular morphology (bottom) [23].</b>	<b>149</b>
<b>2-10:</b>	<b>The dependence of the transformation temperature (<math>M_s</math>) on titanium content in TiNi alloys [4].</b>	<b>150</b>
<b>2-11:</b>	<b>Composition dependence of the crystallization temperature and the activation energy for amorphous Ti-Ni alloys [75].</b>	<b>151</b>
<b>2-12:</b>	<b>Theoretical calculation of the free energy diagram for Ti-Ni alloys at 235 K [78].</b>	<b>151</b>
<b>2-13:</b>	<b>Sputtering yield of nickel as a function of ion energy and ion mass [84].</b>	<b>152</b>
<b>2-14:</b>	<b>Variation of sputtering yield with angle of incidence for 1 keV Ar<sup>+</sup> incident on Ag, Ta, Ti and Al [85].</b>	<b>153</b>
<b>2-15:</b>	<b>Structure diagram for thick films produced by sputtering [87].</b>	<b>154</b>
<b>3-1:</b>	<b>Flow chart summarizing the experimental methods used in the present study.</b>	<b>155</b>
<b>3-2:</b>	<b>Schematic drawing of (a) the triode magnetron sputtering apparatus, and (b) the substrate holder assembly.</b>	<b>156</b>
<b>3-3:</b>	<b>(a) Arrangement of the ion sources, the substrates and related devices for ion beam assisted deposition. The devices shown were contained in a 14" metal chamber. (b) Schematic drawing of the substrate holder.</b>	<b>158</b>
<b>3-4:</b>	<b>Modified arrangement of the ion sources, the target, the faraday probes and the substrates for ion beam assisted deposition.</b>	<b>160</b>
<b>3-5:</b>	<b>Deposition procedures for (a) triode magnetron sputter-deposition and (b) ion beam assisted deposition.</b>	<b>161</b>

<b>3-6:</b>	<b>(a) Deposition rates and ion current densities and (b) I/A ratios plotted as a function of the lateral displacement of the specimen from the sputtering target centerline.</b>	<b>163</b>
<b>3-7:</b>	<b>Schematic drawing of the electrical resistivity measurement apparatus.</b>	<b>164</b>
<b>3-8:</b>	<b>Schematic drawing of the cooling stage attached to a Rigaku X-ray diffractometer.</b>	<b>165</b>
<b>4-1:</b>	<b>Secondary electron micrograph of as-sputtered SL film showing the fracture surface and the top surface.</b>	<b>166</b>
<b>4-2:</b>	<b>X-ray diffraction patterns of as-sputtered SL, PML-9, PML-12, and PML-16 films showing a broad first-order peak belonging to the amorphous phase.</b>	<b>167</b>
<b>4-3:</b>	<b>TEM results for Ti-Ni thin films: (a) ion-sputtered at <math>T_{\text{sub}}=373</math> K; (b) IBAD with <math>I/A=0.33</math>, <math>T_{\text{sub}}=383</math> K; (c) IBAD with <math>I/A=0.60</math>, <math>T_{\text{sub}}=423</math> K; (d) IBAD with <math>I/A=0.81</math>, <math>T_{\text{sub}}=403</math> K.</b>	<b>168</b>
<b>4-4:</b>	<b>IBAD film irradiated with a 500 eV assist-beam and 1.08 I/A ratio, showing extensive argon gas incorporation.</b>	<b>169</b>
<b>4-5:</b>	<b>IBAD with <math>I/A=0.33</math>, <math>T_{\text{sub}}=473</math> K: (a) bright field image; (b) diffraction pattern; (c) dark field image formed with innermost diffraction ring and (d) dark field image formed with third diffraction ring.</b>	<b>169</b>
<b>4-6:</b>	<b>Comparison between the calculated composition and the measured composition of PML films.</b>	<b>170</b>
<b>4-7:</b>	<b>The total fraction of the film resputtered by a 50, 100 and 500 eV assist-beam as a function of I/A ratio.</b>	<b>171</b>
<b>4-8:</b>	<b>The change of titanium concentration of the IBAD processed Ti-Ni films as a function of I/A ratio, relative to the expected composition of the film in the absence of an assist-beam. Data are shown for 50, 100 and 500 eV beams.</b>	<b>171</b>

- 4-9: The change in titanium content for IBAD processed Ti-Ni films as a function of the total fraction of the film resputtered by the assist-beam, relative to the expected composition of the film in the absence of an assist-beam. Data are shown for 50, 100 and 500 eV beams. 172
- 4-10: Differential scanning calorimetry data: (a) free-standing SL film; (b) free-standing PML-9 film; (c) PML-9 film on Si (100) substrate and (d) PML-18 film on Cu substrate at a heating rate of 10 K/min. 173
- 4-11: Plot of  $\ln(s/T^2)$  versus the inverse of crystallization temperature yielding the activation energies of crystallization for a number of magnetron sputter-deposited films. 174
- 4-12: X-ray diffraction patterns of a number of magnetron sputter-deposited films after an isotropic anneal in the DSC cell. 174
- 4-13: Comparison of the crystallization temperatures of ion sputter-deposited and magnetron sputter-deposited films, and melt-quenched ribbons. (Both ion sputter-deposited films and ribbons are binary Ti-Ni alloys.) 175
- 4-14: Comparison of the activation energies of crystallization of magnetron sputter-deposited films and melt-quenched ribbons. 175
- 4-15: Cross-section secondary electron micrograph for the SL film annealed at 923 K for one hour showing grain size and grain morphology. 176
- 4-16: In-plane TEM micrograph for the SL film annealed at 923 K for one hour showing grain size and microstructure. 177
- 4-17: Electron diffraction patterns acquired from the matrix phase of the 923 K annealed SL films at room temperature in (a)  $\langle 111 \rangle_{B_2}$  and (b)  $\langle 110 \rangle_{B_2}$  zone axes showing streaks in  $\langle 110 \rangle$  and  $\langle 112 \rangle$  reciprocal directions respectively. 177

- 4-18: A room temperature bright field image of the SL film annealed at 923 K for one hour showing small precipitates with distorted Moiré fringes roughly perpendicular to the [100] B<sub>2</sub> direction. 178
- 4-19: Convergent beam diffraction patterns taken from small precipitates in a 923 K annealed SL film. A tetragonal cell with  $a = 0.31$  nm and  $c = 0.80$  nm is evident from the diffraction patterns and the rotation angles between them. 179
- 4-20: Energy dispersive X-ray fluorescence spectra of matrix and precipitates of a SL film annealed at 923 K for four hour. 180
- 4-21: A bright field micrograph of the (NiCu)<sub>2</sub>Ti precipitates taken almost parallel to  $\langle 100 \rangle_{B_2}$  direction showing the morphology and habit plane of the precipitates. The misfit dislocation network (see enclosed rectangular area) lies on the (001) precipitates interface. 181
- 4-22: (a) Bright field micrograph of the annealed SL film showing three precipitate variants in matrix; (b) corresponding diffraction pattern showing [100] and [010] (NiCu)<sub>2</sub>Ti zone axes parallel to  $\langle 100 \rangle_{B_2}$ , and (c-d) dark field images taken from spot c and d in (b) respectively. 182
- 4-23: A bright field image of the annealed SL film showing grain boundary precipitates. The associated diffraction pattern is in an  $\langle 112 \rangle$  zone axis of Ti<sub>2</sub>Ni phase. 183
- 4-24: X-ray diffraction patterns of the SL films annealed at 923 K for (a) 0.25 hour; (b) 1 hour; and (c) 4 hours. 184
- 4-25: Electron micrograph showing the grain size and microstructure of a PML-16 film annealed at 923 K for one hour. 185
- 4-26: Electron micrograph of the grain boundary precipitates for a PML-16 film annealed at 923 K for one hour. The associated diffraction pattern is in an  $\langle 110 \rangle$  zone axis of Ti<sub>2</sub>Ni phase. 185

- 4-27: Electron micrograph of a PML-16 film annealed at 923 K for one hour showing  $\text{Ti}_2\text{Ni}$  precipitates observed in the grain interior. The associated diffraction pattern corresponds to two (111) twin-related  $\langle 123 \rangle$  zones of  $\text{Ti}_2\text{Ni}$  phase. 186
- 4-28: Electron micrograph of a PML-16 film annealed at 923 K for one hour showing blade-like precipitates. The corresponding diffraction patterns are in an  $\langle 110 \rangle_{\text{B2}}$  zone axis and a [011] precipitate zone axis, indexed using an orthorhombic unit cell with  $a = 0.441$  nm,  $b = 0.882$  nm and  $c = 1.35$  nm. 187
- 4-29: (a) Bright field micrograph of a PML-16 film annealed at 923 K for one hour showing misfit dislocations lying on the interface of  $\text{Ni}_3\text{Ti}_2$  type precipitates. (b) The corresponding diffraction pattern, taken from a rod-like precipitate located between two  $\text{Ni}_3\text{Ti}_2$  particles, corresponds to an  $\langle 110 \rangle$  zone axis of  $\text{Ti}_2\text{Ni}$  phase. 187
- 4-30: X-ray diffraction spectra for the PML-16 films annealed at 923 K for (a) 5 minutes; (b) 1 hour and (c) 6 hours. 188
- 4-31: Electron micrograph of a PML-9 film annealed at 923 K for one hour showing the grain size and microstructure. 189
- 4-32: Electron micrograph of a PML-9 film annealed at 823 K for one hour showing the grain size and microstructure. 189
- 4-33: Bright field micrograph of a PML-9 film annealed at 923 K for one hour showing the size and morphology of second phase particles in the grain interiors. 190
- 4-34: Selected area diffraction patterns in (a)  $[110]_{\text{B2}}$  and (b)  $[111]_{\text{B2}}$  zone axes showing that the precipitates have an fcc unit cell with  $a = 1.132$  nm with  $(100)_{\text{precipitate}} // (100)_{\text{B2}}$  and  $[010]_{\text{precipitate}} // [010]_{\text{B2}}$ . 190

4-35:	3 g dark field electron micrograph showing strain contrast around the precipitates.	191
4-36:	X-ray diffraction spectra for the PML-9 films annealed at 923 K for (a) 5 minutes and (b) one hour.	191
4-37:	Electrical resistivity as a function of temperature for (a) the target alloy, (b) the SL film annealed at 923 K for 0.25 hour and (c) the SL film annealed at 923 K for one hour.	192
4-38:	Differential scanning calorimetry data for (a) the target alloy and (b) the SL film annealed at 923 K for one hour.	193
4-39:	X-ray diffraction spectra for the SL film annealed at 923 K for 0.25 hour acquired at various temperature.	194
4-40:	X-ray diffraction spectra for the SL film annealed at 923 K for one hour acquired at various temperature.	195
4-41:	TEM micrograph of an one-hour annealed SL film taken at 255 K. The associated $[012]_{B_2}$ diffraction pattern shows well defined $1/3$ spots in the $\langle 321 \rangle_{B_2}$ direction.	196
4-42:	Electron micrograph of one-hour annealed SL film taken at 255 K. The associated diffraction patterned which can be identified as an $[11\bar{2}0]_R$ zone axis using a hexagonal unit cell with $a = 0.738$ nm and $c = 0.532$ nm.	196
4-43:	Bright field image of an one-hour annealed SL film taken at 160 K. The corresponding diffraction pattern showing $[100]$ zone of martensite.	197
4-44:	Electron micrograph of an one-hour annealed SL film taken at 160 K showing small martensite variants. The associated $[3\bar{2}1]$ diffraction patterns and dark filed micrograph showing $(11\bar{2})$ twin relation between neighboring variants.	198

- 4-45: (a) Bright field micrograph showing plate-like R-phase variants; (b) associated diffraction pattern revealing the R-phase variants oriented perpendicular or parallel to  $[110]_{B2}$  reciprocal direction and (c-d) dark field images taken from spots c and d in (b) respectively showing labyrinth-like R-phase domains. 199
- 4-46: Electrical resistivity as a function of temperature of a PML-16 film annealed at 923 K for one hour in a vacuum of  $2.6 \times 10^{-3}$  Pa. 200
- 4-47: Differential scanning calorimetry data for a PML-16 film annealed at 923 K for one hour in a vacuum of  $2.6 \times 10^{-3}$  Pa. 200
- 4-48: Differential scanning calorimetry data for a PML-16 film annealed at 823 K for one hour in a vacuum of  $2.6 \times 10^{-4}$  Pa. 201
- 4-49: Cold-stage X-ray diffraction patterns of a PML-16 film annealed at 923 K in a vacuum of  $2.6 \times 10^{-4}$  Pa. 202
- 4-50: Cold-stage X-ray diffraction patterns of the PML-16 film annealed at 823 K in a vacuum of  $2.6 \times 10^{-4}$  Pa. 203
- 4-51: Electron micrograph and corresponding  $[1\bar{5}43]_R$  diffraction pattern of 823 K annealed PML-16 film taken at 215 K showing R-phase variants with plate-like variants. 204
- 4-52: Electron micrograph and corresponding  $[023]_{B2}$  diffraction pattern of 823 K annealed PML-16 film taken at 215 K showing plate-like R-phase variants. The  $[023]_{B2}$  diffraction patterns is superimposed with two (100) twin-related  $[\bar{5}14\bar{2}5]_R$  diffraction patterns. 204
- 4-53: Electron micrograph and corresponding  $[0\bar{2}21]_R$  diffraction pattern of 823 K annealed PML-16 film taken at 215 K showing labyrinth-like variant-combination of the R-phase. 205
- 4-54: Electron micrograph of 823 K annealed film taken at 215 K showing martensite plates in R-phase matrix. The corresponding diffraction pattern

shows a $[010]_{\text{mono}}$ pattern and a $[011]_{\text{B2}}$ pattern with $1/3$ spots in $\langle 111 \rangle$ reciprocal directions.	206
4-55: Microstructure of monoclinic martensite in annealed PML-16 films taken at 170 K: (a) band-like variants and (b) zigzagged variants.	207
4-56: TEM micrographs of self-accommodated monoclinic martensite taken at 170 K: (a) bright field image; (b) $[010]$ and $[2\bar{1}\bar{1}]$ diffraction patterns; (c) dark field image taken from $(100)+(01\bar{1})$ spots labeled in (b); and (d) $[110]$ and $[101]$ diffraction patterns.	208
4-57: An electron micrograph of the 823 K annealed film illuminated by converged electron beam showing zigzagged martensite plates retained in the B2 matrix. The associated diffraction pattern are in $[001]_{\text{mono}}$ and $[011]_{\text{B2}}$ zone axes.	209
4-58: An electron micrograph of the 823 K annealed film illuminated by converged electron beam showing zigzagged martensite plates retained in B2 matrix. The associated diffraction pattern shows two $(111)$ twin-related $[3\bar{1}2]_{\text{mono}}$ zone, corresponding to two sets of martensite plates.	209
4-59: Schematic drawing showing the labyrinth-like morphology of R-phase.	210
4-60: Orientation dependence of the shape strain for Type-I twinning derived from solution 1 listed in Table 4-5.	211
4-61: Electrical resistivity as a function of temperature of the PML-9 film annealed at 923 K for one hour in a vacuum of $2.6 \times 10^{-3}$ Pa.	212
4-62: Differential scanning calorimetry data for the PML-9 film annealed at 923 K for one hour in a vacuum of $2.6 \times 10^{-3}$ Pa.	212
4-63: Cold-stage X-ray diffraction patterns of the PML-9 film annealed at 923 K in a vacuum of $2.6 \times 10^{-3}$ Pa.	213
4-64: Cold-stage X-ray diffraction patterns of the PML-9 film annealed at 923 K in a vacuum of $2.6 \times 10^{-4}$ Pa.	214

- 4-65: Cold-stage X-ray diffraction patterns of the PML-9 film annealed at 823 K in a vacuum of  $2.6 \times 10^{-4}$  Pa. 215
- 4-66: Retained austenite observed at 160 K: (a) bright field micrograph; (b) corresponding [110] diffraction pattern and (c) dark field image from  $(200)_{B2}$  spot labeled in (b). 216
- 4-67: Orthorhombic martensite at ambient temperature: (a) dark field image; (b) corresponding diffraction pattern in the  $[010]_{\text{mono}}$  and  $[011]_{B2}$  zone axes; (c) diffraction pattern in a  $[101]_{\text{mono}}$  zone axis; ; and (d) crystallographic nature of the martensite plate. 217
- 4-68: TEM micrographs of self accommodated orthorhombic martensite taken at room temperature: (a) bright field micrograph; (b) [110] diffraction pattern taken from area B; (c) [110] diffraction patterns taken from area C; (d) [101] diffraction pattern taken from area D; (e) dark field image taken from spot a in (b) showing four martensite variants a, b, c and d; (f) dark field image taken from spot g in (d) at higher magnification showing three martensite variants e, g and f; and (g) schematic drawing showing the variant distribution. 219
- 4-69: Self accommodated orthorhombic martensite taken at room temperature: (a) bright field micrograph; (b) corresponding diffraction pattern showing three (111) twin-related [101] patterns and (c) dark field image taken from spot a in (b) showing three martensite variants a, b and c. 222
- 4-70: Crystallographic nature of the martensite variants shown in Figure 4-69. 223
- 4-71: Electron micrograph and corresponding [121] diffraction pattern showing (111) twins in a thin-plate form of orthorhombic martensite taken at room temperature. 224
- 4-72: TEM micrographs of self accommodated orthorhombic martensite taken at room temperature: (a) bright field micrograph; (b) [100] diffraction pattern

- taken from area B showing one set of (011) twins and (c) [100] diffraction pattern taken from area C showing another set of (011) twins. 225
- 4-73: Electron micrograph taken at 123 K showing the monoclinic martensite inherits (011) twin-related orthorhombic variants. The associated diffraction pattern showing the electron beam is almost parallel to  $[100]_{\text{mono}}$ . 226
- 4-74: Self accommodated monoclinic martensite at 140 K: (a) bright field image; (b) diffraction patterns of martensite variants a, b and c in [101] zone axes; (c) dark field image shows variant a, b and c. Fine striations were observed inside the martensite variants. 227
- 4-75: Self-accommodated monoclinic martensite at 123 K: (a) bright field micrograph; (b) corresponding [110] diffraction patterns and (c) dark field image taken from spot c in (b). The streaks of diffraction spots in [001] reciprocal directions result from (001) twins. 228
- 4-76: Electron micrograph and corresponding  $[110]_{\text{mono}}$  diffraction pattern taken at 123 K showing (001) twins with an average spacing of 4 nm. 229
- 4-77: (a) Untransformed B2 structure in which a fct cell is delineated. (b) orthorhombic cell transformed from the fct cell. Principle axes ( $i', j', k'$ ) are obtained by  $45^\circ$  rotation about the  $k$  axis. 230
- 4-78 Stereographic projection in  $[001]_{\text{B2}}$  direction showing the twinning relationships between orthorhombic martensite variants. 231
- 4-79: Orientation dependence of the shape strain for orthorhombic martensite. 232

## 1. INTRODUCTION

About thirty years ago, Buehler and his coworkers in the U. S. Naval Ordnance Laboratory developed a new series of engineering alloys based on the intermetallic compound TiNi. These near-equiatomic TiNi alloys undergo a thermoelastic martensitic transformation at near- or sub-ambient temperature, and possess a distinctive mechanical memory ability which is known as the "shape memory effect" (SME) [1,2]. Phenomenologically, when a TiNi alloy is mechanically deformed at below its transformation temperature, rather severe plastic deformation ( 5~10 %) can be produced at a relative low stress level, by twinning-detwinning mechanisms not relying on the dislocation glide. On heating above its transformation temperature, however, the alloy can spontaneously recover its original, pre-deformed shape. The nature of SME is illustrated in a simplified two-variant schema in Figure 1-1. Figure 1-1(a) shows an single crystal of TiNi alloy in its high temperature state (austenite). This single crystal transforms to two<sup>1</sup> twin-related martensite variants on cooling below its transformation temperature, to minimize the total strain energy associated with the transformation, as shown in Figure 1-1(b). On loading, the two-variant configuration is rearranged, through the movement of the variant boundaries, to release the stresses. The rearrangement of martensite variants results in an one-variant dominated arrangement, and a shape change of the material as shown in Fig. 1-1(c). However, both of the martensite variants will revert back to the same austenite lattice orientation on heating, due to the special orientation

---

<sup>1</sup>A simplified two variant model is used to simplify the schematic representation. In reality, there are 24 twin-related variants of the monoclinic martensitic in the TiNi system.

correspondence between austenite and each martensite variant, and hence the material reverts to the original shape as shown in Fig. 1-1(d).

The application of stress can also induce the martensitic transformation within a certain temperature interval. The large anelastic strain (~5%) associated with the stress-induced transformation is recoverable upon unloading, which give rise to the superelastic effect (SE). Therefore, the superelastic effect is also known as an isothermal shape memory effect.

Equiatomic titanium-nickel alloys also provide high ductility, superior fatigue resistance and high damping capacity, which give rise to the best combination of mechanical properties (compared to other shape memory alloys such as CuAlNi and CuZnAl [3]) for engineering applications when the superelasticity effect or the shape memory effect is required [4]. Consequently, TiNi alloys have been commercially used as thermal actuators, tubing couplings and fasteners using shape memory, and in medical instrument applications requiring superelasticity. Recently, TiNi thin films, which also undergo reversible thermoelastic transformations, have attracted attention for potential application as a superelastic surface coatings to improve fatigue or erosion resistance, and in microelectromechanical systems where SME can be used in actuators [5,6]. Superelastic thin films are expected to sustain high cyclic straining without accumulating severe the slip damage that enhances nucleation of fatigue cracks at free surfaces. On the other hand, thermoelastic thin films applied to structural materials can also serve as large-force or long-stroke actuators in miniaturized devices based on the shape memory effect. The purpose of the present work is to investigate the details of thermoelastic behavior in TiNi thin films in anticipation of the emerging importance of such applications.

In the past twenty years, considerable effort has been devoted to the development of bulk TiNi alloys, whereas thin film experiments are relatively recent. One of the challenges for thin film processes is close control of composition, since the transformation temperatures for TiNi are extremely sensitive to titanium concentration (changing by as

much as 100 K per at% Ti). The transformation behavior of TiNi alloys is also affected by their thermomechanical history. Thermomechanical treatments which have been well-established for bulk alloys, such as annealing at intermediate temperatures after cold work, however, are not able to easily translate to thin film fabrication. In addition, titanium is a sluggish diffuser which results in an amorphous phase for the vapor deposited films. Subsequent annealing for crystallization may produce unfavorable residual stress and /or interface reaction problems. Finally, successful application will require a detailed understanding of thermodynamics, kinetics and crystallography of thermoelastic transformations in thin films.

In modern microelectronic technology, alloy thin films are often fabricated by physical vapor deposition such as sputtering or evaporation. The quality of thin films, described by properties such as residual stress-state, adhesion, density, topography, defect density, texture, composition homogeneity, impurity concentration, etc., is determined by processing parameters. In addition to the two most important parameters of background pressure and substrate temperature, energetic particle bombardment of the growing films is also known to modify film properties. One of the applied techniques is called ion beam assisted deposition (IBAD), which employs independent ion source to irradiate films during deposition. Energetic ion bombardment is thought to enhance the mobility of adatoms and near-surface atoms through energy transfer processes, and thus to change nucleation and growth mechanisms. Energetic particle bombardment, which may result in a composition drift in alloy or compound films, occurs in most sputtering operations because high energy sputtering-gas atoms are reflected from the sputter-target and reach the substrate. Thus, when either conventional sputtering or IBAD is used, an understanding of the effects of energetic particle bombardment on structure and composition are important.

The objects of the present study are basically twofold: The first is to fabricate TiNi thin films, with desired composition, which can behave thermoelastically, and to gain better understanding of compositional and structural variations of TiNi thin films induced by

energetic particle bombardment during processing. The second goal is to study the phase transformation characteristics of TiNi thin films. For reasons which will be detailed later, an alloy system in which about 5 at% Cu is substituted for Ni, has been chosen for detailed study. The present study has demonstrated that Ti(NiCu) thin films deposited by magnetron sputtering can behave thermoelastically after annealing, and show certain aging effects which do not appear in similar bulk alloys. The difference is attributed essentially to the kinetic conditions of deposition which resulted in films with an amorphous structure. The films, after subsequent solid-state crystallization reaction and heat treatment, possessed microstructures characterized fine grain size and special precipitate distributions, neither of which are easily attainable in materials made by traditional melt-solidification processes. The thermoelastic transformation characteristics of thin films were significantly affected by the nature of these microstructures. The fine grain size also allowed observation of self-accommodation morphologies of various martensites by TEM in whole grains.

*Organization of the Dissertation.* Following this general overview, Chapter 2 provides a detailed review of phase equilibria and stability of near-equiatomic TiNi and Ti(NiCu) alloys, thermoelastic transformations in TiNi and Ti(NiCu) alloys, crystallization behavior of amorphous Ti-Ni alloys, thin film processing by sputtering and ion beam assisted deposition, and results of recent research on TiNi thin films. The experimental arrangements and procedures are described Chapter 3. Chapter 4 presents results and discussion. These are arranged with the first section covering the compositional and structural characteristics of amorphous thin films and their crystallization behavior, while second section includes the microstructure evaluation of annealed Ti(NiCu) films. The third section provides both experimental observation and theoretical calculation of various types of thermoelastic transformations found in annealed Ti(NiCu) films. Finally, a comparison of TiNi alloy behavior in the form of thin films and in the bulk is made in the last section of Chapter 4. Chapter 5 summarizes the findings of the present study and lists the detailed conclusions.

## **2. LITERATURE REVIEW**

**The present work was undertaken as part of a project entitled "Surface Superelastic Microalloying for Improved Fatigue Performance in Ni, Ti, Fe and Cu Based Alloys", supported by Nation Science Foundation under grant # MSS-8821755. One of the objects of this study was investigation of microstructure and thermoelastic transformation characteristics in sputter-deposited TiNi thin films with special attention paid to the potential for thin films to behave superelastically. Bulk TiNi alloys with 5 to 10 at% copper substituting for nickel have been found to have superior superelastic properties, that is, smaller stress hysteresis, wider superelastic temperature range, and stable superelastic characteristics under cyclic loading, without sacrifice of ductility and fatigue resistance as compared with binary alloys [7]. In addition, transformation temperature of Ti(NiCu) alloys are also less sensitive to thermal cycling and Ti content variation than that of binary alloys [8]. This character makes it possible to control the transformation temperatures more precisely in thin film fabrication. As a consequence, the Ti(NiCu) system, rather than binary TiNi, has been chosen for the present study.**

**In this chapter, general aspects of the thermoelastic transformation, the shape memory effect (SME), as well as the superelastic effect (SE), and the crystallography of martensitic transformations are first described to provide a background for the discussion which follows. In the second section, the phase equilibria and phase stability of near-equiatomic TiNi and Ti(NiCu) alloys are reviewed. The third section provides detailed review of the thermoelastic transformation characteristics of TiNi and Ti(NiCu) alloys. Since the as-sputtered films are usually amorphous, the crystallization behavior of amorphous Ti-Ni alloys is described in the forth section. The fifth section provides a**

review of the basic sputtering phenomena, the correlation between processing parameters and resulting film structure, ion-solid interactions, and related work on ion beam assisted deposition. Finally, the sixth section provides an up-to-date review of progress on the investigation of TiNi thin films.

## **2.1. General Aspects of Martensitic Transformation**

### ***2.1.1. Thermoelastic Transformation, Shape Memory Effect and Superelastic Effect***

Martensitic transformations are diffusionless phase transformations in which atoms are cooperatively rearranged into a new crystal lattice without changing their nearest-neighbor configuration. Since no long-range atomic movement is involved, the progress of the martensitic transformation does not depend on time, but primarily depends on temperature. On cooling, the transformation starts at a temperature designated as  $M_s$ , and does not finish until a lower temperature,  $M_f$ , is reached. In the temperature interval between  $M_s$  and  $M_f$ , the high temperature phase (austenite) and the low temperature phase (martensite) coexist. The primary driving force of the transformation is the free energy difference between austenite and martensite. However, a strain energy is accumulated in the lattice during the transformation which resists further progress of the transformation unless higher driving force is supplied by a subsequent decrease in temperature [9,10].

The martensitic transformations in some materials such as InTi [11], TiNi [1] and AuCd [12] are reversible, that is, martensite reverts, without re-nucleation, directly back to austenite on heating. The start temperature of the reverse transformation is designated as  $A_s$ , and the finish temperature as  $A_f$ . Here  $A_s$  and  $A_f$  are higher than  $M_f$  and  $M_s$  respectively, that is, there is a hysteresis in the transformation. The transformation hysteresis originates from the friction associated with the movement of martensite-austenite interfaces [13]. In fact, the austenite-martensite interface is glissile, and the reversible transformation involves the shrinkage of martensite domains rather than the nucleation of new austenite crystals [14]. The reversible martensitic transformation is also called a

thermoelastic transformation. Three requirements for their occurrence are: (1) small lattice deformation for the transformation; (2) martensite containing internal twins that can be easily detwinned; and (3) martensite having an ordered structure that is not destroyed by slip during the transformation [10].

Almost all physical properties of austenite are different from those of martensite due to a significant change of crystal structure during the thermoelastic transformation. One typical example is the yield strength. The yield strength of TiNi austenite is about two to six times higher than that of martensite [4]. The low yield strength of thermoelastic martensite is due to relatively high mobility of the twin boundaries between neighboring variants. Electron microscopy study of a CuAlNi alloy conducted by Shimizu and Otsuka [15] revealed that the twin-related variant boundaries are quite mobile on loading. In other words, the critical shear stress for twin boundary movement is lower than that for dislocation motion. Moreover, a single austenite grain usually converts into a twin-related multi-variant configuration in a thermoelastic transformation on cooling. The multi-variant configuration is a result of a self-accommodation process through which the overall transformation strain associated with the lattice change is minimized. On loading, the martensite variant which can yield a maximum shear strain along the loading direction will grow at the expense of the neighboring variants. In TiNi, martensite can be deformed up to 5 to 10 %, by the coalescence of martensite variants, without activating dislocation slip [4, 16]. The plastic strain resulting from the rearrangement of martensite variants at low temperature ( $T < M_s$ ) are recoverable on heating above  $A_f$ , since each martensite variant reverts to austenite in the original orientation. This is the shape memory effect (SME) which was first found in TiNi [17]. The mechanism of the SME described above was first proposed by de Lange and Zijderveld [18], and then was modified by Otsuka *et al.* [19, 20].

The shape memory alloys can have another unique mechanical property: the superelastic effect (SE). Phenomenologically, in the superelastic effect, material suffering

large anelastic strain (1~10%) on loading can revert back to its original shape upon unloading in a certain temperature interval ( $M_s < A_f < T < M_d^1$ ). The origin of the superelastic effect is a stress-induced martensitic transformation. In other words, the application of stress has a similar effect on the transformation as a decrease in temperature [21]. This can be explained by employing the Clausius-Clapeyron equation which can be written as

$$\frac{d\sigma^{A-M}}{dT} = -\frac{\rho\Delta H^{A-M}}{\varepsilon^{A-M}T_o} \quad (2.1.1)$$

where  $\sigma^{A-M}(T)$  is the applied stress which can induce martensitic transformation at temperature  $T$ ,  $\rho$  is the density,  $\varepsilon^{A-M}$  is the strain corresponding to complete transformation,  $\Delta H^{A-M}$  is the transformation enthalpy and  $T_o$  is the temperature at which the stress free austenite and martensite have the same free energy [22]. Accordingly,  $\sigma^{A-M}(T)$  equals zero at  $M_s$ , and increases monotonically with an increase of temperature. The temperature at which  $\sigma^{A-M}(T)$  equals the critical stress for slip is designated as  $M_d$ . A material cannot behave superelastically unless its  $M_d$  temperature is higher than  $A_f$ . The  $M_d$  and  $A_f$  temperatures thus become the upper bound and lower bound for the superelastic effect. From a microscopic point of view, the applied stress induces the nucleation and growth of certain martensite variants which can provide maximum transformation strain along the stress direction to release the elastic strain [23]. On unloading, since  $T > A_f$ , the stress-induced martensite variants become unstable and reverts to austenite at a stress  $\sigma_a^{M-A}$ . The value of  $\sigma_a^{M-A}$  is lower than that of  $\sigma_a^{A-M}$  since the friction of austenite-martensite interfaces postpones the reverse transformation.

### 2.1.2. Crystallography of Martensitic Transformation

The crystallographic origin of martensitic transformation has been described successfully by a phenomenological crystallographic theory developed independently by

---

<sup>1</sup> $M_d$  temperature is the upper bound for the superelastic effect.

Bowles and Mackenzie [24] (BM theory) and by Wechsler, Lieberman and Read [25] (WLR theory). The basic assumption of these theories is that the austenite-martensite interface (habit plane) should be one of zero distortion, in a macroscopic sense, to minimize total strain energy, which has been proved by later experimental observation [26]. Under these circumstances, a lattice invariant shear and a rigid body rotation are necessary, in addition to a lattice strain which deforms the high temperature structure to a new crystal lattice (martensite) during the transformation (unless one of the principal transformation strain vanishes) [20]. The need for a lattice invariant shear and a lattice rotation can be explained schematically as shown in Figure 2-1. Figure 2-1(a) shows the crystal structures of martensite and austenite respectively. After a lattice deformation transforming austenite to martensite, the interface does not satisfy the requirement of zero distortion (Fig. 2-1(b)). A lattice invariant shear, as shown in Figure 2-1(c), is thus needed to maintain an undistorted interface. The lattice invariant shear can be performed in a reversible manner (by twinning) or in an irreversible one (by slip); the former is strictly the case for thermoelastic martensites. Finally, a rigid body rotation is required to bring the transformed volume back into contact with the parent crystal.

As shown in Figure 2-1(d), there is plane strain associated with the transformation. In order to minimize the total strain energy, the martensite crystals in thermoelastic alloys will accommodate themselves through a twinning process which results in a multi-variant combination, also known as the self-accommodation morphology. The ability of self-accommodated martensite to be deformed by means of detwinning is a fundamental factor underlying shape memory properties.

The description of the phenomenological theory can also be expressed in mathematical form as follows

$$\mathbf{E} = \mathbf{RPT} \quad (2.1.2)$$

where  $E$  is called the total distortion matrix, and  $R$ ,  $P$  and  $T$  are matrices representing a lattice rotation, lattice invariant shear and lattice distortion, respectively [27]<sup>2</sup>. Let us consider the transformation to be one in which a single crystal of austenite is transformed to a banded structure of twin-related martensite plates [25], as shown in Figure 2-2. A macroscopic undistorted habit plane can be obtained if the ratio of the thickness of twins 1 and 2 has a certain critical value. In Fig. 2-2, a vector  $r = OV$  lying on the habit plane in the austenite single crystal becomes a broken vectors  $OA'$ ,  $A'B'$ ,  $B'C'$ ... $U'V'$  after transformation. However, the summation of the vectors yields a new vector  $r'$  having the same length as the original vector  $r$ . If  $M_1$  and  $M_2$  are the matrices that describe the lattice correspondence between austenite and variant 1 as well as variant 2 respectively, i.e.,

$$r' = [(1-x)M_1 + xM_2] r, \quad (2.1.3)$$

then the total distortion matrix  $E$  can be written as

$$E = (1-x)M_1 + xM_2. \quad (2.1.4)$$

The matrix  $M_i$  represents the distortion to which variant  $i$  is subjected, and is in general impure. An impure distortion matrix is asymmetric and causes the magnitude and direction of a vector in the austenite lattice to be changed after transformation. In general, an impure distortion matrix can be decomposed into a pure distortion matrix  $T$  and a rotation matrix  $\Phi$ , i.e.,

$$M_1 = \Phi_1 T_1 \text{ and } M_2 = \Phi_2 T_2 \quad (2.1.5)$$

Thus

$$E = (1-x)M_1 + xM_2$$

---

<sup>2</sup> $E$ ,  $R$ ,  $P$ , and  $T$  are matrices rather than tensors. According to the definition in linear algebra, if  $X$  and  $Y$  are two vector spaces, each vector  $x$  in  $X$  can be assigned a unique vector  $y$  in  $Y$ . The assignment is called a mapping (or transformation or operator) of  $X$  into  $Y$ , and can be expressed as

$$y = Fx$$

where  $F$  is the mapping matrix. In crystallography, a mapping which does not distort size and shape of objects is called a point isometry, such as rotation and inversion. In the present case, only  $R$  is a point isometry.

$$= (1-x)\Phi_1 T_1 + x\Phi_2 T_2 \quad (2.1.6)$$

where  $x$  represents the volume fraction of the major twin variant 2. Matrices  $T_1$  and  $T_2$  can be obtained using the approach proposed by Bain[28]. On the other hand,  $\Phi_1$  and  $\Phi_2$  can not be obtained at the moment, however, the rigid body rotation  $\Phi$  between Twin 1 and Twin 2 can be derived since these two regions have to maintain a coherent twin relation. Hence

$$\Phi_2 = \Phi_1 \Phi \quad (2.1.7)$$

and the total distortion matrix  $E$  can be written as

$$E = \Phi_1 [(1-x)T_1 + \Phi T_2] = \Phi_1 F \quad (2.1.8)$$

where

$$\begin{aligned} F &= (1-x)T_1 + x\Phi T_2 \\ &= PT. \end{aligned} \quad (2.1.9)$$

In general,  $F$  is nonsymmetric and therefore represents an impure distortion which can be expressed as the product of a rotation matrix  $\Psi$  and a pure distortion matrix  $F_s$ ,

$$F = \Psi F_s. \quad (2.1.10)$$

$E$  then becomes

$$E = \Phi \Psi F_s \quad (2.1.11)$$

Moreover, a rotation matrix  $\Gamma$  can be found which diagonalizes the symmetric matrix  $F_s$ , so that

$$F_s = \Gamma F_d \Gamma^*, \quad (2.1.12)$$

where  $F_d$  can be written as

$$F_d = \begin{bmatrix} \lambda_1 & 0 & 0 \\ 0 & \lambda_2 & 0 \\ 0 & 0 & \lambda_3 \end{bmatrix} \quad (2.1.13)$$

Lieberman *et al.* [26] proved that the necessary and sufficient condition for an undistorted habit plane to exist is one of the principle distortion  $\lambda_i$  in  $F_d$  to be unity, that is, no distortion along one of the principle axes. This criterion allows us to derive the normal of the habit plane based on the principle axis system. As a consequence, the related parameters of the transformation can be obtained after the habit plane is found. In chapter 4, the WLR theory will be employed to calculate transformation strain of Type-I (11 $\bar{1}$ ) twinning in monoclinic martensite, and crystallographic parameters, such as habit plane, orientation relationship and transformation strain, of a B2-to-orthorhombic martensite transformation.

## 2.2. Diffusional Transformations in Near-Equiatomic TiNi and Ti(NiCu) Alloys

Copper-containing TiNi alloys are found to be attractive to the present work because of the reduced sensitivity of  $M_s$  temperature on titanium content and superior superelasticity. Therefore, the diffusional transformations and martensitic transformations in both TiNi and Ti(NiCu) alloys will be reviewed in section 2.2 and 2.3 respectively.

The titanium-nickel phase diagrams available to date [29] (see Figure 2-3) show stoichiometric  $\beta$ -TiNi phase (with a B2 structure) at high temperature, with a much steeper solvus boundary on Ti-rich side, and predict an eutectoid decomposition of TiNi to  $Ti_2Ni$  +  $Ni_3Ti$  at  $903 \pm 15$  K. Though the existence of the eutectoid reaction has been supported by several studies [30-33], many investigators [34-37] have argued against it. Wasilewski *et al.* [36] proposed a peritectoid reaction ( $TiNi + Ni_3Ti \rightarrow Ni_3Ti_2$ ) in Ni-rich side at  $898 \pm 20$  K, but others [34, 35, 37] hold  $\beta$ -TiNi to be a stable phase with very limited composition range below this temperature. To solve this controversy, Nishida *et al.* [38]

undertook a study of phase stability on Ti-50 at% Ni and Ti 52 at% Ni alloys. They concluded that neither the eutectoid nor peritectoid reactions occur, and the precipitation sequence in the non-stoichiometric Ti-52 at% Ni alloy could be expressed as:  $\text{TiNi} \rightarrow \text{Ni}_4\text{Ti}_3^3 + \text{TiNi} \rightarrow \text{Ni}_3\text{Ti}_2 + \text{TiNi} \rightarrow \text{Ni}_3\text{Ti} + \text{TiNi}$ , where  $\text{Ni}_4\text{Ti}_3$  and  $\text{Ni}_3\text{Ti}_2$  are metastable phases. At the same time, Beyer *et al.* [40] also studied the precipitation process in Ni-rich alloys and TiNi-Ni diffusion couples, and similar conclusions were drawn. However, as pointed out by Gupta *et al.* [33] the eutectoid decomposition is a sluggish process that might result in a relative stable  $\beta$ -phase .

The  $\text{Ti}_2\text{Ni}$  precipitate has been widely observed in TiNi alloys, partially because of the limited solubility of titanium in TiNi. Moreover, the presence of oxygen and nitrogen can enhance its precipitation [2]. Duwez and Taylor [30] concluded that the  $\text{Ti}_2\text{Ni}$  phase has a face centered cubic unit cell with 96 atoms in it. Later investigation [41] showed that oxygen is soluble interstitially in  $\text{Ti}_2\text{Ni}$  up to 15 at%. The resultant  $\text{Ti}_4\text{Ni}_2\text{O}_x$  phase is isomorphous with  $\text{Ti}_2\text{Ni}$  with a lattice parameter increasing slightly from 1.132 nm ( $\text{Ti}_2\text{Ni}$ ) to 1.134 nm ( $\text{Ti}_4\text{Ni}_2\text{O}$ ). Oxygen was proposed to play a role as an electron acceptor in  $\text{Ti}_2\text{Ni}$ , and hence stabilized this phase. Melton[4] pointed out, according to the Ni-Ti-O phase diagram obtained at 1200 K by Chattopadhyay and Kleykamp [42] (see Figure 2-4), that contamination by oxygen in TiNi decreases the single phase range and can terminate compositions within a three phase region consisting of TiNi,  $\text{Ti}_4\text{Ni}_2\text{O}_x$  and  $\text{Ni}_3\text{Ti}$ . Therefore,  $\text{Ni}_3\text{Ti}$  can be present in a Ti-rich alloy and, more often, oxygen-containing  $\text{Ti}_2\text{Ni}$  is found in Ni-rich alloys. The presence of  $\text{Ti}_2\text{Ni}$  precipitates is usually not favorable because of deleterious effects on hot workability [4].

In Ni-rich alloys, the metastable  $\text{Ni}_4\text{Ti}_3$  phase is coherent with the matrix in the early stages of precipitation [43]. The crystal structure of the  $\text{Ni}_4\text{Ti}_3$  phase is rhombohedral with  $a = 0.6704$  nm and  $\alpha = 113.85^\circ$  [39]. The orientation relationship

---

<sup>3</sup>This was designated as a  $\text{Ni}_{14}\text{Ti}_{11}$  phase in the original literature. However, later study conducted by Saburi *et al.* (39) proposed that it might be more appropriate to express this as a  $\text{Ni}_4\text{Ti}_3$  phase, based on the crystal structure.

between B2 matrix and the  $\text{Ni}_4\text{Ti}_3$  phase is determined to be  $(1\bar{1}0)_{\text{Ni}_4\text{Ti}_3} // (\bar{3}21)_{\text{B2}}$  and  $[111]_{\text{Ni}_4\text{Ti}_3} // [111]_{\text{B2}}$ . Maximum internal stress fields are distributed in  $\langle 111 \rangle_{\text{B2}}$  directions perpendicular to the interfaces, due to the largest mismatching of d-spacing (2.9%) between precipitates and matrix. The internal stresses associated with the precipitation of  $\text{Ni}_4\text{Ti}_3$  were found to change the thermoelastic transformation behavior, which will be described in the next section.

The titanium-nickel-copper ternary phase diagrams at 1143 and 1073 K were explored by van Loo *et al.* [44] and are shown in Figure 2-5. The substitution of Cu in  $\beta$ -TiNi for Ni can be up to 30 at% at 800 °C without destroying thermoelastic characteristics, but the solubility of titanium decreases with more than 3 % copper substitution. Copper is also soluble in  $\text{Ti}_2\text{Ni}$  and  $\text{Ni}_3\text{Ti}$  to 6 % and 4 % at 800 °C respectively. Bricknell *et al.* [45] reported the lattice parameter of the B2 austenite increased slightly from 0.302 nm to 0.304 nm with copper addition up to 10%, and then leveled off. However, Pelton *et al.* [46] undertook a microstructure study on an as-cast  $\text{Ti}_{50}\text{Ni}_{40}\text{Cu}_{10}$  alloy and found  $(\text{NiCu})_2\text{Ti}$  and  $\text{Ti}_2(\text{NiCu})$  phases co-existed with the B2-Ti(NiCu) phase. No further information about phase stability of these ternaries is available at the moment. However, initial experimental results [47] indicate that these phases can also alter thermoelastic behavior in ternary thin films.

## 2.3. Thermoelastic Transformations in TiNi-Based Alloys

### 2.3.1. Thermoelastic Transformation in TiNi Alloys

Three kinds of thermoelastic transformations,  $\text{B2} \leftrightarrow \text{R-phase (R)}$ ,  $\text{B2} \leftrightarrow \text{monoclinic phase (M}_M)$  and  $\text{R-phase} \leftrightarrow \text{monoclinic phase}$ , can occur in TiNi alloys. For convenience in the following discussion, both the  $\text{B2} \leftrightarrow \text{M}$  and  $\text{R} \leftrightarrow \text{M}$  transformations are referred to a "martensitic transformation" while the  $\text{B2} \leftrightarrow \text{R}$  transformation is called the "R-phase" transformation. The R-phase transformation was first treated as a precursor phenomenon to the martensitic transformation [48]. There are several indications in

association with this transition, such as a negative temperature coefficient of electrical resistivity<sup>4</sup>, softening of elastic modules, and appearance of extra diffraction spots. Later investigation showed, however, that the R-phase transformation does not necessarily occur prior to the martensitic transformation, and the former actually is not a precursor phenomenon [49]. Hwang *et al.* [50] studied the R-phase transformations in Ti(NiFe) alloy, and interpreted it as an incommensurate-to-commensurate charge density wave transition. According to the electrical resistivity curves shown in Figure 2-6, Hwang *et al.* [50] interpreted that the B2 parent phase first underwent a second order transition to an incommensurate state associated with an abrupt resistivity increase and a rhombohedral distortion that produces 1/3 (110) and (111) reflections. The onset temperature of the B2-to-incommensurate phase transition was designated as  $T_I'$ . The extra superlattice reflections in fact were not located in the exact 1/3 positions (thus the phase "incommensurate"), and their intensities kept increasing on cooling. A subsequent first order transition occurred involving a structure change from a distorted incommensurate B2 phase to a rhombohedral one causing the extra reflections lock into precise 1/3 positions. The onset temperature of the incommensurate-to-commensurate phase transformation  $T_I$  was defined to be the inflection point in the resistivity curve as labeled in Fig. 2-6. Further decrease of temperature induced the martensitic transformation which resulted in a resistivity decrease, starting at  $M_s$ . The reverse transformation were also thought to be a two-stage transformation. On heating, the resistivity increased up to  $A_s$  where the curve changed its slope. At  $A_f$ , the heating curve crossed the cooling curve. Here the  $A_s$  and  $A_f$  points represented the onset and finish temperature of the martensite-to-R phase transformation respectively. The followed R  $\rightarrow$  B2 transition finished at about  $T_I$ , due to the small hysteresis ( $\sim 1$  K) of the B2  $\leftrightarrow$  R transition.

The crystal structure of the R-phase was given by Goo and Sinclair [51] as a hexagonal lattice with  $a = 7.37$  and  $c = 5.32$  nm. The orientation relationship between B2

---

<sup>4</sup>The temperature coefficient of electrical resistivity  $C = dR_E / dT$  of binary TiNi alloys associated with the martensitic transformation is positive.

and R can be expressed as  $(111)_{B2} // (0001)_R$  and  $\langle \bar{2}11 \rangle_{B2} // \langle \bar{2}\bar{1}\bar{1}0 \rangle_R$ . An enthalpy associated with the transformation was also obtained as 0.2 kJ/mole.

Wu and Wayman [52] proposed that four R-phase variants can be formed from the B2 lattice by elongating any one of the  $\langle 111 \rangle_{B2}$  directions. Twinning relations between R-phase variants with respect to  $\{110\}_{B2}$  and  $\{100\}_{B2}$  planes were observed by Hwang *et al.* [50]. Miyazaki and Wayman [53] proposed that these two twinning systems are compound twins and have exchangeable elements of  $K_1$ ,  $\eta_1$  and  $K_2$ ,  $\eta_2$ . For example, the twinning relationships between variant A (corresponding to  $(\bar{1}11)$  habit plane) and variant B (corresponding to  $(111)$  habit plane) can be  $(011)$  twin or  $(\bar{1}00)$  twin, which is illustrated by the  $(\bar{1}11)$  stereographic projection shown in Figure 2-7. The twinning elements, therefore, are  $K_1 = (011)$ ,  $\eta_1 = [100]$ ,  $K_2 = (100)$ ,  $\eta_2 = [011]$  and  $K_1 = (\bar{1}00)$ ,  $\eta_1 = [0\bar{1}\bar{1}]$ ,  $K_2 = (0\bar{1}\bar{1})$ ,  $\eta_2 = [\bar{1}00]$ .

According to optical microscope observation, Miyazaki and Wayman [53] proposed a four-variant combination for self-accommodation of the R-phase in which twelve variant grains were divided by three  $\{100\}$  and three  $\{110\}$  twinning planes, as shown in Figure 2-8.

On the other hand, the crystallographic characteristics of martensitic transformation in near equiatomic TiNi has been a confusing issue for a long time. Otsuka *et al.* [54] first deduced the crystal structure of martensite to be a distorted B19 type with a monoclinic unit cell for which the lattice parameter is  $a = 0.2889$  nm,  $b = 0.4120$  nm  $c = 0.4622$  nm and  $\beta = 96.8^\circ$ . The orientation relationship between austenite and martensite was expressed as  $(001)_M$   $6.5^\circ$  from  $(101)_{B2}$  and  $[\bar{1}10]_M // [\bar{1}\bar{1}1]_{B2}$ . This monoclinic martensite was proposed resulting from  $1/6$   $(001)[010]$  planar shuffles on alternate  $(001)_M$  (or  $\{101\}_{B2}$ ) planes. Detailed analysis carried out by several researchers [55-57] later found the monoclinic martensite has a three dimensional close-packed structure, rather than a layered one.

$(\bar{1}\bar{1}1)$  Type-I twinning [54, 58, 59]  $[011]$  Type-II twinning [60, 61] and  $(001)$  compound twinning [62] have all been observed by electron microscopy in TiNi alloys and related ternaries. Theoretical calculations carried out by Knowles and Smith [60] showed that only the  $(\bar{1}\bar{1}1)$  and the  $[011]$  twins can accomplish the lattice invariant shear. Matsumoto et al. [63] studied the stress-induced martensitic transformation in a bulk Ti-49.8 at% Ni single crystal and concluded that only Type-II  $[011]$  twinning is responsible for the lattice invariant shear. On the basis of prior results, Miyizaki, Otsuka and Wayman [23] deduced a three-variant self accommodation mechanism, as shown in Figure 2-9, which forms a triangle bounded by three  $\{754\}_{B2}$  habit planes. There are three junction planes between variants in the triangle and they are one Type-I  $(001)$  twinning plane and two Type-II twinning planes respectively. The Type-I  $(\bar{1}\bar{1}1)$  twins thus were thought to have been caused by a thin foil effect [63].

Martensitic transformation temperatures of TiNi are strongly dependent on composition, particularly on the Ni-rich side [2], as shown in Figure 2-10. The  $M_s$  temperature changes over 100 K/at% on the Ni-rich side, whereas the change is only about 30 K/at% on the opposite side. The transformation temperatures are also sensitive to impurity content. A detailed study of the effect of oxygen content on the transformation temperature [64] showed that the  $M_s$  temperature decreased monotonically with an increase of oxygen content as the materials were annealed above 700 K, which was expressed as

$$M_s \text{ (K)} = 351.4 - 92.63X_O \text{ (mole\%)} \quad (2.3.1)$$

where  $X_O = 0.13 \sim 1.06$  mole%. There are some other factors which affect the transformation temperatures as following [65]:

- (1) Aging after solution treatment
- (2) Annealing at temperatures below the recrystallization temperature after cold work.
- (3) Thermal cycling.

## (4) Substitution of a third element (usually for Ni).

The first factor is effective for Ni-rich alloys in which the precipitation of Ni-rich intermetallic phase increases the matrix titanium concentration [38]. However, the internal stress fields associated with coherent precipitates,  $\text{Ni}_4\text{Ti}_3$ , have a strong effect on suppressing the  $M_s$  temperature. Similar results have been found when the rearranged dislocations were introduced. Coherent precipitates and dislocations also make the transformation temperature interval ( $M_f - M_s$ ) larger [65]. Proft *et al.* [66] found that the  $M_s$  temperature of an annealed binary alloy decreased about 20 K during the first ten thermal cycles. The effect of thermal cycling was attributed to dislocations introduced on forward and reverse transformations. In addition, substitution of a third element, such as Cr, Al or Fe is also effectively suppresses the  $M_s$  temperature.

The R-phase transformation usually overlaps the martensitic transformation in a solution-treated alloy. Some of the artificial effects mentioned above, however, can lower the martensitic transformation temperature relative to the R-phase and are summarized as follow [67]:

- (1) the introduction of rearranged dislocations, produced by annealing after cold work or thermal cycling;
- (2) the introduction of coherent precipitates by aging Ni-rich alloys;
- (3) Adding third elements such as Fe or Al.

The R-phase transition start ( $T_R$ ) temperature of an alloy in which the dislocations and/or precipitates are introduced is almost constant of about 300 to 330 K irrespective of composition [68].

### 2.3.2. The Effects of Copper Addition on Martensitic Transformation

Copper-containing NiTi shape memory alloys were first investigated systematically by Melton and his co-workers [8, 69, 70]. They concluded that the major effects of Cu substitution are to reduce the distortion needed to form martensite from austenite, and to

reduce the dependence of  $M_s$  temperature on titanium content. Alloys with Cu additions up to 25 at% undergo martensitic transformation similar to those observed in binary alloys and their  $M_s$  temperatures are not greatly affected by the amount of Cu added. However, later study conducted by Tadaki and Wayman [71] showed the Cu content did change the transformation behavior. Alloys with Cu content less than 3 at% undergo an R-phase transition prior to the martensitic transition on cooling, but in a 19 at% Cu alloy, the B2 to R-phase transformation was not observed. No unambiguous results were obtained for the R-phase transformation in alloys of intermediate Cu content (3 at% to 19 at%). Low temperature martensite in alloys where Cu content is less than 8 at% had a monoclinic lattice with common  $(11\bar{1})$  transformation twins, but in the 19 at% Cu alloy an orthorhombic martensite was found. This B2-to-orthorhombic transformation does not require a lattice invariant shear according to the phenomenological theory, although both untwinned and twinned martensite were observed in this alloy.

At the same time, Shugo *et al.* [72] also studied the effects of Cu addition.  $M_s$  temperature was reported to increase slightly from 70 °C to 90 °C with Cu concentration up to 30 at%, whereas at a constant Cu concentration it decreased with decreasing Ti content from stoichiometry. The dependence of  $M_s$  temperature on Ti concentration in a 5 at% Cu alloy is almost the same as in binary NiTi, i.e., 120 K per at% Ti, while in a 10 at% Cu alloy it is only about 40 K per at% Ti. Orthorhombic martensite was also observed in the alloys with more than 10% Cu addition.

The ambiguity of martensite crystal structure in Ti(NiCu) alloys mainly arises from the existence of a two-step transformation in the medium Cu content (~10 at%) alloys. This two-step transformation was first studied in a  $Ti_{50}Ni_{40}Cu_{10}$  alloy by Shugo and Hoama [73]. They concluded that there occurs first a B2-to-orthorhombic, and subsequently an orthorhombic-to-monoclinic transformation. The two transitions have a temperature interval of about 50 °C, and result in two steps increase of resistivity as well as two exothermal peaks on cooling [73a]. However, monoclinic martensite was also

observed in a 25 at% Cu alloy in the as-cast condition [7]. The monoclinic martensite transformed to orthorhombic martensite after the sample was annealed at high temperature for a long period, indicating the prior thermal and processing history can affect the crystal structure of martensite.

#### 2.4. Crystallization Behavior of Ti-Ni Alloys

Titanium-nickel is an easily amorphized alloy system. Though amorphous  $\text{Ti}_x\text{Ni}_{(1-x)}$  ribbons fabricated by melt spinning in the composition range  $0.23 < x < 0.46$  and  $0.55 < x < 0.64$  have been reported [74, 75], liquid quenched binary alloys are crystalline.  $\text{Ti}_x\text{Ni}_{(1-x)}$  alloys made from physical vapor deposition with  $0.46 < x < 0.55$  are amorphous unless the substrate temperature is higher than approximately 823 K [76]. This difference can be attributed to the higher cooling rate in the vapor quench. However, Buschow [75] pointed out that there is no correlation between thermal stability and the glass-forming ability in Ti-Ni alloys since the crystallization temperatures only vary slightly with respect to nickel content. Figure 2-11 shows the crystallization temperatures and activation energies of amorphous  $\text{Ti}_x\text{Ni}_{(1-x)}$  ribbons versus their composition [75].

The stability of the amorphous alloy is due to the small free energy gap between amorphous and crystalline phases, and the sluggish diffusion of titanium. A large negative enthalpy of mixing (~30 kJ/mole) in the amorphous phase of titanium-nickel results in relative stability [77]. Figure 2-12 shows the calculated free energy diagram at 235 K, deduced by Schwarz *et al.* [78], where the thick solid line and dotted lines represent the free energies of amorphous phase and equilibrium intermetallic phases respectively. Experimental results also indicate that the crystallization enthalpy of near-equiatom TiNi thin film is as low as 1.9 kJ/mole [79]. Moreover, the amorphous-to-crystalline transformation can be regarded as a thermally activated process which needs the collective atomic rearrangement of both nickel and titanium atoms, since all the crystalline phases involved are ordered intermetallic compounds. The diffusion rate of titanium atoms in the

crystalline B2 phase is approximately an order of magnitude lower than that of nickel atoms [80]. In the amorphous phase, there is a lack of data for the Ti-Ni system, but the interdiffusion constant and intrinsic diffusion constant of nickel in amorphous Zr-Ni have been measured. The results showed that the value of these two diffusion coefficients were very close, indicating zirconium is a slow diffuser in amorphous phase [81]. Because of the similarity of Ni-Ti and Ni-Zr systems, titanium is thought to be a relatively immobile species in amorphous phase, too. Under this circumstance, the diffusion of titanium atoms appears to be the kinetic constraint on nucleation and growth of crystalline phases.

## **2.5. Thin Film Processing**

### **2.5.1. Thin Film Deposition by Sputtering**

*General Features.* Thin films can be fabricated by many methods, including thermal evaporation, sputtering, ion plating and chemical vapor deposition. Among these methods, sputtering deposition permits better control of composition and dimensions of the deposited film and greater flexibility in the type of materials that may be deposited [82]. Sputtering is a physical process in which surface or near-surface atoms are ejected from the surface of a solid or a liquid due to the momentum exchange associated with energetic particle bombardment. Generally speaking, in sputtering deposition, the bombarding species ( so-called the projectiles) are inert gas ions with energies in a range of 500 eV to 50 keV. The average number of ejected atoms per incident ion is defined to be the sputtering yield  $Y$ , which is a function of a number of variables, including the energy, the mass, and the incident angle of the projectile, as well as the mass and the surface binding energy of the ejected atom [83]. Figure 2-13 shows the energy dependence of the sputtering yield of nickel [84]. The sputtering yield is also a function of the incident angle of the projectile, with respect to the normal of target surface [85], as shown in Figure 2-14. The increase of sputtering yield follows a  $(\cos\theta)^{-1}$  relation with the incident angle  $\theta$  and

reaches a maximum at  $\theta = 65^\circ \sim 75^\circ$ . This is a critical point which accounts for differences in sputtering behavior for different target surface morphologies.

In the low energy regime the sputtering rate is extremely sensitive to the variation of ion energies ( $E_i$ ) and energy of sputtering threshold ( $E_{th}$ ) [84]. Bohdansky *et al.* [86] derived a scaling law for low energy sputtering in which the sputtering yield,  $Y$ , is given by

$$Y(E') = Q(M_1, M_2, E_B) F(E') \quad (2.5.1)$$

where  $M_1$  and  $M_2$  are the masses of irradiated atom and target atom respectively,  $E_B$  is the bonding energy and  $E'$  is a normalized energy defined by  $E' = E_i/E_{th}$ , where  $E_{th}$  is the threshold energy of sputtering. In this equation  $Q$  is an experimentally determined yield factor which can be written as

$$Q \cong aM_2 [4M_1M_2 / (M_1 + M_2)^2]^{5/3}, \quad (2.5.2)$$

where  $a$  is a material constant, and  $F$  is an universal yield energy curve given approximately by

$$F(E') = 8.5 \times 10^{-3} E'^{1/4} (1 - 1/E')^{7/2}. \quad (2.5.3)$$

As a result, a higher  $E_{th}$  results in a lower sputtering yield at a constant ion energy.

The condensation process of the sputtered atoms can be divided into three steps [87]. First incident atoms transfer kinetic energy to substrate or coating lattice and become loosely bonded "adatoms". Second, the adatoms diffuse over the surface until they either become trapped at low energy site or are desorbed by evaporation or back-sputtering. Finally, the incorporated atoms readjust their positions within the coating by bulk diffusion. Atoms sputtered by ion bombardment have energies of about 10 to 40 eV, which is one to two orders of magnitude greater than the thermal energy of a typical metal lattice interstitial. However, the sputtered atoms may lose part of their energy to collisions in flight from the target to the substrate. Higher ambient pressure results in more collisions

and thus decreases the energy of the arriving atoms. Clemens found that an increase of "structural disorder" of Ti/Ni multilayers was directly related to the increase of ambient pressure (or the decrease of adatom mobility) [88]. The term "structure disorder" was used to describe the lack of texture and poor layering of multilayered TiNi.

In addition, adatom mobility is affected by the surface homologous temperature  $T/T_m$ , where  $T_m$  is the melting point of the coating. The resulting microstructures of the sputter-deposited films are therefore governed by two primary factors: the homologous temperature  $T/T_m$  of the substrate and coating, and the ambient gas pressure. They are expressed concisely in a structure zone diagram [87], as shown in Figure 2-15. At low film temperatures, shadowing (a simple geometric interaction between the roughness of the growing surface and the incident angle of the arriving atoms) results in poor-quality films (called Zone 1 structure) with voided boundaries. Increasing ambient pressure extends the Zone 1 structure to higher temperature regime. At very high homologous temperatures, bulk diffusion enhances the recrystallization process which produces large columnar or equiaxed grains (Zone 3 structure). With limited atom mobility to overcome the shadowing effect, dense fibrous structures (Zone T) and columnar structures (Zone 2) are formed at intermediate temperatures. Computer simulation results indicated that, with zero adatom mobility, larger voids formed as the angle of incidence were increased, even though the substrate was perfectly smooth. However, a dense and smooth film was obtained at normal incidence associated with a slight degree of adatom mobility [89].

*Sputtering of Alloy.* When a virgin alloy target is subjected to energetic particle bombardment, the elemental composition of the sputtered flux is usually not the same as that of the target surface. In other words, components of which the alloy consists have different sputtering yields. This phenomenon is called preferential sputtering [90]. The preferential removal of components from sputter-target surface leads to the formation of the so-called "altered-layer" which is the region with composition different from the bulk. At sufficiently low temperatures, where diffusion is negligible, the thickness of

altered-layer is limited to the depth in which the collision cascade occurs. Especially, steady-state conditions can be attained, in which case the sputtered flux and the bulk alloy are constrained to have the same composition. When steady-state has been achieved, the film composition will depend in interaction of the sputtered flux with the working gas, and by differential sticking coefficients and differential re-sputtering at the substrate.

*Triode Sputtering.* For plasma-based sputtering, the triode source is known to achieve high deposition rate at low pressure (5 to 50 Pa) and target voltage by supplying electrons to the plasma from a thermionic filament in addition to secondary electrons emitted from the target [91]. Therefore, the target voltage and target ion current are independently controlled. A magnetic field is usually employed to minimize the radial plasma losses, but also produces a distortion of the current distribution over the target [87]. Since the triode source is usually operated at lower pressure, the sputtered atoms can pass through the plasma while preserving most of their kinetic energy. This ensures the adatoms have higher mobility. Furthermore, the growing film is also subjected to bombardment by energetic electrons, emitted from target, and energetic neutrals reflected by sputter-target [87]. The former is the primary source of substrate heating, and the latter can result in various effects, such as resputtering and densification of the growing films, which will be discussed in section 2.5.2..

*Ion Beam Sputtering.* Ion beam sputtering supplies some unique features, comparing to the plasma-based sputtering techniques. Both the target and the substrate may be located in places which provide greater isolation of the substrate from the ion generation process. Ion beam sputtering permits an independent control of the energy and the current density of ions. Discrete ion sources usually supply ions with a narrow energy spread of 1-10 eV ( Kaufman source) to 10-50 eV (cold cathode penning source) and at lower pressure (0.01 to 0.1 Pa) [92]. Furthermore, the incident angle of ions, with respect to target normal, and the incident angle of the sputtered atoms, with respect to the substrate

normal, can be independently arranged. However, resputtering of the growing films by energetic reflected neutrals also occurs due to low ambient pressure [93].

### ***2.5.2. Ion Beam Assisted Deposition (IBAD)***

**Ion beam assisted deposition (IBAD) is the process in which a growing film is simultaneously bombarded with an independent controlled ion beam. Among various plasma and ion-based modification techniques, IBAD possesses advantages such as allowing a thicker film to be attained than either direct ion implantation or ion mixing, and permitting independent control of the process variables which are impractical in complex plasma processes.**

**Simultaneous ion bombardment during physical vapor deposition has been observed to produce beneficial modifications in thin film properties, including improved adhesion, densification, modification of grain size and morphology as well as grain orientation, control of residual stresses, and control of composition [94, 95]. Furthermore, ion bombardment enhances the adatom mobility, providing the possibility of low-temperature deposition by which the interdiffusion between film and substrate, and significant amount of extrinsic stress, can be avoided. However, some disadvantages are associated with the employment of ion bombardment during deposition, including the change in composition by preferential re-sputtering [96] and incorporation of the assist-beam working gas [97].**

**Energetic ions bombarding a growing film can produce a variety of effects, including sputtering, desorption, structure disordering, and enhanced diffusion. All these effects result from two different energy loss processes: elastic collision and inelastic collision. Elastic collisions involve the repulsive Coulombic force between the static nuclei and incoming ions. The displaced atoms and deflected ions undergo additional collisions in what is called a collision cascade. The incoming ion can also inelastically interact with electrons in inner and outer shells and produce ionization or excitation of the electrons. The**

energy of the bombarding particle is an important parameter to determine the proportion of these two processes. For low energy (50-1000 eV) ion beams, the energy loss process is dominated by elastic collisions. These result in resputtering, incorporation of the impinging ion species, lattice vibration, defects, and displacement of surface atoms [94].

Bombardment of a surface with energetic particles influences the nucleation and the early stages of growth of the deposits. Marinov [98] deposited silver films on amorphous carbon substrates at room temperature. The results showed that the silver island size increased, with an associated decrease in island number density, as a consequence of the concurrent Ar ion irradiation. The energies of ions varied from 1 to 10 keV. Pronounced adatom-depleted zones were found around large silver islands resulting from ion bombardment. The author thus concluded that concurrent ion bombardment of the growing films enhanced surface mobilities of both adatoms and crystallites. On the other hand, a study of the deposition of aluminum on a dielectric substrate under simultaneous 5 keV Ar ion bombardment showed an increase of island density and a decrease of island size [99]. Similar results were obtained by Lane and Anderson [100] which were interpreted using the assumption that preferential nucleation sites were created by the ion bombardment. It is obvious that concurrent ion bombardment of a growing film influences nucleation and growth mechanisms. However, no single model is yet able to explain all of the observed irradiation effects.

Since the nucleation and growth mechanisms of a growing film are influenced by the employment of ion bombardment, changes of the resultant film microstructure are expected. Microstructure of thin silver film fabricated by dual ion gun sputter-deposition and by thermal evaporation was studied by Huang *et al.* [101]. They found ion beam sputter-deposited films bombarded by Ar ions showed much less texture, smaller grain size and higher defect densities in comparison to an evaporated film. The substrate adhesion of evaporated germanium films was also found to be improved substantially by using Ar ion bombardment [102]. This improvement resulted from an annealing effect, caused by atomic

rearrangement in bombardment-induced thermal spikes, which decreased the tensile residual stress of the films. Furthermore, concurrent ion bombardment was also found to extend the composition range in which the resultant deposits were crystalline [103]. In this study, Ni-La alloy films were deposited by triode sputtering from a cylindrical Ni/La composite target with an overall composition gradation along axial direction. Substrate bias was employed to accelerate ions. The unbiased films were amorphous at a La concentration of 4 at% or higher. However, the films deposited at a bias voltage of -175 volts contained the crystalline phase at wider composition region of 0 to 17 at% La. Martin *et al.* [104] found that ion bombardment of the evaporated  $ZrO_2$  films with 600 eV Ar ions or 1200 eV  $O_2^+$  at room temperature produced crystalline  $ZrO_2$  with a cubic unit cell. The evaporated films without ion irradiation were amorphous.

The component in an alloy or a compound with lower surface binding energy will be sputtered faster, causing a composition change. A simplified model of this preferential resputtering for alloy was established by Haper and Gambino [96], assuming no gas incorporation and unity sticking coefficient during deposition. The film composition  $A_yB_{(1-y)}$  produced under ion bombardment was written in terms of the target composition  $A_xB_{(1-x)}$ , the sputtering yield ratio  $Y = Y_A/Y_B$ , and the fraction resputtered  $X_r$ :

$$y_A = [\alpha + (\alpha^2 + 4x_A\beta)^{1/2}]/2\beta \quad (2.5.4)$$

where  $\alpha = (X_r + x_A Y - x_A - Y X_r - 1)$ ,  $\beta = (X_r + Y - X_r Y - 1)$ ,  $x_A$  is the atomic composition of element A, and  $X_r$  is the fraction of total film resputtered by the ion flux at the substrate. The experimental measurement in this study also found that the sputtering yield ratio of elements in alloys may differ from the ratio of elemental yields, and that the former may be strongly composition dependent. For example, the elemental yield ratio of Gd and Co is 0.37 while the yield ratio in the binary alloy is in a range of 2 to 6. Preferential sputtering becomes more pronounced at lower bombarding ion energy. Tarng and Wehner [105] measured the surface composition of a Constantan target ( $Cu_{55}Ni_{45}$ )

after it was sputtered by Ar ions with various energies. The Auger electron spectroscopy results showed that the sputtering yield ratio  $Y = Y_{Cu}/Y_{Ni}$  was about 1.6 at ion energies of above 150 eV whereas  $Y$  increased dramatically from 1.6 to 7 with a decrease of ion energies from 150 eV to 35 eV.

The incorporation of inert gas ions is strongly dependent on ion energy [106]. In bias rf sputtering, the inert gas content,  $C_g$ , was found empirically to follow a quadratic function of substrate bias [98],

$$C_g = KV_b^2 \quad (2.5.5)$$

where  $V_b$  is the bias voltage. Kornelsen [106] measured the sticking probability of various inert gases in tungsten as a function of ion energy, and found that it drops rapidly in the low energy regime. For argon, for example, the threshold of incorporation is about 100 eV, due to the high reflection coefficient.

Thin films deposited by physical vapor deposition, such as sputtering and evaporation, possess a residual stress which can result in film buckeling, cracking or delamination. Most importantly, the existance of residual stress in TiNi films can shift the  $M_s$  temperature, according to the Clausius-Clapeyron equation described in section 3.1.1. Current ion bombardment of the growing film was also known to modify film stress state[94]. Residual stresses in as-deposited and annealed (873 K, 15 min.) TiNi thin films bombarded by  $Ar^+$  during deposition were studied by Walles [159]. The results showed that the films deposited by ion beam sputtering without assist-beam bombardment had residual stress of about 50 MPa in tensile. After annealed, the stress increased to about 380 MPa in tensile. On the other hand, the stress in the as-deposited IBAD films decreased to 0 or even became compressive monotonically with increasing I/A ratio. The stress in the annealed IBAD films varied with I/A ratio in the same way, however, the I/A value corresponding to zero stress shift from 0.05 in the as-deposited films to 0.45 in the annealed films.

One of the effects of bombardment of the growing film by energetic particles is to enhance the adatom mobility. The enhanced mobility can contribute to thermally activated surface diffusion and impact enhanced surface diffusion. Gilmore *et al.* [107] evaluated the contribution of a thermal spike to the thermally activated events during depositing Au on NaCl with 100 eV Ar<sup>+</sup> ion bombardment. They assumed ions strike a surface creating a point source of thermal energy, and a classical heat transfer equation was employed. The results showed that this thermal spike had little effect on adatom diffusion since the temperature pulse was limited to a radius of about 1 nm within  $3 \times 10^{-13}$  second. The number of thermally activated diffusion events was in the order of  $10^{-5}$  for each impinging ion. On the other hand, Rossnagel *et al.* [108] calculated the number of adatom jumps of Ta impurity on Cu surface induced by Ar ion impingement from experimental data and found this number can be in the order of  $10^2$  to  $10^3$  per ion, depending on the substrate temperature and ion current density.

## 2.6. Current Research on TiNi Thin Films

TiNi thin films with near-equiatomic overall compositions have been fabricated by various methods. Periodic multilayers of titanium and nickel deposited by dual-source magnetron sputtering were studied by Clemens [109]. The as-sputtered films were amorphous when the compositional wavelength was less than 19 Å. Films with larger wavelength were composed of crystalline Ni and Ti. Annealing of the films with wavelength of 200 Å at temperatures between 423 K and 598 K produced amorphous alloys. However, Auger depth profile for a sample annealed at 513 K for 22 hours still showed composition perturbation. High energy ion irradiation was also employed to mix bilayered nickel and titanium films deposited by electron beam evaporation [110, 111]. Gaboriaud and Delage [110] reported that an amorphous TiNi layer was formed after irradiating by 300 keV Kr ions with dose range from  $2 \times 10^{-15}$  to  $2 \times 10^{-16}$  ions/cm<sup>2</sup>. On the other hand, crystalline TiNi with B2 structure was found in a bilayered sample after

bombardment by 55 keV  $\text{Kr}^+$  with total ion dose of  $5.5 \times 10^{-16}$  ions/cm<sup>2</sup> [111]. Although the total doses of ions were almost the same in both cases, the current density of the latter experiment was about three to four order of magnitude higher, which brought the substrate temperature up to about 730 K.

Amorphous TiNi films with composition of  $\text{Ti}_{44}\text{Ni}_{56}$  were also prepared by planar magnetron sputtering [112]. Detailed processing parameters were not available. Nevertheless, DSC results showed that the  $\text{Ti}_{44}\text{Ni}_{56}$  film has a crystallization temperature of 791 K when a heating rate of 10 K/min was used. Further electron microscopy study showed that small  $\text{Ti}_3\text{Ni}_4$  particles were formed in the amorphous matrix at a temperature (778K) which is lower than the start temperature of the crystallization exotherm. Films isochronically annealed at temperature from 300 K up to 873 K showed a fully crystalline structure which was a mixture of the  $\text{Ti}_3\text{Ni}_4$  phase and the R-phase. After annealing at 873 K for seven days, the film was composed of mainly  $\text{Ti}_2\text{Ni}_3$  phase and a small amount of B2 TiNi. An amorphous  $\text{Ti}_{48}\text{Ni}_{52}$  film was also reported to be deposited from a  $\text{Ti}_{50}\text{Ni}_{50}$  target by R. F. magnetron sputtering [113]. The argon gas pressure during sputtering was 32 mtorr and the substrate temperature was maintained at room temperature. The depletion of titanium may have resulted from the employment of substrate bias of -120 V during deposition.

Johnson and his coworkers have conducted research on shape memory properties in TiNi thin films since the late 1980s. TiNi films were deposited from alloy targets by DC magnetron sputtering. The sputtering condition were:  $P_{\text{Ar}} = 0.08$  Pa,  $I = 0.5$  A and  $V = 450$  V. The resulting films were amorphous for substrate temperatures of about 423 to 473 K during deposition [114, 115]. No significant composition shift (< 0.5 at%) between the targets and the resulting films were observed. DSC result for a 49.7 at% Ti film showed the crystallization exotherm located at about 753 K. After annealing in DSC cell, this film showed a two-step thermoelastic transformation on both heating and cooling with transformation temperatures of about 100 K lower than those of the target alloy.

X-ray diffraction and electron microscopy results showed that the post-annealed film might be a mixture of primarily disordered BCC TiNi and fine precipitates of ordered B2 phase. The depression of transformation temperatures was attributed to fine grain size (about 1  $\mu\text{m}$  in diameter) and oxygen contamination. Tensile tests carried out at two different temperatures,  $T < M_f$  and  $T > A_f$ , were also conducted to evaluate the SME and SE. The sample deformed at low temperature began yielding at 85 MPa and produced a recoverable strain of 3 % at 180 MPa. Moreover, a 10- $\mu\text{m}$ -thick film was able to lift a 0.4 g object on heating, demonstrating a recovery stress of up to 480 MPa which is comparable to the bulk TiNi. On the other hand, a total of 2.5 % strain was recoverable upon unloading as deformed at high temperature.

The influence of heat treatment and precipitation on phase transformations in sputter-deposited films were also studied [116]. Films annealed isothermally at 813 K showed a decrease of  $M_s$  temperature and a more pronounced appearance of the R-phase transition with an increase of annealing time. When the films were annealed isochronically from room temperature up to various temperatures (813 K to 1073 K) within thirty minutes, an increase of annealing temperature resulted in similar results, i.e., a decrease of  $M_s$  temperature and a more pronounced appearance of the R-phase transition. Two types of precipitates were observed in electron microscope. The precipitates formed in the grain boundaries were identified as  $\text{Ti}_2\text{Ni}$ , and those appearing in the grain interiors were  $\text{Ti}_3\text{Ni}_4$ . No  $\text{Ti}_2\text{Ni}$  was found in the films annealed at 813K for less than two hours. A small amount of  $\text{Ti}_2\text{Ni}$  precipitates were found in 8-hour and 16-hour annealed films and also in the 873 K annealed films, and much larger quantities of  $\text{Ti}_2\text{Ni}$  were observed in the 973 K and 1073 K annealed films. The precipitation of the  $\text{Ti}_3\text{Ni}_4$ , however, was only observed in the 973 K and 1073 K annealed films respectively. Therefore, the decrease of  $M_s$  temperature in the 813 K annealed films was attributed to the depletion of titanium in the matrix due to the precipitation of  $\text{Ti}_2\text{Ni}$ . The slight decrease of  $M_s$  temperature in the 873 K annealed film then was explained by the same argument. A further depression of the  $M_s$

temperature in the 973 K and 1073 K annealed films was explained by the effect of internal stress associated with the appearance of the  $\text{Ti}_3\text{Ni}_4$  particles.

A hot-stage TEM study carried out by Johnson [6] revealed that the crystallization reaction progressed more rapidly in the thicker part of the film, indicating that the reaction is governed by bulk nucleation. The austenite grain size was about 1 to 3  $\mu\text{m}$ . At lower temperature, martensite variants formed, but the number of variants in a single austenite grain was limited. Some grains only contained two martensite variants.

Thick TiNi films which exhibited reversible shape memory effect were made by Kuribayashi *et al.* [117]. Films with 10  $\mu\text{m}$  thickness were deposited onto NaCl plates and were separated from substrates afterward. The free standing films were annealed at 1073 K for 10 minutes and then were constrained in a glass pipe with 3.7 mm in diameter for a second annealing at 673 K for six hours. The annealed film was afterward cut in a horseshoe-like shape with each pad connecting to a electrical power source. Using a rectangular wave electrical current to heat the film horseshoe, a reversible bending motion with a maximum frequency of 5 Hz was demonstrated.

A planar film spring of TiNi alloy was also fabricated by Walker *et al.* [118, 119]. TiNi thin films was deposited onto a silicon substrate which had been coated with a 3  $\mu\text{m}$ -thick polyimide film. The thickness of TiNi film was 2  $\mu\text{m}$ . A wet-etch was employed to produce a zigzagged spring pattern of TiNi film. The as-sputtered films were given a crystallization anneal at 623 K for one hour and yielded columnar structure with grain size of 0.5-1  $\mu\text{m}$ . Afterward the film pattern was released using an isotropic etch to remove the polyimide spacer. Both the as-sputtered film pattern and annealed film pattern released from spacer exhibited some curling due to residual stress. The curled films then returned toward their original, unreleased configuration after a resistive heating was applied.

Ikuta *et al.* [76] argued that the "shape memory effect" observed in both amorphous and crystalline TiNi thin films in the above work by Walker *et al.* [118] might actually result from thermal expansion effects. They deposited TiNi thin films at various substrate

temperatures by sputtering and found that crystalline films were produced only for substrate temperatures of exceeding 673 K. Films deposited at lower substrate temperatures were amorphous and were annealed at 673 K for one hour. No significant crystal peaks were observed in X-ray spectra for the annealed films, although a thermal hysteresis appeared in their electrical resistivity curves. The as-sputtered amorphous films were also heated by applying electrical current. Maximum current density of about  $6000 \text{ A/cm}^2$  (i.e.,  $1.6 \times 10^5 \text{ W/cm}^2$ ) was applied to the amorphous films but the joule heat failed to trigger the crystallization reaction.

*Comment and Prospect.* The study of a sputter-deposited  $\text{Ti}_{49.7}\text{Ni}_{50.3}$  film carried out by Busch *et al.* [115] demonstrated the potential of TiNi films when shape memory effect and superelastic effect is required. Constrained annealing, the processing procedure which has been well-developed to generate reversible shape memory effect in bulk alloys, were also successfully applied in thick TiNi films [117]. However, a full-scale development of thermoelastic TiNi thin films relies on several crucial issues. One is the control of film composition and film structure during processing. TiNi thin films has been fabricated primarily by ion beam mixing and sputtering. Ikuta *et al.* [76] reported the lower-bound substrate temperature of 673 K to yield crystalline films by sputtering. Rai and Bhattacharya [113] showed that negative substrate biasing resulted in titanium depletion in the as-sputtered films. Though both studies supplied important information about film fabrication, more systematic studies must be carried out to improve the understanding of the relationship between processing parameters and film composition and structure.

Other important issues are the thermal stability of microstructure, the thermoelastic transformation characteristics and associated mechanical properties in thin films. Busch *et al.* [116] showed that high temperature and/or long time annealing caused second phase precipitation and transformation behavior variation. This is not the usual case for bulk alloys. The stability of B2 austenite in thin films therefore may be affected by external

factors such as gas contamination at high temperature. Moreover, the appearance of  $\text{Ti}_3\text{Ni}_4$  precipitates at 973 K and 1073 K also challenges the TTT diagram [38], derived from a  $\text{Ti}_{48}\text{Ni}_{52}$  bulk alloy, according to which the upper-bound temperature where the precipitates can appear is about 950 K. In addition, observation of ultra-fine grain size and limited number of crystallographic martensite variants within austenite grains, reported by Johnson [6], showed that thin films have pronounced differences in microstructure, as compared with bulk alloys. This indicated that the mechanical properties of thin films may also be different from those of bulk alloys. However, dedicated and systematic studies on the correlation between microstructures, transformation behavior and mechanical properties in thin films are still not available.

Walker *et al.* [118,119] demonstrated a deposition and patterning procedure which could be accommodated to the present processing techniques used in silicon-based microelectronics. However, the lack of basic characterization on as-sputtered and annealed films makes the results of this work dubious, since in both case, the films ought to be amorphous according to the crystallization data reported by Busch *et al.* [115] and Kim *et al.* [112].

In summary, the present research on near-equiatomic TiNi alloys in the form of thin films are still scattered and inconsistent. The present work is accordingly designed to address on two major issues: The correlation between processing parameters and film composition, and the corresponding microstructure and transformation characteristics of magnetron sputter-deposited Ti(NiCu) films.

### 3. EXPERIMENTAL METHODS

The principal goals of the work are the study of the microstructure and transformation characteristics in TiNi thin films, with emphasis on the relationship between processing parameters, structure and properties as they compare with similar bulk alloys. For this purpose, single layer and periodic multilayered Ti(NiCu) films were prepared by triode magnetron sputtering. The as-sputtered structure, the crystallization behavior, the post-annealing microstructure, and the thermoelastic transformation characteristics were then studied using various methods. Ion beam assisted deposition experiments were undertaken to develop a better understanding of the composition shift found in the magnetron sputter-deposited films. The effect of ion bombardment on film structure was also studied. A flow chart summarizing the experiments is provided in Fig. 3-1. This chapter describes the method used to fabricate Ti(NiCu) and TiNi thin films, and the characterization methods employed to study their composition, crystallization behavior, as-sputtered and post-annealed microstructure, and thermoelastic transformation behavior.

#### 3.1. Materials

In this section, the specification of sputtering target materials, substrate materials and related materials used in the present work will be provided.

The sputtering target alloys with composition of  $\text{Ti}_{50.05}\text{Ni}_{44.99}\text{Cu}_{4.96}$  and  $\text{Ti}_{50.17}\text{Ni}_{49.83}$  respectively were donated by a commercial vendor. Both alloys were cut from hot extruded rod, 62 mm in diameter<sup>1</sup>. The ternary alloy was then machined into a

---

<sup>1</sup>No further information of the trace element contents and fabrication procedures was available from the donor.

round disk, 57 mm in diameter and about 7 mm thickness, for triode magnetron sputtering. The binary alloy was further rolled at about 1200 K into a thin plate, 85 mm in diameter and 3 mm thickness, for ion beam sputtering. Both target surfaces were final ground using #600 abrasive grit papers. In addition, a custom pure titanium target (99.91 at% Ti), fabricated by Varian Associates Inc., was supplied by Professor William Pratt in the Department of Physics and Astronomy at Michigan State University for magnetron sputtering, and used without further preparation.

In ion beam assisted deposition (IBAD) experiments, titanium foils and wires were widely employed for parts, such as ion gun apertures, target shielding and composition trimming wires, which directly suffered from sputter-beam irradiation<sup>2</sup>. All the foils and wires, purchased from Johnson Matthey Company, had the same composition of 99.8 at% Ti with majority of impurity of about 0.102 at% oxygen, 0.031 at% iron and 0.009 at% nitrogen. After machining, the titanium parts were first cleaned in an etchant, consisting of one part HF, three part HNO<sub>3</sub> and five part % H<sub>2</sub>O in volume and then by distilled water, acetone and methanol subsequently. The substrate shutter and substrate holders were made from 1000 series aluminum alloy sheets. All the aluminum parts were cleaned in the same procedures prior to installation, and then coated with TiNi prior to the IBAD runs to control stray contamination.

Five kinds of materials were used in triode magnetron sputtering and IBAD as the substrates. Potassium chloride wafers were cut from a 12 mm x 12 mm x 76 mm cleaved single crystal, purchased from Harshaw/Filtrol Partnership, and were employed to deposit films for transmission electron microscopy (TEM), and differential scanning calorimetry (DSC) studies. Films for electrical resistivity measurements were made on fused silica plates, 1 mm thick, which were cut into 12 mm x 12 mm squares by a diamond blade

---

<sup>2</sup>Even though convergent grids were employed for the sputter-beam source, divergence of the ion beam still existed. For example, sputtering of 800 eV ions, generated from a distance of 10 cm without aperture, produced a visible mark with about 15 cm in diameter on the titanium shielding. Therefore, apertures were used to reduce beam divergence and a shielding positioned behind the target (so-called target shielding) was used to control contamination.

wheel. One-side polished (100) silicon single crystals and pure copper foils (99.9 at% Cu) of 0.1 mm thickness, purchased from Virginia Semiconductor Inc. and EM Science Company respectively, were also used as substrates in magnetron sputtering and IBAD. Finally, microscope slides (25 mm x 76 mm) were used in the IBAD experiments for film thickness measurement.

## **3.2. Deposition Equipment**

### ***3.2.1 Magnetron Sputter-deposition Apparatus***

*System Geometry.* Magnetron sputtering was carried out in an apparatus equipped with four Simard 383 triode magnetron sources. A schematic drawing of the sputtering system is shown in Figure 3-2(a). The triode source assemblies were situated to fire upward, and were held by side-mounted 8-inch knife-edge flanges with an angle of 90 degrees between them. Four target shutter plates, controlled by a rotary feedthrough on the bottom of the chamber, were situated 3 cm above each triode source with two chimneys on each one of them. One of the chimneys was blocked by aluminum foils while another had a 5 mm x 5 mm window. Substrates were loaded face-down on a rotary table which was positioned 10 cm above the sputtering sources. The table allowed a maximum of eight substrate holders to be installed, each of which could be loaded with two 12 mm square substrates. Each holder was self-shuttered while out of duty, as shown in Fig. 3-2(b). A side-mounted wobble stick manipulator was employed to open or close the shutter by rotating the shutter plate 90 degrees. High pressure cold nitrogen gas, passing through a tubing filled with liquid nitrogen coaxially, was introduced into the central rod which held the rotary table to cool the table and substrates. The motion of substrate table was controlled by an 80386-based computer driving a stepper motor.

*Pumping Capacity and Gas Pressure Monitor.* The system was pumped by a rotary mechanical pump first, and then by an 8-inch cryopump (CTI Cryo-Torr 8) with pumping speed of 1500 l/s of air. After baking for over 24 hours at about 340 K, the

chamber is able to attain a base pressure of  $1.3 \times 10^{-6}$  Pa consistently. Furthermore, a Dycor M102 quadrupole mass spectrometer was attached to the chamber to measure the partial pressures of residual gases.

**Thickness Monitors.** Two quartz crystal thickness monitors (Temescal FTM-3000), consist of quartz crystal sensors and monitor/controller units, were employed to measure deposition rate of each sputtering source. Quartz crystal was fabricated into a disk with 12 mm in diameter, and had a 6.0 MHz resonant frequency. The quartz crystal sensors were held diagonally about 1 cm above the apparatuses on the substrate table, without water-cooling, as shown in Fig. 3-2(a).

In principle, the resonant frequency,  $f_q$ , of the quartz crystal sensor varies as a function of the mass of film deposited [120]. As a result, the mass of film deposited can be expressed as

$$m_f = (N_q \rho_q / \pi f_c Z) \{ \tan^{-1} [z \tan(\pi (f_q - f_c) / f_q)] \} \quad (3.2.1)$$

where  $N_q$  is the frequency constant for AT-cut quartz crystal,  $\rho_q$  is the density of quartz,  $f_q$  is the resonant frequency of uncoated quartz,  $f_c$  is the resonant frequency of coated quartz and  $Z$  is the acoustic impedance ratio which is written as

$$Z = (\rho_q \mu_q / \rho_f \mu_f)^{1/2} \quad (3.2.2)$$

where  $\rho_f$  is the density of deposited film, and  $\mu_q$  and  $\mu_f$  are the shear moduli of quartz crystal and deposited film respectively. The deposited film thickness can be calculated from film mass and film density accordingly. In the present work, the density of alloy film and Ti film are replaced by their bulk densities of  $6.5 \text{ gm/cm}^3$  and  $4.5 \text{ gm/cm}^3$  respectively to calculate their deposition rates. The acoustic impedance of  $14.03 \times 10^5 \text{ dyne/cm}^3$  for titanium is used. Moreover, the acoustic impedance of amorphous Ti(NiCu) alloy film is not available, and is replaced by the value for quartz crystal ( $8.83 \text{ dyne/cm}^3$ ).

The primary error in deposition rate measurement results from the difference between of bulk density and film density. According to equation 3.2.1, film deposition rate  $R_{dep}$  can be written as

$$\begin{aligned} R_{dep} &= d(m_f / \rho_f) / dt \\ &= (dm_f / dt) / \rho_f. \end{aligned} \quad (3.2.3)$$

The value of  $(dm_f / dt)$  is a constant and therefore  $\Delta R_{dep}$  can be expressed as

$$\Delta R_{dep} = (1/\rho_f) - (1/\rho_b) \quad (3.2.4)$$

where  $D_b$  is the density of bulk material.

The shear modulus of equiatomic TiNi was reported by Buehler and Wang [1] to be 24.8 GPa. Accordingly, the acoustic impedance of bulk TiNi is calculated to be  $12.7 \times 10^5$  dyne/cm<sup>3</sup>. However, Li [121] pointed out that the ratio between elastic moduli of amorphous and crystallized alloys is generally between 0.7 and 0.8. If this is the case for Ti(NiCu) film deposited, the acoustic impedance is hence estimated to be about  $9.5 \times 10^5$  dyne/cm<sup>3</sup> (75 %), which is only 7% larger than the value of quartz crystal used in the present work. Moreover, calculation results shows that the film mass measured varies less than 2 %<sup>3</sup>, as the Z value changes from 0.5 to 1. As a result, it is reasonable to conclude that the approach used in the present work results in a negligible effect on the accuracy of film thickness measurement.

*Sputtering Sources and Work Gas.* The Simard 383 sources were driven by two power supplies: a Simard TS/2 power supply operated at  $V = 550$  volts and  $I = 0.9$  amperes for sputtering cathode, and a Simard PD/2000 one operated at  $V = 60$  V  $I = 24$  amperes for thermionic emitter in the present work. The sputtering target was soldered with indium onto a copper heat sink which was cooled by water. Argon was used as a working gas for sputtering, which was purified by passing through a cold trap ( kept at

---

<sup>3</sup>The deviation of  $m_f$  increases with the increase of  $(f_c - f_q)/f_q$ .

about 90 K) to remove water vapor, and a hot-titanium gas purifier (Hydrox Model 8301) to minimize contamination with reactive gases.

### *3.2.2. Ion beam Assisted Deposition (IBAD) Apparatus*

*System Geometry.* The sputtering-deposition system, contained in a 14-inch metal bell jar, consisted of a 85 mm diameter alloy target, a 3-cm Kaufmann-type ion gun (Ion Tech Model 3.0-1500-100), a 5-cm cold cathode ion gun (Anatech IG-5C), substrates and relative assemblies, as shown in Figure 3-3(a). The alloy target had a nominal composition of  $\text{Ti}_{50.2}\text{Ni}_{49.8}$ , over which were stretched 11 bundles of three titanium wires, 0.25 mm in diameter, spaced at 6.3 mm intervals, bringing the average effective target surface composition to  $\text{Ti}_{53}\text{Ni}_{47}$ . The target was equipped with liquid nitrogen cooling and was situated at 45 degrees with respect to both the ion gun and the substrate. The substrate holder was a circular plate, 76 mm in diameter, situated coaxially on a rotary stage, as shown in Figure 3-3(b). Four 12 mm x 12 mm substrates could be loaded on the holder, and had a 90-degree angle between them. The substrates were covered by an aperture, located 0.5 cm above the substrates, having a 24 mm hole arranged to allowed substrates to be exposed to the sputtered species and ion flux one at a time. A aluminum shutter (coated with NiTi to control stray contamination) was positioned 1.5 cm above the substrate holder, and controlled by a central rotary feedthrough. Titanium apertures and shielding were used to control contamination by stray sputtering from chamber structures.

*Ion Source and Working Gas.* The sputter target was irradiated with 800 eV argon ions, having an incident angle of 45 degrees, using the 3-cm Kaufmann-type gun fitted with converging optics. The 3-cm ion gun was driven by an Ion Tech MPS-3000 FC powder supply, running with a discharge voltage of 55 volts and an accelerator current of 2-3 mA at about 400 volts. The assisted beam was generated by the 5-cm cold cathode gun mounted with its axis normal to the substrates. Argon gas, with purity of 99.996 %,

supply to both ion guns was pass through a drying column and a gas purifying cartridge (OxiClear DGP-250 R1) to remove trace water and oxygen. Gas flow to the 3-cm gun and 5-cm gun during sputtering brought the chamber pressure to  $2.0 \times 10^{-3}$  Pa and  $2.6 \times 10^{-2}$  Pa respectively. Gas flow rates were not generally measured

*Pumping Capacity and Gas Pressure Measurement.* The 14-inch metal bell-jar were equipped with an Alcatel 5400 turbomolecular pump, having a pumping speed of 400 l/s of air, and an APD cryopump with pumping speed of 1200 l/s of air. The chamber base pressure attained about  $1.3 \times 10^{-5}$  Pa after baked for 4 hours. Residual gas partial pressures were monitored by a Dycor MA 100 quadrupole mass spectrometer.

*Ion Current Measurement.* The assisted beam current was measured by a faraday cup situated on the substrate shutter, as shown in Fig. 3-3(b). The faraday cup, 9.5 mm in diameter and 5 mm height, was biased by a negative potential of 40 volts supplied by the MPS-3000 FC power supply. The ion current was displayed on a digital meter, with resolution of 0.01 mA, on the power supply.

*Substrate Heating.* During deposition, substrate heating was accomplished by radiation from a 600 W quartz lamp situated underneath the specimen fixture, illuminating the substrate through an aperture in the specimen retaining plate. Temperature was controlled by a powerstat and monitored with a fine gauge type-K thermocouple loosely mounted on the back of substrate.

### 3.2.3. Modified IBAD Arrangement

*System Geometry.* A modified IBAD experiment was designed to study the effect of varying ion/atom arrival ratio on film characteristics. The target position was modified in a way that the normal of target did not intersect with the assist-beam axis. Instead, the target was rotated about 30 degrees with respect to the vertical feedthrough on which the target was situated, and still kept an angle of 45 degrees with the Kaufmann gun

axis<sup>4</sup>. The substrates were arrayed in a manner, shown in Figure 3-4, which exploited the inherent assist-beam current profile, together with the natural angular falloff of the deposition flux, to generate a systematic variation in the ion/atom ratio during deposition.

*Ion Current Measurement.* Assist-beam currents were measured with four separate biased faraday cups, 9.5 mm in diameter. The faraday cups were situated on a substrate shutter which was fixed onto a rotary feedthrough, and could be swung into position symmetrical to the specimen location with respect to the axis of the assist-beam gun. The ion current was then displayed on a digital meter with resolution of 0.1  $\mu\text{A}$ .

### 3.3. Deposition Procedures

#### 3.3.1. Triode DC Magnetron Sputtering Deposition

The preparation and deposition procedures of the ternary alloy films are described below. The relative deposition parameters of five deposition runs were tabulated in Table 3-1.

*Substrate Cleaning.* All the substrates, except potassium chloride, were cleaned by acetone and methanol subsequently in ultrasonic cleaner for five minutes to remove grease contamination prior to being installed. The substrate holders were cleaned by an etchant of one part HF, four part  $\text{HNO}_3$  and five part  $\text{H}_2\text{O}$  in volume first to remove previously deposited coatings, and then by water, and subsequently in acetone and methanol in an ultrasonic cleaner.

*Evacuation.* The vacuum chamber was evacuated by cryopump for more than 48 hour after the pressure was brought down to 0.1 Pa by a mechanical pump. As was mentioned in section 3.2.1., the chamber base pressure attained about  $1.3 \times 10^{-6}$  Pa after baking. The exact base pressure and the partial pressures of water vapor, oxygen gas and nitrogen gas of each deposition run are listed in Table 3-1.

---

<sup>4</sup>The 3-cm ion gun was also relocated to maintain the desired geometry.

***Pre-sputtering.*** Except the first deposition run (# 170), two sputtering targets, a pure titanium one and a  $\text{Ti}_{50.05}\text{Ni}_{44.99}\text{Cu}_{4.96}$  one were employed to deposit the films. After attaining a chamber base pressure of about  $1.3 \times 10^{-6}$  Pa, argon gas was introduced and the chamber pressure was maintained at 0.3 Pa by adjusting the stroke of the gate valve. Virgin alloy targets were pre-sputtered for 0.5 hour at full power level to attain steady state sputtering conditions prior to exposure of the substrates. Afterward, both the titanium target and the Ti(NiCu) alloy target were pre-sputtered for 10 minutes at full power level in the beginning of each deposition run. Sputtering parameters have been described in section 3.2.1.

***Deposition Rate Measurement.*** In the beginning of each experiment run, the whole substrate assemble (including substrate table, substrate table and fixture of quartz crystal sensors) was first cooled by cold nitrogen gas to about 220 K. After each target was pre-sputtered for at least 10 minutes, one of the thickness monitors was positioned above the selected sputtering source by rotating the substrate table to measure the deposition rate. Exposure of the sensor to the sputtering source was limited to one minute to avoid temperature increase of the quartz crystal, however, the exact temperatures of the quartz crystals were not known. The deposition rates were assumed to be constant for all films deposited afterward unless the sources was shut off. Typically after three samples were made, the substrate temperature was close to 373 K and the power of both sources were shut off for one to two hours. Deposition rate of each source were measured again after power was restored. The fluctuation of deposition rate in each experiment run stayed within  $\pm 0.1 \text{ \AA}$ . The thicknesses of as-sputtered films were measured once by profilometer, and the results indicated that the average deviation of true thickness and desired thickness was about  $\pm 5\%$ <sup>5</sup>.

***Film Deposition.*** Prior to exposure of substrates the desired sputtering sources, the deposition rate of each source, and desired layer or film thickness were entered

---

<sup>5</sup>This  $\pm 5\%$  deviation is a typical value for films deposited by the same system, according to the personal communication with other users.

into a computer to determine the time intervals for which the substrates were exposed to each source. The substrate shutter and source shutters were then opened subsequently to deposit samples. Substrate temperature was monitored by thin gauge thermocouples attached to the back of selected substrates. The substrate temperature was not constant, but was maintained below 373 K during deposition. The films deposited from single alloy target are hereafter called single layer (SL) films, and those which deposited from alternating alloy target and titanium target are called periodic multilayer (PML) films. For all the PML films, the titanium layer was 1 nm thickness whereas that of alloy layer varied from 9 to 18 nm. In the following text, the terminology of PML-"N" will be used to represent the PML films with alloy-layer thickness of N nm. For instance, PML-9 film means that the film is composed of alternate Ti-layer and alloy-layer with thickness ratio of 1 nm/9 nm. Detailed deposition procedures are shown schematically in Figure 3-5(a).

### 3.3.2. Ion Beam Assisted Deposition (IBAD)

In order to study the ion-solid interaction effects on film structure, thin films of TiNi binary alloy were prepared on KCl substrates by ion beam assisted ion sputter-deposition in a 14-inch metal bell-jar with system arrangement described in section 3.2.2. Two runs were performed with the experimental parameters listed in Table 3-2. Below are description of the deposition procedures.

*Evacuation.* The chamber was first pumped by turbomolecular pump to about  $P = 1.3 \times 10^{-3}$  Pa, and then evacuated by both turbomolecular pump and cryopump. The based pressure is  $4.0 \times 10^{-5}$  Pa and  $2.0 \times 10^{-5}$  Pa for run #1 and #2 respectively.

*I/A Ratio determination.* Ion-to-atom arrival ratios were determined from the deposition rate ( $R_{dep}$ ) and ion current density ( $I$ ). The measurement of ion current density has been described in section 3.2.2. However, the deposition rate was not measured *in-situ* for the following reason: First, the deposition rate was estimated to be about 0.5 Å/sec which was small compared to the resolution of the thickness monitor of 0.1 Å/sec.

In addition, the use of thickness monitor increased the difficulty of stray contamination control. As a consequence, a sample was made in separate run while sputtering with the Kaufmann gun, running with a discharge current of 0.6 A at 55 V and an accelerator current of 2 mA at 450 V, to produce an 0.8 keV, 30 mA beam. The sputter deposition rate was determined by dividing film thickness, measured by profilometer, by the total deposition time. Therefore sputtering rates for the test specimens were maintained at the pre-determined level by keeping the Kaufmann gun parameters constant.

The I/A ratios were then calculated using the following equation:

$$I/A = \frac{\frac{I(F)}{A(F)} \cdot \frac{1}{1.6 \times 10^{-19}}}{\frac{R_{dep} \cdot 10^{-9} \cdot \rho_{TiNi}}{W_{TiNi}} \cdot 2 \cdot 6.02 \times 10^{23}} \quad (3.3.1)$$

where  $I(F)$  is the ion current,  $A(F)$  is surface area of faraday cup,  $\rho_{TiNi}$  is the bulk density of TiNi and  $W_{TiNi}$  is the molecular weight of TiNi (106.6).

**Preconditioning.** Sputtering target was pre-sputtered for 10 minutes with an 800 eV ion beam generated by 3-cm Kaufmann gun operated at the same conditions described above. Meanwhile, the 5-cm ion gun was fired with emitter current of 120 mA at  $V_{emitter} = 360$  volts and beam voltage of 500 volts to obtain a stable condition. In addition, the substrate was pre-heated by a quartz lamp to attain the desired temperature.

**Film Deposition.** Thin films for direct TEM observation were deposited onto cleaved potassium chloride crystals. Prior to the opening of substrate shutter, the beam voltage of 5-cm ion gun was adjusted to desired value and the ion current was recorded. Deposition for approximately 0.35 hours produced final film thicknesses of 20-75 nm. The specimens were not rotated and the sputtered flux was thus incident at roughly 45 degrees. Detailed procedures are shown schematically in Figure 3-5(b). Table 3-2 summarizes the deposition parameters for the various films, with references to results shown in the next chapter.

IBAD films were directly observed in a JEOL 100 CX transmission scanning electron microscope (STEM) operated with acceleration voltage of 100 kV. Samples prepared for electron microscope study will be described in section 3.8.3.

### 3.3.3. *Modified IBAD*

For each of the deposition runs, four 12-mm square cleaved potassium chloride crystals were arrayed together with a 76 mm x 25 mm rectangular glass substrate which had been fitted with a copper foil mask, 0.1 mm thick, to produce a step equal to the film thickness. The glass substrates were cleaned according to the method described in section 3.3.1. The system was brought to a base pressure lower than  $1.3 \times 10^{-5}$  Pa, which accompanying by partial pressures of water vapor, oxygen gas and nitrogen gas tabulated in Table 3-3 for each deposition run. The deposition procedures were basically the same as those described in section 3.3.2. Table 3-4 summarizes the deposition parameters for the various films.

*I/A Ratio determination.* As shown in Table 3-4, there were three control runs, without concurrent ion bombardment, carried out to measure the deposition rates. The ion-beam current densities were measured in three IBAD runs with assist-beam energy of 50, 100 and 500 eV respectively. Figure 3-6 shows effective deposition rates, ion current density and ion-to-atom arrival (I/A) ratio respectively, each plotted as a function of the lateral position of the substrates, for which the zero point corresponds to a location which was coaxial with the sputtering target. A second X-axis scale is shown which gives the effective assist-beam incidence angle,  $\theta$ , which is taken as zero for normal incidence (i.e., for a position on the cold cathode gun axis) and rises to approximately 25 degrees for the specimens located near the sputtering target centerline, as shown in Fig. 3-4. The deposition rate curves, determined by dividing the as-deposited film thickness by the total sputtering time, are shown in Figure 3-6(a) for three separate control runs. The deposition rate curves reflect the angular dependence of the sputtered flux from the alloy target, and

the increased effective substrate-target distance for the specimens displaced from the sputter target axis. The dramatic increase of the deposition rate in control-1 run resulted from the use of convergent grids of Kaufmann gun while divergent grids were employed in control-2 and control-3 runs. The sputtering-beam current of 65 mA used in control-3 run was higher than that in control-2 run (50 mA), which resulted in a difference in the deposition rates. In addition, ion current density curves are also shown in Figure 3-6(a) for three separate IBAD runs. These curves reflect the radial current density distribution in the ion beam, which depends on the ion energy and total ion beam current. As a result, the experimental arrangement shown in Figure 3-4 can generate a systematic variation in the  $I/A$  ratio for several specimens in a single deposition run.

The calculated  $I/A$  ratios were thus determined from the unassisted deposition rates and the incident ion current as measured during deposition. These values are seen in Figure 3-6(b) to vary from 0.19 to 1.13 for the 500 eV IBAD run, and from 0.17 to 0.57 for the 100 eV IBAD run, and 0.08 to 0.14 for the IBAD run at 50 eV. Because of the falloff of assist-beam current with deviation from the axial location, and because of the increase in the sputter deposition flux as the specimen location approached the axis of the sputter target, higher values of  $\theta$  gave rise to lower  $I/A$  ratios.

Modified IBAD runs were conducted to fabricate thick films for composition analysis and sputtering rate measurement, which will be described in section 3.6 and 3.7 respectively.

### **3.4. Crystallization Behavior of As-Sputtered Ti(NiCu) Thin Films**

#### ***3.4.1. Crystallization Temperature and Enthalpy***

The crystallization characteristics of as-sputtered films, including free-standing SL films, PML-18 films on Cu substrates, PML-9 films on Si substrates, and free-standing PML-9 films, were studied by DuPont 910 differential scanning calorimeter (DSC), using dry nitrogen, with a flow rate of 50 c.c./min, as purging gas. Specimens loaded in sealed

aluminum pans were heated with constant rates of 2, 10, 30 and 50 K/min, respectively, from ambient temperature to 823 K. The sample was weighted by an electronic balance, with maximum resolution of 0.1 mg, prior to be sealed in the aluminum pan. Since the weight of the films on Cu and Si substrates could not be measured directly, the whole sample (film plus substrate) was weighed first. Afterward the film surface area was estimated from substrate weight ( $W_s$ ), density ( $\rho_s$ ) and thickness ( $t_s$ ) as follows:

$$A = W_s / (\rho_s \times t_s) \cong (W_s + W_f) / (\rho_s \times t_s) \quad (3.4.1)$$

where ( $W_f + W_s$ ) is the overall sample weight. The weight of film ( $W_f$ ) was then computed as

$$W_f \cong \rho_f / (A \times t_f) \quad (3.4.2)$$

where the  $\rho_f$  is film density which was replaced by the bulk density of 6.5 g/cm<sup>3</sup> in the calculation and  $t_f$  the desired film thickness, estimated from the deposition rate and total deposition time. In the present case, the thickness of copper foil and silicon wafer was measured by calipers to be 0.12 mm and 0.26 mm respectively. Errors can arise from the use of bulk density, the roughness of the sample edges and the film thicknesses which were not checked by profilometer.

The crystallization temperature was referred to the peak position of the first sharp exotherm in the DSC trace, and the transformation enthalpy was the integral under the whole exotherm peak minus background. The activation energies of crystallization of the ternary films were then calculated by using Kissinger's model [122]. Here it is assumed that the temperature of maximum deflection,  $T_p$ , in differential thermal analysis (DTA) coincides with the temperature at which the reaction rate is at a maximum. For most solid-solid reactions, the rate equation can be expressed as

$$\frac{dx}{dt} = A(1-x)^n \exp\left(-\frac{E}{RT}\right) \quad (3.4.3)$$

If the temperature rises at a constant rate of  $s = dT/dt$ , then by differentiation of equation 3.4.3,

$$\frac{d}{dt}\left(\frac{dx}{dt}\right) = \frac{dx}{dt} \left( \frac{Es}{RT^2} - An(1-x)^{n-1} \exp\left(-\frac{E}{RT}\right) \right). \quad (3.4.4)$$

At  $T = T_p$ ,  $\frac{d}{dt}\left(\frac{dx}{dt}\right) = 0$  and

$$\frac{Es}{RT_p^2} = An(1-x)^{n-1} \exp\left(-\frac{E}{RT_p}\right). \quad (3.4.5)$$

An approximation of  $n(1-x)_p^{n-1} = 1$  was used by Kissinger and the activation energy  $E$  was written as

$$E = R \frac{d\left(\ln \frac{s}{T_p^2}\right)}{d(T_p^{-1})} \quad (3.2.6)$$

This method has been widely employed in the analysis of the kinetics of crystallization reaction, and has been proved to be valid for both DTA and DSC [123, 124].

### 3.4.2. X-ray Diffraction

The crystal structures of as-sputtered and isochronally annealed films were studied by X-ray diffraction on a Scintag XRD 2000 diffractometer operated at  $V = 40$  kilovolts and  $I = 30$  mA using Cu  $K\alpha$  radiation. The as-sputtered samples were scanned from two theta of  $30^\circ$  to  $60^\circ$  in a rate of  $0.4^\circ/\text{min}$ . The annealed films were scanned from two theta of  $37^\circ$  to  $49^\circ$ , since the strongest peak of most ternary phases, such as B2 TiNi,  $\text{Ti}_2(\text{NiCu})$ ,  $\text{Ti}(\text{NiCu})_2$ , and  $\text{Ti}_{40}\text{Ni}_{56.5}\text{Cu}_{3.5}$ , are located in this range. The scanning rate was  $0.15^\circ/\text{min}$ .

### 3.5. Heat Treatment

The as-sputtered films were given a crystallization and/or homogenization anneal at various temperatures, mainly 823 K and 923 K, in either a quartz-tube vacuum furnace or a 14" stainless steel vacuum chamber. The tube furnace was pumped by a 15-cm diffusion pump which maintained a pressure of about  $2.6 \times 10^{-3}$  Pa during anneal. Samples were held in an alumina crucible situated in the center of the heating zoom. Temperature was monitored by a Type-K thermocouple whose tip was situated inside the heating zone about 1 cm above the tube center. The temperature was maintained within  $\pm 2^\circ$  K during annealing. On the other hand, the metal chamber was able to attain a better base pressure of  $1.3 \times 10^{-5}$  Pa and increased to about  $2.6 \times 10^{-4}$  Pa during the anneal. A 500 watt quartz-halogen lamp was employed as the heat source to anneal samples at a distance of 30 mm, and was manually controlled by a powerstat. A 0.1 mm-thick stainless steel foil with a thin-gauge Type-K thermocouple spot-welded on the back was positioned next to the sample to measure the annealing temperature. The fluctuation of the annealing temperature was limited within  $\pm 4^\circ$  K. Afterward, samples were cooled in vacuum in a rate of about 20 K/min.

### 3.6. Composition Analyses

Elemental composition of the films was determined by energy dispersive X-ray microanalysis in a JEOL 100 CX scanning transmission electron microscope (STEM) and a Hitachi S-2500 scanning electron microscope (SEM) respectively. Thin films prepared by electrochemical polishing, which will be described in 3.8.3, were used in the STEM, operated at 100 kV in scanning transmission mode, to collect spectra. A specimen was loaded in a graphite holder and tilted 30 degrees toward the detector to obtain a high X-ray take-off angle. Two standards, a  $\text{Ti}_{50.1}\text{Ni}_{49.9}$  alloy and the sputter-target ( $\text{Ti}_{50.05}\text{Ni}_{44.99}\text{Cu}_{4.96}$ ), were used to determine the intensity ratios of Ni, Ti and Cu.

Since the thin film criterion was satisfied, the film composition was calculated according to the Cliff-Lorimer method [160] which can be expressed as:

$$\frac{C_B(u)}{C_A(u)} = \frac{I_B(u)}{I_A(u)} \times K_{AB} = \frac{I_B(u)}{I_A(u)} \times \frac{I_A(s)}{I_B(s)} \times \frac{C_B(s)}{C_A(s)} \quad (3.6.1)$$

$$\frac{C_C(u)}{C_A(u)} = \frac{I_C(u)}{I_A(u)} \times K_{AC} = \frac{I_C(u)}{I_A(u)} \times \frac{I_A(s)}{I_C(s)} \times \frac{C_C(s)}{C_A(s)} \quad (3.6.2)$$

$$C_A + C_B + C_C = 1 \quad (3.6.3)$$

where  $C_i$  is the concentration of element  $i$ ,  $I_i$  the intensity of the characteristic x-ray line of element  $i$ ,  $C(u)$  the composition of film and  $C(s)$  the composition of standard respectively. The term  $K_{ij}$  varies with operating voltage, but is independent of sample thickness and composition as the intensities are measured simultaneously. Thus, the values of  $K_{ij}$  obtained from standards can be used to determine the film compositions.

Composition analysis carried out in the SEM-EDS system employed a different approach. Films with thickness of 5  $\mu\text{m}$  on Si or glass substrates were illuminated by the electron beam with an energy of 15 to 20 keV. Since no silicon characteristic radiation was observed, the substrate was taken to have no interaction with electrons, and the spectra could be thus treated by a ZAF correction. A program called ZAF-4, supplied by Link analytical Inc. was used to analyze all the spectra, which were collected under carefully controlled conditions. The optics of electron beam and the geometry between lens, sample and X-ray detector were rigorously consistent during data collection. The  $\text{LaB}_6$  electron source hence has to be stabilized for at least 1.5 hour prior to taking any spectra. All the spectra were collected at the same working distance (15 mm), magnification (1000 x), tilting angle, dead time percentage and time interval. The electrical parameters of the lenses remained untouched throughout the whole process to yield a consistent electron intensity. The sample image was thus focused by adjusting the height of sample to maintain a consistent working distance. The  $K\alpha$  peak acquired from a pure nickel standard was

employed to be the calibration spectrum which was collected every 15 to 20 minutes. Pure copper, nickel and a  $\text{Ti}_{50.1}\text{Ni}_{49.9}$  alloy were employed to be the standards for Cu, Ni and Ti respectively, and the composition of target alloy was also calculated to evaluate the accuracy of this method. The bulk materials were last polished by using 0.05  $\mu\text{m}$  alumina powder to yield mirror-like surfaces and then cleaned by acetone and methanol. The specimens, including standards, were loaded on a graphite stage without tilting.

The composition of sputter-target alloy determined by the ZAF method is: 50.2 at% Ti, 45.7 at% Ni and 4.1 at% Cu. The result shows that the measured titanium content of the target alloy is in good agreement with the real value<sup>6</sup> whereas the nickel content is about 0.7 at% higher, and the copper content is 0.85 at% lower than the real values. Larger deviations of the copper and nickel concentration can be ascribed to the overlap of  $\text{Cu K}\alpha$  and  $\text{Ni K}\beta$  characteristic peaks, which results in an overestimate of one element (Ni in the present case) and underestimate of another.

Both methods mentioned above have been used to examine the composition of IBAD films deposited onto copper foils. The 100 eV and 500 eV IBAD films and their control films were analyzed by the Cliff-Lorimer method carried out in the JEOL 100 CX operated at 40 kV, since this EDS system was the one available at that time. The 50 eV IBAD films and the associated control sample were later studied in the H-2500 SEM, using ZAF method.

### 3.7. Thickness Measurement

The IBAD films and the associated control films deposited onto glass substrates were used to determine the deposition rate by measuring the total sample thickness. A Dektak II profilometer was employed to scan across a 3 mm wide step, produced from

---

<sup>6</sup>The composition of sputter-target alloy ( $\text{Ti}_{50.05}\text{Ni}_{44.99}\text{Cu}_{4.96}$ ) was supplied by the donor, U.S. Tinitol Company. However, no further information was available about what technique was employed to determine the composition.

covering a copper foil during deposition, and then yield the thickness profile. The scanning distance was 5 mm with the lowest speed of 1 mm/min.

### **3.8. Microstructure Evaluation**

#### ***3.8.1. X-ray Diffraction***

The phase constituents of annealed Ti(NiCu) films were studied by using the same Scintag XRD 2000 diffractometer described in section 3.4.2. The samples were scanned in a step-scan mode for  $0.05^\circ$  per step and with a dwell of 15 seconds for each step.

#### ***3.8.2. Scanning Electron Microscopy (SEM)***

The morphology of both the as-sputtered and annealed Ti(NiCu) films produced by magnetron sputter-deposition were studied by SEM. The as-sputtered films deposited on silicon substrates were bent to fracture to provide surfaces transverse to the film plane for observation in a Hitachi S-2500 scanning electron microscope operated at 20 kV.

To observe the cross-section of the annealed films, free-standing films were first mounted in acrylic, and then polished by using  $0.05\ \mu\text{m}$  alumina powder. The polished samples were chemically etched in a solution consisting of 20 %  $\text{H}_2\text{SO}_4$  and 80 % methanol, and finally coated with gold ( $\sim 10\ \text{nm}$ ). The samples were also observed in a Hitachi S-2500 scanning electron microscope operated at 20 kV.

#### ***3.8.3. Transmission Electron Microscopy (TEM)***

Thin IBAD films deposited onto KCl substrates were first broken into 2~3 mm squares, and then floated onto deionized water with the film upward. After the film flake separated from KCl and floated on water, a 100 mesh folding grid was used to lift it. After being dried in air, these samples were studied using a Hitachi H-800 transmission electron microscope (TEM) operated at 200 kV, or a JEOL 100 CX scanning transmission electron microscope (STEM) at 100 kV.

The TEM samples of the magnetron sputter-deposited films were prepared as follows: Annealed free-standing films were cut into 3 mm squares using a surgical blade, and then sandwiched between two Cu grids with 2 mm x 1 mm slot. Afterward the films were thinned by electropolishing using the twin jet polisher operated at  $V = 30$  Volt and  $I = 90$  mA at ambient temperature, using an electrolyte consisting of 5% perchloric acid and 95% acetic acid.

The microstructure of the free standing films was then examined by using a Hitachi H-800 TEM operated at 200 kV with a double-tilt holder. Crystal structure investigation of precipitate phases in the SL films was carried out using convergent beam diffraction on a JEOL 2000 FX microscope in the Electron Optical Laboratory at University of Michigan, and refined elemental analysis of precipitates was done on a Vacuum Generators 501 HB dedicated STEM.

### **3.9. Martensitic Transformations in Ti(NiCu) Thin Films**

#### ***3.9.1. Differential Scanning Calorimetry (DSC)***

Martensite transformation temperatures and enthalpies of the isothermally annealed films were determined by DSC, which was described in section 2.1, with 5 K/min heating and cooling rates. The transformation start and finish temperatures were assigned to those corresponding to 5 % and 95 %, respectively, of total heat released or absorbed during the exo- or endothermal reaction.

#### ***3.9.2. Electrical Resistivity Measurement***

The transformation temperatures of the films on glass substrates were studied by four-probe resistivity method, using 5 K/min heating and cooling rates. The resistivity measurement apparatus is shown schematically in Figure 3-7. Samples for electrical resistivity measurement were deposited on fused silica substrates overlaid with an aluminum mask to produce a 2 mm wide strip with five attachment pads for electrodes and a thermocouple, as shown in Fig.3-7. The sample was situated in the middle of a 35x100

mm test tube which was wrapped by heating wire and positioned in a dewar flask. Thin gauge copper wires and a T-type thermocouple were soldered with pure indium onto film pads. A battery supplied a constant current of 0.4 mA through the circuit, while the voltage drop ( $\Delta V_s$ ) across a 3 mm long film strip was recorded by both a XY recorder and a 8086 based computer. For a 5- $\mu\text{m}$  thick film,  $\Delta V_s$  value was about 0.2 mA and the noise level was less than 0.01 mA. The typical electrical resistivity was estimated to be about 200  $\mu\Omega\text{-cm}$ . Steady cooling and heating rates were accompanied by adjusting the flow rate of cold nitrogen gas, and the output of power supply which is connected to the heating wire.

### 3.9.3. X-ray Diffraction

A Rigaku RU-200B X-ray diffractometer, operated at  $V = 50$  kV and  $I = 100$  mA, equipped with a Rigaku CN 2351B1 cold stage was employed to study the crystal structure of the isothermally annealed Ti(NiCu) films at various temperature from 323 K to 80 K. The whole cold stage resides in a sealed vacuum chamber, as shown schematically in Figure 3-8. The sample holder with a build-in heater was mounted on a cold finger which is connected to a liquid nitrogen dewar. Sample temperature was controlled by adjusting the current of heater and the stroke of the liquid nitrogen stopper. Samples were irradiated by Cu  $K\alpha$  radiation in a scan rate of  $1^\circ/\text{min}$  from two theta angle of 35 to 50 degrees. All the samples were first heated up to 323 K, and then cooled subsequently to desired temperatures to collect spectra. The temperature fluctuation during scanning was maintained within  $\pm 1$  K.

### 3.9.4. Transmission Electron Microscopy (TEM)

The martensite phase, which was stable at ambient temperature, was studied using the Hitachi 800 TEM, operated at 200 kV, with a double-tilt stage. In addition, the JEOL 100 CX STEM with a Gatan 626 single-tilt cooling stage was employed to study the thermoelastic transformations *in-situ* at low temperature. The sample temperature was

detected by a silicon diode mounted near the sample holder. A 30 W heater was mounted inside the supporting rod, cooled by liquid nitrogen, to control the sample temperature.

The accuracy of the temperature reading was not supplied by the vendor.

## **4. RESULTS AND DISCUSSION**

The experimental findings presented in this chapter are divided into three sections, each containing both results and discussion of independent topics. Section 4.1 reports on the correlation between processing parameters and microstructure as well as composition of the as-sputtered TiNi films. The crystallization behavior of the magnetron sputter-deposited films is also presented in this section. The microstructures of the annealed Ti(NiCu) films, fabricated by magnetron sputter-deposition, are described in section 4.2. Section 4.3 presents the thermoelastic transformation characteristics of the annealed Ti(NiCu) films. Section 4.4 discusses the resultant microstructure and transformation behavior of the magnetron sputter-deposited films in comparison with bulk alloys of thermoelastic TiNi.

### **4.1. Fabrication of TiNi Thin Films**

Section 4.1.1 describes the structure of the as-sputtered Ti(NiCu) and TiNi films, fabricated using the triode magnetron sputtering apparatus described in section 3.2.1, and the dual ion beam sputter-deposition system described in section 3.2.2. The compositional analysis results of the magnetron sputter-deposited Ti(NiCu) films are reported in section 4.1.2. The composition variation found in the deposited films is rationalized by results from a series of IBAD experiments according to methods described in section 3.2.3 and 3.3.3. Section 4.1.3 reports on the crystallization behavior of the magnetron sputter-deposited Ti(NiCu) films.

#### 4.1.1. Structural Characterization of Sputter-Deposited Films

*Morphology and Structure of As-Sputtered Ti(NiCu) Films .* An as-sputtered SL film deposited on a silicon substrate was bent to fracture and observed by scanning electron microscopy (SEM). The micrograph shown in Figure 4-1 reveals that the top surface of the film is smooth and that the fracture surface is free from voids. No indication of the existence of a zone structure, which is a common feature of the sputter-deposited films, is found. Long, wavy slip bands, propagating in roughly the same direction, were observed to extend from the fracture surface. The lack of well-defined slip planes indicates that the film is amorphous. The morphology of the as-sputtered PML films showed similar features. X-ray diffraction spectra of as-sputtered SL, PML-9, PML-12 and PML-16 films shown in Figure 4-2 verify that these films were amorphous in the as-sputtered condition as indicated by the broad first-order peaks located at a two theta angle of approximately 42 degrees.

The density and smoothness of the films fabricated by triode magnetron sputtering can be attributed to several factors. All films were deposited at low working pressure (0.33 Pa) which allowed the adatoms to have higher average kinetic energy, promoting surface diffusion and thus the density and smoothness [125]. In addition, elevated surface temperature<sup>1</sup> resulted from heat of fusion deposited by the adatoms and from energy transferred by bombardment with energetic particles, including electrons, ions and neutrals. This further decreases the sticking probability of inert gas and increases the surface diffusion rate of adatoms [126]. Also, bombardment by high energy neutrals reflected from target during deposition may further densified the growing films [94]. The lack of

---

<sup>1</sup>Although the substrate temperatures were maintained below 373 K, i.e.,  $T / T_m = 0.285$ , interface reaction and/or diffusion between film and Si (100) substrate were commonly observed, and resulted in a bonding which is so strong that fracture occurred mostly inside the silicon when the film was peeled off. The real temperature on the film surface during deposition therefore may be 100 to 200 K higher than that measured from the backside of the substrate. On the basis of studies which have indicated that interdiffusion between Ni-Si, Ti-Si and NiTi-Si at temperatures above 473 K results in formation of silicides and amorphous phases.

sharp surface facets on the growing amorphous film, and the normal incidence angle of the deposition flux minimized the self-shadowing effect.

*TEM Observation for IBAD TiNi Thin Films .* In the present study, it was also of interest to determine whether IBAD could induce crystallization of growing films at moderate substrate temperatures (300-500 K) [104]. Figure 4-3 shows a variety of TEM results for the ion-sputtered film (Fig. 4-3(a)) and for various IBAD processed films in Figure 4-3(b) through (d). The ion-sputtered film (Fig. 4-3(a)) is fully amorphous, as indicated by the diffuse first order ( $d \sim 0.215$  nm) and second order ( $d \sim 0.125$  nm) halos, and the complete lack of contrast in the bright field image. Figure 4-3(b) through 4-3(d) show bright field images and diffraction patterns of IBAD films processed with increasing ion-to-atom arrival ratios and assist-beam energies. The diffraction patterns of the IBAD films basically contain two diffraction halos which have the same  $d$ -values as those shown in Fig. 4-3(a), indicating that the structures are mainly amorphous. However, some changes in structure are evident as the ion-to-atom arrival ratio increases. A third diffraction halo ( $d \sim 0.280$  nm) adjacent to the zero order spot appears in the diffraction patterns shown in Fig. 4-3(c) and (d). The appearance of additional faint diffraction halo can be explained by the enhancement of short-range ordering [127]. In addition, nano-scale mottled contrast in the microstructures, shown in Fig 4-3(b) through (c), was observed. Similar structure changes, reported by Murri *et al.* [128], were found in RF sputter-deposited GaAs films, and were attributed to the transition of the structure from random network to one having nano-scale ordering. They also reported that the average diameter,  $D$ , of the 'agglomerates' has a weak dependence on processing parameters. The  $D$ -value increased from 3 to 9 nm with a decrease in ambient pressure from 9 Pa to 0.4 Pa, which resulted in more energetic particle bombardment.

In the present work, at higher energy (500 eV) and high ion-to-atom arrival ratio (1.08), inert gas incorporation become quite marked, as shown in Figure 4-4. Extensive porosity, associated with argon gas bubbles, is apparent. The diffraction pattern and bright

field image of one IBAD film, as shown in Figure 4-5, formed with a substrate temperature of 473 K and a 100 eV assist-beam (giving an I/A ratio of 0.33), show different features from the others. The bright field image displays very fine particles, on the order of 5-10 nm in diameter, which have been nucleated in the film during deposition. The corresponding diffraction pattern contains a variety of rings which confirm the presence of a crystalline phase. Two dark field images, made from the brightest of the rings in Fig. 4-5(b), unambiguously associate the particles with the ring system. Table 4-1 tabulates d-spacings of all the rings appeared on the original negative. All can be associated with the d-values for the TiN phase, having the NaCl structure with  $a = 0.4224$  nm [129].

Electron micrographs and their associated diffraction patterns shown in Fig. 4-3 indicate that an increase of substrate temperature and I/A ratio can increase the degree of short-range ordering. The structural relaxation of metallic glasses on heating has been widely studied, and the observed phenomena are divided into changes in topological short-range order (TSRO) and compositional short-range order (CSRO) respectively [130, 131]. Because of the large negative heat of mixing for Ti-Ni alloys, the occurrence of CSRO is rather likely and has been reported in both melt quenched and mechanically alloyed Ti-Ni [78, 131]. This means that the quenched-in as-sputtered structure has higher free energy than the relaxed one, due to the higher configurational entropy. However, the relaxation of quenched-in structure is a thermally activated process which can be performed by increasing sample temperature to about 400 to 700 K [78, 131]. The evidence of short range ordering observed in the IBAD films suggests that the ion bombardment can enhance the thermally activated processes, such as diffusion, so that adatoms and/or near-surface atoms can rearrange themselves into a lower energy configuration. In fact, the crystallization of amorphous alloys requires the same kind of atomic motion in which, however, many more atoms are involved. Therefore, it is apparent that low energy ion irradiation of the growing film can enhance thermal relaxation.

Chen [132] proposed that the thermal relaxation process leads amorphous alloys to experience an irreversible change ( i.e., TSRO) which increases the activation energy for crystallization by a factor  $[1+(d \ln S_c)/(d \ln T)]$ , where  $S_c$  is the configurational entropy. Experimental results on the crystallization temperatures of vapor-deposited and melt-quenched amorphous nickel [133] supported the proposed theory. However, as pointed out by Buschow [75], compositional short-range ordering may decrease the activation energy, through a change of kinetic path. Schwarz *et al.* [134] has also suggested that lower crystallization temperatures observed in mechanically alloyed powder, with composition close to  $TiNi_3$ , is due to the existence of CSRO.

In the present study, the correlation of the thermal stability of Ti-Ni films and their atomic structure has not been established yet. Therefore, an overall survey is needed to understand the effect of chemical short range ordering on the crystallization behavior of amorphous Ti-Ni films. In general, it was not found to be possible to crystallize growing films with an ion assist-beam. However, as will be seen later, IBAD experiments provided useful information about compositional effects of ballistic impingement.

The TiN precipitates observed in the present study may have resulted from contamination of gas supply lines to the ion sources, and/or from high nitrogen base pressure. TiN precipitates were found in directly  $N^+$  implanted TiNi alloy with the dose fluency in a range of  $10^{13}$  ion/cm<sup>2</sup> to  $10^{17}$  ion/cm<sup>2</sup> by popoola *et al.* [135]. Thick TiN coatings were also made by Kant *et al.* [136] to deposit Ti with concurrent argon ion bombardment in a nitrogen atmosphere. Optimum deposition conditions were a  $N_2$  to Ti ratio of 5 and  $Ar^+$  to Ti ratio of 0.3-0.4 at  $Ar^+$  energy of 500 eV. Ion bombardment was found to increase the surface nitrogen concentration and to convert physically absorbed  $N_2$  molecule to a chemisorbed nitrogen atom [137]. In the present study, the base pressure of the experimental run which yielded the TiN containing film was 40  $\mu Pa$ . The nitrogen partial pressure is therefore estimated to be about 1  $\mu Pa$ . The impingement rate of nitrogen is then estimated to be about  $10^{12}$  particle/cm<sup>2</sup>/sec [138], which yields a  $N_2/Ti$  ratio of

about 0.01. Since the assist-beam energy (100 eV) and the I/A ratio of 0.4 are very close to the optimum conditions described above, the appearance of nanocrystalline TiN particles is understandable. However, TiN precipitates were found only in one IBAD film which was the first sample made in that experimental run in which three substrates were loaded. The second and the third samples are those shown in Fig. 4-3(b) and (c) respectively. In case gas supply lines of the ion sources was contaminated, TiN phase should also appeared in the other two samples, since they were bombarded by ions with similar energies (100-200 eV) and dose fluency (I/A of 0.4-0.6). Under these circumstances, the formation of TiN phase in this IBAD film may have resulted from high initial nitrogen partial pressure, or from a effective purge of the supply line after the initial deposition.

#### 4.1.2. Composition of Sputter-Deposited Thin Films

*Compositions of Magnetron-Sputtered Ti(NiCu) Thin Films.* Compositions of single layer (SL) and periodic multilayered (PML) Ti(NiCu) thin films, fabricated by triode magnetron sputtering, are tabulated in Table 4-2. Compared to the composition of the target alloy, the titanium content in the SL film decreased about 2.6 at%, while the nickel content increased 1.5 at% and the copper content increased 1.1 at%, according to the ZAF results. Since the result for the target alloy indicates that the copper content has been underestimated, the real copper content in the SL films should be higher. The analysis for thin foils by the Cliff-Lorimer method for the SL film yielded similar value for titanium content, and about 1 at% increase in Ni and 1 at% decrease in Cu respectively, as compared to the ZAF results.

The addition of titanium multilayers brought the overall titanium concentration in the PML-16 and PML-9 films to 49.2 at% and 51.0 at % respectively. On the assumption that the real deposition rate,  $dm_f/dt$ , of each sputtering source is constant, the compositions of the PML films can be estimated in the following way: The real mass (per unit area) deposited of each layer,  $m$ , can be expressed in terms of the desired thickness,  $T$ , the

deposition rate  $R_{dep}$ , determined by thickness monitor in equation 3.2.3, and the real deposition rate  $dm/dt$  as follows

$$\begin{aligned} m_{alloy} &= (T_{alloy} / R_{dep}(alloy)) (dm_{alloy} / dt) \\ &= T_{alloy} \rho_b(alloy) \end{aligned} \quad (4.2.1)$$

and

$$\begin{aligned} m_{Ti} &= (T_{Ti} / R_{dep}(Ti)) (dm_{Ti} / dt) \\ &= T_{Ti} \rho_b(Ti) \end{aligned} \quad (4.2.2)$$

where  $\rho_b$  is the bulk density employed to determine the deposition rate in equation 3.2.3. The weight percentage of Ti, Ni and Cu in alloy-layer is obtained from the composition of the SL film, determined by the ZAF method, as 42.1 % Ti, 50.7 % Ni and 7.2 % Cu respectively. The Ti content in the PML films are thus calculated and plotted versus Ti-layer thickness ratios in Figure 4-6. The measured Ti contents are about 0.6 at% lower than the expected one.

Before further discussion, it should be pointed out that using bulk density in measurement of deposition rate may produce films with thickness greater than the desired value<sup>2</sup>, but has no effect on the deviation of composition described above. Hence, the 0.6 at% deviation may have resulted from two factors. First, the titanium concentration determined by the ZAF method was estimated to have a  $\pm 0.2$  at% error which was labeled in Fig. 4-6. Second, the real deposition rate,  $dm_f/dt$ , might have suffered small fluctuations during operation. The  $\pm 5$  % deviation of resultant film thickness, found in the present magnetron sputtering system as mentioned in section 3.3.1, could be attributed primarily to the fluctuation of the real deposition rate. The Ti concentrations in the PML films were thus re-calculated assuming fluctuation occurred in the alloy source only and

---

<sup>2</sup>Sputter-deposited films are usually less dense than bulk materials, especially the alloy-layer is amorphous. Vapor phase deposited titanium films are usually polycrystalline. However, the X-ray diffraction study on multilayered Ti-Ni thin films, conducted by Clemens [109], showed that both Ti-layer and Ni-layer are amorphous as the thickness of each layer was less than five monolayers. In the present case, the Ti-layer consists of about three to four monolayers, and thus can be treated as amorphous.

plotted in Fig. 4-6. The deviation resulting from the fluctuation of the real deposition rate increases with the increase of Ti-layer thickness ratio. However, in the present case, an average  $\pm 0.2$  at% error on the titanium content is calculated with a  $\pm 5$  % fluctuation of deposition flux.

Severe titanium depletion, relative to the sputter-target composition, was found in the SL films. Since the sputtering target was preconditioned by sputtering for 30 minutes prior to deposition, and was cooled by water, the surface composition of the sputtering target was expected to reach a steady-state. As mentioned in section 2.5.1, the sputtering flux and the sputter-target alloy have the same composition once the steady-state is attained. In other words, the film composition should be the same as that of the sputter-target alloy, unless the growing films were bombarded by energetic species, resulting in preferential resputtering, and/or the alloy components have different sticking coefficients [90].

Preferential resputtering of the growing film is due to components of the film having different sputtering yields, and usually results from direct ion irradiation on biased substrate and/or bombardment by energetic neutrals reflected from sputter-target. At low ambient pressure, these neutrals suffer few collisions during transit, and arrive at the substrate with high energy. In the present case, the films were deposited at a relatively low pressure (0.33 Pa, corresponding to a mean free path value of 2.5 cm) at which preferential resputtering is expected, though substrates was kept neutral. A Ni depletion<sup>3</sup>, produced by preferential resputtering, is expected according to published sputtering-yield data of elemental Ni and Ti which results in a yield ratio of  $Y_{Ti} / Y_{Ni} \sim 0.5$  [84]. However, the Ti loss found in the SL film indicates that the sputtering properties of Ni and Ti in amorphous Ti-Ni alloys and in pure elements may be different. The IBAD experiments described below have produced additional information in this regard.

*Sputter Yield Ratio Analyses.* Ion beam assisted deposition (IBAD) experiments were designed accordingly to gain better understanding of the sputtering

---

<sup>3</sup>For simplicity, here the discussion was limited in a Ti-Ni two-component system instead a more complicate ternary one.

behavior of Ti and Ni in amorphous Ti-Ni alloys. The analysis of Harper and Gambino [96], as described in section 2.5.2, is employed. The film composition is thus written as

$$y_{Ti} = [\alpha + (\alpha^2 + 4x_{Ti}\beta)^{1/2}]/2\beta \quad (2.5.4)$$

where  $\alpha = (X_r + x_{Ti}Y - x_{Ti} - YX_r - 1)$ ,  $\beta = (X_r + Y - X_rY - 1)$ . Therefore, the sputtering yield ratio,  $Y$ , at certain ion energy, can be obtained by measuring a number of thickness fractions of film resputtered ( $X_r$ ), and film compositions ( $x_{Ti}$ ) both of which vary with the ion-to-atom arrival (I/A) ratio. A dual ion beam system for the IBAD experiment has been described in section 3.2.3 and shown in Figure 3-4, which exploited the inherent assist-beam current profile, together with the natural angular falloff of the deposition flux, to generate a systematic variation in the I/A ratio during deposition. Figure 3-6(b) give an example of the variation in the I/A ratio with respect to the substrate position.

The total fraction of the film resputtered by the assist-beam,  $X_r$ , can be determined by comparing the film thicknesses of ion sputtered films with the thickness of the IBAD film at the corresponding substrate location, according to:

$$X_r = \frac{t_{IBS} - t_{IBAD}}{t_{IBS}} \quad (4.1.2)$$

in which  $t_{IBS}$  and  $t_{IBAD}$  are the film thicknesses for the ion beam sputtered film without an assist-beam, and the ion beam assisted deposit thicknesses, respectively. Results of this analysis, in which  $X_r$  is plotted as a function of the ion-to-atom (I/A) arrival ratio, are shown in Figure 4-7. For the 500 eV assist-beam energy, the expected trend of increasing  $X_r$  for increasing I/A ratio is produced, and the curve shows the expected tendency toward  $X_r = 0$  as the I/A ratio goes to zero. The resputtered fraction for 100 eV IBAD is seen to initially decrease from a high initial value, reaching a minimum at I/A = 0.4, and then to begin to rise slightly at I/A = 0.55. As the assist-beam energy is lowered to 50 eV, the

resputtered fraction increases slightly with the increase of I/A value, levels off and then drops to about 0.02 at I/A = 0.13. (A second set of X-axes are also attached to these plots to demonstrate the relations between the assist-beam incident angle,  $\theta$ , and the sputtered fraction  $X_r$ .)

The titanium depletion is plotted in Figure 4-8 as a function of I/A ratio. The results show a general trend of titanium depletion in the IBAD processed films which increases with increasing of I/A ratio. As is expected, 500 eV assist-beam energy yields the largest amount of Ti-depletion. The data for the 50 eV and the 100 eV IBAD films can, however, be fitted with a single curve, revealing that ions with energy of 50 eV and 100 eV respectively can produce similar amount of titanium depletion in TiNi films.

In Figure 4-9, the change in titanium content from the control value is plotted against  $X_r$  for 50, 100 and 500 eV ion beam assisted depositions. A monotonic decrease in titanium content of the films is evident for the higher assist-beam energy (500 eV), whereas the 100 eV data distribute in a opposite trend across the extrapolation of the 500 eV data. The titanium depletion for the 50 eV assist-beam energy first decrease monotonically with an increase of  $X_r$ , and then deviate toward the same trend as the 100 eV data shown.

Knowledge of the variation of film composition with the total fraction resputtered by an "etching" beam may be used to determine the relative sputter yields of the components of the film. Equation 2.5.4. may be recalled as  $y_{Ti} = [\alpha + (\alpha^2 + 4x_{Ti}\beta)^{1/2}]/2\beta$  where  $\alpha = (X_r + x_{Ti}Y - x_{Ti} - YX_r - 1)$ , and  $\beta = (X_r + Y - X_rY - 1)$ . In the present context,  $x_{Ti}$  represents the Ti content of the films prepared without concurrent ion irradiation, rather than the sputtering target composition. The latter was found to be 0.485 for 500 and 100 eV IBAD films, and 0.535 for 50 eV IBAD films respectively. Using values of  $X_r$  and  $x_{Ti}$  from a linear least squares fit to the 500 eV data results in  $Y = Y_{Ti}/Y_{Ni} = 1.75$ . The data for the 100 eV assist-beam energy do not lend themselves to a curve fit to estimate the value of  $Y$ , though the data

cluster around a value consistent with the high energy result. On the other hand, a fraction of the 50 eV data, which corresponds to lower  $I/A$  ratio (or higher assisted-beam incident angle), can be treated in the same manner to yield another value of  $Y = Y_{Ti}/Y_{Ni} = 9$ . With the increase of  $I/A$  ratio (or the decrease of  $\theta$ ), the data tend to deflect toward higher ratio.

A dramatic increase of the sputtering yield ratio  $Y = Y_{Ti}/Y_{Ni}$  is found at low assist-beam energy. The assisted-beam energies of 50 eV used in the present study are close to the sputtering threshold energies of about 5 to 50 eV for most of materials [139]. In the low energy regime the sputtering rate is extremely sensitive to the variation of ion energies ( $E_i$ ) and energy of sputtering threshold ( $E_{th}$ ) [84]. Bohdanský *et al.* [86] derived a scaling law for low energy sputtering in which the sputtering yield,  $Y$  is given by

$$Y(E') = Q(M_1, M_2, E_B) F(E') \quad (4.2.3)$$

where  $M_1$  and  $M_2$  are the masses of irradiated atom and target atom respectively,  $E_B$  is the bonding energy and  $E'$  is a normalized energy defined by  $E' = E_i/E_{th}$ , where  $E_{th}$  is the threshold energy of sputtering. In this equation  $Q$  is an experimentally determined yield factor which can be written as

$$Q \cong aM_2 [4M_1M_2 / (M_1 + M_2)^2]^{5/3}, \quad (4.2.4)$$

where  $a$  is a material constant, and  $F$  is an universal yield energy curve given approximately by

$$F(E') = 8.5 \times 10^{-3} E'^{1/4} (1 - 1/E')^{7/2}. \quad (4.2.5)$$

As a result, a higher  $E_{th}$  results in a lower sputtering yield at a constant ion energy, and the sputtering yield ratio deduced at higher energy hence may no longer hold. Tarng and Wehner [105] found that the sputtering yield ratio of copper and nickel in a  $\text{Cu}_{55}\text{Ni}_{45}$  alloy showed a pronounced increase with a decrease of bombarding ion energy in the low energy regime (<150 eV). They noted that the sputtering threshold of copper is 17 eV which is smaller than that of nickel (21 eV). Similarly, the sputtering yield ratios derived from

Fig. 4-9 for 50 eV and 500 eV assisted-beam energies imply that nickel has a higher threshold energy than titanium. The increase of sputtering yield ratio can also explain high titanium depletion rate for the 50 eV assist-beam energy shown in Fig. 4-8.

However, the observed behavior of the resputtering rate found at low energy regime cannot be entirely explained by the change of sputtering yield ratio. One possibility is that, at low energy, the angular dependence of the resputtering rate becomes the dominant effect. For the present experimental setup, an increasing I/A ratio corresponds to a decreasing incidence angle of the assist-beam. In the range of 0 to 25 degrees applicable to this study, the angle-dependence of the sputtering rate for Ti sputtered with 1 keV Ar<sup>+</sup> is quite pronounced [85], increasing by a factor of about 25% over that range. For light ions such as H<sup>+</sup>, D<sup>+</sup> and He<sup>+</sup> (1 to 8 keV), this angular dependence of sputtering rate of nickel, reported by Bay and Bohdansky [140], is even greater, increasing about 50 % in the range of 0 to 25 degrees. Considering an elastic collision between an energetic particle and an atom with zero initial energy, limited by the conservation of energy and momentum, the energy transferred by a 1 keV H<sup>+</sup> is in similar amount as that of a 50 eV argon ion. The observation of greater angular dependence of sputtering yield for light ions mentioned above should be able to apply on low energy, heavy ion bombardment. Thus, it may be speculated that the incidence angle effect dominates the resputtering rate at intermediate angles, whereas the I/A ratio dependence begins to exert control for specimens at both near-normal assist-beam incidence angles (corresponding to high I/A ratios), and high angles (at which I/A ratio approaches zero). Furthermore, Yamamura and Bohdansky [141] proposed that the threshold energy  $E_{th}$  decreases with the increase of the ion incidence angle with respect to normal incidence. As discussed above, the sputtering rate is extremely sensitive to the energy of incident ions  $E_i$  when  $E_i$  is close to  $E_{th}$ . Under such circumstances, a stronger angular effect is expected with the decrease of ion energies. The 50 eV data shown in Fig. 4-2 indicates that the angular effect is so strong that the resputtering rate decreases only when the I/A ratio approaches zero, coinciding with the argument. The

incidence angle effect may also explain why the 100 eV data do not appear to tend in a simple fashion toward  $X_r = 0$  at  $I/A = 0$ .

As is the case for the dependence of resputtering ratio,  $X_r$ , on  $I/A$  ratio and on ion incidence angle, the composition dependence on  $X_r$  for 50 eV and 100 eV data shows a decrease in Ti resputtering rate with increasing total fraction resputtered (Fig. 4-9). The data suggest that the *relative* sputter yields of Ni and Ti are also dependent on assist-beam incidence angle. As a consequence, the ratio of sputtering yield,  $Y_{Ti}/Y_{Ni}$ , has a maximum value as sputtered by an assist-beam with a normal incident angle, and then decrease gradually with the increase of incident angle. In other words, the same amount of titanium depletion can be produced with lower total resputtering rate. Again, the results can be rationalized by considering the angular dependence of the sputtering threshold energies and the difference of  $E_{th}$  (Ti) and  $E_{th}$  (Ni). According to the model proposed by Bohdanský *et al.* [86], an order of magnitude change of the sputtering rate can result from a change of energy parameter  $E' = E_i/E_{th}$  from 2 to 8. For 50 eV assist-beam energy, the energy parameter for nickel at normal incidence angle may be close to unity but that for titanium may be two or three times higher, which results in an high value of  $Y_{Ti}/Y_{Ni}$ . The value of sputtering yield ratio then decreases with an increase of ion incidence angle, since  $Y_{Ti}$  has a weaker angular dependence than  $Y_{Ni}$ . The angular dependence of sputtering yield ratio is weaker for 100 eV assist-beam energy due to a larger value of energy parameters for both titanium and nickel. The tendency of the decrease in Ti resputtering rate with increasing total fraction resputtered then becomes more obvious at larger ion incidence angles as shown in Fig. 4-9.

According to the IBA results, the titanium depletion in the magnetron sputter-deposited films is rationalized by the preferential resputtering of Ti by the energetic neutrals reflected from the sputter-target. Vossen [142] reported that the bombarding ions have a high possibility of being neutralized prior to impacting the target surface. They may then be reflected as energetic neutrals without being influenced by the electric field over the

target surface. In the present case, low ambient pressure of 0.33 Pa, corresponding to a mean free path value of 2.5 cm, during deposition allows a fraction of reflected neutrals to preserve much of their initial kinetic energy during transit to the substrates. Therefore, the bombardment of the energetic neutrals results in preferential resputtering. However, the reflected neutrals have a wide energy spectrum which make it difficult to estimate the incident flux of these bombarding particles.

The ratio for sputtering yield of pure titanium and pure nickel,  $Y = Y_{Ti}/Y_{Ni}$ , is about 0.5 in moderate ion energy regimes (500 to 1000 eV) according to the published data [84], which is approximately the inverse of the ratio obtained in Ti-Ni alloy films in the present study. A similar result was deduced for Gd-Co system [96]. Moreover, the elemental sputtering yield of copper is slightly higher than that of nickel. The enrichment of copper in the SL films seems to coincide with the empirical relation deduced from Ti-Ni system in the present study.

As a conclusion, the relation of the sputtering yields of copper, nickel and titanium in ternary amorphous alloys can be expressed as

$$Y_{Ti} > Y_{Ni} > Y_{Cu}$$

in low and intermediate energy regimes. The sputtering yield ratio of Ti and Ni in amorphous TiNi alloys increase from 1.75 at 500 eV of  $Ar^+$  to about 9 at 50 eV of  $Ar^+$ . The titanium depletion of the deposited films observed in the present study may also result from different sticking coefficients of Ni and Ti. However, the absence of experimental data limits further discussion.

#### *4.1.3. Crystallization Behavior of Ti(NiCu) Thin Films*

The crystallization behavior of the magnetron sputter-deposited Ti(NiCu) thin films was studied by differential scanning calorimetry (DSC). Figure 4-10 shows the DSC traces of various magnetron sputter-deposited films subjected to heating at a rate of 10 K/min to 773 K. The exothermal peak appearing at around 750 K in each curve represents

the amorphous-to-crystalline reaction, with an enthalpy in a range of 1.3 to 2.3 kJ/mole. Prior to crystallization, one or two broad exotherms located between 400 and 700 K were also observed. This phenomenon has been reported in Ti-Ni amorphous alloys produced by mechanical alloying [78, 143], and was attributed to a thermal relaxation process which resulted in a short-range ordered structure. Another broad exothermal peak overlapping the crystallization peak in the DSC trace of the PML 18 films probably resulted from the oxidation of the copper substrates used for these specimens. A small side peak is also observed in the traces of the PML-9 films at about 755 K. The nature of this small peak is not yet understood.

Table 4-3 lists the crystallization temperatures ( $T_c$ ) and the corresponding enthalpies for DSC scans conducted at various heating rates,  $s$ . The increase in heating rate raises the crystallization temperature, but depresses the associated enthalpy. The films showed some change in color, indicating a reaction with the gas remaining in the aluminum pan or with the purging gas. The 2 K/min films suffered serious oxidation whereas the 50 K/min annealed films remained mirror bright over most of their surface area. Therefore, the decrease of enthalpy can be attributed to the decrease of effective mass which was still amorphous (i.e., not reacted) prior to reaching the onset of the crystallization reaction. The plot of  $s/T_c^2$  versus the inverse crystallization temperature,  $T_c^{-1}$  [122], as shown in Figure 4-11, yields the activation energies of crystallization for the SL films and the PML films as 485 kJ/mole and 390 +/- 6 kJ/mole respectively.

Figure 4-12 shows the X-ray diffraction patterns for the isochronally annealed films. No peaks other than  $(110)_{B2}$  could be identified at two theta angle between 37 and 49 degrees, revealing that the major product in the amorphous-to-crystalline reaction was ordered B2 NiTi in all the films studied.

The crystallization temperature  $T_c$ , of binary ion sputter-deposited films [144], ternary magnetron sputter-deposited films from the present study, and, for reference,  $T_c$  for

binary alloy ribbons obtained by Buschow<sup>4</sup> [75] are each plotted as a function of titanium concentration and are shown in Figure 4-13.  $T_c$  for binary ribbons decreases monotonically with increase in titanium content in the composition range of 45 at% Ti and 65 at% Ti. The data from binary ion sputter-deposited films [144] and ternary magnetron sputter-deposited films from this study follow this trend also, except that the overall crystallization temperatures of the ternary films in this composition range are about 40 K lower. Figure 4-14 shows a comparison of activation energies between ternary thin films of the present study and binary ribbons obtained by Buschow [75]. The activation energies for crystallization also increase with decreasing titanium content, and those of the ternaries are about 150 kJ/mole lower than those of the binaries. The reduction of crystallization temperature and activation energy of ternary thin films may be attributed to the effect of the third element addition which depresses the melting temperature. Schwarz *et al.* [78] pointed out that for compositions far from those near deep eutectics, the ratio of crystallization temperature to melting point,  $T_c/T_m$ , is approximately equal to 0.5. Considering the fact that the melting point of TiCu is only 1255 K (328 K lower than that of TiNi), and only a two-phase region lies between TiNi and TiCu, the melting point of Ti(NiCu) is expected to decrease with the increase of copper addition. Thus the  $T_c$  values decrease, too. As a result, the addition of Cu substituting for Ni in TiNi alloys can substantially decrease their crystallization temperature.

X-ray diffraction results (Fig. 4-12) show B2 Ti(NiCu) is the only resultant phase after crystallization in all of the ternary films studied. This fact indicates the crystallization process is a polymorphic reaction in which a single phase with the same composition is formed [145]. In other words, the polymorphic reaction needs only single jumps of atoms

---

<sup>4</sup>The crystallization temperatures ( $T_c$ ) tabulated in reference [75] referred to a heating rate of 50 K min<sup>-1</sup>. However, the  $T_c$  values refer to a heating rate of 10 K min<sup>-1</sup> can be yielded by using the approximate Kissinger method as

$$T_c(10) = [\ln(50) \cdot T_c(50)] / \ln(10)$$

which has been discussed in reference [160].

across the interface into their lattice sites [145]. A similar result was found by Battezzati *et al.* [77] for the crystallization process of amorphous  $\text{Ti}_{50}\text{Ni}_{50}$  powders after mechanical alloying. The polymorphic reaction occurred only in concentration ranges near the single phase region [145]. However, this crystalline phase is not necessarily the thermodynamically stable phase at the crystallization temperature. This fact indicates that regardless of whether a eutectoid reaction ( $\text{TiNi} \rightarrow \text{Ti}_2\text{Ni} + \text{TiNi}_3$ ) exists or not, in an amorphous alloy with composition deviating slightly from stoichiometry, a super-saturated single phase solid solution of B2 TiNi can still form. In bulk material, the steep solidus line in Ti-rich side of the B2 TiNi region makes the precipitation of the  $\text{Ti}_2\text{Ni}$  phase during solidification and homogenization virtually unavoidable.

## 4.2. Microstructure Evaluation

This section presents the results of the microstructure study for magnetron sputter-deposited films with overall composition of  $\text{Ti}_{47.4}\text{Ni}_{46.5}\text{Cu}_{6.1}$  (SL film),  $\text{Ti}_{49.2}\text{Ni}_{44.8}\text{Cu}_{6.0}$  (PML-16 film) and  $\text{Ti}_{51.0}\text{Ni}_{44.4}\text{Cu}_{4.6}$  (PML-9 film) respectively. A discussion follows the experimental results for each independent topic presented.

### 4.2.1. SL Films

The overall composition of the SL films located in a two-phase region consisting of a B2 phase and a  $(\text{NiCu})_2\text{Ti}$  phase, according to the TiNiCu ternary phase diagram at 1073 K [44]. However, a Ti-rich  $\text{Ti}_2\text{Ni}$  type phase was found to precipitate in the grain boundaries. This section reports the results of a detailed study on the microstructure of the annealed SL films.

*SL Films: General Features.* The general features of grain size, grain morphology and microstructure of the annealed SL films are shown in Figure 4-15 and 4-16, respectively. Figure 4-15 is a cross-section secondary electron micrograph for a SL film annealed at 923 K for one hour. The grains are equiaxed throughout with average size of 1  $\mu\text{m}$ . Figure 4-16 is an in-plane transmission electron micrograph showing similar grain size and morphology. Numerous small precipitates, about 10 nm to 100 nm in size, are distributed in the grain boundaries and within the grains. Electron diffraction patterns taken at room temperature, shown in Figure 4-17, reveal that the matrix phase is cubic with a CsCl-type stacking order, referred to as the B2 structure. The lattice parameter is 0.301 nm. Diffuse streaks were observed in  $\langle 110 \rangle$  and  $\langle 211 \rangle$  reciprocal directions. The appearance of such diffuse streaks has been reported as a precursor phenomenon of the R-phase transition [48].

*SL Films: Precipitates in the Grain Interiors.* The precipitates in the grain interiors produced distorted Moiré fringes, as shown in Figure 4-18, which are all roughly perpendicular to  $[100]$  direction in the B2 lattice, indicating that a consistent orientation

relation existed between the parent lattice and the precipitates. The distortion of the fringes further suggests the presence of local stress fields associated with precipitates. Since the diffracted spots generated by the precipitates are very close to the matrix spots, the crystal structure of the precipitates was studied by using convergent beam diffraction technique to avoid ambiguity. Figure 4-19 is a series of convergent beam electron diffraction patterns from the precipitate phase which have been indexed to a tetragonal cell with  $a = 0.31$  nm and  $c = 0.80$  nm. The size of the converged electron spot is about 80 nm in diameter, which is still too big to generate diffraction information coming from the precipitate alone. The higher-order Laue zone lines which should appear inside the transmitted and diffracted spots have been obscured by interference from the matrix lattice. Therefore, no atomic symmetry information is available.

X-ray fluorescence microanalysis indicates that the precipitate phase is enriched in copper compared to the matrix, as is apparent from data shown in Figure 4-20. Using the overall (matrix + precipitates) spectrum, shown in Fig. 4-20(a), as a standard yields a composition estimate for the precipitate phase of  $Ti_{0.33}Ni_{0.43}Cu_{0.24}$ , which corresponds to the  $(NiCu)_2Ti$  phase. The lattice parameters, reported by van Loo *et al.* [44] for this ternary phase, of  $a = 0.308 - 0.314$  nm and  $c = 0.792 - 0.800$  nm also agree well with the present results. Thus, the second phase is here identified as  $(NiCu)_2Ti$ . The composition of B2 matrix is also calculated from the spectrum in Figure 4-20(b) as  $Ti_{47.6}Ni_{48.6}Cu_{3.8}$ , using the same standard, which indicates no significant titanium enrichment in the matrix due to the precipitation of the (nickel+copper)-rich phase.

Figure 4-21 shows a bright field image taken approximately parallel to  $\langle 100 \rangle$  in the B2 lattice, demonstrating the typical morphology of the precipitates. The  $(NiCu)_2Ti$  phase appears as a thin rectangular plate with a habit plane parallel to one of the  $\{100\}_{B2}$  planes. Their average size is 100 nm in the longitudinal direction and 30 nm in thickness. A misfit dislocation network can be discerned in the  $\{100\}_{B2}$  interfaces. This dislocation network indicates that the interface is semicoherent. Figure 4-22(a) shows the bright field image in

which three variants of the precipitate in the B2 matrix are observed. The corresponding diffraction patterns shown in Figure 4-22(b) are in an  $[100]_{B2}$  zone axis, which is parallel to two  $[100]_{(NiCu)_2Ti}$  zones. The  $(010)_{B2}$  and  $(001)_{B2}$  are found to parallel to each of the  $(001)_{(NiCu)_2Ti}$  precipitate planes respectively. The dark field images of two precipitate variants, taken from spots *c* and *d* in Figure 4-22(b), are shown in Figure 4-22(c) and 4-22(d) respectively, illustrating the habit plane of the precipitate phase is  $(001)_{(NiCu)_2Ti} // (100)_{B2}$  plane. Consequently, the precipitates oriented themselves in such a way that their three principle lattice axes are parallel to those of the matrix.

In summary, the crystal structure and lattice parameters of the  $(NiCu)_2Ti$  phase observed in this (Ni+Cu)-rich film coincide with the results reported by van Loo *et al.* [44]. Furthermore, the present study provides the first reported data on the morphology, the habit plane and the interfacial structure of the  $(NiCu)_2Ti$  particles, and their orientation relation with B2 parent phase in their early stage of precipitation.

*SL Films: Grain Boundary Precipitates.* TEM study showed that the grain boundary precipitates have two different morphologies: an equiaxed one and a thin-plate one, as shown in Figure 4-23. The rectangular plates are accordingly  $(NiCu)_2Ti$  precipitates. Analysis of the associated diffraction pattern (see Fig. 4-23) reveals that it contains a set of diffraction spots generated by the equiaxed particles. These spots can be indexed in a  $[112]$  zone axis of a  $Ti_2Ni$  phase, having a fcc unit cell with lattice parameter of  $a = 1.132$  nm. The average size of the  $Ti_2Ni$  particles is approximately 20 nm in diameter, and they were only found in the grain boundaries.

Later investigation indicated these grain boundary precipitates are most likely  $Ti_4(NiCu)_2O_x$  phase.  $Ti_2Ni$  and  $Ti_4(NiCu)_2O_x$  have the same crystal structure, which is the  $Fe_3W_3C$  type, with lattice parameters of 1.132 nm and 1.133 nm respectively [41], which are difficult to distinguish by electron diffraction. The partial substitution of Cu for Ni may further alter the lattice parameters. Similar grain boundary precipitates in annealed TiNi thin films have been analyzed by Busch *et al.* [116] using windowless EDS detector.

However, no unambiguous results were yielded, since oxygen was found in both the precipitates and the adjacent area (with no precipitates). As a result, the terminology  $Ti_2Ni$  will be used in the following text to represent either  $Ti_2(NiCu)$  or  $Ti_4(NiCu)_2O_x$ , unless otherwise noted.

*SL Films: Thermal Phase Stability.* X-ray diffraction was employed to study the thermal stability of the B2 phase. Figure 4-24 are diffraction patterns from films annealed at 923 K, for 0.25 hour, one hour, and 4 hours respectively. The broad peak at two-theta of 41.2 degrees consisted of two partly overlapped peaks of  $(110)_{(NiCu)_2Ti}$  at  $41.15^\circ$  and  $(333)_{Ti_2(NiCu)}$  plus  $(115)_{Ti_2(NiCu)}$  at  $41.4^\circ$ . The  $(113)_{(NiCu)_2Ti}$  peak at  $44.9^\circ$  also partly overlapped with the  $(440)_{Ti_2(NiCu)}$  peak at  $45.28^\circ$ . The patterns have been normalized such that the  $(110)_{B2}$  peaks in all the patterns have the same intensity. The intensity of the precipitate peaks, hence, represent the relative volume fraction of each precipitate in the matrix. It is obvious that the volume fraction of both  $(NiCu)_2Ti$  and  $Ti_2(NiCu)$  phases increases with annealing time.

In summary, the annealed SL films with composition of  $Ti_{47.4}Ni_{46.5}Cu_{6.1}$  contained two kinds of precipitates in the B2 matrix: The equiaxed  $Ti_2Ni$  particles appeared in the grain boundaries with diameter of about 20 nm, and the  $(NiCu)_2Ti$  phase was distributed in the grain boundaries and throughout the grain interiors. The  $(NiCu)_2Ti$  precipitates have the morphology of a thin rectangular plate whose plate-plane is the  $(001)_{(NiCu)_2Ti}/\{100\}_{B2}$  habit plane. In addition, the principle lattice axes of these precipitates were found to parallel to those of the B2 matrix.

The next section presents the microstructure of the annealed PML-16 film with overall composition of  $Ti_{49.2}Ni_{44.8}Cu_{6.0}$ . The volume fraction of the second phase precipitates is much lower as compared to that of the SL films. However, the B2 grain boundaries were also decorated by  $Ti_2Ni$  type precipitates.

#### 4.2.2. PML-16 Films

**PML-16 Films: General Features.** Figure 4-25 shows the microstructure of the PML-16 films annealed at 923 K for one hour at  $P = 2.6 \times 10^{-4}$  Pa. The grain morphology is similar to that of the SL films. The average grain size is about 2  $\mu\text{m}$ , and the grain boundaries are decorated with small equiaxed precipitates. Only few scattered precipitates were observed in the grain interiors, and some of them were associated with dislocations. The microstructure of the films, annealed at 823 K for one hour at  $P = 2.6 \times 10^{-4}$  Pa, have similar features, however, with fewer precipitates in both the grain boundaries and the grain interiors.

**PML-16 Film: Grain Boundary Precipitates.** Figure 4-26 shows a bright field image, and its corresponding diffraction pattern, of the grain boundary precipitates, taken from a film annealed at 823 K for one hour. The grain boundary precipitates are about 30 nm in diameter. The diffraction pattern is a typical  $\langle 110 \rangle$  zone of face-centered cubic structure, and the lattice parameter is calculated to be 1.13 nm, which is in good agreement with the published value for the fcc  $\text{Ti}_2\text{Ni}$  phase [41]. Although about one third of the precipitates shown in the image share the same set of diffraction spots, no specific orientation relationship between matrix and precipitates was found.

**PML-16 Films: Precipitates in the Grain Interiors.** In the PML-16 films annealed at 923 K for one hour, a small number<sup>1</sup> of  $\text{Ti}_2\text{Ni}$  particles with a diameter of about 100 nm were found in the grain interiors, often associated with dislocations. Figure 4-27 is a bright field micrograph and its corresponding diffraction pattern of two (111) twin related  $\text{Ti}_2\text{Ni}$  particles. No specific orientation relation between the precipitates and the matrix was found.

Blade-like precipitates distributed in the grain interiors of the films annealed at 923 K and 823 K for one hour, showed distorted Moiré fringes in the wide side. The fringes

---

<sup>1</sup>No quantitative estimate of the volume fraction of the  $\text{Ti}_2\text{Ni}$  phase was made at the moment. However, the  $\text{Ti}_2\text{Ni}$  precipitates were found only in part of the austenite grains in a limited amount (< 10 particles/grain).

are perpendicular to  $\langle 110 \rangle_{B2}$  directions with a spacing of 7.0 nm. Figure 4-28 is a bright field image, and the corresponding diffraction patterns of the precipitates taken from a film annealed at 923 K for one hour. The diffraction patterns consists of a  $[110]_{B2}$  zone pattern and a  $[011]$  zone pattern from the precipitates, which is indexed using the lattice parameters of  $Ni_3Ti_2$  phase as:  $a = 0.441$  nm,  $b = 0.882$  and  $c = 1.35$  nm [38]. As shown in the diffraction patterns, the  $(01\bar{1})$  and  $(200)$  precipitate planes are parallel to  $(001)$  and  $(\bar{1}10)$   $B2$  planes respectively within  $\pm 1$  degree. The spacing of Moiré fringes, calculated from parallel  $(\bar{1}10)_{B2}$  and  $(200)_{Ni_3Ti_2}$ , would be 6.8 nm which is close to the measured value of 7.0 nm. Therefore, the orientation relationship between  $B2$  matrix and the  $Ni_3Ti_2$  type phase is expressed as:  $[\bar{1}10]_{B2} // [011]_{ppt}$  and  $(110)_{B2} // (200)_{ppt}$ . The precipitate blade is about 150 nm wide and 500 to 1000 nm in the longitudinal direction which is parallel to  $\langle 110 \rangle_{B2}$  direction. Dislocations are observed on the interface roughly parallel to the  $\langle 110 \rangle_{B2}$  and then extended into the matrix. These interface dislocations can be observed more clearly in Figure 4-29(a) which is a bright field image showing two parallel  $Ni_3Ti_2$  precipitates. Two sets of dislocations lying in the interfaces intersect with each other to form a network, showing the interface is semi-coherent. Figure 4-29(b) is the associated diffraction patterns which contained an  $\langle 110 \rangle$  fcc zone generated by a particle located between these two  $Ni_3Ti_2$  precipitates, indicating it is a  $Ti_2Ni$  phase.

The blade-like particles observed in the PML-16 films annealed at both 823 K and 923 K is first treated as a ternary phase,  $Ti_{40}Ni_{56.5}Cu_{3.5}$ , based on the ternary phase diagram at 1073 K shown in Fig. 2-5(a). The  $Ti_{40}Ni_{56.5}Cu_{3.5}$  phase is an thermodynamically stable phase, which was first reported by van Loo *et al.* [44], at 1073 K but not at 1143 K. However,  $Ti_{40}Ni_{56.5}Cu_{3.5}$  was reported to have a tetragonal unit cell with  $a = 0.44$  nm and  $c = 1.32$  nm [44], whereas the blade-like particles in the present study have an orthorhombic unit cell. A  $Ti_2Ni_3$  phase with similar structure was also found in binary alloy by Wasilewski *et al.* [36] to precipitate at a temperature below 1000 K. This phase was proposed to be a metastable phase by Nishida *et al.* [38], having a

tetragonal lattice with the same lattice parameter as that of the  $\text{Ti}_{40}\text{Ni}_{56.5}\text{Cu}_{3.5}$  phase at temperatures of above 400 K. The tetragonal phase was reported to undergo a two-step thermoelastic transformation at temperatures between 323 to 400 K in a sequence of tetragonal  $\leftrightarrow$  orthorhombic  $\leftrightarrow$  monoclinic [146]. The orthorhombic phase has a lattice parameter of  $a = 0.44$  nm,  $b = 0.88$  nm and  $c = 1.32$  nm, and the monoclinic phase inherits its lattice parameter with  $\gamma = 89.3^\circ$ . Therefore, it is possible that the  $\text{Ti}_{40}\text{Ni}_{56.5}\text{Cu}_{3.5}$  phase observed in the present study has also undergone a similar transformation from tetragonal to orthorhombic or monoclinic symmetry above ambient temperature. On the other hand, the similarity of the room temperature x-ray diffraction patterns of the  $\text{Ti}_2\text{Ni}_3$  phase and the  $\text{Ti}_{40}\text{Ni}_{56.5}\text{Cu}_{3.5}$  phase, pointed out by van Loo *et al.* [44], may indicate that the crystal unit cell of the latter is orthorhombic rather than tetragonal. However, a further study is necessary to clarify the ambiguity.

The  $\text{Ti}_2\text{Ni}_3$  particles have been reported elsewhere [36, 38] to have a plate-like morphology in the early stage of precipitation. An orientation relationship between monoclinic  $\text{Ti}_2\text{Ni}_3$  and B2 TiNi was also deduced to be  $[111]_{\text{B2}} // [501]_{\text{Ti}_2\text{Ni}_3}$  and  $(\bar{1}10)_{\text{B2}} // (010)_{\text{Ti}_2\text{Ni}_3}$  by Nishida *et al.* [38]. This orientation relationship is different from that between  $\text{Ti}_{40}\text{Ni}_{56.5}\text{Cu}_{3.5}$  and B2 matrix, found in the present study to be  $[\bar{1}10]_{\text{B2}} // [011]_{\text{Ti}_2\text{Ni}_3}$  and  $(110)_{\text{B2}} // (200)_{\text{Ti}_2\text{Ni}_3}$ , though the morphologies of the  $\text{Ti}_2\text{Ni}_3$  phase and the  $\text{Ti}_{40}\text{Ni}_{56.5}\text{Cu}_{3.5}$  phase are similar.

*PML-16 Films: Thermal Phase Stability.* Normalized X-ray diffraction patterns shown in Figure 4-30 reveal that the film annealed at 923 K for 5 minutes at  $P = 2.6 \times 10^{-4}$  Pa has no indication of second phase precipitation. After one hour annealing, peaks from both the  $\text{Ti}_2\text{Ni}$  phase and the  $\text{Ni}_3\text{Ti}_2$  phase can be identified. Peaks for  $\text{Ni}_3\text{Ti}_2$  precipitates are barely recognized, illustrating a very small volume fraction existed, which coincides with the TEM observation. The diffraction pattern of the film annealed for six hours shows apparent increase of the volume fraction of  $\text{Ni}_3\text{Ti}_2$  phase relative to the precipitation of  $\text{Ti}_2\text{Ni}$ .

In summary, the microstructure study for annealed PML-16 films showed that the B2 grain boundaries were decorated with small  $\text{Ti}_2\text{Ni}$  precipitates (about 30 nm in diameter). In the grain interiors, a small number of  $\text{Ti}_2\text{Ni}$  and a  $\text{Ti}_{40}\text{Ni}_{56.5}\text{Cu}_{3.5}$  precipitates were observed. The  $\text{Ti}_2\text{Ni}$  precipitates were about 100 nm in diameter and no specific orientation relation with B2 matrix. On the other hand, the  $\text{Ti}_{40}\text{Ni}_{56.5}\text{Cu}_{3.5}$  precipitates with a thin blade-like morphology have an orthorhombic unit of  $a = 0.441$  nm,  $b = 0.882$  nm and  $c = 1.35$  nm, rather than a tetragonal one according to published data [38]. An orientation relationship between the  $\text{Ti}_{40}\text{Ni}_{56.5}\text{Cu}_{3.5}$  precipitates and the B2 phase were found as:  $[\bar{1}10]_{\text{B2}} // [011]_{\text{ppt}}$  and  $(110)_{\text{B2}} // (200)_{\text{ppt}}$ .

The microstructure of the annealed PML-9 films, with an overall composition of  $\text{Ti}_{51.0}\text{Ni}_{44.4}\text{Cu}_{4.6}$ , is presented in the following section. Only  $\text{Ti}_2\text{Ni}$  type precipitates would be expected to appear in this Ti-rich film.

#### 4.2.3. PML-9 Films

*PML-9 Films: General Features.* Figure 4-31 shows the microstructure of the free-standing PML-9 films, annealed at 923 K for one hour at  $P = 2.6 \times 10^{-3}$  Pa, in a bright field TEM image. The average grain size is about 2  $\mu\text{m}$  and large numbers of second phase particles appear in a fine dispersion throughout the grain interiors with an average diameter of about 15 nm. A precipitate-free zone is apparent adjacent to the grain boundaries, which are themselves decorated with precipitate particles. The particle size and density of the precipitates observed in the film annealed at 923 K for one hour at  $P = 2.6 \times 10^{-4}$  Pa are essentially the same as those shown in Fig. 4-32. However, the microstructure of the films annealed at 823 K for one hour at  $P = 2.6 \times 10^{-4}$  Pa, shown in Figure 4-32, has slightly different features. The grain boundaries are still decorated with small equiaxed particles, whereas more than one kind of precipitates is observed in the grain interiors. The equiaxed precipitates distributed in the grain interiors have a size of

only about 5 nm in diameter. The other precipitates are too small to be identified without ambiguity.

*PML-9 Films: Ti<sub>2</sub>Ni Precipitates.* In Figure 4-33 the particles in the grain interiors are shown at high magnification and display a roughly equiaxed, though sometimes faceted shape, and average about 20 nm in diameter. Plane, undistorted Moiré fringes, perpendicular to [110]<sub>B2</sub>, with a spacing of 3.16 nm, are also present on a large fraction of the precipitates, indicating a strong particle-matrix crystallographic orientation relationship. Electron diffraction patterns in [110] and [111] directions shown in Figure 4-34 reveal that the small particles have a face centered cubic unit cell with a lattice parameter of 1.132 nm, which can be associated with the Ti<sub>2</sub>Ni phase [41]. The diffraction patterns show that the three principle lattice axes of the particles and the B2 matrix are parallel, i.e. that [100]<sub>ppt</sub> // [100]<sub>B2</sub> and (010)<sub>ppt</sub> // (010)<sub>B2</sub>. The expected spacing of the Moiré fringes formed from parallel (440)<sub>ppt</sub> and (110)<sub>B2</sub> planes was calculated as 3.19 nm, which is in a good agreement with the measured value of 3.16 nm. Large *d*-spacing difference ( 6.5 % of {440}<sub>ppt</sub> and {110}<sub>B2</sub>) and the planar Moiré fringes indicated no coherency between the matrix and precipitates lattices. However, a close examination of a TEM micrograph shown in Fig. 4-33 reveals the existence of strain field which results in lobe-like contrast around the fine precipitates as indicated by arrow. A 3 g weak beam micrograph, taken from the same sample, is shown in Figure 4-35 in which the strain contrast can also be identified. Consideration of the lattice parameters of B2 matrix and Ti<sub>2</sub>Ni phase reveals that volume misfit strain may exist in the early stage of precipitation since the Ti<sub>2</sub>Ni phase contain higher ratio of the large Ti atom [147]. The volume misfit is calculated to be 9.7% accordingly, based on the lattice parameters of the B2 phase and the Ti<sub>2</sub>Ni phase. Additional electron diffraction study also showed that the precipitates distributed on the grain boundaries are the same Ti<sub>2</sub>Ni phase, but with no apparent orientation relationship to the B2 grains on either side of the boundary. Moreover, the fine equiaxed precipitates found in the PML-9 film annealed at 823 K for one hour at

$P = 2.6 \times 10^{-4}$  Pa were also  $Ti_2Ni$  phase with the same orientation relationship to the B2 matrix as mentioned above.

***PML-9 Films: Thermal Phase Stability.*** Figure 4-36 are normalized X-ray spectra of films annealed at 923 K for five minutes and one hour respectively. A weak peak located at two theta of  $41.4^\circ$  is discerned in the spectrum for the five-minute annealed film, indicating that the  $Ti_2Ni$  phase begins to form. After one hour annealing, no more phases can be identified in addition to B2  $TiNi$  and  $Ti_2Ni$ , coinciding with the TEM result.

A well-defined orientation relationship between the parent B2 phase and a  $Ti_2Ni$  precipitate phase is deduced for the first time in the present study. A possible reason that this orientation relationship has not been previously identified in bulk  $TiNi$  alloys in some previously studies [32, 33] is described as follows: According to the Ti-Ni phase diagram [29] shown in Fig. 2-3, the steep solidus line on Ti-rich side restricts the formation of a single phase (B2) solid solution with over-saturated titanium. In other words, in bulk Ti-rich alloys, the  $Ti_2Ni$  phase should have already precipitated after solidification and/or homogenization. The processing procedures employed by Gupta *et al.* [33] in which, for instance, the Ti-rich alloys were hot rolled and then homogenized at 1173 K for one hour prior to annealed at 1173 K for one hour would destroy the orientation relationship between the  $Ti_2Ni$  particles and B2 matrix (if it existed) by deformation and subsequent recrystallization of B2 phase. In the present case, however, a polymorphic reaction at about 750 K allows the multilayered PML-9 films crystallize to a single B2 phase, with super-saturated in titanium. The X-ray diffraction study showed that no  $Ti_2Ni$  peaks were detected in the PML-9 film after isothermal annealing at 923 K for 5 minutes (Fig. 4-37), confirming that most of the  $Ti_2Ni$  precipitates nucleated *after* the crystallization of the B2 phase. As a result, the  $Ti_2Ni$  particles precipitating from this over-saturated matrix can maintain well-defined orientation relationship with the B2 parent phase.

In summary, an fcc  $\text{Ti}_2\text{Ni}$  phase was found to precipitate in a wide dispersion in the annealed PML-9 films. The equiaxed precipitates in the grain interior were 5-15 nm in diameter, depending on the annealing temperature, and had a well-defined orientation relationship to the B2 parent phase, this is:  $[100]_{\text{Ti}_2\text{Ni}} // [100]_{\text{B2}}$  and  $(010)_{\text{Ti}_2\text{Ni}} // (010)_{\text{B2}}$ .

#### 4.2.4. Further Discussion

A key issue for the employment of titanium multilayers to increase titanium content in B2 matrix is whether or not the driving force of chemical homogenization can complete with that of precipitation. Both of them depend on the same kinetic process: diffusion. The chemical diffusion coefficient in equiatomic B2 TiNi alloy has been deduced by Bastin and Rieck [37] to be

$$\bar{D} \text{ (cm}^2\text{/sec)} = 0.0020 \exp(-E / RT) \quad (4.2.1)$$

where  $E = 142000$  joule/mole, which yields  $\bar{D} = 1.84 \times 10^{-11}$  cm<sup>2</sup>/sec and  $\bar{D} = 1.94 \times 10^{-12}$  cm<sup>2</sup>/sec at 923 and 823 K, respectively. The study also revealed that the intrinsic diffusion coefficient of Ni is about an order of magnitude higher than that of Ti. In amorphous TiNi alloy, titanium atoms were also found to be a slow diffuser [81]. Accordingly, the approximate diffusion distance,  $(Dt)^{1/2}$ , of titanium at 923 K and 823 K for one hour are estimated by using  $D_{\text{Ti}} = 0.1 \bar{D}$  to be 814 nm and 264 nm respectively. Both values are much larger than the layer thicknesses of 9 and 16 nm. Therefore, it is reasonable to conclude that the composition in the B2 matrix of the annealed PML films are homogeneous throughout.

In addition to the chemical homogeneity of the matrix phase, the true titanium content in the matrix, rather than the overall composition, of the PML films after annealing must be addressed. An extreme case will be that segregated titanium atoms in the Ti layer results in extensive precipitation of Ti-rich phases in the early stage of annealing. If these Ti-rich precipitates remain stable throughout the anneal, the titanium content in the B2

matrix will not be increased effectively by the addition of the Ti layer. In fact,  $\text{Ti}_2\text{Ni}$  particles were found in the grain interiors of the PML-16 film. The lack of orientation relationship between B2 matrix and the particles suggests that they may have nucleated near the Ti layers prior to the crystallization reaction. A simplified calculation was conducted to estimate the density of the  $\text{Ti}_2\text{Ni}$  particles, assuming that all the titanium atoms in the titanium layers were consumed in the precipitation reaction. The result shows that about eighty  $\text{Ti}_2\text{Ni}$  particles with the observed size of  $(100 \text{ nm})^3$  should be found in an  $1 \mu\text{m} \times 1 \mu\text{m} \times 0.1 \mu\text{m}$  volume. This number is at least one order of magnitude larger than that found in the PML-16 films according to the present TEM observation. This fact indicates that less than 10 % of titanium added exists in the  $\text{Ti}_2\text{Ni}$  particles which formed prior to crystallization. Results of X-ray diffraction for the PML-16 and PML-9 films shown in Fig. 4-30 and 4-36, respectively, confirm that no peaks from  $\text{Ti}_2\text{Ni}$  phase can be identified after annealing at 923 K for 5 minutes. Therefore, it is reasonable to conclude that the addition of periodic Ti layers effectively increases the titanium content in the B2 matrix phase.

The extensive observation of  $\text{Ti}_2\text{Ni}$  type precipitates in grain boundaries of TiNi films was also reported by Busch *et al.* [116], for samples that were either annealed isothermally at 813 K for various lengths of time, or annealed isochronically up to temperatures between 813 K and 1073 K. The volume fraction of grain boundary precipitates was found to increase with an increase in both annealing temperature and annealing time. In their study,  $\text{Ti}_3\text{Ni}_4$  precipitates distributed in the grain interiors were also observed in conjunction with the appearance of  $\text{Ti}_2\text{Ni}$  in the films isochronically annealed to 973 K and 1073 K respectively. They concluded that the grain boundary precipitates were  $\text{Ti}_2\text{Ni}$  instead of  $\text{Ti}_4\text{Ni}_2\text{O}_x$ , according to EDS analyses. However, these films were annealed in sealed quartz tubes which were evacuated to a pressure of about 0.1 Pa prior to anneal. This vacuum condition could cause serious contamination from reactive gases such as oxygen and nitrogen. Furthermore, B2 TiNi is a thermodynamically

stable phase at a temperature above 923 K, which has been confirmed by many studies [30-36]. Therefore, the precipitation of  $Ti_2Ni$  in a Ti-rich film at high temperatures should not be associated with an appearance of a Ni-rich phase, which has been demonstrated in the present case of PML-9 films. On the contrary, the  $Ti_2Ni$  phase would not be presumed to appear in a Ni-rich film during high temperature annealing. The appearance of  $Ti_2Ni$  are mostly in the grain boundaries is particularly suspicious, and suggests oxygen contamination.

Since oxygen has been found to stabilize the  $Ti_2Ni$  phase [41], one possibility is that oxygen diffused along the grain boundaries during annealing, and enhanced the precipitation of  $Ti_4Ni_2O_x$  phase. The X-ray diffraction pattern in Fig. 4-31 also reveals that more  $Ti_2Ni$  type phase formed in PML-16 films in the early stage of annealing. The concomitant depletion of titanium atoms in the matrix thus enhanced the further precipitation of  $Ti_2Ni_3$  thereafter. Therefore, the grain boundary precipitates extensively observed in the (NiCu)-rich films in the present study are concluded to be the  $Ti_4Ni_2O_x$  phase. On the other hand, the  $Ti_2Ni$  type precipitates observed in the PML-9 films are a mixture of  $Ti_2Ni$  and  $Ti_4Ni_2O_x$ . In the grain boundaries, most of precipitates are  $Ti_4Ni_2O_x$ , whereas the particles in the grain interiors is expected to be  $Ti_2Ni$  due to the super-saturation of titanium.

### 4.3. Thermoelastic Transformation Characteristics

The thermoelastic transformation behavior of the Ti(NiCu) thin films studied in section 4.2 is presented in this section. Crystallographic data on the martensites will also be reported and discussed.

#### 4.3.1. Transformations in SL Films

The thermoelastic transformation behavior of the annealed SL films with overall composition of  $\text{Ti}_{47.4}\text{Ni}_{46.5}\text{Cu}_{6.1}$  is described in the following section. The transformation temperatures, transformation sequences and crystal structures of the transformation products were studied by electrical resistivity measurement, differential scanning calorimetry and X-ray diffraction. Transmission electron microscopy was employed to study the microstructure of the martensitic phase *in-situ*.

*SL Films: Electrical Resistivity and DSC Results.* The electrical resistivity curves for the target alloy and the SL films, annealed at 923 K for 0.25 hour and for one hour, respectively, at  $P = 2.6 \times 10^{-3}$  Pa, are shown in Figure 4-37. The electrical resistivity of sputter-target alloy has a negative temperature coefficient, i.e.,  $C_T = dR_E/dT < 0$ , during the thermoelastic transformation, which has been reported for Ti(NiCu) ternary alloys with more than 5 at% Cu addition [148]. On cooling, the appearance of martensite is accompanied by an abrupt increase in resistivity beginning at 315 K, leveling off at 292 K, and falling again after the transformation has apparently finished. On heating, the resistivity increase ceases at 308 K, indicating the start of reverse transformation, after which the resistivity drops sharply until 335 K is reached. The nominal  $M_s$ ,  $M_f$ ,  $A_s$  and  $A_f$  temperatures for the sputter-target material are accordingly determined to be 315 K, 292 K, 308 K and 335 K respectively.

The resistivity curves for the film annealed at 923 K for 0.25 hour also shows a negative coefficient at sub-ambient temperature, accompanied by an one-degree hysteresis. However, another resistivity variation associated with a larger hysteresis is found at lower

temperature ( $< 210$  K). This second-stage variation of hysteresis is not found in the sputter-target alloy, and may be associated with an unidentified thermoelastic transformation.

For the one-hour annealed film, the two-stage change of resistivity is more pronounced. The onset temperature of the second-stage variation on cooling is about 20 K lower than that in the 0.25-hour annealed film, whereas the reverse variation of resistivity on heating starts at temperature which is about 30 K higher. That is, the two-stage variation of resistivity in the one-hour annealed films has larger hystereses of about 10 K (first stage) and 50 K (second stage), compared to those of about 1 K and 30 K in the 0.25-hour annealed film<sup>1</sup>.

In general, both the 0.25-hour annealed film and the one-hour annealed film show behavior which is similar to that reported for TiNi and Ti(NiFe) alloys having well-separated R-phase and martensitic transformations [67], as shown in Fig 2-6. Accordingly, the resistivity curves for each of the annealed SL films are interpreted in a way which has been used for the two-step transformation described in section 2.3.1. The temperature of the initial resistivity rise on cooling is associated with the R-phase transition and is designated  $T_R$ <sup>2</sup>. The final transformation to the monoclinic martensite coincides with the onset temperature of the resistivity decrease, and is designated  $M_S$ . Finally,  $M_f$  is determined in each case as the temperature at which the heating and cooling curves converge at low temperatures, which is below the range which our apparatus could attain. Austenite transformation temperatures are conversely determined from the heating resistivity curves. In this case,  $A_S$  is assigned to the onset of abrupt resistivity slope

---

<sup>1</sup>The hysteresis of the second-stage variation of resistivity is not well-defined. The numbers shown above come from a rough estimation by measuring the average width between the heating and cooling curves.

<sup>2</sup>In the present study, the R-phase transition is used to represent a combination of the second B2-to-incommensurate phase transition and the first order incommensurate-to-commensurate phase transformation. The onset temperature of the R-phase transition  $T_R$  thus corresponds to that of the B2-to-incommensurate phase transition  $T_R'$  in reference [50], which has been explained in section 2.2.3.

change on heating, and  $A_f$  to the top of the resistivity peak<sup>3</sup>. The  $T_r$ ,  $M_s$ ,  $M_f$ ,  $A_s$  and  $A_f$  temperatures are accordingly determined, and are labeled in Fig. 4-38.

Differential scanning calorimetry was also employed to study the transformation behavior. Figure 4-38 shows DSC traces of target alloy for reference, and SL film annealed at 923 K for one hour at  $P = 2.6 \times 10^{-3}$  Pa. Single exothermal and endothermal peaks were observed in target alloy with average transformation enthalpy of 1091 J/mole. The cooling scan for the one-hour annealed SL film shows severe noise with one broad and ill-defined peak located in between 278 K and 239 K. This noisy background is a common feature in cooling scans, especially for the films with a weight of several milligrams. However, the heating scan shows two endothermal peaks with temperature ranges that correspond relatively well to the  $A_s$  and  $A_f$  temperatures assigned to the heating resistivity curve. The enthalpies of the low temperature peak and high temperature one are 175 J/mole and 125 J/mole, respectively. Repeat of the DSC scans shows that the heat of the low-temperature peak varies with temperature to which the sample was cooled. On the contrary, the high-temperature exotherm has a relative constant value of enthalpy which is close to published value for the R-phase transition [51].

*SL Films: X-Ray Diffraction Results.* X-ray diffraction patterns from SL films annealed at 923 K for 0.25 hour and one hour respectively at  $P = 2.6 \times 10^{-3}$  Pa, were acquired at various temperatures as shown in Figure 4-39 and Figure 4-40. In Fig. 4-39, only peaks from B2 austenite, and the  $(\text{NiCu})_2\text{Ti}$  phase appear at 297 K, that is, above the nominal  $A_f$  temperature of 283 K. The broad peak at  $2\theta$  of  $41^\circ$  may result from the overlapping of the (110)  $(\text{NiCu})_2\text{Ti}$  peak and the (333)  $\text{Ti}_2\text{Ni}$  peak. As the film was cooled, the  $(110)_{\text{B2}}$  peak became broader. This is one of the precursory phenomena of the R-phase transformation [48, 149]. The pattern taken at 239 K shows that a side peak starts to split from the left shoulder of the  $(110)_{\text{B2}}$  peak, indicating that the austenite transforms

---

<sup>3</sup>The way to define the  $A_s$  point is the same as that in reference [50], but the  $A_f$  temperature is designated to be the top of the heating curve instead of the crossing point of the cooling and heating curves.

fully to the R-phase[149]. The rhombohedral distortion continues on cooling after the R-phase transition, illustrated by the increase of the two-theta angle between the split peaks, corresponding to  $(11\bar{2}2)_R$  peak and  $(03\bar{3}0)_R$  peak respectively. This result coincides with the report of Ling *et al.*[49]. Very weak peaks are discerned at two theta of  $37^\circ$  and  $39^\circ$  at temperatures below 193 K, which may indicate that a very small amount of martensite has formed. In Figure 4-40 for the film annealed at 923 K for one hour, splitting of  $(110)_{B2}$  peak starts at temperature slightly above 223 K. In addition, more martensite was formed at the temperature below 173 K. Consequently, the 0.25-hour and one-hour annealed films have similar R-phase transition temperatures, but the martensitic transformation in the former is more sluggish. The increase of the intensities of  $(110)$  and  $(013)$  precipitate peaks resulted from the overlapping of peaks from R-phase and martensite.

Recalling the resistivity data and DSC data, it is clear that the increase of resistivity between about 280 K and 240 K on cooling corresponds to the R-phase transformation which also results in a broad exotherm in the DSC trace. The further decrease of resistivity at about 190 K thus is associated with the martensitic transformation. On heating, an R-phase-to-austenite transition follows the reverse transformation from martensite to R-phase, producing two separate DSC endotherms. Accordingly, the low-temperature peak, corresponding to the abrupt increase of resistivity, represents the martensite-to R-phase transformation, and the high-temperature one characterize the reverse R-phase transition which results in a decrease of resistivity. As a result, the SL films undergo separate  $B2 \leftrightarrow R$  and  $R \leftrightarrow M$  transformations which has not been previously reported in any Cu containing TiNi alloys.

*SL Films: Transmission Electron Microscopy Results.* Room temperature electron diffraction patterns acquired from the SL films annealed at 923 K for one hour at  $P = 2.6 \times 10^{-3}$  Pa indicate that the structure are primarily composed of the B2 austenite with no martensite or R-phase present. However, diffuse streaks appear along certain crystallographic directions, such as  $\langle 110 \rangle_{B2}$  and  $\langle 211 \rangle_{B2}$ , as shown in Figure 4-18.

At a temperature of 255 K, the bright field image and its corresponding diffraction pattern in Figure 4-41 show well-defined  $1/3$  spots in the  $\langle 321 \rangle_{B2}$  directions, indicating that most or all of the R-phase transformation was complete at this temperature, but that no martensite was yet present. No contrast change was observed in either bright field or dark field images as the sample was tilted. Figure 4-42 shows a bright field image and its corresponding diffraction pattern taken along the  $\langle 112 \rangle_{B2}$  direction. The diffraction patterns can be indexed with a hexagonal unit cell, having  $a = 0.738$  nm and  $c = 0.532$  nm, as proposed by Goo and Sinclair [51], and are found to be in an  $\langle 11\bar{2}0 \rangle$  zone axis. The orientation relationship between B2 austenite and R-phase is accordingly expressed as  $(111)_{B2} // (0001)_R$  and  $[\bar{2}11]_{B2} // [2\bar{1}\bar{1}0]_R$ , also coinciding with the result for Ti(NiFe) alloy reported by Goo and Sinclair [51].

At 160 K (31 K below the onset temperature of the resistivity decline observed during cooling) the specimen produced the  $[100]$  martensite diffraction patterns and the fine martensite plates shown in Figure 4-43. The martensite variants are about 100 nm in size with dense transformation defects. These dense defects indicate that martensite has a monoclinic unit cell, which require twinning as lattice invariant shear during transformation. Electron diffraction study revealed that neighboring martensite variants usually had a Type-I  $(11\bar{1})$  twinning relationship. Figure 4-44 shows an example in which the bright field micrograph contains various fine martensite variants oriented in different directions. The associated diffraction pattern contains two  $[3\bar{2}1]$  martensite zone axes which are  $(11\bar{1})$  twin-related. One set of variants corresponds to this twinning relation is shown in the dark field micrograph taken from a  $(012)_M$  spot. The habit plane between neighboring variants coincides with the twin plane. (An effort for further analyze other martensite variants in the same austenite grain was limited by the single-tilt holder and fine variant size.)

The R-phase is still the predominant phase in the SL film at 160 K, and some plate-like variants were discerned in the R-phase as the sample was oriented in certain directions.

The size of the R-phase variants is similar to that of the martensite variants, but the former can be identified according to the lack of fine internal defects. A typical example is shown in Figure 4-46. The bright field micrograph in Fig. 4-45(a) shows two sets of plate-like variants with boundaries oriented perpendicular to each other. Fig. 4-45(c-d) are the dark field images taken from diffraction spots *c* and *d* respectively labeled in Fig. 4-45(b). They show the detailed structure of two labyrinth-like R-phase domains which are composed of two sets of plate-like variants with their boundaries roughly parallel and perpendicular to  $\langle 110 \rangle_{B2}$  reciprocal direction respectively. Additional diffraction observation revealed the presence of the R-phase at temperatures as low as 120 K, indicating the martensitic transformation finish temperature ( $M_f$ ) is below this temperature.

*SL Films: Transformation Sequences and Temperatures.* Near equiatomic TiNi alloys with 4 to 8 at% copper substitution for Ni have been generally thought to undergo a  $B2 \leftrightarrow M$  transformation [7, 71, 72]. Only in alloys with less than 3 at% Cu were  $B2 \leftrightarrow R$  transition observed by Tadaki and Wayman [71]. However, no reports have shown that the copper containing alloys could undergo separate  $B2 \rightarrow R$  and  $R \rightarrow M$  transformations after aging or thermomechanical treatment, as has been widely observed in binary TiNi alloys. In the present study, the thermoelastic transformation in the SL films on cooling is identified to be a two-step transformation in which B2 austenite undergoes an R-phase transition prior to a martensitic transformation. This two-step transformation was also reported in several ternaries including TiNiFe [50], TiNiAl [150] and TiNiCr [151]. The change of transformation behavior in the ternaries was attributed to difference of free energy changes between the R-phase and martensite [65]. However, this is apparently not the case in the Ti(NiCu) alloys, because the two-step transition is not a general feature of the thermoelastic transformation. According to the EDS analyses, the titanium content in B2 matrix of the SL films is close to the overall titanium content of 47.4 at %, indicating that the precipitation of  $Ti_4(NiCu)_2O_x$  in the grain boundaries had offset the titanium enrichment due to the precipitation of  $(NiCu)_2Ti$  phase. Under these circumstances, the  $M_s$

temperature would be estimated [72] to be only 50 K, in contrast to the measured value of about 200 K. Both the existence of a two-step transformation, and the relatively high transformation temperatures for such low titanium content, are believed to be related to the precipitation of semi-coherent  $(\text{NiCu})_2\text{Ti}$  particles, and a detailed discussion will be given below.

*Effect of  $(\text{NiCu})_2\text{Ti}$  Precipitates on Transformation Behavior in SL Films.* First, the EDS analyses shown in Fig. 4-21 reveals that the precipitation of the  $(\text{NiCu})_2\text{Ti}$  phase decreases the copper content in the B2 matrix from 6.1 at% to 3.8 at%. Tadaki and Wayman [71] mentioned that the temperature coefficient of resistivity,  $C_T = dR_E/dT$ , has a positive value associated with martensitic transformation in binary alloys and ternaries containing less than 5 at% Cu, whereas it has a negative coefficient in ternary alloys with more than 5 at% Cu addition. In the present study, the SL films having a positive  $C_T$  value coincides with the copper depletion in the B2 matrix detected by EDS. Tadaki and Wayman also suggested that the addition of copper in TiNi suppressed the B2  $\rightarrow$  R transformation [71]. Accordingly, lowering the copper content in the B2 matrix of the SL films is expected to release the constraint of the B2  $\rightarrow$  R transformation.

However, the decrease of the copper content itself does not necessarily result in a well-separated two-step transformation. The effect of precipitates must also be considered. As mentioned in Section 2.3.2., a two-step transformation in Ni-rich binary alloys can result from the appearance of coherent or semi-coherent precipitates of  $\text{Ti}_3\text{Ni}_4$ , or the existence of rearranged dislocations<sup>4</sup>. An orientation relationship between  $\text{Ti}_3\text{Ni}_4$  particles and the austenite, and with the martensite, has been deduced to be  $[111]_{\text{Ti}_3\text{Ni}_4} // [111]_{\text{B2}} // [\bar{1}01]_{\text{mono}}$  [43]. Consideration of the lattice parameters of the B2 phase and  $\text{Ti}_3\text{Ni}_4$  phase indicates that the (111) precipitate plane and (111) austenite plane have the largest  $d$ -spacing mismatch of about 2.7% [43]. This implies that a maximum tensile stress exists in the matrix along a direction perpendicular to the (111)

<sup>4</sup>These rearranged dislocations result from annealing at intermediate temperature, preceded by cold deformation.

habit plane. Since both  $[111]_{B2}$  and  $[\bar{1}01]_{mono}$  are the most extensible directions<sup>5</sup> during the R-phase and martensitic transformations respectively, this tensile internal stress along  $\langle 111 \rangle_{B2}$  would seem to either both transformations [43]. However, the formation of either R-phase or martensite variants generates a back stress around the precipitate, which tends to resist continued forward transformation. Here the back stress is the elastic stress needed to maintain the lattice coherency between precipitates and the resulting phase after transformation. Consequently, larger lattice deformation associated with the martensitic transformation generates higher back stress.

The calculation of elongation along  $[111]_{B2}$  and  $[\bar{1}01]_{mono}$  during the R-phase and martensitic transformations yields values of about 1 % and 10.5 % respectively. This suggests that the R-phase transformation is both more easily induced by internal stress and less interfered with by back stress than the martensitic transformation. In fact, the martensitic transformation is suppressed by the back stress in the early stage of precipitation, according to the results reported by Wu and Lin [152], and Nishida and Honma [68]. Recent TEM study carried out by Xie *et al.* [61] showed that fine, coherent  $Ti_3Ni_4$  precipitates do not provide nucleation sites for the martensite, but coarse, semi-coherent  $Ti_3Ni_4$  particles do favor nucleation of martensite at precipitate interfaces, but constrain it from further growth. In other words, the  $M_s$  temperature is elevated at the expense of the widening of the transformation temperature interval ( $M_s - M_f$ ).

In the present study, semi-coherent  $(NiCu)_2Ti$  precipitates were observed in the SL film annealed at 923 K for one hour. As demonstrated by TEM observation, lattice coherency only exists in the  $\{001\}/(001)$  habit plane of the B2 phase and  $(NiCu)_2Ti$  phase. Further calculation reveals that the  $d$ -spacing of  $(100)_{B2}$  is about 2.7 % smaller than the  $(100)$  and  $(010)$  spacing in  $(NiCu)_2Ti$ . This mismatch results in dilatation of the matrix

---

<sup>5</sup>Considering the lattice deformation needed in a martensitic transformation, each lattice vector in austenite will be strained in order to transform to a lattice vector in martensite. Accordingly, there is one lattice vector will experience the largest tensile strain during the transformation, based on the special lattice orientation relationship between austenite and martensite, which is so-called the most extensible direction.

lattice which can produce an elongation along four  $\langle 111 \rangle_{B2}$  of as much as 2%, which is smaller than that produced by the  $Ti_3Ni_4$  precipitates. However, these internal stresses favor four R-phase variants. In other words, the back stress associated with the transformation can be reduced by the formation of self-accommodated R-phase. In fact, self-accommodated, plate-like R-phase variants with about 20 nm in width were observed in the one-hour annealed SL films, as shown in Fig. 4-43. Therefore, it is suggested here that internal strains produced by semi-coherent  $(NiCu)_2Ti$  precipitates act to raise the R-phase transformation temperature by providing a population of favorable heterogeneous nucleation sites.

Both the SL films annealed at 923 K for 0.25 hour and one hour, respectively, yield a similar  $T_f$  temperature of about 280 K. This coincides with the observation, reported by Nishida and Honma [68], which showed that the  $T_f$  temperature is relatively insensitive to the annealing time. However, the value of  $T_f$  in the present study is 20 to 40 degrees lower than those reported in the binary alloys. The lower  $T_f$  value, in fact, is expected because the  $(NiCu)_2Ti$  precipitates produce less tensile strain (about 2 %) along  $\langle 111 \rangle_{B2}$  directions versus the 2.7 % produced by the  $Ti_3Ni_4$  phase in binary alloys.

It is apparent, then, that the effect of the semicoherent  $(NiCu)_2Ti$  precipitates on martensitic transformation may be similar to that of the semicoherent  $Ti_3Ni_4$ . Xie *et al.* [61] found that coarse  $Ti_3Ni_4$  particles provided nucleation sites for martensite variants and then elevated the  $M_s$  temperature. In the present study, TEM observation shows that the variant size of the martensite is similar to or smaller than the particle size of the  $(NiCu)_2Ti$  phase. Moreover, unlike the single R-phase variant found around the  $Ti_3Ni_4$  particles in [43], multiple R-phase variants formed prior to the martensitic transformation may assist the self-accommodation process of the martensite variants and further decrease the back stress effect. As a result, the  $M_s$  temperatures of the SL films annealed at 923 K are about 150 K higher than the expected value based on its matrix titanium contents.

The reverse transformation in the one-hour annealed SL films was also a two-step transformation, according to the DSC and resistivity data. The coarse  $(\text{NiCu})_2\text{Ti}$  precipitates seem to stabilize the martensite and postpone the reverse transformation. As a result, the  $A_s$  temperature of the one-hour annealed SL film is about 30 K higher than that of the 0.25-hour annealed film. Postponed reverse transformations also results in a larger hysteresis (11K) of the R-phase transition in the one-hour annealed film versus that of 1 K in the 0.25-hour annealed film.

In conclusion, the precipitation of the semicoherent  $(\text{NiCu})_2\text{Ti}$  phase in this  $\text{Ti}_{47.4}\text{Ni}_{46.5}\text{Cu}_{6.1}$  film decreased the matrix copper content and produced internal tensile stresses both of which promoted the R-phase transformation and resulted in a two-step transformation.

#### *4.3.2. Transformations in PML-16 Films*

The thermoelastic transformation behavior of the annealed PML-16 films with overall composition of  $\text{Ti}_{49.2}\text{Ni}_{44.8}\text{Cu}_{6.0}$  is now described. According to the microstructure study reported in section 4.2, no  $(\text{NiCu})_2\text{Ti}$  precipitates appeared in the annealed PML-16 films. In fact, the grain interiors of these films were relatively free from precipitates. Different transformation behavior of the annealed PML-16 films is therefore expected.

*PML-16 Films: Electrical Resistivity and DSC Results.* Figure 4-46 shows electrical resistivity curves from a PML-16 film annealed at 923 K for one hour at  $P = 2.6 \times 10^{-3}$  Pa. These curves are qualitatively similar to that of the sputter-target alloy, except that the transformation temperatures were substantially depressed. The transformation temperatures,  $M_s$ ,  $M_f$ ,  $A_s$  and  $A_f$ , therefore, are determined according to the method described in section 4.3.1. to be 287 K, 228 K, 238 K and 297 K respectively, which yield an average transformation temperature interval of 59 K, and a hysteresis of 10 K.

Figure 4-47 shows DSC results for a free standing PML-16 film, annealed at 923 K for one hour at  $P = 2.6 \times 10^{-3}$  Pa, showing results which are also similar to those for the sputter-target alloy. Both  $A_f$  and  $M_s$  temperatures are about 12 K lower than those determined from resistivity measurement. The width of endo- and exothermal peaks in the calorimeter scans, which give the transformation temperature interval,  $\Delta T$ , are only about 20 K, whereas the transformation hysteresis of 9 K is similar to that obtained from the resistivity measurements. The average transformation enthalpy obtained from the integral of both peaks is 685 J/mole. Additional DSC surveys were performed for the films annealed under various conditions, and results are tabulated in Table 4-4. The film annealed at 923 K for 6 hours in a vacuum of  $2.6 \times 10^{-3}$  Pa yielded a lower transformation enthalpy of 427 J/mole without a change in transformation temperatures. On the other hand, the films annealed at  $P = 2.6 \times 10^{-4}$  Pa for one hour yields transformation enthalpies of 1113 J/mole (923 K annealed) and 854 J/mole (823 K annealed), respectively, which are close to the value of 1076 J/mole for the sputter-target alloy.

It is worth noting that the film annealed at 823 K for one hour at  $P = 2.6 \times 10^{-4}$  Pa has a larger transformation temperature interval, about 35 K, compared to that of 9 K for the 923 K annealed films. The DSC exo- and endotherms of the 823 K annealed film are shown in Figure 4-48 which reveal that two exothermal peaks appear on cooling between 242 K and 202 K. Pronounced background noise makes the determination of transformation temperatures more difficult. The first cooling peak has an enthalpy of about 150 J/mole which is close to published values for the R-phase transition [51]. In addition, a shoulder is observed on the higher temperature side of the heating endotherm, indicating that it consists of two overlapped peaks. The transformation sequence of PML-16 films annealed at 823 K for one hour at  $P = 2.6 \times 10^{-4}$  Pa is, therefore, identified to be  $B2 \rightarrow R \rightarrow M$  on cooling and  $B2 \rightarrow M$  and/or  $B2 \rightarrow R \rightarrow M$  on heating.

*PML-16 Films: X-Ray Diffraction Results.* Cold-stage X-ray diffraction studies for the films annealed at 923 K and 823 K, respectively, for one hour at  $P = 2.6 \times 10^{-4}$  Pa

were undertaken to verify the DSC results. Figure 4-49 is the X-ray diffraction patterns of the film annealed at 923 K taken at various temperatures. Only peaks from B2 austenite and second phase precipitates are observed at 293 K, indicating no martensite exists. At 251 K, below the  $M_f$  temperature determined by DSC, monoclinic martensite ( $M_M$ ) peaks can be identified and the peak intensity of  $(110)_{B2}$  decreases about 50 %, indicating that the  $B2 \rightarrow M_M$  transformation is only about half way done. The martensitic transformation is found to finish at about 201 K, which is about 50 K lower than that determined by DSC. Figure 4-50 show results for the films annealed at 823 K, showing that no martensite peaks can be identified yet at 249 K, though the  $(110)_{B2}$  peak intensity decreases about 25 %. The decrease of the  $(110)_{B2}$  peak intensity is associated with a slight peak broadening which is known to be a precursory phenomenon of the R-phase transformation. At 198 K, only martensite peaks are observed, showing the whole transformations finish at or above 198 K, which is very close to the  $M_f$  temperature of 202 K determined by DSC. As a consequence, the cold-stage x-ray diffraction data for the films annealed at 823 K coincides with the DSC results very well. However, the  $M_f$  temperature determined by X-ray diffraction in the films annealed at 923 K is about 50 K lower than that obtained from the DSC results.

*PML-16 Films: Transmission Electron Microscopy Results.* Cold-stage TEM observation shows that the PML-16 films annealed at 923 K for one hour undergo a  $B2 \rightarrow M_M$  transformation on cooling. No R-phase was found in the films. However, the sample annealed at 823 K for one hour at  $P = 2.6 \times 10^{-4}$  Pa shows a transformation sequence of  $B2 \rightarrow R \rightarrow M_M$  on cooling. The crystallographic nature of the monoclinic martensites observed in all the films is essentially the same regardless the prior transformation sequence. Consequently, the majority of the following results are taken from a sample annealed at 823 K for one hour at  $P = 2.6 \times 10^{-4}$  Pa unless noted otherwise.

Both the R-phase and martensite formed first at a thick portion of the sample on cooling, and the transformation temperatures were found to be a function of foil thickness

in a range from 0 to about 300 nm, and the temperatures reported below may not correspond well to the resistivity and DSC data. Figure 4-51 shows a bright field micrograph and its corresponding diffraction pattern taken at 215 K. The bright field image shows three R-phase domains, labeled A, B and C, with plate-like substructures, formed in the austenite grain. The corresponding diffraction pattern taken from domain A can be indexed to the  $[1\bar{5}43]_R$  zone, using the hexagonal unit cell proposed by Goo and Sinclair [51], or to the  $[012]_{B2}$  zone with  $1/3$  spots along  $\langle 123 \rangle_{B2}$  reciprocal lattice vectors. The plate-like substructures in domain A are about 30 nm in width and elongated across the variants in a direction parallel to the  $[100]_{B2}$  reciprocal lattice vector. The substructures in domain B have the same size and morphology, but orient perpendicular to the  $[100]_{B2}$  reciprocal lattice vector. Figure 4-52 shows a bright field micrograph and its corresponding diffraction pattern acquired along  $[023]_{B2}$  direction at 215 K. The bright field image confirms that the plate-like domains are parallel to the  $\langle 100 \rangle_{B2}$  reciprocal direction and are inclined with respect to the beam direction. Trace analyses indicate that the plate-like domains are parallel to  $\{110\}_{B2}$  or  $\{100\}_{B2}$  planes. As a consequence, they may be the (100) or (110) type twins similar to those which have been observed in Ti(NiFe) alloys by Hwang *et al.* [153]. The diffraction patterns reveal that neighboring domains are also (100) twin-related.

A labyrinth-like substructure is also observed as shown in Figure 4-53. The associated diffraction pattern is in a  $[0\bar{2}2\bar{1}]_R$  zone axis which is generated from the area having the darker contrast level. The trace directions of the substructure boundaries are in approximately  $[\bar{4}134]_R$  and  $[8\bar{5}\bar{3}4]_R$  reciprocal vector directions respectively. It is also found that the  $[0\bar{2}2\bar{1}]_R$  zone axis is only  $11.75^\circ$  from the nearest  $\langle 01\bar{1} \rangle_{B2}$  direction. As the  $[0\bar{2}2\bar{1}]_R$  zone axis is rotated toward the  $[01\bar{1}]_{B2}$  direction,  $[\bar{4}134]_R$  and  $[8\bar{5}\bar{3}4]_R$  were found to align with  $[100]_{B2}$  and  $[011]_{B2}$  reciprocal vector directions within  $\pm 1$  degree. Therefore, the substructure boundaries are thought to be  $(100)_{B2}$  and  $(011)_{B2}$

planes respectively, coinciding with the above observations shown in Fig 4-51 and Fig. 4-52.

Monoclinic martensite plates were also found at 215 K as shown in Figure 4-55. The associated diffraction pattern shows  $[110]_{B2}$  pattern containing  $1/3$  type reflections superimposed with  $[010]_{MM}$  pattern, indicating that the martensite is consuming the R-phase instead of B2 austenite.

As the temperature was lowered to 170 K *in-situ*, all the R-phase and B2 austenite transformed to martensite, except in very limited thin area near the edge of the hole. Figure 4-55 shows the general features of the martensite variants and how they accommodated each other. In Figure 4-55(a) the martensite formed band-like variants in a width of 50 to 200 nm across the original austenite grain. Fine transformation defects with a spacing of about 20 nm can be observed inside the band-like variants. Figure 4-55(b) shows the zigzag variant arrangement in which two variants with planar transformation defects formed predominantly in the original austenite grain, accompanied by some scattered third-variants. In both case no well-defined martensite variant boundaries are found. Moreover, cases in which one variant dominated the whole austenite grain was rarely found.

Type-I  $(11\bar{1})$  transformation twins were the most common transformation defects observed in the monoclinic martensite. Figure 4-56(a) shows an electron micrograph of zigzagged martensite plates formed in the austenite grain. The diffraction pattern in Fig. 4-56(b) shows superimposed  $[010]$  and  $[2\bar{1}\bar{1}]$  martensite zone axes. A dark field image taken from  $(100)_{mono} + (01\bar{1})_{mono}$  spots labeled in Figure 4-56(b) is shown in Figure 4-56(c) in which two sets of martensite plates, labeled *a* and *b* respectively, are observed to taper off near the interfaces as shown in the enclosed area, confirming that they have different crystallographic orientations. As the sample was tilted along the  $[001]$  reciprocal axis by  $33.5^\circ$ , a diffraction pattern containing two  $(11\bar{1})$  twin-related  $[110]_{mono}$  zones and one  $[101]_{mono}$  zone was acquired as shown in Figure 4-56(d). Dark field

microscopy proves that the  $[110]_{\text{M}}$  patterns correspond to horizontally parallel plates *a* and *c*, respectively, in which  $(11\bar{1})$  twinning acts as the lattice invariant shear. Moreover, analysis of the diffraction patterns indicates that the horizontally and vertically oriented plates *a* and *b* shown in Fig. 4-56(c) are also  $(11\bar{1})$  twin-related. (The single tilt holder limited further study of the crystallographic orientation of the fourth set of martensite plates.)

Martensite was found to revert back to austenite when the electron beam was converged to heat the foil. An interesting feature is that, before the reverse transformation was complete, most of the remaining martensite plates were those which were situated at the center of the austenite grains. Figure 4-57 shows a set of leaf-like martensite plates left in the center of an austenite grain. These martensite leaves are about 200 nm in width and 500 nm in the longitudinal direction, and are still accommodated in a zigzag form. The associated diffraction patterns contains a  $[001]$  martensite zone and a  $[011]$  B2 zone without  $1/3$  spots. The reverse transformation is therefore believed to be an one-step transition which bypasses the R-phase. Moreover, the grain boundaries seems to constrain the nucleation of martensite plates, since the last remained martensite upon heating is usually the first one which nucleates on cooling [14]. Figure 4-58 shows that another sets of thin-leaf martensite plates in a neighboring grain. The corresponding  $[3\bar{1}2]$  diffraction patterns reveal that the two sets of martensite plates have an  $(111)$  twin relationship.

*Transformation Behavior of the PML-16 Films.* DSC traces of all the PML-16 films annealed at 923 K show that only one exo- and one endothermal peak was found in cooling and heating scans respectively. This feature coincides with the TEM observation that no R-phase appeared during the transformation. However, the film annealed at 823 K for one hour at  $P = 2.6 \times 10^{-4}$  Pa shows a two-step transformation on cooling and an overlapped transformation on heating, according to both DSC and TEM data. Moreover, the  $M_s$  temperatures of the 823 K annealed films are 40 to 50 degrees lower than the  $M_s$  of the 923 K annealed films. The real reason for this difference is not presently known, since they have similar composition and microstructures, except that fewer second phase particles

were observed in the 823 K annealed films. Although low transformation temperatures can be attributed to lower titanium content resulting from fabrication process, or higher volume ratio of  $Ti_4((NiCu)_2O_x)$  with respect to  $Ti_2Ni_3$  in the 823 K annealed films, the low titanium content alone cannot account for the two-step transformation.

*Microstructures of the R-phase.* The self-accommodation morphologies of the R-phase found in the PML-16 films are essentially different from those reported for bulk binary alloys [53], as shown in Fig. 2-8. The phenomenological theory calculation carried out by Miyizaki and Wayman [53] showed that the R-phase transition does not require a lattice invariant shear. Therefore, the {100} or {110} twin-related plate-like substructures shown in Fig. 4-52 through 4-54 are R-phase variant grains rather than the lattice invariant twins. R-phase variants with similar morphology (which was called a needle-like domain) have been observed in Ti(NiFe) alloys [153] and in TiNi alloys [61]. However, these variant plates were reported to have an average thickness for about 450 nm [153] which is more than ten times larger than that of 30 nm found in the present study. Moreover, no well-defined self-accommodation morphology of these plate variants was found in thin foils made from bulk Ti(NiFe) and TiNi alloys in TEM [61, 153].

In the present work, two plate-like R-phase variants combined in a single domain. Within a single austenite grain, as many as three such domains were observed (Fig. 4-51), with plate-like variants oriented in different directions. The habit planes between variants are {100}<sub>B2</sub> or {110}<sub>B2</sub> twin planes. By using the distortion matrices derived by Miyizaki and Wayman [53], the total distortion matrix  $E$  is calculated for this two-variant domain as follow

$$\begin{aligned}
 E &= 1/2 (E_A + E_B) \\
 &= \begin{bmatrix} 1.0000 & 0.0000 & 0.0000 \\ 0.0000 & 1.0000 & -0.0047 \\ 0.0000 & -0.0047 & 1.0000 \end{bmatrix} \quad (4.3.1)
 \end{aligned}$$

where  $E_A$  and  $E_B$  are the distortion matrices of variant  $A$  (corresponding to  $(\bar{1}11)$  habit plane) and variant  $B$  (corresponding to  $(111)$  habit plane) respectively. This result shows that the total distortion matrix of a two-variant self-accommodation combination contains only two non-zero but relatively small shear components. This result indicates that the two-variant combination can effectively reduce the total strain energy associated with the transformation. Moreover, the existence of multiple self-accommodation combinations in a single austenite grain may further minimize the overall distortion associated with the R-phase transformation. Another possibility is that these two-variant combinations, having different crystal orientations, nucleated at the grain boundaries and then extended into the grain interiors on cooling to form the multiple-combination configuration. However, as mentioned above, the grain boundaries seems to constrain the nucleation of martensite plates. This may also be true for the nucleation of the R-phase. However, further observation is suggested to clarify the origin of the multiple-combination configuration. As a result, it is reasonable to conclude that the two-variant domain can act as a basic self-accommodation unit of the R-phase.

The labyrinth-like R-phase domains observed in the SL film as shown in Fig. 4-44 have one of their boundaries parallel to  $(110)_{B2}$  plane. This fact indicates that two sets of domains are  $(110)$  twin-related. If each set of domain contains only one R-phase variant, the other set of domain boundaries should be  $(001)_{B2}$  plane, according to the twin relations explained in Fig. 2-7. Otherwise, they can be  $(011)_{B2}$  or  $(101)_{B2}$ . The former case has been demonstrated in Fig. 4-53 in which a set of R-phase variants grow in two directions and accommodate with another set of variants through two conjugate twins to form the labyrinth-like combination which is illustrated in Figure 4-59. In the upper part of the same picture, another variant combination can be observed, here the plate-like variants are maintained. This indicates that a two-variant combination is a basic way for the R-phase variants to self-accommodate.

*Microstructures of Monoclinic Martensite* . The martensite variants observed in the SL films have a diameter of less than 100 nm, which is much smaller than those of about 1  $\mu\text{m}$  in diameter, observed in the PML-16 films. The TEM study conducted by Xie *et al.* [61] showed that the coarse  $\text{Ti}_3\text{Ni}_4$  precipitates favor of the nucleation of martensite variants, but constrain the martensite variants from further growth. Consequently, the martensite variants had a similar size to that of the precipitates. In the present study,  $(\text{NiCu})_2\text{Ti}$  precipitates are proposed to play a similar role with respect to thermoelastic transformation as the  $\text{Ti}_3\text{Ni}_4$  precipitates have been shown to do. Therefore, small martensite variant size observed in the SL films, as shown in Figure 4-43 and 4-44, is to be expected on the basis of the size of the  $(\text{NiCu})_2\text{Ti}$  precipitates found. On the other hand, without the interference of the semicoherent precipitates, martensite variants observed in the PML-16 films grow continuously and attain a larger size.

Type-I  $(11\bar{1})$  twinning was the only twinning mode found in both SL and PML-16 films to give the lattice invariant shear and self-accommodation. The calculation conducted by Knowles and Smith [60], using phenomenological theory, showed that both Type-I  $(11\bar{1})$  twinning and Type-II  $[011]$  twinning can perform the lattice invariant shear in TiNi alloys. Most of the crystallographic data measured from bulk single crystals showed good agreement with this calculation using the latter as the lattice invariant shear. However, Type I  $(11\bar{1})$  twinning has been widely observed in TiNi alloys and related ternaries in TEM studies [54, 59]. Matsumoto *et al.* [63] proposed that the appearance of Type-I  $(11\bar{1})$  twins was caused by a thin foil effect. If this is the case, the crystallographic data based on Type II  $[011]$  twinning acquired from bulk alloys may no longer be of value for application to thin films.

Table 4-5 is the crystallographic data deduced by Knowles and Smith [60] for  $(11\bar{1})$  twinning as the lattice invariant shear. The phenomenological theory calculation yields two sets of solutions, labeled Solution-1 and Solution-2 respectively. The "total distortion matrix",  $E$ , as described in section 2.1. hence can be expressed as

$$E = (1-x) M_1 + x M_2 \quad (4.3.2)$$

where  $x$  is the thickness ratio of the major twin fraction, and  $M_1$  and  $M_2$  are the distortion matrices to which the two twin regions, 1 and 2, are subjected, as listed in Table 4-5. Under these circumstances, the transformation strain,  $m$ , can be evaluated by consideration of Fig. 2-1 which indicates that the result of the transformation on a unit vector normal to the habit plane  $n$ . From the figure,

$$m = n' - n \quad (4.3.3)$$

where  $n' = En$ . The direction of shear and the transformation shear strain are therefore obtained as

$$m_s = n' - (n' \cdot n) n \quad (4.3.4)$$

$$m_s = | n' - (n' \cdot n) n | \quad (4.3.5)$$

The results for habit-plane variants 1 and 2 are listed in Table 4-5, revealing that the transformation strain of about 0.11 which is smaller than that of 0.13 reported for Type II twins [63]. This result predicts that NiTi alloys may display less maximum shape strain when applied in the form of a thin film, because of this difference in the preferred twinning mode. The orientation dependence of the transformation strain is also calculated and plotted in Figure 4-60 for solution 1. The result for solution 2 is almost the same as that of solution 1 because the shear direction for the former ( $m_2$ ) is roughly parallel to  $n_1$  and  $m_1$  is almost parallel to  $n_2$ . The direction which yields the maximum Schmid factor is roughly in  $[5\bar{3}5]_{B2}$ , as shown in Figure 4-60, which is slightly different from that in  $[\bar{2}\bar{2}1]_{B2}$  for Type-II twinning [154]. However, in both cases the  $\langle 100 \rangle_{B2}$  directions are less favorable for the applications requiring shape memory effect and superelasticity. This knowledge can be important in improving both shape memory effect and superelastic effect in polycrystalline TiNi films, if a texture is developed during deposition or during crystallization annealing.

### 4.3.3. Transformations in PML-9 Films

This section describes the thermoelastic transformation behavior of the annealed PML-9 films with overall composition of  $\text{Ti}_{51.0}\text{Ni}_{44.4}\text{Cu}_{4.6}$ . A wide dispersion of the  $\text{Ti}_2\text{Ni}$  precipitates were found in the grain interiors of this Ti-rich film, as mentioned in section 4.2.3. An orthorhombic martensite is found to be an intermediate phase during the martensitic transformation in which the monoclinic phase is still the final product on cooling. The appearance of the orthorhombic phase changes the microstructure of the monoclinic phase, as compared to that described in section 4.3.2.

*PML-9 Films: Electrical Resistivity and DSC Results.* Martensite transformation characteristics for the films, annealed at 923 K for one hour at  $P = 2.6 \times 10^{-3}$  Pa, are shown in Figure 4-61 and Figure 4-62, respectively. Electrical resistivity data are plotted in Figure 4-61 which reveal transformation behavior similar in nature to that of the sputter-target alloy, as shown in Fig. 4-37. The nominal  $M_s$ ,  $M_f$ ,  $A_s$  and  $A_f$  temperatures are thus determined to be 305 K, 225K, 247K and 322K respectively, giving transition temperature intervals of 80 K on cooling and 75 K on heating which are about four times larger than that of the sputter-target alloy. However, the transformation hysteresis of 17 K is essentially the same. Figure 4-62 shows data from DSC scans for the film annealed under the same conditions which indicate that the martensitic transition begins at 297 K on cooling and austenite finish temperature on heating is 312 K, or about 9 degrees below the corresponding transitions obtained from resistivity measurements. The widths of endo- and exothermal peaks in the calorimeter scans are only about 12 Kelvins, which is the same as those of the sputter-target alloy, and the average transformation enthalpy obtained from the integral of both peaks is 482 J/mole. The DSC curves also yielded similar transformation hysteresis of 15 K. Table 4-6 summarizes the apparent transformation temperatures and properties associated with DSC and electrical resistivity measurements. In addition, PML-9 films annealed at 823 K and 923 K, respectively, for one hour at

$P = 2.6 \times 10^{-4}$  Pa, were studied by DSC, and the results are also tabulated in Table 4-6. The films annealed at 923 K with  $P = 2.6 \times 10^{-3}$  Pa, at 923 K with  $P = 2.6 \times 10^{-4}$  Pa and at 823 K with  $P = 2.6 \times 10^{-4}$  Pa, respectively, have similar transformation temperatures (as determined by DSC), but with different enthalpies. The 823 K annealed film yields an average transformation enthalpy twice as great as that of the film annealed at 923 K at  $P = 2.6 \times 10^{-3}$  Pa. For the films annealed at the same temperature (923 K), higher vacuum results in a higher heat of transformation.

*PML-9 Films: X-ray Diffraction Results.* As was mentioned, the cold-stage X-ray diffraction results for the PML-16 films annealed at 923 K for one hour at  $P = 2.6 \times 10^{-4}$  Pa yield a  $M_f$  temperature which was about 50 K lower than that determined from DSC. Cold-stage X-ray diffraction patterns were also taken for the PML-9 films annealed under various conditions, and are shown in Figures 4-63 through Figure 4-65. Figure 4-63 shows diffraction patterns for a film annealed at 923 K for one hour at  $P = 2.6 \times 10^{-3}$  Pa. Only  $Ti_2Ni$  and B2 peaks<sup>6</sup> appear at 323 K, that is, above the nominal  $A_f$  temperature as determined by the DSC data. The B2 (110) peak is not present at 143 K and has thus vanished at some temperature below 222K. However, martensite and austenite are seen to coexist at 268 K and 222 K, although the DSC data would indicate that the martensite transition had finished at 285 K. The low temperature ( $T = 143K$ ) X-ray spectrum also shows that the martensite has a monoclinic unit cell with  $a = 0.292$  nm,  $b = 0.411$  nm,  $c = 0.462$  nm, and  $\beta = 96^\circ$ . Examination of the spectra taken at 268 K and 222K reveals a shift of  $(110)_{B2}$  peak toward higher two-theta value. However, this shift must be caused by mechanical drift during cooling, since a similar amount of shift is also observable in the (002) lead peak. An abnormal increase in X-ray intensity at a two-theta angle around  $42.5^\circ$  is also observed at 268 K which may result from

---

<sup>6</sup>An (002) Pb peak shown in the spectra throughout is from a thin lead plate on which the films were attached.

the appearance of the (020) orthorhombic peak<sup>7</sup>. This increase of intensity is not caused by an overlap of (110)<sub>B2</sub> and (020)<sub>ortho</sub> peaks, because a similar situation does not occur between (110)<sub>B2</sub> and (11-1)<sub>mono</sub> peaks, though in the latter pair, the peaks are more closely spaced. The angular difference between the (110)<sub>B2</sub> peak and the (020) orthorhombic peak is larger than expected. However, the exact position of the (020) orthorhombic peak is difficult to determine from the spectrum due to the interference of the (110)<sub>B2</sub> and (020)<sub>mono</sub> peaks.

Figure 4-64 and 4-65 are the X-ray diffraction patterns for the films annealed at 923 K and 823 K respectively, for one hour, at a lower pressure of  $P = 2.6 \times 10^{-4}$  Pa (and hence, presumably, under conditions less prone to oxidation). In Figure 4-64, the diffraction pattern taken at 323 K shows the same features as that in Fig. 4-56, whereas the intensity of (110)<sub>B2</sub> peak at 221 K is so low that it is barely distinguishable. In other words, the film annealed at lower pressure acquired a higher  $M_f$  temperature. The coexistence of the orthorhombic and monoclinic peaks at 270 K indicates the film was undergoing an orthorhombic-to-monoclinic transformation in this interval.

The diffraction patterns of the 823 K annealed film (at  $P = 2.6 \times 10^{-4}$  Pa) is shown in Figure 4-66. The intensities of  $Ti_2Ni$  peaks are significantly lower than those in the patterns of 923 K annealed films. A broad peak appearing at 270 K is probably contains a strong orthorhombic peak, a moderate monoclinic peak and a weak B2 one. This strong orthorhombic peak indicates that a large fraction of austenite had already transformed to orthorhombic martensite, whereas the second stage of transition was still in progress. As a consequence, the relations of the 'true' PML-9  $M_f$  temperatures determined by X-ray diffraction can be expressed as:

$$M_f(823 \text{ K at } 10^{-4} \text{ Pa}) > M_f(923 \text{ K at } 10^{-4} \text{ Pa}) > M_f(923 \text{ K at } 10^{-3} \text{ Pa}).$$

---

<sup>7</sup>The orthorhombic phase is found to be an intermediate phase of the B2-to-monoclinic martensite transformation, having lattice parameter of  $a = 0.291$  nm,  $b = 0.425$  nm and  $c = 0.340$  nm, and will be described in the following subsections.

Figure 4-66 is a transmission electron micrograph and a corresponding diffraction pattern taken at 160 Kelvins from a sample annealed at 923 K for one hour at  $P = 2.6 \times 10^{-3}$  Pa. Though this is below the nominal  $M_f$  temperature obtained from DSC and resistivity measurements, residual austenite diffraction spots in the [110] zone axis could still be observed. A dark field image from the  $(200)_{B2}$  spot, as indicated by arrow in the diffraction pattern, shows that this retained austenite is distributed between the martensite variants. The austenite domains are distributed throughout the original austenite grain and have diameter of 10 to 100 nm.

*Retained Austenite in the PML Films.* The apparent transformation temperatures of the PML films associated with the various measurements, including cold-stage X-ray diffraction, DSC, and resistivity curves, are summarized in Table 4-7. All the PML films show some retained austenite at the temperature below the  $M_f$  point determined by DSC. However, all the retained austenite does finally transform to martensite at lower temperatures. In other words, the B2 austenite-to-martensite transformation occurs in two stages. In the first stage, on cooling, a fraction of the austenite apparently transforms to martensite within a short temperature interval of about 20 K. It is this 'normal' transformation whose exotherm appears in the DSC scans. The following step is a more sluggish process which proceeds over an interval of cooling which can be as large as 100 K. This slower (or so called 'microscopic'<sup>8</sup>) transformation probably produces DSC peaks which are too broad to be readily discernible. On heating, the 'microscopic' transformation occurs first, followed the 'normal' transition. The enthalpies recorded from the DSC exo- and endotherm are therefore represent only that involving the first stage transformation. Thus the low transformation enthalpy generally associates with low 'true'  $M_f$  value (the  $M_f$  temperature determined by either resistivity curves or cold-stage X-ray diffraction). In addition, the retained austenite can also explain why the electrical resistivity

---

<sup>8</sup>The terminology 'microscopic' here represents the total volume fraction of material which undergoes the martensitic transformation is too small to be identified by DSC.

curves usually yield a much lower  $M_f$  and  $A_s$  values although the  $M_s$  and  $A_f$  temperatures coincide with the DSC data relatively well.

*In situ* TEM observation in the PML-16 films annealed at 823 K for one hour at  $P = 2.6 \times 10^{-4}$  Pa indicated that the central regions of the austenite grains had higher transformation temperatures. This has been shown in Fig. 4-57 and 4-58 in which the 'retained' martensite plates were located in the center region of the austenite grains after the sample was heated by converging the electron beam. According to the optical microscopy study of the martensitic transformation in a  $Ag_{55}Cd_{45}$  alloy carried out by Tong and Wayman [14], the martensite plates produced first on the forward transformation (austenite  $\rightarrow$  martensite) is the last to undergo the reverse transformation. Accordingly, micrograph shown in Fig. 4-57 and 4-58 indicated martensite in each austenite grain started to nucleate at the center of the grain on cooling. However, study of martensite nucleation in a AuCd alloy, conducted by Ferraglio and Mukherjee [155], found that the nucleation of the thermoelastic martensite was heterogeneous, and grain boundaries were one of the favorite heterogeneous nucleation sites. *In situ* TEM observations in a Ni-rich TiNi alloy were also reported that showed the martensite first appearing preferentially at grain boundaries, and at the matrix-inclusion interfaces [61]. As a consequence, the absence of the 'retained' martensite appearing in or near the grain boundaries in the PML-16 films cannot be explained unless the near-boundary region has a lower transformation temperatures than the central region.

On the basis of the *in situ* TEM observation in the PML-16 films, a possible explanation for a portion of the austenite transforming to martensite at lower temperatures involves titanium depletion at grain boundaries and free surfaces due to the precipitation of  $Ti_4Ni_2O_x$ . Examining the data listed in Table 4-7, we find that both the PML-9 and PML-16 films annealed at 923 K at a pressure of  $2.6 \times 10^{-3}$  Pa have the lowest 'true'  $M_f$  temperatures and enthalpy values, respectively. On the contrary, the films annealed at 823 K at  $P = 2.6 \times 10^{-4}$  Pa have the highest true  $M_f$  values. Furthermore, X-ray diffraction

results, shown in Fig. 4-30 for the PML-16 films and in Fig. 4-36 for PML-9 films respectively, reveal that increase of volume fraction of the  $Ti_2Ni$  type phase (including  $Ti_4Ni_2O_x$ ) corresponds to decrease of the true  $M_f$  value in the PML films. Shugo *et al.* [64] has reported that the addition of oxygen in TiNi alloys decreased their transformation temperatures primarily by forming the  $Ti_4Ni_2O_x$  oxide which deplete titanium in B2 matrix. An earlier report [156] also indicated that the  $Ti_2Ni$  type precipitates could be stabilized by nitrogen. Therefore, the formation of Ti-rich precipitates in grain boundaries and at free surfaces of the PML-16 films substantially decreases the titanium content in the surrounding area, for which the  $M_s$  temperature is subsequently depressed. The situation may be worse in the PML-9 films because of the precipitation of the  $Ti_2Ni$  phase in the grain interior which results in further composition perturbation, especially since titanium is a slow diffuser in the B2 matrix. The electron micrograph shown in Fig. 4-66 reveals that small austenite domains with a size of 10-100 nm are distributed throughout the original austenite grain in the PML-9 films. It is thus proposed that a fraction of austenite not having suffered a change of composition transforms to martensite in the first stage ('normal') transition, and the remaining austenite, which has different transformation temperature due to a lower titanium content, transformed to martensite at a lower temperature. According to the above discussion, the PML-9 film, annealed at 923 K at  $P = 2.6 \times 10^{-3}$  Pa, is expected to have the largest amount of retained austenite and the lowest 'true'  $M_f$  temperature, which coincides with the experimental results.

Furthermore, the precipitation of the  $Ti_2Ni/Ti_4Ni_2O_x$  particles produced compressive stress fields in the matrix which may further constrain the martensitic transformation on cooling. Hedayat *et al.* [157] reported that the residual stresses associated with an annealed carbon coating on TiNi introduced a surface constraint which postponed the forward transformation on cooling. That is, a portion of alloy close to the TiNi/C interface had lower transformation temperatures. As a consequence, the retained

austenite observed in the present study may result from effects combining the titanium depletion and the stress constraint.

The phenomenon of retained austenite in bulk TiNi alloys has not been previously reported, since the portion contaminated by oxygen during anneal usually is too small to be significant. However, data recently reported in TiNi films by Busch *et al.* [116] showed that increasing annealing temperature and annealing time resulted in a decrease of  $M_s$  temperature and a widening of transformation temperature interval,  $\Delta T = M_s - M_f$ , due to the precipitation of  $Ti_2Ni$  in the grain boundaries [116]. In general, these results underline the importance of stringent vacuum condition for annealing TiNi thin films.

*PML-9 Films: Transmission Electron Microscopy Results* TEM study showed that a small fraction of the B2 austenite in a PML-9 sample annealed at 923 K for one hour at  $P = 2.6 \times 10^{-4}$  Pa had already transformed to martensite at ambient temperature, but there is no indication of the presence of the R-phase or  $1/3$  diffraction spots. Interestingly, the electron diffraction patterns taken at 298 K indicate that this room temperature martensite is orthorhombic rather than the more usual monoclinic. Figure 4-67 is a typical example, showing a dark field image of martensite plates which have developed in the B2 matrix, and a corresponding diffraction patterns in the  $[010]_{ortho}/[011]_{B2}$  direction. A  $[101]_{ortho}$  diffraction pattern taken from martensite nearby is also shown in Fig. 4-67(c). The angle between (100) and (001) martensite planes is  $90^\circ$  which proves the martensite is not monoclinic. The lattice parameters of orthorhombic cell, calculated from electron diffraction patterns in Fig. 4-67(b), using the matrix spots as a calibration standard, are  $a = 0.291$  nm,  $b = 0.425$  nm and  $c = 0.450$  nm. The orientation relationship between this orthorhombic martensite and B2 austenite can be interpreted as  $[010]_{ortho} // [011]_{B2}$  and  $(202)_{ortho}$  near parallel to  $(2\bar{1}1)_{B2}$ . The martensite plates are all oriented roughly parallel to  $(3\bar{2}2)_{B2}$ . However, close examination shows that the plates, which have thicknesses of 15 to 50 nm, do not extend in a simple lateral fashion. Instead, they grow zigzaggedly, first along  $(3\bar{2}2)_{B2}$  and then  $(2\bar{1}1)_{B2}$  planes, alternating every 100 to 300

nm, as illustrated in Figure 4-67(d). As a result, the austenite-martensite interfaces are composed of  $(3\bar{2}2)_{B2}$  and  $(2\bar{1}1)_{B2}$  steps.

When the sample was dipped in liquid nitrogen and then warmed back to room temperature, the structure became fully orthorhombic-martensite, as observed in the electron microscope. The morphology of orthorhombic martensite differed from that of the monoclinic martensite observed in the SL and PML-16 films, that is, no transformation defects such as twinning and stacking faults were found inside the martensite variants. This untwinned martensite has been previously reported by Tadaki *et al.* [71] and by Moberly and Melton [7] in orthorhombic martensites. Furthermore, the orthorhombic variants have a average size which is less than one-tenth of the austenite grain size.

The small variant size allows an observation of the self-accommodation morphology of the orthorhombic martensite to be undertaken, which has not previously been possible in bulk materials with large grain size. A multi-variant combination is shown in Figure 4-68. The bright field micrograph in Fig. 4-68 reveals the size of original austenite grain of about 3.5  $\mu\text{m}$ . The diffraction patterns shown in Fig. 4-68(b) through 4-68(d) were taken from different regions, labeled *B*, *C* and *D* respectively in Fig. 4-68(a), at the same tilting angle. The diffraction patterns taken from region *B* and *C* contain two  $(111)_{\text{ortho}}$  twin-related  $[110]_{\text{ortho}}$  zones as shown in Fig. 4-68(b) and (c) respectively. The angle between the  $[1\bar{1}0]$  and  $[001]$  reciprocal vectors is 90 degrees which again confirms the martensite is orthorhombic. In addition, the diffraction pattern in Fig. 4-68(d) reveals that region *D* contains three martensite variants having a common zone axis along the  $[101]_{\text{ortho}}$  direction, with a  $\pm 120^\circ$  angle between them. Figure 4-68(e) is a dark field image showing that region *B* contains two sets of variants which accommodate themselves with respect to the  $(111)_{\text{ortho}}$  twin plane. In region *C* the variant parallelograms having the darkest tone and the brightest tone are variant *c* and *d*, respectively, which correspond to the diffraction patterns shown in Fig. 4-68(c). These two variants also have a junction plane on the  $(111)_{\text{ortho}}$  twin plane. However, the

neighboring variants with intermediate contrast have different, but unidentified orientations. In other words, area *C* consists of two sets of two-variant combinations. The dark field image in Fig. 4-68(f), taken at high magnification, allows closer examination of the three-variant combination. These three variants are twin related relative to three  $(111)_{\text{ortho}}$  planes, with  $120^\circ$  angle between them, and are referred to variant *e*, *f* and *g* respectively. As a result, at least nine martensite variants coexist in this austenite grain with a diameter of only about  $3.5 \mu\text{m}$ .

In addition to the predominant multi-variant self-accommodation morphology, a two-variant combination was also sometimes observed. Figure 4-69(a) through (c) show a bright field image, its corresponding diffraction pattern, and a dark field image, respectively. The diffraction pattern in Fig. 4-69(b) is similar to that in Fig. 4-68(e), and reveals that the original austenite grain contains at least three martensite variants, referred to variant *a*, *b* and *c* respectively. Figure 4-69(c) is a dark field image taken from the  $[010]_{\text{ortho}}$  spot of variant *a* showing the variant distribution and morphology. Most grains of variant *a* and variant *b* have a shape of parallelogram bounded by two  $(111)_{\text{ortho}}$  planes, and two  $(131)_{\text{ortho}}$  planes or two  $(101)_{\text{ortho}}$  planes, whereas grains of variant *c* and neighboring variants of *a* and *b* are bounded by two sets of  $(111)_{\text{ortho}}$  planes. Figure 4-70 illustrates the crystallographic nature of these martensite parallelograms. As shown in Fig 4-70, variants *a*, *b* and *c* accommodated themselves through three  $(111)_{\text{ortho}}$  twin planes. On the other hand, the majority of variants *a* and *b* form a self-accommodation pattern which is divided by parallel  $(111)_{\text{ortho}}$  twin planes into several divisions. Each division contains interchanged variants *a* and *b* having junction planes of  $(101)_{\text{ortho}}/(131)_{\text{ortho}}$ .

Occasionally, however, further variants in the morphology of orthorhombic martensite were observed in the PML-9 films. Figure 4-71 is a electron micrograph and its corresponding diffraction pattern of  $(111)_{\text{ortho}}$  twins found in a thin-plate form similar to the internally-twined monoclinic martensite in binary alloy, with about 10 to 20 nm

thickness. The spherical particles shown in the bright field micrograph are the  $Ti_2Ni$  precipitates. In addition,  $(011)_{ortho}$  twinned martensite is present and shown in Figure 4-72. The bright field micrograph shows that two martensite variants form thick plates across the austenite grain in the upper left part (region *B*). Fig. 4-72(b) is the associated diffraction pattern taken from region *B* shows that these thick plates are  $(011)_{MO}$  twin-related. The wedge-like variants shown in the lower right part (region *C*) are  $(01\bar{1})_{ortho}$  twin-related, according to the diffraction pattern shown in Fig. 4-72(c). Since variants *b* and *c*, as labeled in the micrograph and diffraction patterns, are not twin related with respect to either  $(011)_{ortho}$  or  $(01\bar{1})_{ortho}$  planes, The variant *c* which is thought to be formed afterward, hence must taper before reaching variant *b*, and then results in the wedge-like shape.

As the sample was cooled well below the  $M_f$  temperature determined by resistivity measurement, most of the original orthorhombic variant morphology was still maintained, though later TEM study showed that the martensite was monoclinic. However, the relative size of the diverse variants did change, i.e., there occurred some intervariant boundary migration. Figure 4-73 is a electron micrograph and associated diffraction pattern of an original austenite grain taken from a direction approximately parallel to  $[100]_{mono}$  at 123 K, showing  $(011)$  twin-related variants in a self-accommodation unit. Figure 4-74 shows an electron micrograph and diffraction patterns, taken at 140 K, of three monoclinic variants which still retain the accommodation morphology formed at orthorhombic state. However, some fine structures in plate-like forms are observed inside the variants (see enclosed area in the micrograph), indicating that an internal change occurs during the orthorhombic-to-monoclinic transformation. Figure 4-75 shows the electron micrograph of two monoclinic martensite variants. Its corresponding diffraction pattern contains two  $(11\bar{1})_{mono}$  twin-related  $[110]_{mono}$  zone. Each set of patterns shows streaks in  $[001]_{mono}$  reciprocal direction. These streaks are not symmetrical with respect to the main spots, and weak and elongated spots can be identified in the streaks, as indicated by arrows. Therefore the

streak do not result from stacking faults, but from thin (001) internal twins. Furthermore, the monoclinic variants show an irregular plate morphology which is different from the well-defined plates or parallelograms of the orthorhombic variants described in Fig. 4-68 through 4-72, indicating rearrangement of variant boundaries may occur during the transformation. A high magnification micrograph and its associated diffraction shown in Figure 4-76 reveal these (001) twins have a spacing of only 4 nm. Further TEM study shows that the PML-9 film having different annealing conditions, i.e., annealed at 923 K for one hour at  $P = 2.6 \times 10^{-3}$  Pa and at 823 K for one hour at  $P = 2.6 \times 10^{-4}$  Pa, have the same features of the martensitic microstructure that are shown above.

*Transformation Properties of the PML-9 Film.* X-ray diffraction and TEM results show that the PML-9 films, with about 5 at % copper content, undergo thermoelastic transformations in a sequence of  $B2 \leftrightarrow M_O \leftrightarrow M_M$ . The appearance of orthorhombic martensite as an intermediate phase during the thermoelastic transformation in PML-9 films demonstrates the complexity of this alloy system. Ternary alloys with about 10 at% Cu addition were reported to undergo a two step transformation which will be referred to a  $B2 \leftrightarrow M_O \leftrightarrow M_M$  transformation [7, 73, 73a]. Increase of Cu content to 15 at% or higher results in a  $B2 \leftrightarrow M_O$  transformation [7, 73]. However, the martensite structure and the transformation sequence in moderate and high copper-containing alloys were found to be process dependent. As pointed out by Tsuji and Nomura [73a], annealing after cold work can stabilize the orthorhombic phase at low temperature. On the other hand, an as-cast alloy with 25 at% Cu addition yielded a monoclinic martensite on cooling [7].

Several possible reasons may contribute to the appearance of the orthorhombic phase in this 5%-Cu films. First, an enrichment of copper in the matrix may result from the precipitation of  $Ti_2Ni$ -type phases, if the solubility of copper in  $Ti_2Ni$  decreases at lower temperature. However, the increase of copper in the matrix is estimated to be less

than 2 at%, for zero solubility of copper in  $Ti_2Ni$  [44], which seems insufficient for a  $B2 \leftrightarrow M_O \leftrightarrow M_M$  transition.

Another possibility is that a compressive stress field results from the precipitation of  $Ti_2Ni$  phase which may suppress the R-phase and the  $B2 \leftrightarrow M_M$  transformations relative to the  $B2 \leftrightarrow M_O$  transformation. From a thermodynamic point of view, the addition of copper in  $TiNi$  in substituting for Ni has the tendency to decrease the free energy of the orthorhombic phase and to increase the free energy of R-phase relative to that of monoclinic one [7]. The variation of the relative free energy levels among these three phases results in a change of transformation sequence from  $B2 \leftrightarrow R \leftrightarrow M_M$  to  $B2 \leftrightarrow M_M$  to  $B2 \leftrightarrow M_O \leftrightarrow M_M$  and finally to  $B2 \leftrightarrow M_O$  with an increase of copper content.

In addition to copper content, the stress is another variable in the thermoelastic systems, as was mentioned in section 2.1. The report on the ability of annealing after cold work to stabilize the orthorhombic phase [73a] coincides with the observation that the back stress of dislocations can effectively suppress the  $B2 \rightarrow M_M$  martensite transformation [63]. Furthermore, a compressive stress is not favorable to R-phase transformation [52, 67]. As a result, the existence of the compressive stress fields around the  $Ti_2Ni$  precipitates are expected to increase the free energies of the R-phase and monoclinic martensite, and results in a  $B2 \leftrightarrow M_O \leftrightarrow M_M$  transformation.

*Crystallographic Calculation of the  $B2 \leftrightarrow$  Orthorhombic Transformation.* The orthorhombic martensite found in the present study is transformed from austenite without involvement of a lattice invariant shear, coinciding with the observation reported by Tadaki and Wayman [71], and by Moberly and Melton [7]. The untwinned martensite indicates that an undistorted habit plane already exists between the B2 austenite and orthorhombic martensite without the assistance of lattice invariant shear. According to the phenomenological theory derived by Wechsler, Lieberman and Read (WLR theory) [25], the necessary and sufficient condition for a plane of zero distortion to exist is that one of the three principle lattice distortions ( $\eta_i$ ) is unity, and  $\eta_j > 1$  and  $\eta_k < 1$  respectively. As was

point out by Wechsler *et al.* [25], the smallest lattice distortion for a B2 austenite to transform homogeneously to an orthorhombic phase is a Bain distortion such as is illustrated in Figure 4-77. In Figure 4-77, a f.c.t. cell is delineated in an untransformed B2 structure. The cubic axis system is  $(i, j, k)$ , and the principle axes  $(i', j', k')$  for the orthorhombic cell is obtained by  $45^\circ$  rotation about the  $k$  axis. The matrix which describe this distortion will be diagonal in the  $(i', j', k')$  axis system and is expressed as

$$T' = \begin{bmatrix} \eta_2 \left( \frac{b}{\sqrt{2}a_0} \right) & 0 & 0 \\ 0 & \eta_3 \left( \frac{c}{\sqrt{2}a_0} \right) & 0 \\ 0 & 0 & \eta_1 \left( \frac{a}{a_0} \right) \end{bmatrix} \quad (4.3.6)$$

where  $a_0$  is the lattice parameter of austenite and  $a$ ,  $b$ , and  $c$  are the lattice parameters of the orthorhombic phase. In the present case, the principle lattice distortions are calculated to be  $\eta_1 = 0.966$ ,  $\eta_2 = 0.995$  and  $\eta_3 = 1.07$ , respectively, according to the lattice parameters determined by electron diffraction. These values are similar to those calculated by Tadaki and Wayman [71] in a 19 at% Cu alloy ( $\eta_1 = 0.950$ ,  $\eta_2 = 0.991$  and  $\eta_3 = 1.05$ ). As a consequence, the principle distortions may be regarded roughly as  $\eta_1 < 1$ ,  $\eta_2 \sim 1$  and  $\eta_3 > 1$ , and thus meet the requirements of the WLR theory. A theoretical calculation was undertaken on the assumption that  $b = \sqrt{2} a_0$ , which yields a distortion matrix expressed as

$$T' = \begin{bmatrix} 1.0000 & 0 & 0 \\ 0 & 1.0687 & 0 \\ 0 & 0 & 0.9659 \end{bmatrix}. \quad (4.3.7)$$

Since all the vectors lying in the habit plane keep the same length after transformation, that is,

$$(r')^2 = (T'r)^2 = (r)^2, \quad (4.3.8)$$

a relation between  $r' = (x', y', z')$  and  $r = (x, y, z)$  is written as

$$\begin{aligned} x'^2 + y'^2 + z'^2 &= (\eta_1^2 x^2 + \eta_2^2 y^2 + \eta_3^2 z^2) \\ &= x^2 + y^2 + z^2 \end{aligned} \quad (4.3.9)$$

which yields

$$y/z = \pm K \quad (4.3.10)$$

where

$$K = \pm \sqrt{\frac{1 - \eta_2^2}{\eta_2^2 - 1}} = \pm 0.8508. \quad (4.3.11)$$

Two vectors in the habit plane are arbitrarily chosen to be  $(0, -Kz_1, z_1)$  and  $(x_2, -Kz_2, z_2)$  and their cross product gives the direction of the habit plane normal to be

$$n = \frac{1}{\sqrt{1+K^2}} \begin{bmatrix} 0 \\ 1 \\ \pm K \end{bmatrix} = \begin{bmatrix} 0 \\ 0.7787 \\ \pm 0.6274 \end{bmatrix}. \quad (4.3.12)$$

A rotation matrix which transforms the deformation matrix to axes aligned along the cubic axes can be written as

$$T' = \begin{bmatrix} \frac{1}{\sqrt{2}} & \frac{1}{\sqrt{2}} & 0 \\ \frac{1}{\sqrt{2}} & \frac{1}{\sqrt{2}} & 0 \\ 0 & 0 & 1 \end{bmatrix}. \quad (4.3.13)$$

Therefore, the normal of the habit plane in the austenite system is written as  $n = [0.5506, 0.5506, +/-0.6274]$ , which is perpendicular to  $[1\bar{1}0]_{B2}$  and is  $3.6^\circ$  from  $[111]$  or  $[11\bar{1}]_{B2}$ , depending on the sign of K value chosen.

Though no lattice invariant shear is required in the austenite-to-orthorhombic transformation, a rigid body rotation may be still necessary to maintain the lattice coherency. By examining the lattice distortion matrix  $T'$ , it is found that only one vector, [100], on the habit plane is not rotated after distortion. In other word, the [100] vector is a rotation axis  $r_0$ , which is expressed as  $[1\bar{1}0]_{B2}$  vector in the cubic system. Consequently, a tilt angle of  $-2.52^\circ$  is found by examining the angle between a vector  $r = n \times r_0$  and the vector  $r' = T'r$ . A angle between the  $(100)_{B2}$  and  $(100)$  plane of orthorhombic phase shown in Fig. 4-67(b) is measured to be  $3^\circ$ , which is in good agreement with the calculated value. The rotation matrix thus can be written in term of the calculated tilt angle  $\theta$  as

$$\Phi = \begin{bmatrix} x_1^2(1 - \cos\theta) + \cos\theta & x_1x_2(1 - \cos\theta) - x_3\sin\theta & x_1x_3(1 - \cos\theta) + x_2\sin\theta \\ x_1x_2(1 - \cos\theta) + x_3\sin\theta & x_2^2(1 - \cos\theta) + \cos\theta & x_2x_3(1 - \cos\theta) - x_1\sin\theta \\ x_1x_3(1 - \cos\theta) - x_2\sin\theta & x_2x_3(1 - \cos\theta) + x_1\sin\theta & x_3^2(1 - \cos\theta) + \cos\theta \end{bmatrix}$$

$$= \begin{bmatrix} 0.9995 & -4.834 \times 10^{-4} & 0.03111 \\ -4.834 \times 10^{-4} & 0.9995 & 0.03111 \\ -0.03111 & -0.03111 & 0.9990 \end{bmatrix}. \quad (4.3.14)$$

The total distortion matrix  $E$  is thus calculated as

$$E = \Phi \Gamma T' \Gamma^*$$

$$= \begin{bmatrix} 1.026 & 0.02631 & 0.02998 \\ 0.02631 & 1.026 & 0.02998 \\ -0.03278 & -0.03278 & 0.9626 \end{bmatrix} \quad (4.3.15)$$

A vector in the direction  $n$  will thus be deformed during transformation, and the deformation direction and the amount of shape strain is yielded by

$$n = n' - n = E n - n = 0.09006 \begin{bmatrix} 0.5305 \\ 0.5305 \\ -0.6611 \end{bmatrix}. \quad (4.3.16)$$

The transformation strain in the austenite-to-orthorhombic transformation is smaller compared that of 11 to 13 % in the austenite-to-monoclinic martensite transformation, which is understandable since the forward orthorhombic-to-monoclinic transformation may contribute an additional fraction of the total shape strain.

*Habit Plane and Self-accommodation of the Orthorhombic Martensite.* The austenite-martensite habit plane found from experimental observation is a zigzagged plane composed of  $\{211\}_{B2}$  and  $\{322\}_{B2}$  planes which is in relatively good agreement with that of a  $\{0.5506, 0.5506, 0.6274\}_{B2}$  (or roughly a  $\{877\}_{B2}$ ) plane from theoretical calculations. Saburi *et al.* [158] carried out an *in situ* TEM study on the early stages of the  $B2 \leftrightarrow M_O$  transformation. The habit plane was determined using trace analysis to be a  $\{334\}_{B2}$  plane. They proposed that this  $\{334\}_{B2}$  habit plane was composed of  $\{211\}_{B2}$  and  $\{011\}_{B2}$  steps with  $\{211\}_{B2}$  step size to be 11 Å. In the present study, the habit plane is observed directly in TEM to be composed of  $\{211\}_{B2}$  and  $\{322\}_{B2}$  steps with a much larger step size of about 100 to 300 nm.

In the present study, the self-accommodation morphology of the orthorhombic martensite in TiNi was observed by TEM, for the first time. According to theoretical calculation, there are twelve habit-plane variants, deriving from six lattice correspondences between B2 austenite and orthorhombic martensite as shown in Table 4-8. These variants can be divided into four groups, in each one of which the variants share a common  $\langle 111 \rangle_{B2}$  pole, and have a  $\{111\}_{ortho}$  twining relation between them. The average shape strain matrix for Group-I is calculated, as an example, to be

$$T_{av} = 1/3 ( T_1 + T_2 + T_3 )$$

$$= \begin{bmatrix} 1.005 & 0.010 & -0.010 \\ 0.010 & 1.005 & -0.010 \\ -0.010 & -0.010 & 1.005 \end{bmatrix}. \quad (4.3.17)$$

The result shows both the diagonal and shear strain components are very small, indicating that this three-variant combination can accomplish efficient for self-accommodation. In

fact, TEM analyses also reveal that the three-variant combination is one of the most frequent morphologies observed in the orthorhombic martensite. Further analysis of the diffraction pattern in Fig. 4-68 indicates that variants *a* and *b* as well as *c* and *d*, appearing as two-variant combinations, have common  $[\bar{1}11]_{B2}$  and  $[1\bar{1}1]_{B2}$  poles respectively, if the variants *e*, *g* and *f* shown in Fig. 4-68(f) have a common pole in  $[11\bar{1}]_{B2}$  direction. In this case, the third variant in Group-II and III as shown in Table 4-8, corresponding to  $[\bar{1}11]_{B2}$  and  $[1\bar{1}1]_{B2}$  poles respectively, may not be able to form in the thin foil sample. Moreover, the average shape strain of these two-variant combinations are also calculated as

$$T_{av} = 1/2 (T_4 + T_5)$$

$$= \begin{bmatrix} 0.994 & 0.030 & 0.001 \\ 0.001 & 1.026 & 0.001 \\ -0.001 & 0.030 & 0.994 \end{bmatrix} \quad (4.3.18)$$

which is also small compared those found in binary alloys, using Type-II twinning as the lattice invariant shear[23]. Therefore, the combination in which three variants join themselves through three  $(111)_{ortho}$  planes is thought to be the basic mechanism for self-accommodation in orthorhombic martensite. The two-variant combination then may be a special case in thin samples.

The twinning relations between martensite variants can also be demonstrated using stereographic projection shown in Figure 4-78, in which solid circles represent the calculated habit planes. Variant 1, for example, is found to have Type-I  $(111)_{ortho}$  (or  $(110)_{B2}$ ) twinning relation with variant 2 and 3; Type-I  $(011)_{ortho}$  (or  $(100)_{B2}$ ) with variant 7 and 10; and compound  $(010)_{ortho}$  with variant 4, as indicated. Therefore it is not difficult to understand that the  $(011)_{ortho}$  type self-accommodation morphology shown in Fig. 4-73

is basically a two-variant combination such as variant 1 and 7 or 1 and 10 demonstrated above. The total transformation strain matrix is calculated accordingly as

$$T_{av} = 1/2 (T_1 + T_{10})$$

$$= \begin{bmatrix} 1.026 & 0 & 0 \\ 0 & 1.026 & 0.030 \\ 0 & -0.033 & 0.993 \end{bmatrix}. \quad (4.3.19)$$

The result indicates that martensite variants accommodating themselves through (011) type twinning can effectively eliminate shear components, but the diagonal components remain. This can explain why this kind of self-accommodation morphology is less commonly observed in the TEM foils.

The orientation dependence of shape strain for orthorhombic martensite is calculated and is shown in Figure 4-79. The maximum shape strain is yielded along a direction close to  $[110]_{B2}$  for variant 1, whereas both  $[100]_{B2}$  and  $[11\bar{1}]_{B2}$  are less favorable. This result is obviously different from the orientation dependence of shape strain for monoclinic martensite in which the favorite direction is along either  $[5\bar{3}5]_{B2}$  for Type-I twinning or  $[2\bar{2}1]_{B2}$  for Type-II twinning. Moreover, the monoclinic martensite in the PML-9 films, transformed from orthorhombic phase, is found to retain features of the orthorhombic variant morphology, and contains  $(001)_{mono}$  transformation twins instead of  $(11\bar{1})$  or  $[011]$  twins. As a result, the monoclinic martensite in the PML-9 films is expected to have slightly different mechanical properties from that in the PML-16 films.

#### *4.3.4. Additional Discussion: Thin Films and TEM Foils versus Bulk Alloys.*

The issue in regard to whether the thermoelastic transformations in thin-film and bulk alloys have the same characteristics is crucial in the development of TiNi thin films. In this section, the thermoelastic transformation characteristics in the Ti(NiCu) films described in

the last three sections is further discussed, based on the comparison with bulk alloys having similar composition and structure.

*Transformations in SL Films.* The annealed SL films, with composition of  $\text{Ti}_{47.4}\text{Ni}_{46.5}\text{Cu}_{6.1}$ , underwent two well-separated  $\text{B2} \leftrightarrow \text{R}$  and  $\text{R} \leftrightarrow \text{M}_M$  transformations which were found in  $\text{Ti}(\text{NiCu})$  alloys for the first time. As discussed in section 4.3.1, this two-step transformation is similar in nature to that found in aged Ni-rich binary alloys. The reason that this two-step transformation has not been previously observed in ternary alloys can be attributed to the limited titanium solubility (<1 at%) in B2 phase, having more than 3 at% Cu substituting for Ni, at higher temperature. This indicates that it is more difficult for bulk ternary alloy to yield a microstructure with fine, coherent or semi-coherent  $(\text{NiCu})_2\text{Ti}$  precipitates distributed uniformly in the matrix. On the other hand, the polymorphic crystallization reaction in the SL films allows a single B2 phase to form prior to the decomposition reaction. Therefore, it is proper to conclude that the two-step transformation in ternary alloy films results from special processing characteristics in thin films, i.e.,  $\text{amorphous} \rightarrow \text{B2} \rightarrow \text{B2} + (\text{NiCu})_2\text{Ti}$ , rather than the "thin film characteristics" itself.

*Transformations in PML-16 Films.* In general, the transformation behavior of the PML-16 films coincides with that observed in the ternary bulk alloy with similar composition. However, the twinning system which responds to the lattice invariant shear in monoclinic martensite has long been unclear. The trace analyses for TiNi single crystals conducted by several researchers [23, 63] concluded that only Type-II [011] twinning could act as lattice invariant shear. Therefore, the Type-I  $(11\bar{1})$  twinning which has been widely observed in TEM was treated as a 'thin foil effect' [63].

In the present work, Type-I  $(11\bar{1})$  twin was also a frequent transformation defect in monoclinic martensite observed in TEM. However, TEM foils, about 0.1  $\mu\text{m}$  thick, are still 'thin' when compared to the TiNi films of 1 to 5  $\mu\text{m}$  thickness, deposited for application on surface superelastic coatings, or for use as microactuators. It is not known

yet that whether the lattice invariant shear in a 5  $\mu\text{m}$  thick films involves Type-I twinning, Type-II twinning, or both. Thus, improvement of our understanding on the dependence of different twinning systems on dimensionality in monoclinic martensite must await more thorough study.

*Transformations in PML-9 Films.* The orthorhombic martensite observed in TEM foils was also detected in the free standing PML-9 films of 5  $\mu\text{m}$  thickness by X-ray diffraction. Thus the appearance of orthorhombic martensite in the PML-9 films with low Cu content did not result from the 'thin foil effects'. As discussed in section 4.3.3, the  $B2 \leftrightarrow M_O \leftrightarrow M_M$  might be caused by an internal stress constraint which suppressed the  $B2 \leftrightarrow M_M$  transformation relative to the  $B2 \leftrightarrow M_O$  one. Furthermore, the product phase of martensitic transformation in Cu-containing *bulk* alloys was also found to be strongly dependent on processing parameters [7, 73a]. Accordingly, the same argument cited for the change of transformation behavior in the SL films can be used in the case of the PML-9 films. That is, a  $B2 \leftrightarrow M_O \leftrightarrow M_M$  transformation resulted from the unique microstructure found in the low-Cu PLM-9 films, rather than their dimensionality.

In addition, the basic self-accommodation morphology of orthorhombic martensite in which three adjacent variants shared a common  $\{111\}_{B2}$  pole should be a general case in both thin-film and bulk alloys, since the theoretical calculations yield a total distortion matrix that is numerically close to unity. On the other hand, the total distortion matrix for the two-variant morphology which involved (011) twinned variants produces the diagonal components which are not unity; only two out of three shear components vanish. Thus, the two-variant morphology may exist in thin foils only whose two-dimensional characteristics can tolerate this unaccommodated dilatation. How thick can 'thin' be in this context? It cannot be said from the limited data available.

## 5. CONCLUSIONS

The present study has been concerned with two major issues: the development of reliable processing techniques for fabrication of Ti(NiCu) thin films with controlled composition; and a thorough understanding of the phase transformation characteristics of these films as compared to bulk materials with similar composition. Since substantial titanium depletion was observed in films deposited by triode magnetron sputtering from a Ti<sub>50</sub>Ni<sub>45</sub>Cu<sub>5</sub> alloy target, a strategy has been developed to compensate the titanium loss by adding thin titanium layers periodically, to form a multilayered structure during deposition. The extremely thin and closely-spaced Ti-layers (1 nm layers spread at 9 to 16 nm intervals) minimized the effective diffusion distance required for complete homogenization. Although interdiffusion during the crystallization anneal can create transient regions with composition favoring precipitation of Ti-rich crystalline phases (such as Ti<sub>2</sub>Ni) their thickness would not exceed about 2 nm, which is small compared to a conservative estimate of the size of a critical GP-zone nucleus (~10 nm). Nucleation of Ti-rich intermetallic phases would thus be difficult from both a kinetic and a thermodynamic point of view, since lateral diffusion of Ti would be required, for which there is no particular driving force. Furthermore, titanium is known as a slow diffuser in both TiNi and β-Ti. Results from DSC and electrical resistivity studies showed an increase in the martensite transformation temperature with increasing overall Ti content, confirming that the titanium content in B2 phase had been effectively increased; that is, no Ti was lost to the B2 matrix by precipitation of Ti-rich intermetallics during the crystallization anneal. It is thus shown

that film composition can be controlled by adjusting the Ti-layer/alloy-layer thickness ratio, according to a semi-empirical relationship obtained by experiment.

Additional analyses of the sputtering yield ratio of Ti and Ni in amorphous TiNi alloys were performed by concurrent argon-ion irradiation of the ion sputter-deposited films. The results revealed that the titanium depletion, observed in both triode magnetron sputtering and ion beam sputtering, was primarily produced by preferential resputtering of titanium by bombardment of energetic neutrals reflected from the sputter-target surface. The preferential resputtering of titanium was enhanced when the bombarding ion energies were close to the sputtering thresholds of Ni and Ti. Moreover, the sputtering yield ratio,  $Y=Y_{Ti}/Y_{Ni}$ , also became more sensitive to small variations in beam incidence angle in these energy regimes. The employment of concurrent ion bombardment to improve film qualities is thus seen to produce non-trivial composition-control problems.

Annealed  $Ti_x(NiCu)_{1-x}$  films, with copper content of approximately 5 at%, showed a variety of microstructures and thermoelastic transformation characteristics which have not been observed in bulk alloys having similar composition. The as-fabricated films were amorphous, and underwent a polymorphic reaction during crystallization to form a B2 phase with a supersaturation of Ni or Ti. Such supersaturations would be difficult to achieve by ingot metallurgy, as the solubility of titanium in the B2 phase is very limited (<1at%) at high temperature. During subsequent annealing (beyond that required for crystallization), second phase precipitates formed in a wide and uniform dispersions, in contrast to the case for ingot-metallurgy alloys where troublesome grain-boundary precipitation is often observed. The precipitates generally showed specific lattice orientations and/or lattice coherency relationships with the B2 matrix. As a result, the thermoelastic transformations were affected by internal stresses resulting from the lattice misfit strains between the precipitates and the B2 matrix.

Self-accommodation morphologies for R-phase, monoclinic martensites and orthorhombic martensites were studied by TEM. Pairs of plate-like R-phase variants alternated to form self-accommodated domains with a lamellar structure. Unlike the four-variant combination observed in bulk TiNi alloys, the total distortion matrix for the two-variant complex had two non-zero shear components, which may be allowed only in the low-dimensional geometry of thin films. Similarly, this low-dimensional geometry may also be responsible for the appearance of  $(11\bar{1})$  lattice invariant twinning, the large variant size, and the ill-defined self-accommodation morphology observed here for the monoclinic martensite. Accordingly, the mechanical properties of the monoclinic martensite in thin films may be expected to be different from those of bulk alloys. On the other hand, the majority of *orthorhombic* martensite variants were found to form as parallelograms bounded by  $\{111\}_{\text{orth}}$  twin planes. Three variants, which shared a common  $\{111\}_{B2}$  pole, formed well-defined self-accommodation units whose total distortion matrix is numerically close to unity. The observation of this three-variant self-accommodation mechanism is a first step toward a more thorough understanding of the shape-memory properties of orthorhombic martensite.

In summary, the present study has demonstrated that Ti(NiCu) thin films fabricated by physical vapor deposition techniques can behave thermoelastically after annealing, and show certain aging effects which do not appear in similar bulk alloys. The difference is attributed essentially to the kinetic conditions of deposition which resulted in films with an amorphous structure. The films, after subsequent solid-state crystallization reaction and heat treatment, possessed microstructures characterized extremely fine grain size and special precipitate distributions, neither of which are easily attainable in materials made by traditional melt-solidification processes. The thermoelastic transformation characteristics of thin films were significantly affected by the nature of these microstructures. The fine grain

size also allowed, for the first time, observation of self-accommodation morphologies of various martensites by TEM in whole grains. The results offer valuable information for interpretation of the shape-memory properties of thin films. It should be pointed out, however, that the self-accommodation morphologies observed here may also have been influenced by the low-dimensional constraints in TEM foils, which were one or two orders of magnitude thinner yet than the sputtered films studied by resistometry and calorimetry.

*Detailed Conclusions:*

(1) Thin films deposited from a  $\text{Ti}_{50.05}\text{Ni}_{44.99}\text{Cu}_{4.96}$  target by triode DC magnetron sputtering yielded a composition of  $\text{Ti}_{47.4}\text{Ni}_{46.5}\text{Cu}_{6.1}$  at an argon ion energy of 550 volts. Concurrent ion-bombardment of the growing TiNi films, with ion energies of 50 eV, 100 eV and 500 eV, verified that titanium atoms were removed preferentially by the energetic particles in amorphous Ti-Ni alloys. The sputtering yield ratio of 500 eV ion bombardment was  $Y = Y_{\text{Ti}}/Y_{\text{Ni}} = 1.75$ . The value of 50 eV ion bombardment was found to be  $Y \geq 9$ .

(2) The addition of 1 nm titanium layer for every 9 and 16 nm alloy layer increased the overall titanium concentration in the films to 49.2 at% and 51.0 at% respectively, which were about 0.6 at% lower than the calculated values. Microstructure in films annealed at 823 K and 923 K coincided relatively well with the predicted one, according to the phase diagram obtained at 1073 K [44]. This revealed that the multilayered structure can be a reliable method for fabrication of TiNi films with controlled composition.

(3) No evidence of Ti-Ni crystallization was found with 100 to 500 eV concurrent argon ion bombardment, at ion-to-atom arrival (I/A) ratios of 0.33 to 1.08, and at substrate temperature of below 500K. However, short range ordering in the films was enhanced as substrate temperature, ion energy, and I/A ratio increased.

(4) TiN particles with about 5 nm in diameter formed in a wide dispersion in an IBAD film, with 100 eV assist-beam energy and I/A ratio of 1.08, when the nitrogen partial pressure approached  $10^{-6}$  Pa.

(5) The amorphous-to-crystalline transformation in  $Ti_x(NiCu)_{1-x}$  films with titanium concentrations in the range of 47.4 at% to 51.0 at % was found to be a polymorphic reaction with a B2 product phase. The crystallization temperatures of these films, at a heating rate of 10 K/min, increased monotonically from 749 K to 764 K as Ti content decreased from 51.0 at% to 47.4 at%. This trend coincides with an extrapolation of the data obtained from TiNi alloy ribbons [75], however, the crystallization temperatures of the ternary films were about 40 K lower as compared to those of the binary alloys with the same titanium content. All the ternary films with compositions between 51.0 at% and 47.4 at% Ti released approximately  $2.2 \pm 0.1$  kJ/mole during crystallization

(6) All the annealed films had austenite grains which were 1 to 2  $\mu\text{m}$  in diameter. The grain boundaries were decorated with  $Ti_2Ni$  type precipitates.

(7) Annealed films with composition of  $Ti_{47.4}Ni_{46.5}Cu_{6.1}$  contained precipitates of  $(NiCu)_2Ti$  phase, appearing in the grain boundaries and in the grain interiors. Specific orientation relationship between the  $(NiCu)_2Ti$  precipitates and the B2 matrix was first deduced to be:  $[100]_{(NiCu)_2Ti} // \langle 100 \rangle_{B2}$  and  $(001)_{(NiCu)_2Ti} // \{001\}_{B2}$ . The  $(NiCu)_2Ti$  phase has a thin-plate morphology with a semi-coherent (001) plate surface. The films annealed at 923 K underwent two separate thermoelastic transformations, not before found in Cu-containing alloys, which consisted of a  $B2 \leftrightarrow R$ -phase transformation and a  $R$ -phase  $\leftrightarrow$  monoclinic-martensite transformation. The change in transformation behavior in this film was closely related to the presence of  $(NiCu)_2Ti$  precipitates, which resulted in copper depletion, and formation of internal stress in the B2 matrix.

(8) Films with a composition of  $Ti_{49.2}Ni_{44.8}Cu_{6.0}$  were relatively free from precipitates. Only a small amount of  $Ti_{40}Ni_{56.5}Cu_{3.5}$  and  $Ti_2Ni$  precipitates were found in the grain interiors. The  $Ti_{40}Ni_{56.5}Cu_{3.5}$  phase was found to have an orientation

relationship with the B2 phase, which could be expressed as:  $[011]_{\text{ppt}} // [011]_{\text{B2}}$  and  $(200)_{\text{ppt}} \sim 1^\circ$  away from  $(0\bar{1}1)_{\text{B2}}$ . This was different from those between the  $\text{Ti}_2\text{Ni}_3$  precipitates and the B2 phase found in Ni-rich TiNi alloys, though they have similar crystal structures. In addition, electron diffraction showed the  $\text{Ti}_{40}\text{Ni}_{56.5}\text{Cu}_{3.5}$  phase had an orthorhombic unit cell rather than a tetragonal one reported by van Loo *et al.* [44]. The films annealed at 923 K for one hour underwent a regular B2  $\leftrightarrow$  monoclinic-martensite transformation in which Type-I  $(11\bar{1})$  twinning, observed by TEM, was the lattice invariant shear. On the other hand, R-phase were observed in the films annealed at 823 K. The self-accommodation morphology of R-phase observed in this (Ni+Cu)-rich film was different from that found in the bulk materials. Two sets of plate-like R-phase variants were arranged alternately through  $\{100\}_{\text{B2}}$  and/or  $\{110\}_{\text{B2}}$  twins to form a accommodated domain. An austenite grain usually contained as many as three sets of two-variant domains.

(9) Extensive precipitation of fine  $\text{Ti}_2\text{Ni}$  particles was found in the grain interiors of the Ti-rich PML films having a composition of  $\text{Ti}_{51.0}\text{Ni}_{44.4}\text{Cu}_{4.6}$ . The  $\text{Ti}_2\text{Ni}$  precipitates were equiaxed, and were first found to have a well-defended orientation relationship with B2 matrix:  $\langle 100 \rangle_{\text{Ti}_2\text{Ni}} // \langle 100 \rangle_{\text{B2}}$  and  $\{010\}_{\text{Ti}_2\text{Ni}} // \{010\}_{\text{B2}}$ . Thermoelastic transformations in these films proceeded by a two-step transformations involving the initial formation of an orthorhombic martensite prior to transformation to the monoclinic phase. This two-step transformation has previously been observed only in bulk ternary alloys having more than 9 at% copper addition. The orientation relationship between B2 and orthorhombic phases was:  $[010]_{\text{ortho}} // [011]_{\text{B2}}$  and  $(202)_{\text{ortho}} // (2\bar{1}1)_{\text{B2}}$ , which coincides with a previous prediction made by Saburi *et al.* [158]. The habit plane was for the first time directly observed by TEM to be a zigzagged plane, composed of alternate  $\{322\}_{\text{B2}}$  and  $\{112\}_{\text{B2}}$  steps, each of which were about 100 to 300 nm in length. Both theoretical calculation and TEM observation indicated that a three-variant combination could be the most stable and the most frequent self-accommodation morphology. Here, three variants,

sharing a common  $\langle 111 \rangle_{B2}$  pole, are bounded by three  $(111)_{ortho}$  twin planes with a  $\pm 120^\circ$  angle between them. Furthermore, austenite grains were sometime found to consist of two band-like variants arranged alternately through  $(011)$  twin planes. Theoretical calculations showed that the shear strain associated with the transformation could be eliminated effectively by this arrangement. The monoclinic martensite descended from this structure can inherit the original orthorhombic variants, but will form  $(001)_{mono}$  twins as the lattice invariant shear.

Finally, successful application for TiNi thin films as micro-actuators and superelastic surface coatings relies on their superior shape memory or superelastic properties. In the present study, the films with slightly different titanium content have shown a wide variety of transformation characteristics, which offered an excellent chance to study the correlation between transformation behavior and corresponding mechanical properties for both applications and academic interest. Further research will required to establish precise stress-strain-temperature relations, and relate them to the transformation characteristics, allowing desired mechanical properties to be made in a predictable and reproducible manner. The mechanical properties of these films may also be affected by the unique microstructures observed, such as the extensive distribution of grain boundary precipitates and the wide dispersion of various precipitates in the grain interiors.

Table 3-1  
Deposition parameters for magnetron sputter-deposited films.

Run	Pressure (torr)	Deposition Rate (Å/sec)	Film, Thickness and Substrate											
			Ti	1	2	3	4	5	6	7	8			
170	$P_{\text{tot}}=1.8 \times 10^{-8}$ $P_{\text{O}_2}=n/a$ $P_{\text{N}_2}=n/a$ $P_{\text{H}_2\text{O}}=n/a$	7.8	TiNiCu	Ti	SL	SL	SL	SL	SL	SL	SL	SL	SL	
					(1.4 μm) SiO <sub>2</sub> (m)* +SiO <sub>2</sub>	(0.5 μm) KCl +Cu	(5.0 μm) SiO <sub>2</sub> (m) +KCl	(6.0 μm) SiO <sub>2</sub> (m) +KCl	(1.4 μm) KCl +Cu					
178	$P_{\text{tot}}=1.8 \times 10^{-8}$ $P_{\text{O}_2}=n/a$ $P_{\text{N}_2}=n/a$ $P_{\text{H}_2\text{O}}=n/a$	8.1	5.8	PML-16	PML-16	PML-16	PML-18	PML-12						
					(5.0 μm) SiO <sub>2</sub> (m) +KCl	(5.0 μm) Ni +KCl	(2.0 μm) SiO <sub>2</sub> (m) +Cu	(2.0 μm) SiO <sub>2</sub> (m) +SiO <sub>2</sub>						
204	$P_{\text{tot}}=1.8 \times 10^{-8}$ $P_{\text{O}_2}=1.4 \times 10^{-10}$ $P_{\text{N}_2}=7.7 \times 10^{-10}$ $P_{\text{H}_2\text{O}}=2.7 \times 10^{-9}$	8.1	5.2	PML-9	PML-9	PML-9	PML-9	PML-16	PML-16	PML-16	SL	SL	PML-9	
					(3.0 μm) KCl x 2	(1.0 μm) SiO <sub>2</sub> (m) x2	(1.0 μm) SiO <sub>2</sub> (m) +SiO <sub>2</sub>	(1.0 μm) SiO <sub>2</sub> (m) x2	(3.0 μm) KCl x 2	(1.0 μm) SiO <sub>2</sub> (m) x2	(3.0 μm) KCl x 2	(1.0 μm) SiO <sub>2</sub> (m) x2	(3.0 μm) KCl x 2	(3.0 μm) SiO <sub>2</sub> (m) +KCl
222	$P_{\text{tot}}=8.9 \times 10^{-9}$ $P_{\text{O}_2}=1.0 \times 10^{-10}$ $P_{\text{N}_2}=1.0 \times 10^{-9}$ $P_{\text{H}_2\text{O}}=2.0 \times 10^{-10}$	8.5	5.7	PML-9	PML-9	PML-9	PML-9	PML-9						
					(3.0 μm) Si +KCl	(3.0 μm) Si +KCl	(3.0 μm) Si							
235	$P_{\text{tot}}=9.0 \times 10^{-9}$ $P_{\text{O}_2}=1.0 \times 10^{-10}$ $P_{\text{N}_2}=1.0 \times 10^{-9}$ $P_{\text{H}_2\text{O}}=3.0 \times 10^{-9}$	8.6	5.8	SL	SL	SL	SL	PML-9	PML-9	50Å TiNi	SL	PML-9	PML-9	
					(1.0 μm) SiO <sub>2</sub> (m) x2	(1.0 μm) SiO <sub>2</sub> (m) x2	(4.0 μm) Si x 2	(4.0 μm) SiO <sub>2</sub> +Si	(4.0 μm) SiO <sub>2</sub> +Si	(5.0 μm) SiO <sub>2</sub> +Si	(5.0 μm) SiO <sub>2</sub> +Si	(4.0 μm) SiO <sub>2</sub> +Si	(5.0 μm) SiO <sub>2</sub> +Si	(5.0 μm) SiO <sub>2</sub> +Si

\*Substrate was overlaid by mask for electrical resistivity measurement.

Table 3-2  
Deposition parameters for ion beam sputter ion beam assisted deposited films fabricated for direct TEM observation.

Figure	Assisted-Beam energy (eV)	Ion-to-Atom Arrival ratio	Substrate Temperature (K)	Sputter Time (minute)	Deposition Rate (Å/sec)
4-7(a)	0	---	373	22	0.55
4-7(b)	100	0.326	388	23	0.55
4-7(c)	200	0.596	423	23	0.55
4-7(d)	300	0.813	403	22	0.55
4-8	500	1.084	403	22	0.55
4-9	100	0.326	473	23	0.55

Table 3-3  
Deposition parameters for ion beam sputter ion beam assisted deposited films.

Substrate and Run	Assist-Beam energy (eV)	Current Density (mA/cm <sup>2</sup> )	Deposition Rate (Å/min)	Ion/Atom Arrival Ratio	Assist-Beam Angle	Sputter Time (minute)
Control 1 SiO <sub>2</sub>	0	0	30.0	0	n/a	307
	0	0	42.4	0	n/a	
	0	0	51.5	0	n/a	
	0	0	57.3	0	n/a	
Control 2 SiO <sub>2</sub>	0	0	17.2	0	n/a	180
	0	0	21.6	0	n/a	
	0	0	25.6	0	n/a	
	0	0	29.2	0	n/a	
Control 3 SiO <sub>2</sub>	0	0	20.5	0	n/a	125
	0	0	25.7	0	n/a	
	0	0	33.0	0	n/a	
	0	0	42.6	0	n/a	
IBAD 1 SiO <sub>2</sub>	50	9.0	29.5	0.16	0	178
	50	6.5	40.1	0.085	7.8	
	50	5.0	48.6	0.054	15.2	
	50	3.6	54.8	0.035	22.2	
IBAD 2 4KCl+SiO <sub>2</sub>	100	27.1	11.1	0.57	0	308
	100	24.1	15.1	0.42	7.8	
	100	18.7	17.0	0.27	15.2	
	100	13.1	17.4	0.17	22.2	
IBAD 3 4KCl+SiO <sub>2</sub>	500	62.3	0	1.13	0	317
	500	49.7	0	0.72	7.8	
	500	33.9	5.8	0.38	15.2	
	500	21.6	14.4	0.19	22.2	

**Table 4-1**  
**Comparison of the d-spacing values of the precipitates shown in Figure 4-5 and the TiN phase [129].**

Precipitates	Intensity	$d_{\text{TiN}}$	Plane	Intensity
2.50	s	2.499	(111)	72
2.11	vs	2.120	(200)	100
1.50	s	1.499	(220)	45
1.29	m	1.279	(311)	19
1.23	m	1.224	(222)	12
1.05	w	1.060	(400)	5
1.03	w	0.973	(331)	6
0.95	m	0.948	(420)	14
0.87	w	0.865	(422)	12
0.82	w	0.816	(333)(511)	7

**Table 4-2**  
**Compositions of target alloy and magnetron sputter-deposited films.**

Materials	Composition (at%)					
	ZAF Method			Cliff-Lorimer Method		
	Ti	Ni	Cu	Ti	Ni	Cu
Target Alloy*	50.2	45.7	4.1			
SL Film	47.4	46.5	6.1	47.5	47.5	5.0
PML-16 Film	49.2	44.8	6.0	49.2	45.5	5.4
PML-9 Film	51.0	44.4	4.6			

\* The composition of target alloy supplied by the donor is 50.05 at% Ti, 44.99 at% Ni and 4.96 at% Cu.

Table 4-3  
Crystallization data for magnetron sputter-deposited Ti(NiCu) films.

Material	Crystallization Temperature (K)				Crystallization Enthalpy (kJ/mole)			
	2*	10*	30*	50*	2*	10*	30*	50*
SL Film	<sup>416</sup> 749	764	776	<sup>507</sup> 780	1.23	1.68	1.92	2.16
PML-9 Film	733	749	761	771	1.48	2.28	1.72	2.13
PML-9 Film on Si	727	753	767	773	0.91	1.61	1.84	2.32
PML-18 Film on Cu	729	747	758	766	1.29	1.29	1.82	2.11

\* : Heat rate in Kelvens per minute.

Table 4-4  
Transformation data for PML-16 films.

Heat Treatment	Method	M <sub>s</sub>	M <sub>f</sub>	A <sub>s</sub>	A <sub>f</sub>	ΔT	Hysteresis	ΔH (J/mole)
923 K, one hour (2x10 <sup>-5</sup> torr)	ER	287	228	238	297	59	10	---
923 K, one hour (2x10 <sup>-5</sup> torr)	DSC	275	253	266	284	20	9	685
923 K, six hours (2x10 <sup>-5</sup> torr)	DSC	275	254	266	284	19	9	427
923 K, one hour (2x10 <sup>-6</sup> torr)	DSC	258	251	259	267	8	9	1016
823 K, one hour (2x10 <sup>-6</sup> torr)	DSC	222	202	243	273	35	31	854

Temperature in Kelvins

Table 4-5  
Crystallographic data for Type-I twinning

Solution 1			Solution 2		
(1-x)=0.32006	x=0.67994		(1-x)=0.32006	x=0.67994	
$n_1 = \begin{bmatrix} 0.58112 \\ -0.81382 \\ -0.00089 \end{bmatrix}$			$n_2 = \begin{bmatrix} 0.43012 \\ 0.27789 \\ 0.85894 \end{bmatrix}$		
$M_{11} = \begin{bmatrix} 1.02518 & 0.09869 & -0.13399 \\ 0.02036 & 1.02179 & -0.05033 \\ 0.05428 & -0.02355 & 0.94746 \end{bmatrix}$			$M_{21} = \begin{bmatrix} 1.02608 & 0.15603 & -0.08709 \\ -0.03877 & 1.01381 & -0.11627 \\ -0.00223 & 0.04698 & 0.94713 \end{bmatrix}$		
$M_{12} = \begin{bmatrix} 1.02518 & -0.09832 & 0.06301 \\ 0.02036 & 0.94782 & 0.02365 \\ 0.05428 & -0.10070 & 1.02461 \end{bmatrix}$			$M_{22} = \begin{bmatrix} 1.02608 & -0.04866 & 0.11760 \\ -0.03877 & 0.95667 & -0.05913 \\ -0.00223 & -0.02423 & 1.01835 \end{bmatrix}$		
$E_1 = \begin{bmatrix} 1.02518 & -0.03527 & -0.0004 \\ 0.02036 & 0.97150 & -0.0003 \\ 0.05428 & -0.07601 & 0.99992 \end{bmatrix}$			$E_2 = \begin{bmatrix} 1.02608 & 0.01685 & 0.05209 \\ -0.03877 & 0.97496 & -0.077418 \\ -0.00223 & -0.00144 & 0.99556 \end{bmatrix}$		
S=0.1088			S=0.1088		
$m_1 = \begin{bmatrix} 0.39866 \\ 0.32205 \\ 0.85869 \end{bmatrix}$			$m_2 = \begin{bmatrix} 0.55758 \\ -0.82876 \\ -0.04760 \end{bmatrix}$		
$m'_1 = \begin{bmatrix} 0.41720 \\ 0.29652 \\ 0.85908 \end{bmatrix}$			$m'_2 = \begin{bmatrix} 0.57077 \\ -0.82085 \\ -0.02072 \end{bmatrix}$		

$n_1, n_2$ =Normals to the habit plane in the cubic basis.

$M_{11}, M_{12}$ =The distortions to which the major and minor twins are subjected, in the cubic basis.

(1-x), x=Volume fractions of major and minor twins respectively.

**Table 4-6**  
Transformation data for PML-9 films.

Heat Treatment	Method	$M_s$	$M_f$	$A_s$	$A_f$	$\Delta T$	Hysteresis	$\Delta H$ (J/mole)
923 K, one hour ( $2 \times 10^{-5}$ torr)	ER	305	225	247	322	78	17	---
923 K, one hour ( $2 \times 10^{-5}$ torr)	DSC	297	285	300	312	12	15	482
923 K, one hour ( $2 \times 10^{-6}$ torr)	DSC	293	286	299	307	8	14	643
823 K, one hour ( $2 \times 10^{-6}$ torr)	DSC	292	286	297	306	8	14	949

Temperature in Kelvins

Table 4-7  
Summary of transformation data for PML films

PML-16 Films							
Heat Treatment	Method	M <sub>s</sub>	M <sub>f</sub>	A <sub>s</sub>	A <sub>f</sub>	ΔH (J/mole)	ΔT
923 K, 1 hr (2.6x10 <sup>-3</sup> Pa)	ER	287	228	238	297		59
	DSC	275	253	266	284	685	20
923 K, 6 hr (2.6x10 <sup>-3</sup> Pa)	DSC	275	254	266	284	427	19
923 K, 1 hr (2.6x10 <sup>-4</sup> Pa)	DSC	258	251	259	267	1016	9
	XRD	>251	~201				>50
823 K, 1 hr (2.6x10 <sup>-4</sup> Pa)	DSC	222	202	243	273	854	25
	XRD	>221	~198				>23
PML-9 Films							
923 K, 1 hr (2.6x10 <sup>-3</sup> Pa)	ER	305	225	247	322		78
	DSC	297	285	300	312	482	12
	XRD		143<	<222			
923 K, 1 hr (2.6x10 <sup>-4</sup> Pa)	DSC	293	286	299	307	643	8
	XRD		~221				
823 K, 1 hr (2.6x10 <sup>-4</sup> Pa)	DSC	292	286	297	306	949	8
	XRD		229<	<270			

Temperature in Kelvins

Table 4-8  
 Crystallographic data for orthorhombic martensite expressed in the cubic basis.

Variant	Lattice Correspondence			Habit Plane	Total Distortion Matrix			Group
	$[100]_M$	$[010]_M$	$[001]_M$					
1	$[001]$	$[1\bar{1}0]$	$[110]$	$(0.5506, 0.5506, 0.6274)$	1.0263	0.0263	0.0300	I ( $11\bar{1}$ )
					0.0263	1.0263	0.0300	
					-0.0328	-0.0328	0.9626	
2	$[100]$	$[011]$	$[0\bar{1}1]$	$(0.6274, -0.5506, 0.5506)$	0.9626	0.0328	-0.0328	I ( $11\bar{1}$ )
					-0.0300	1.0263	-0.0263	
					0.0300	-0.0263	1.0263	
3	$[010]$	$[101]$	$[\bar{1}01]$	$(-0.5506, 0.6274, 0.5506)$	1.0263	-0.0300	-0.0263	
					0.0328	0.9626	-0.0328	
					-0.0263	0.0300	1.0263	
4	$[001]$	$[1\bar{1}0]$	$[110]$	$(0.5506, 0.5506, -0.6274)$	1.0263	0.0263	-0.0300	
					0.0263	1.0263	-0.0300	
					0.0328	0.0328	0.9626	
5	$[100]$	$[01\bar{1}]$	$[011]$	$(-0.6274, 0.5506, 0.5506)$	0.9626	0.0328	0.0328	II (111)
					-0.0300	1.0263	0.0263	
					-0.0300	0.0263	1.0263	
6	$[010]$	$[10\bar{1}]$	$[101]$	$(0.5506, -0.6274, 0.5506)$	1.0263	-0.0300	0.0263	
					0.0328	0.9626	0.0328	
					0.0263	-0.0300	1.0263	

Table 4-8  
(Continued)

Variant	Lattice Correspondence		Habit Plane	Total Distortion Matrix			Group	
	$[100]_M$	$[010]_M$		$[\bar{1}10]_M$	$[010]_M$	$[\bar{1}10]_M$		$[001]_M$
7	[001]	[110]	$[\bar{1}10]$	(-0.5506, 0.5506, -0.6274)	1.0263	-0.0263	0.0300	III ( $\bar{1}11$ )
					-0.0263	1.0263	-0.0300	
					-0.0328	0.0328	0.9626	
8	[100]	$[01\bar{1}]$	[011]	(0.6274, 0.5506, 0.5506)	0.9626	0.0328	0.0328	III ( $\bar{1}11$ )
					-0.0300	1.0263	0.0263	
					-0.0300	0.0263	1.0263	
9	[010]	[101]	$[\bar{1}01]$	(-0.5506, -0.6274, 0.5506)	1.0263	0.0300	-0.0263	III ( $\bar{1}11$ )
					-0.0328	0.9626	0.0328	
					-0.0263	-0.0300	1.0263	
10	[001]	[110]	$[\bar{1}10]$	(-0.5506, 0.5506, 0.6274)	1.0263	-0.0263	-0.0300	IV ( $1\bar{1}1$ )
					-0.0263	1.0236	0.0300	
					0.0328	-0.0328	0.9626	
11	[100]	[011]	$[0\bar{1}1]$	(-0.6274, -0.5506, 0.5506)	0.9626	-0.0328	0.0328	IV ( $1\bar{1}1$ )
					0.0300	1.0263	-0.0263	
					-0.0300	-0.0263	1.0263	
12	[010]	$[10\bar{1}]$	[101]	(0.5506, 0.6274, 0.5506)	1.0263	0.0300	0.0263	IV ( $1\bar{1}1$ )
					-0.0328	0.9626	-0.0328	
					0.0263	0.0300	1.0263	

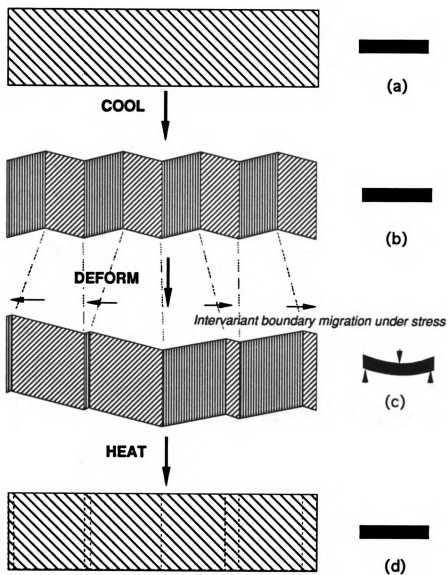
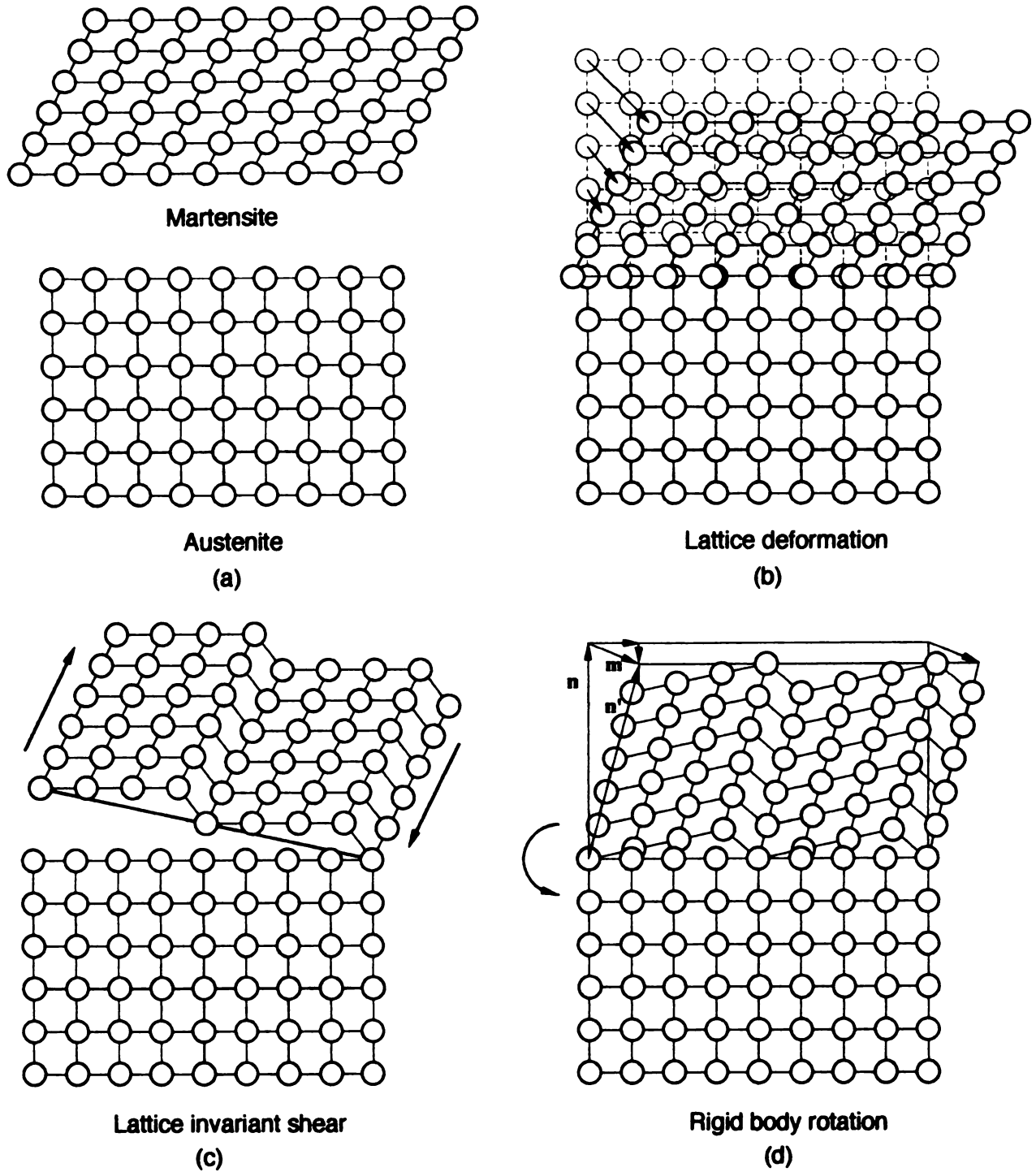


Figure 1-1: Schematic drawing of the shape memory effect: (a) austenite single crystal; (b) martensite consisting of two variants; (c) variant coalescence on loading; and (d) martensite reverting to austenite on heating.



**Figure 2-1: Two dimensional schematic drawing of the martensitic transformation: (a) crystal structures of austenite and martensite respectively; (b) lattice deformation transforming austenite lattice to martensite lattice; (c) lattice invariant shear maintaining an undistorted habit plane; and (d) rigid body rotation maintaining a continuous interface.**

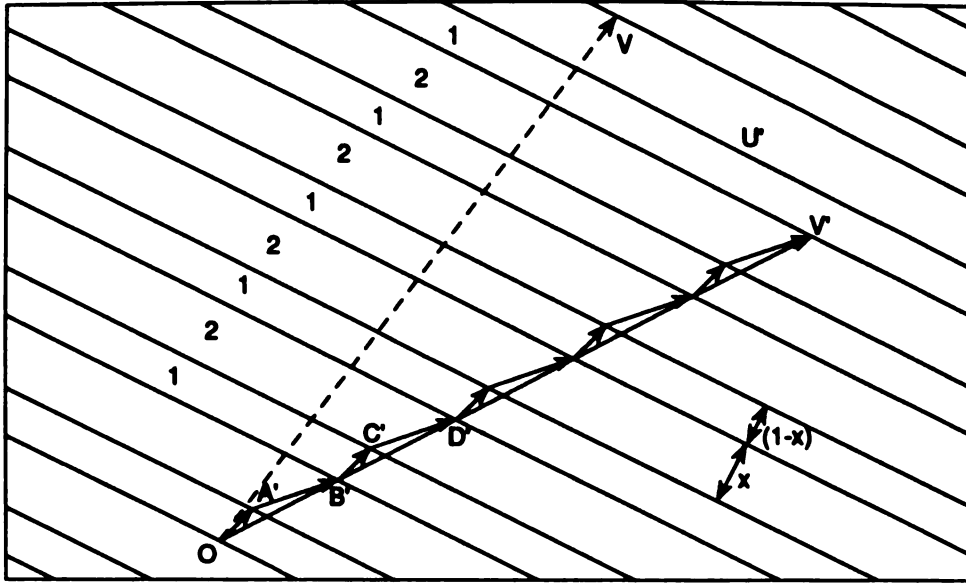


Figure 2-2: Section through a martensite plate, showing the banded structure of relative amounts  $x$  of twin 2 and  $(1-x)$  of twin 1. The plane of paper is perpendicular to the twin planes [25].

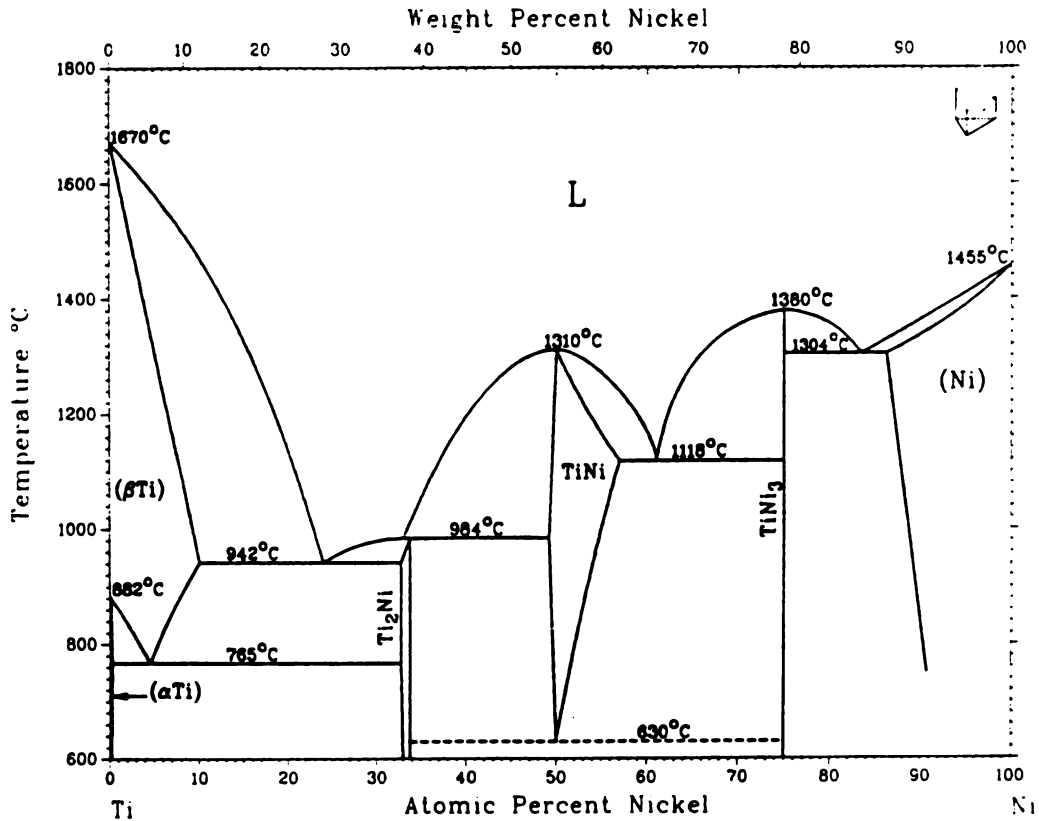


Figure 2-3: Equilibrium phase diagram for Ti-Ni alloys [29].

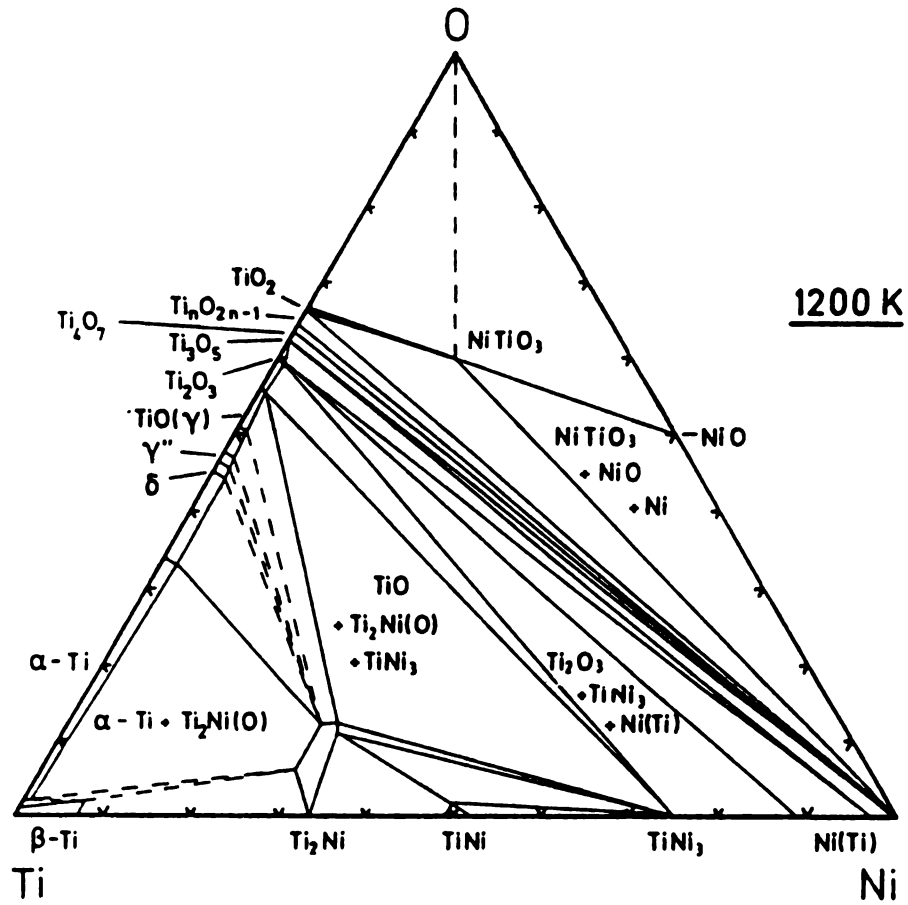


Figure 2-4: Isothermal cross section through the Ti-Ni-O phase diagram at 1200 K [42].

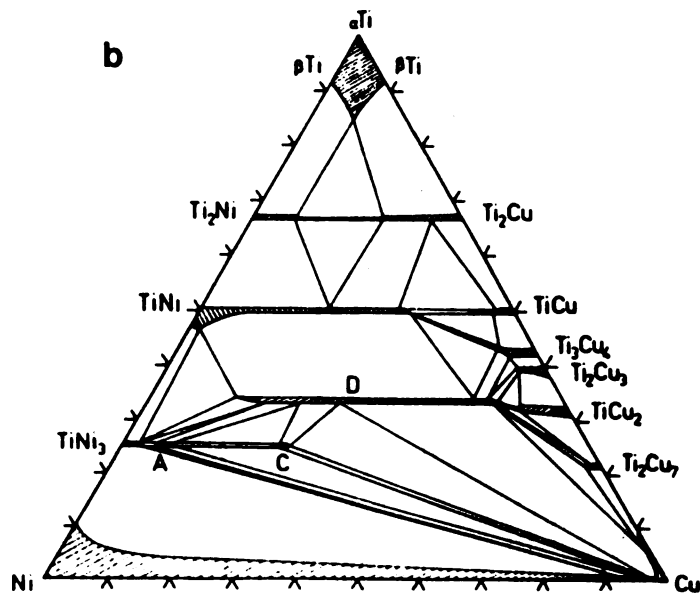
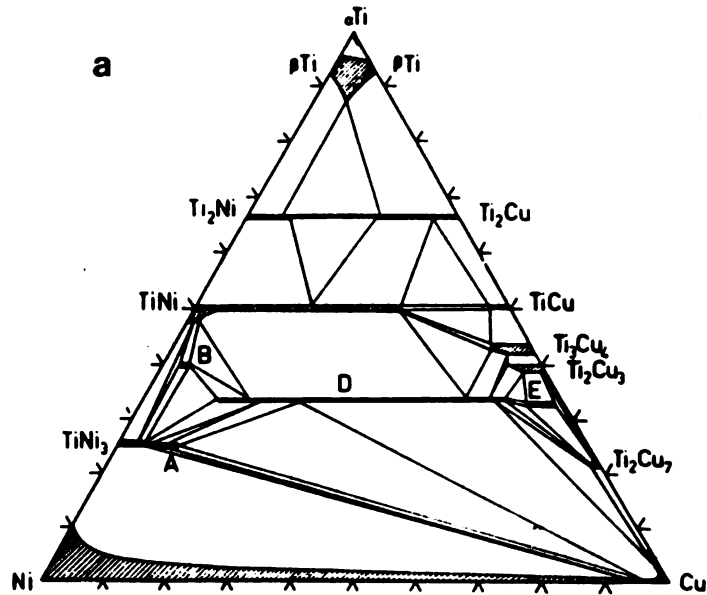


Figure 2-5: Isothermal cross sections through the Ti-Ni-Cu phase diagram (a) at 1073 K and (b) at 1143 K [44].

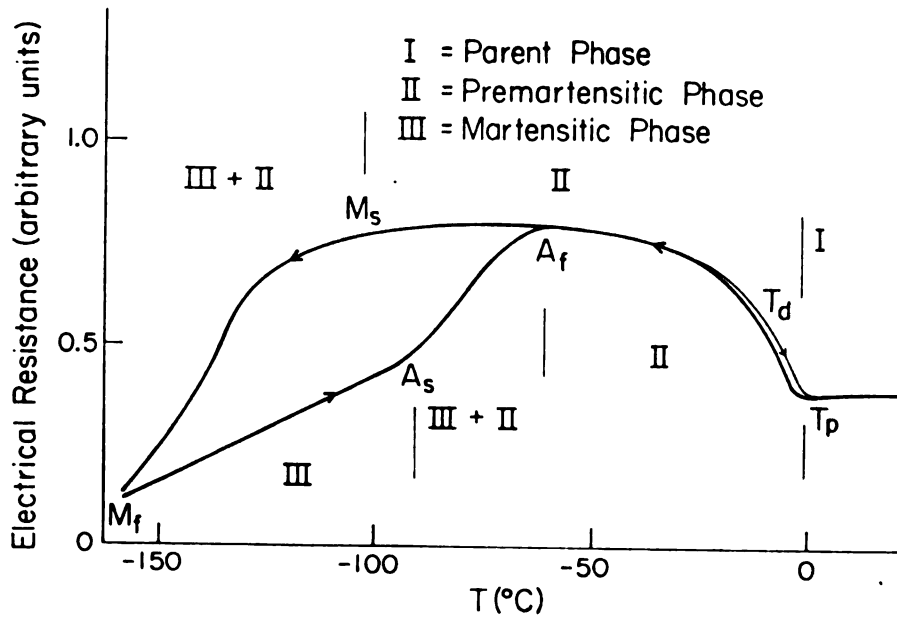


Figure 2-6: Electrical resistance as a function of temperature showing a two-step transformation in a TiNiFe alloy [50].

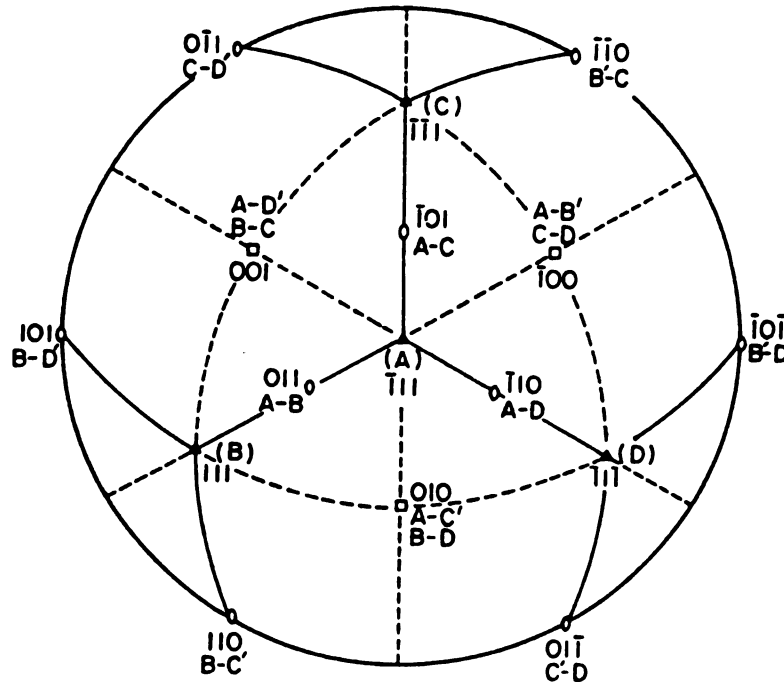


Figure 2-7:  $(\bar{1}11)B2$  stereographic projection showing R-phase variants A, B, C and D and twinning relations between them [53].

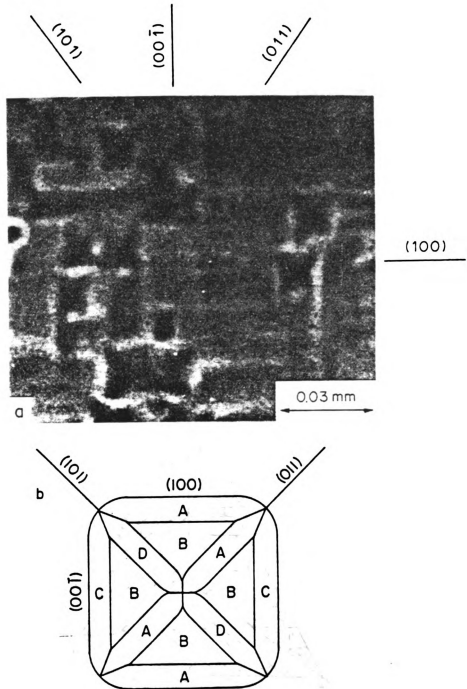


Figure 2-8: Self-accommodation morphology of R-phase (above) and corresponding schematic variant-combination (bottom) [53].

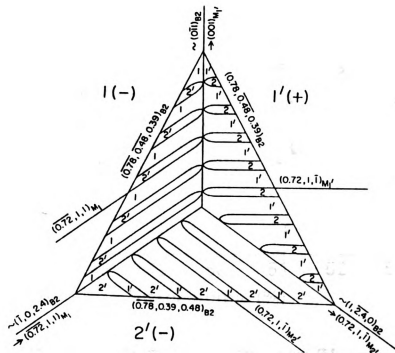
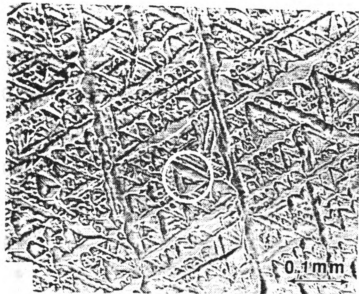


Figure 2-9: Self-accommodation morphology of monoclinic martensite (above), and a sub-micro model depicting crystallographic relationships between variants in the triangular morphology [23].

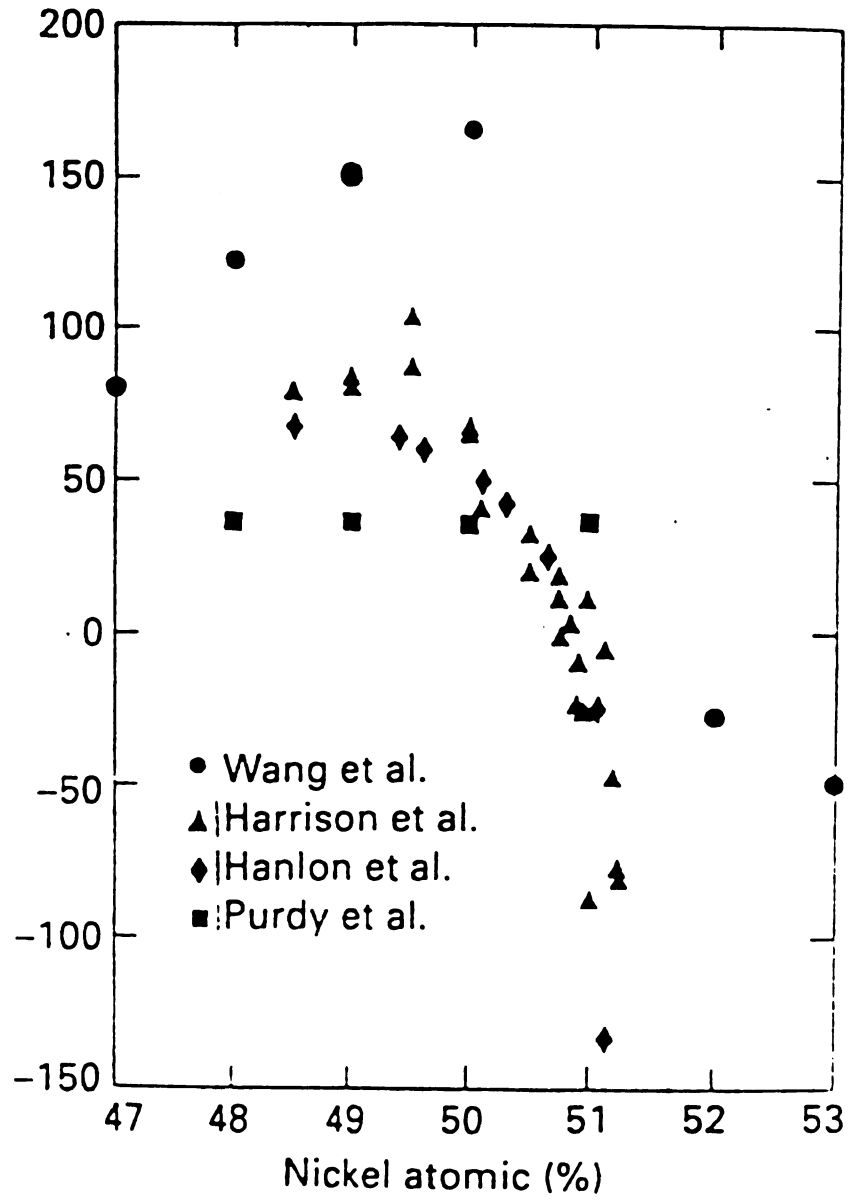


Figure 2-10: The dependence of the transformation temperature ( $M_s$ ) on titanium content in TiNi alloys [4].

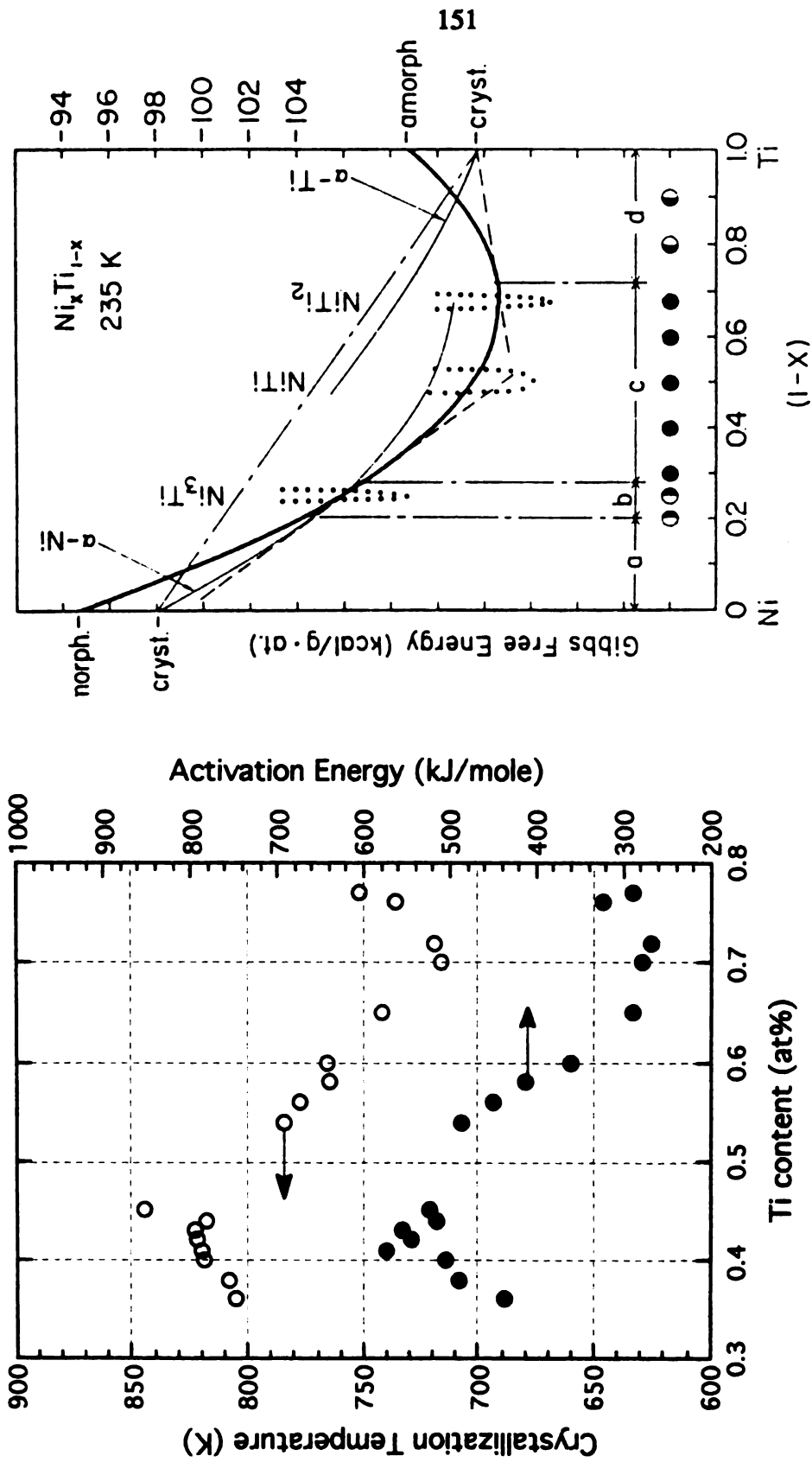


Figure 2-11: Composition dependence of the crystallization temperature and the activation energy for amorphous Ti-Ni alloys [75]. (left)

Figure 2-12: Theoretical calculation of the free energy diagram for Ti-Ni alloys at 235 K [78]. (right)

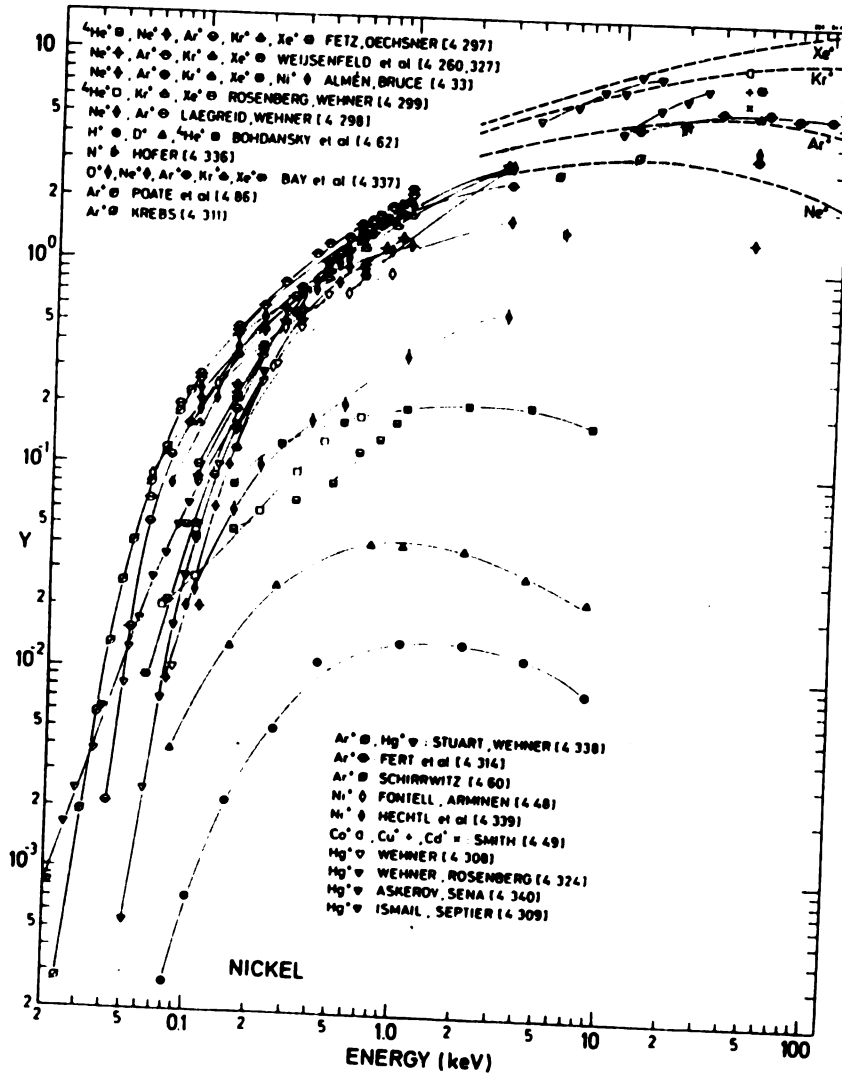


Figure 2-13: Sputtering yield of nickel as a function of ion energy and ion mass [84].

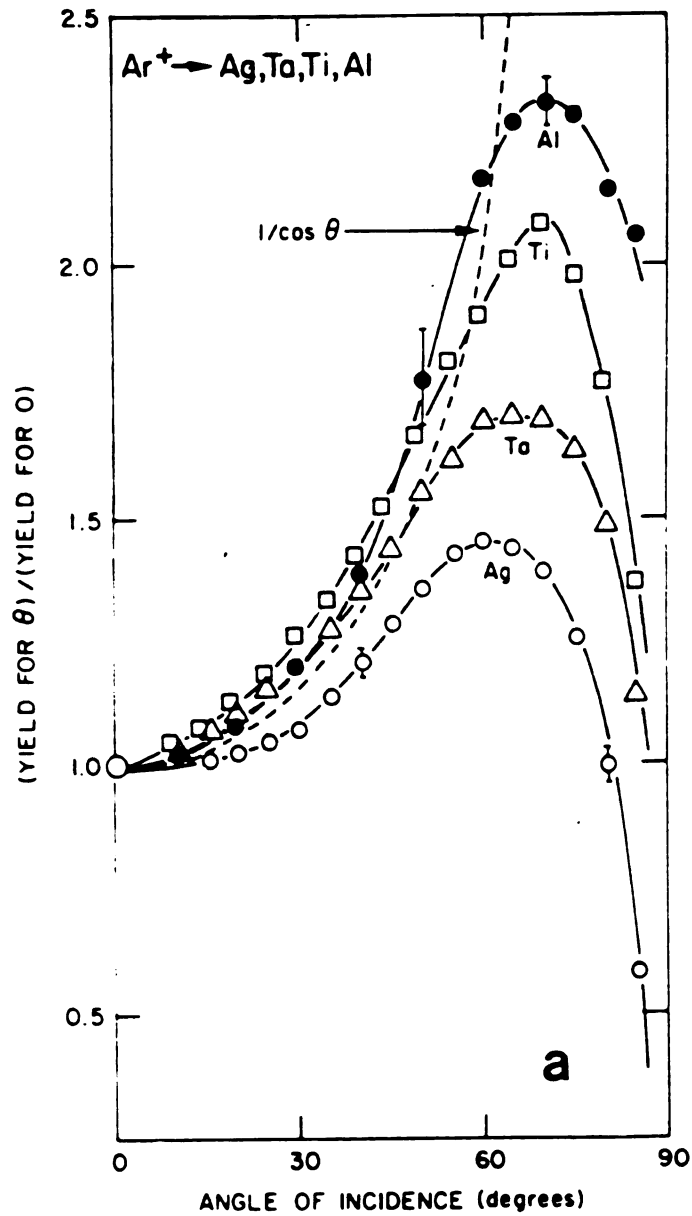
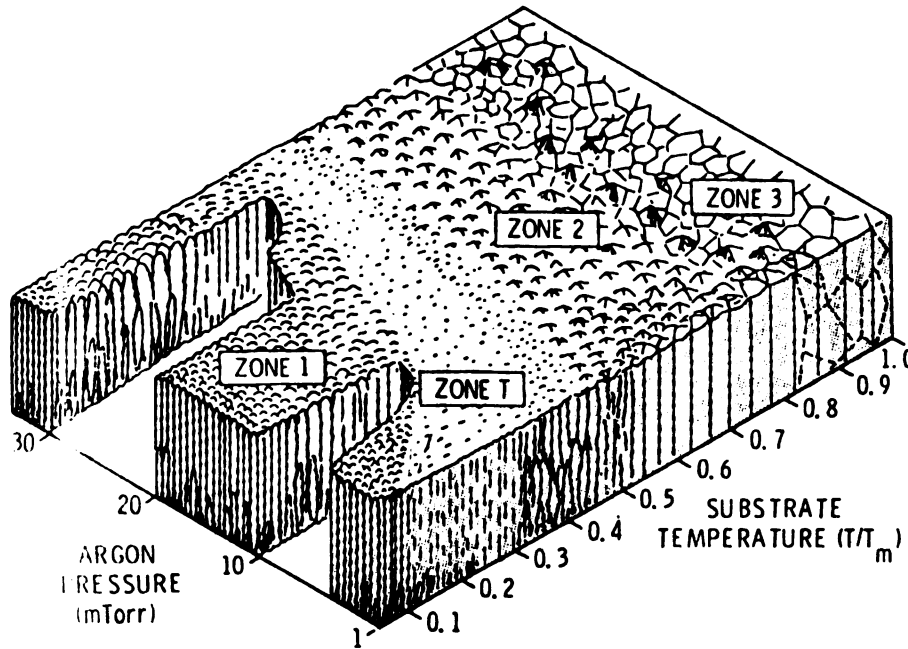


Figure 2-14: Variation of sputtering yield with angle of incidence for 1 keV Ar<sup>+</sup> incident on Ag, Ta, Ti and Al [85].



**Figure 2-15: Structure diagram for thick films produced by sputtering [87].**

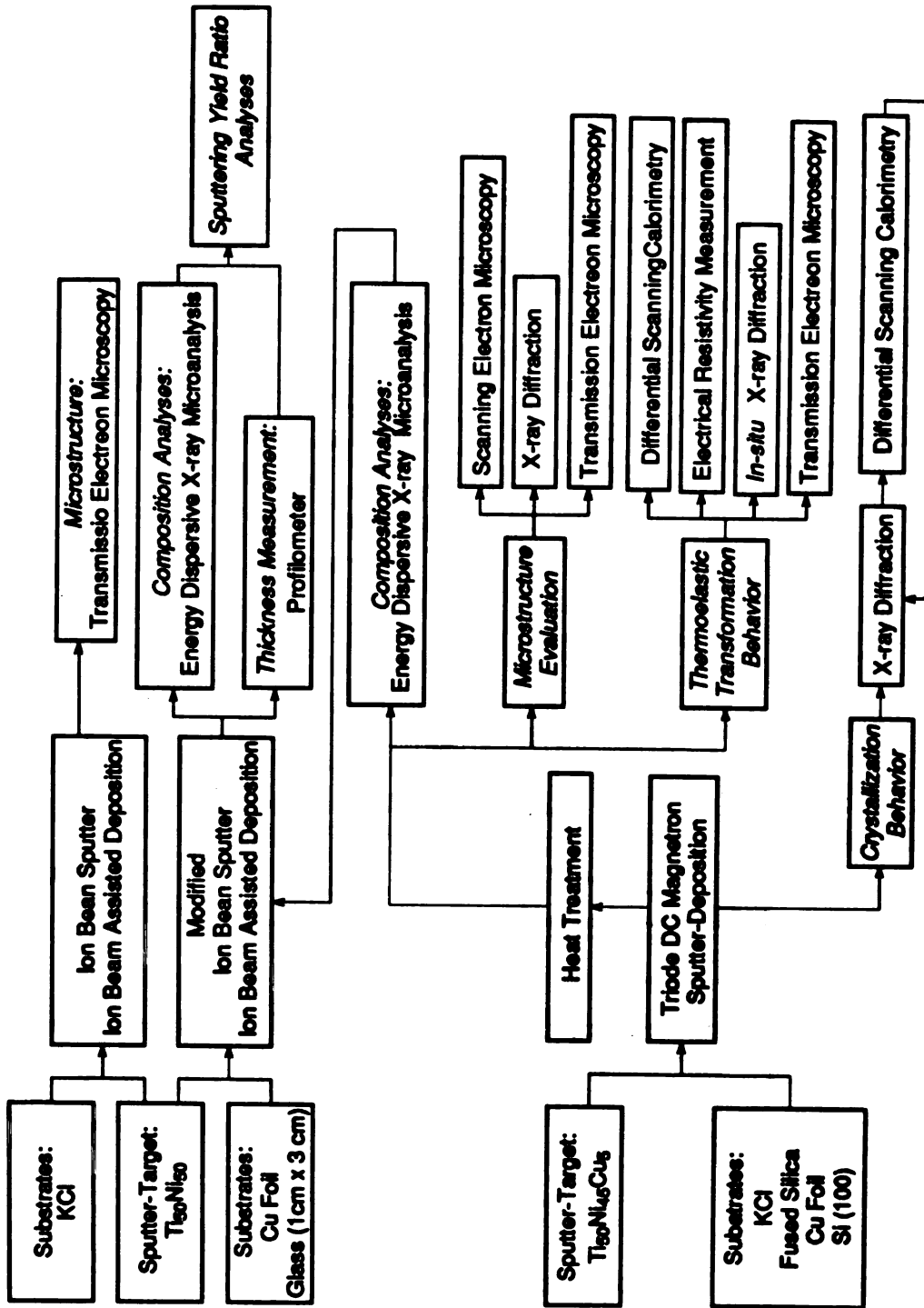


Figure 3-1: Flow chart summarizing the experimental methods used in the present study.

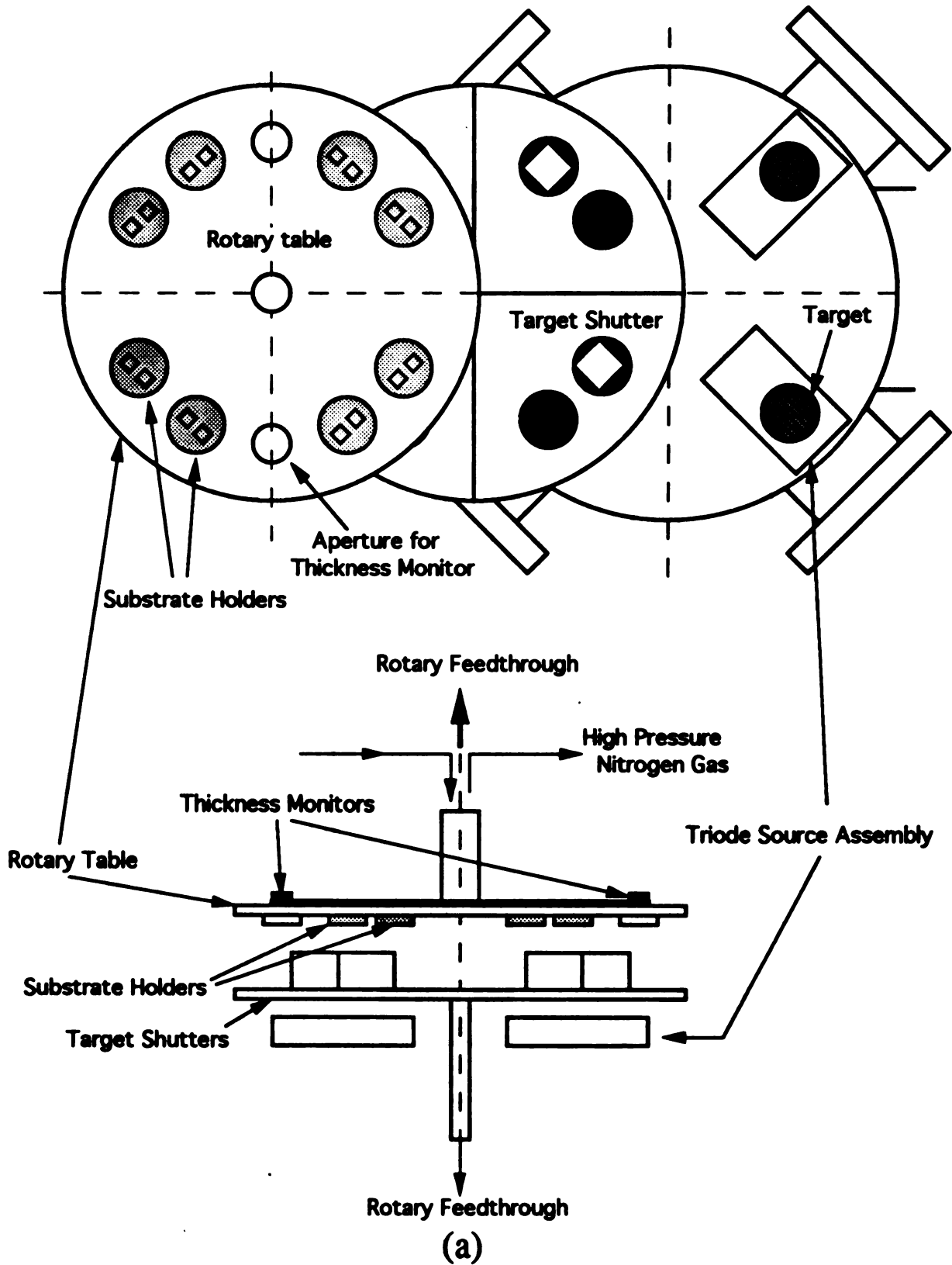
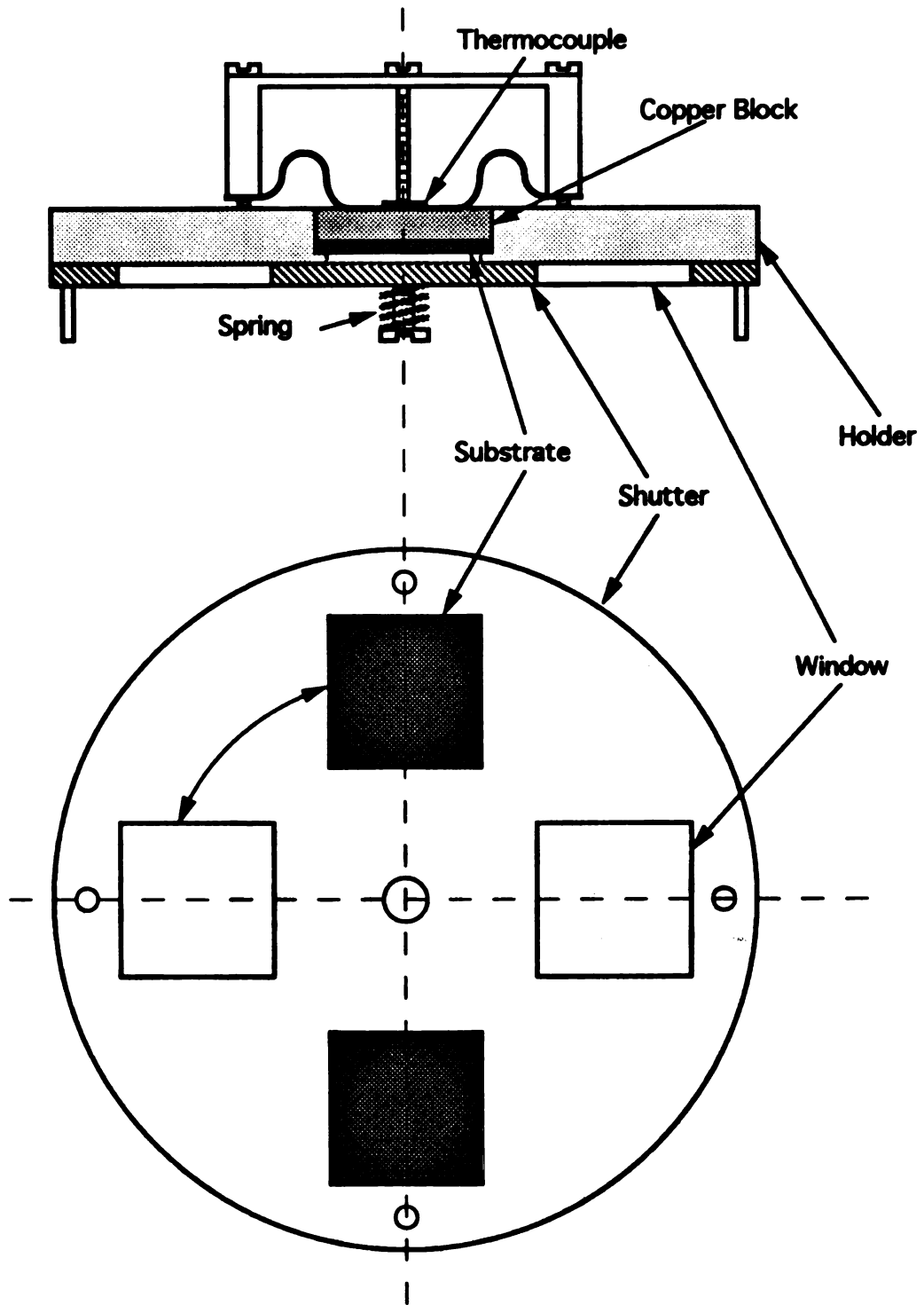


Figure 3-1 Schematic drawing of (a) the triode magnetron sputtering apparatus, and (b) the substrate holder assembly.



(b)

Figure 3-2 (cont'd)

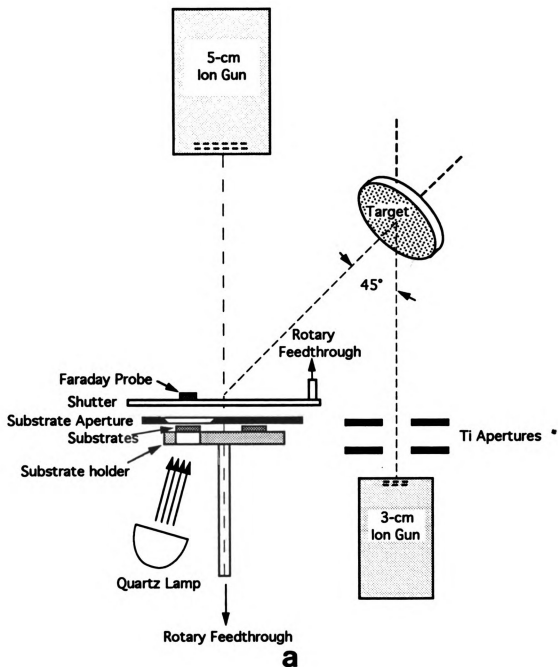


Figure 3-3: (a) Arrangement of the ion sources, the substrates and related devices for ion beam assisted deposition. The devices shown were contained in a 14" metal chamber. (b) Schematic drawing of the substrate holder.

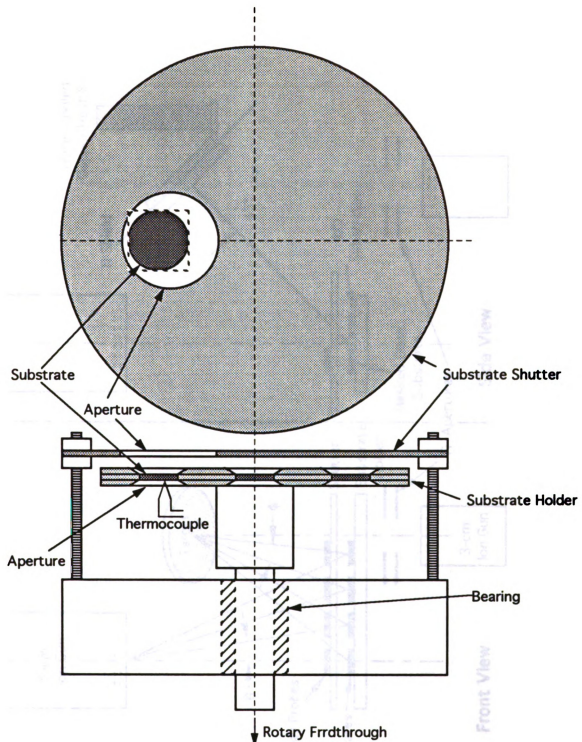
**b**

Figure 3-3 (cont'd)

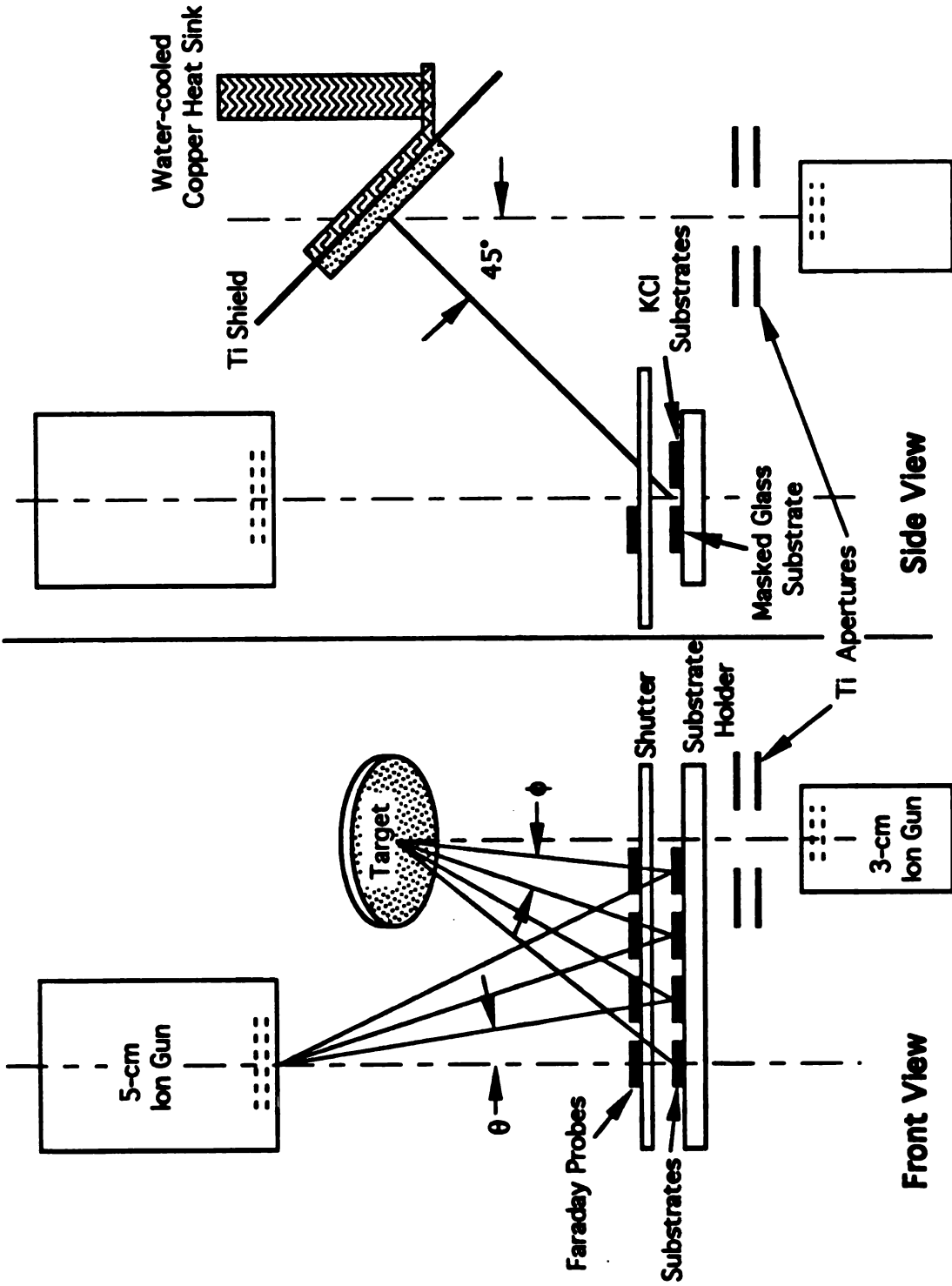
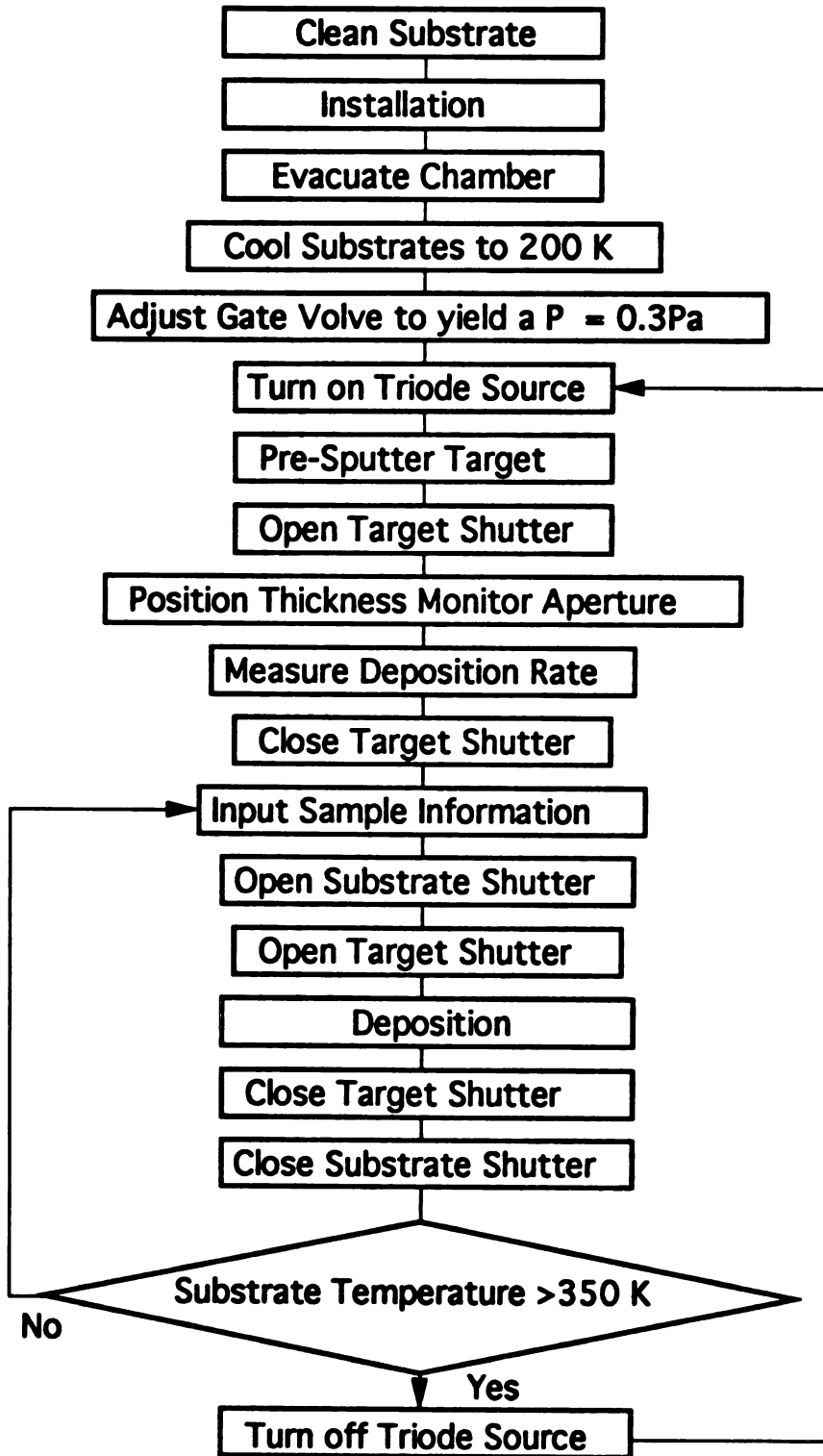
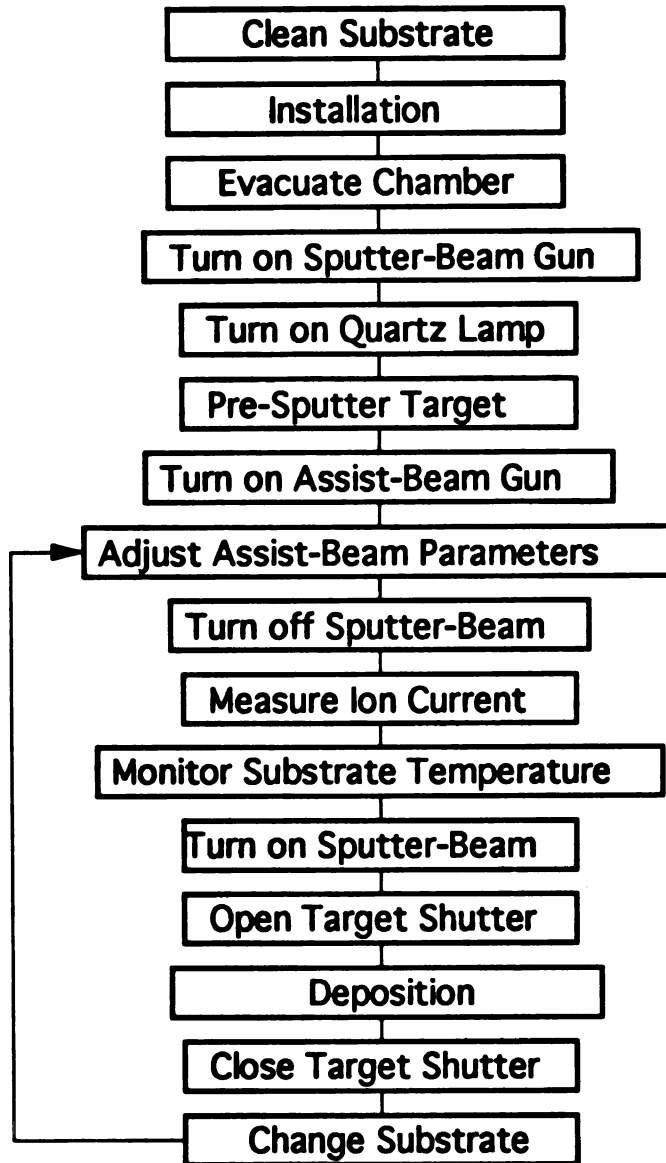


Figure 3-4. Modified arrangement of the ion sources, the target, the faraday probes and the substrates for ion beam assisted deposition.



(a)

Figure 3-5: Deposition procedures for (a) triode magnetron sputter-deposition and (b) ion beam assisted deposition.



(b)

Figure 3-5 (cont'd)

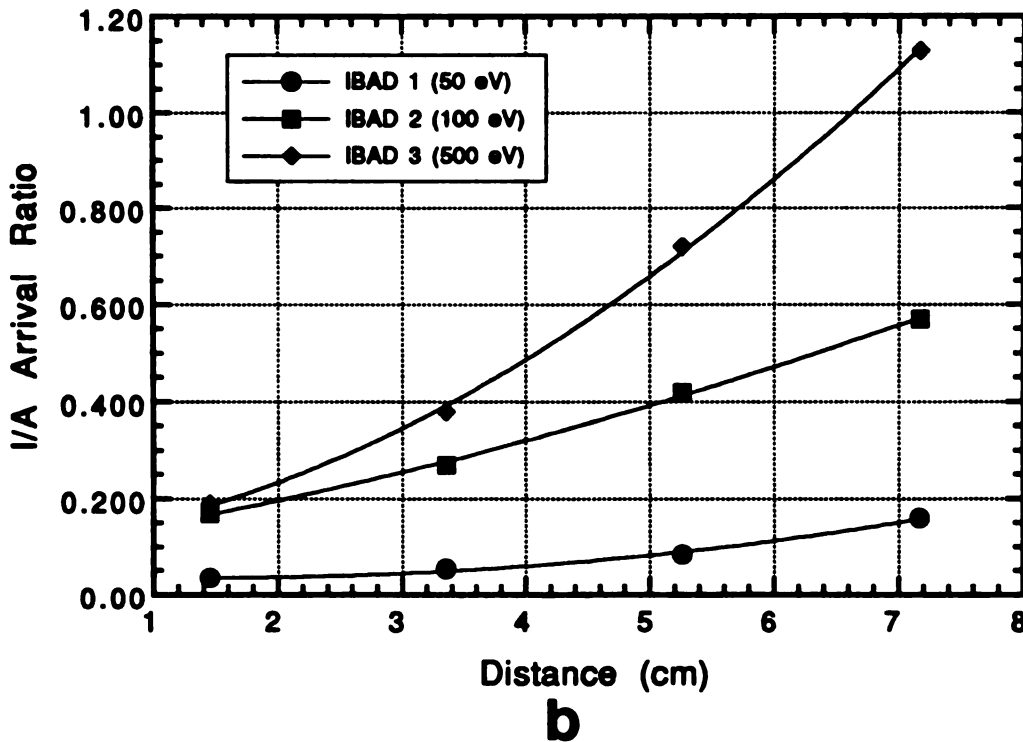
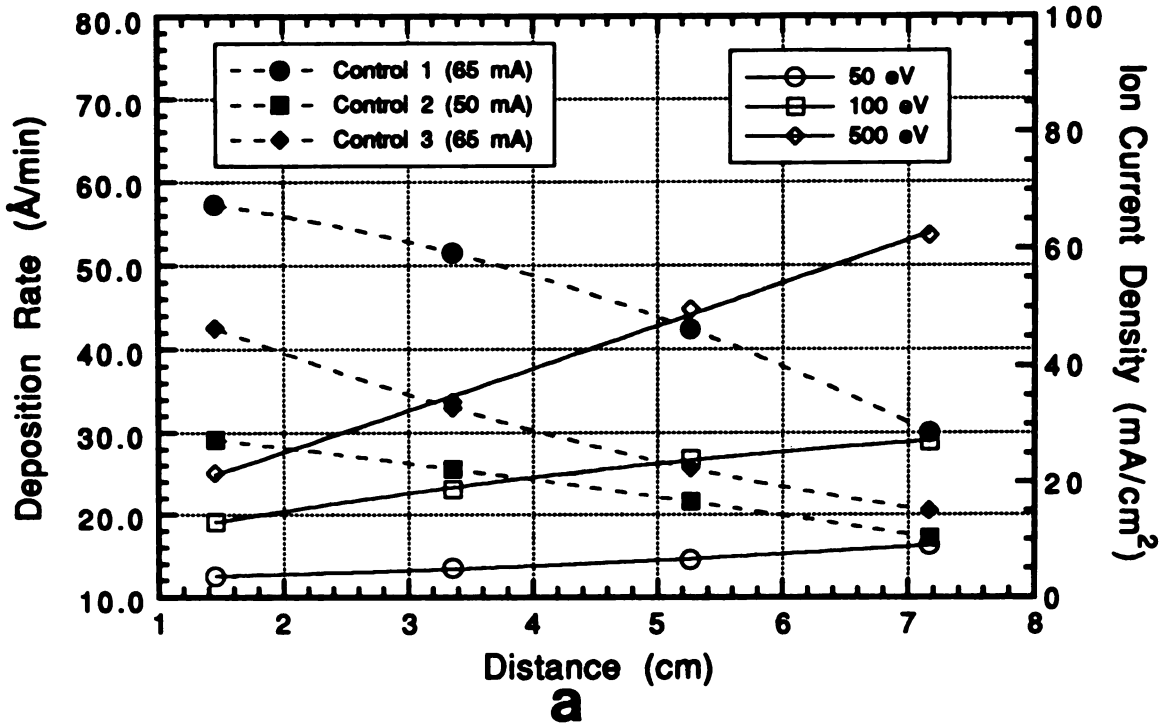


Figure 3-6: (a) Deposition rates and ion current densities and (b) I/A ratios plotted as a function of the lateral displacement of the specimen from the sputtering target centerline.

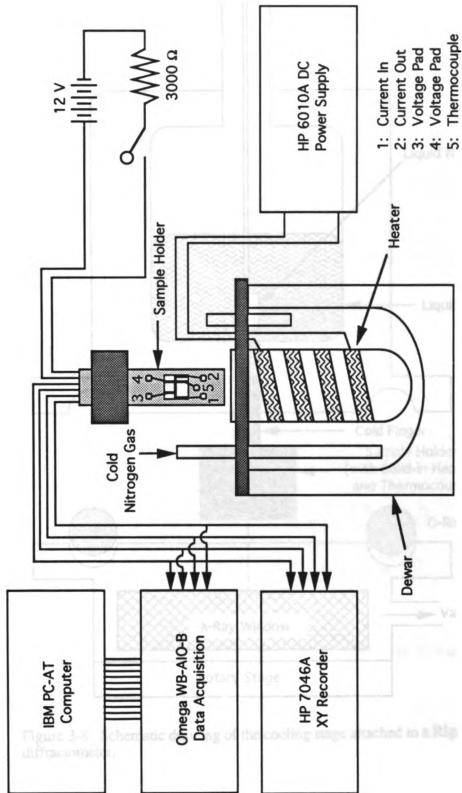
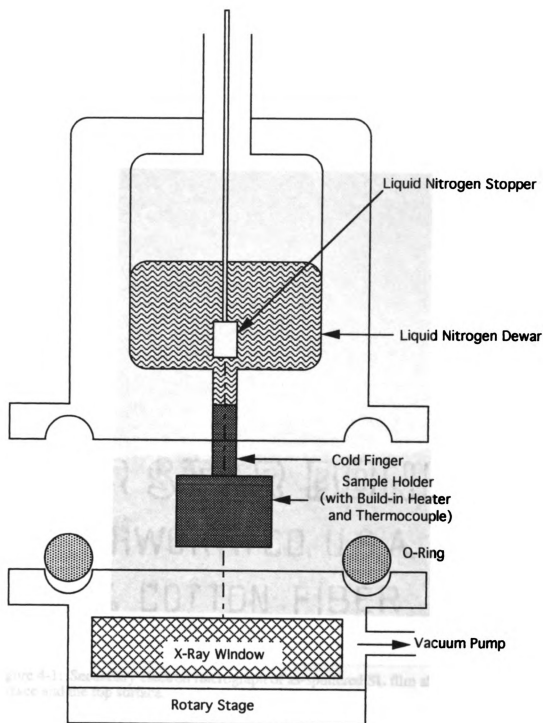


Figure 3-7. Schematic drawing of the electrical resistivity measurement apparatus.



**Figure 3-8:** Schematic drawing of the cooling stage attached to a Rigaku X-ray diffractometer.

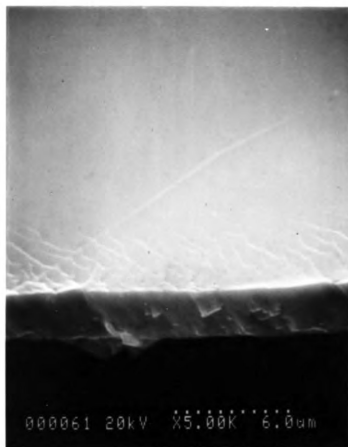
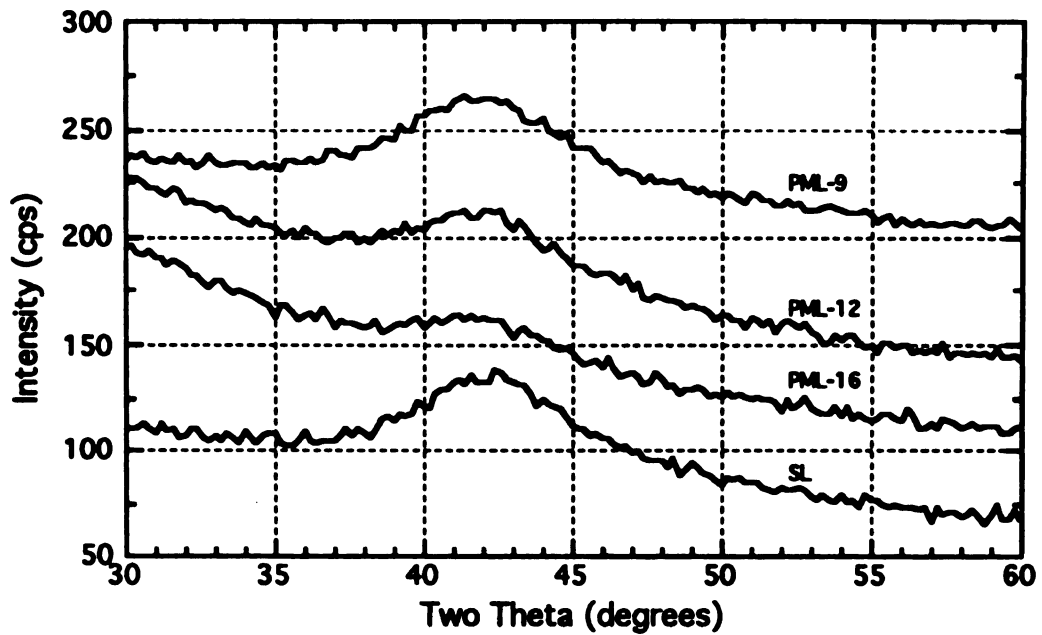


Figure 4-1: Secondary electron micrograph of as-sputtered SL film showing the fracture surface and the top surface.



**Figure 4-2: X-ray diffraction patterns of as-sputtered SL, PML-9, PML-12, and PML-16 films showing a broad first-order peak belonging to the amorphous phase.**

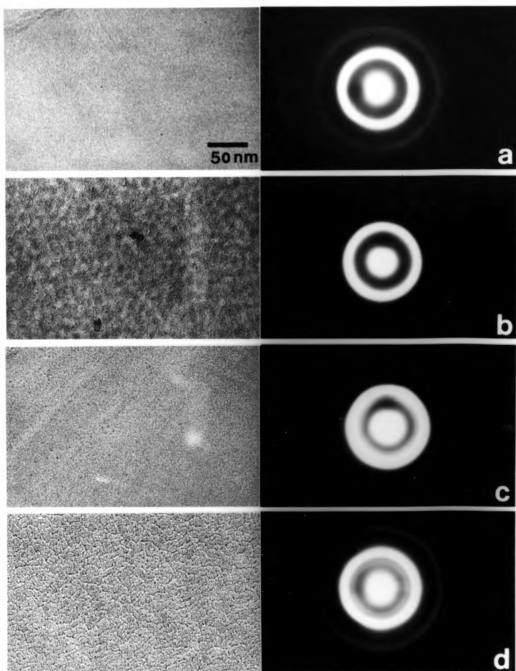


Figure 4-3: TEM results for Ti-Ni thin films: (a) ion-sputtered at  $T_{\text{sub}}=373$  K; (b) IBAD with  $I/A=0.33$ ,  $T_{\text{sub}}=383$  K; (c) IBAD with  $I/A=0.60$ ,  $T_{\text{sub}}=423$  K; (d) IBAD with  $I/A=0.81$ ,  $T_{\text{sub}}=403$  K.

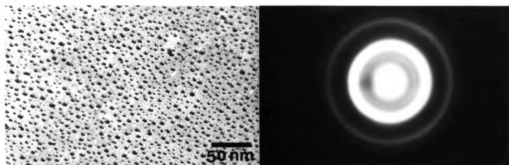


Figure 4-4: IBAF film irradiated with a 500 eV assist-beam and 1.08 I/A ratio, showing extensive argon gas incorporation.

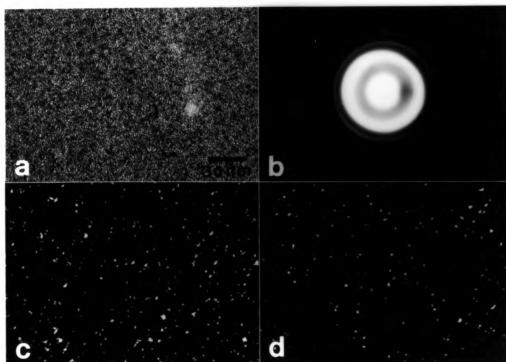


Figure 4-5: IBAF with  $I/A=0.33$ ,  $T_{\text{sub}}=473$  K: (a) bright field image; (b) diffraction pattern; (c) dark field image formed with innermost diffraction ring and (d) dark field image formed with third diffraction ring.

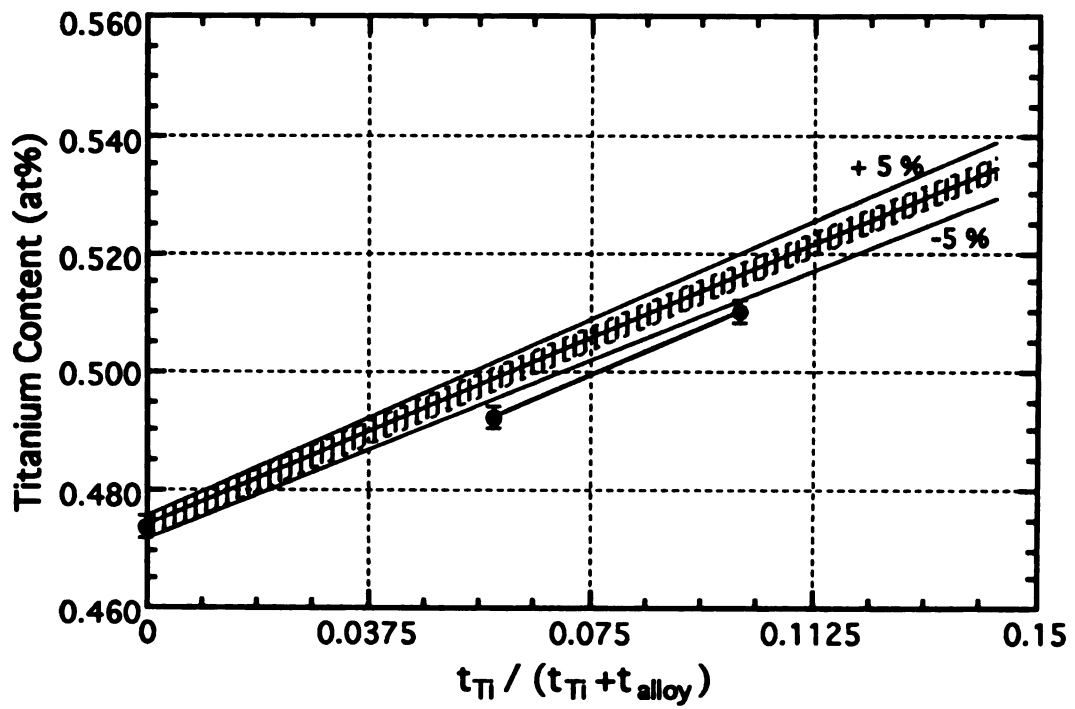


Figure 4-6: Comparison between the calculated composition and the measured composition of PML films.

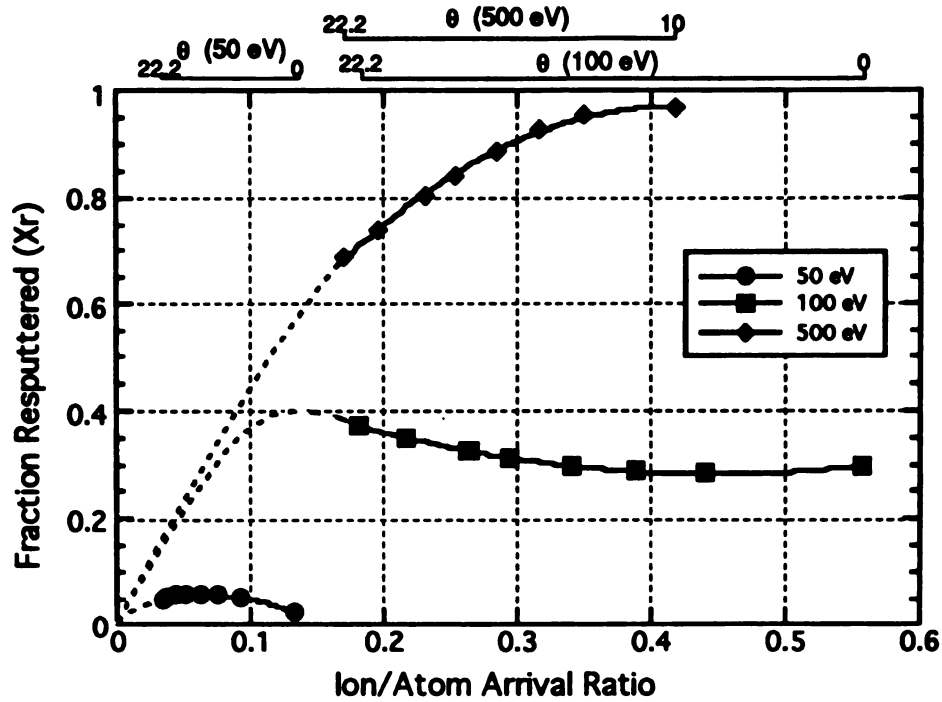


Figure 4-7: The total fraction of the film resputtered by a 50, 100 and 500 eV assist-beam as a function of I/A ratio.

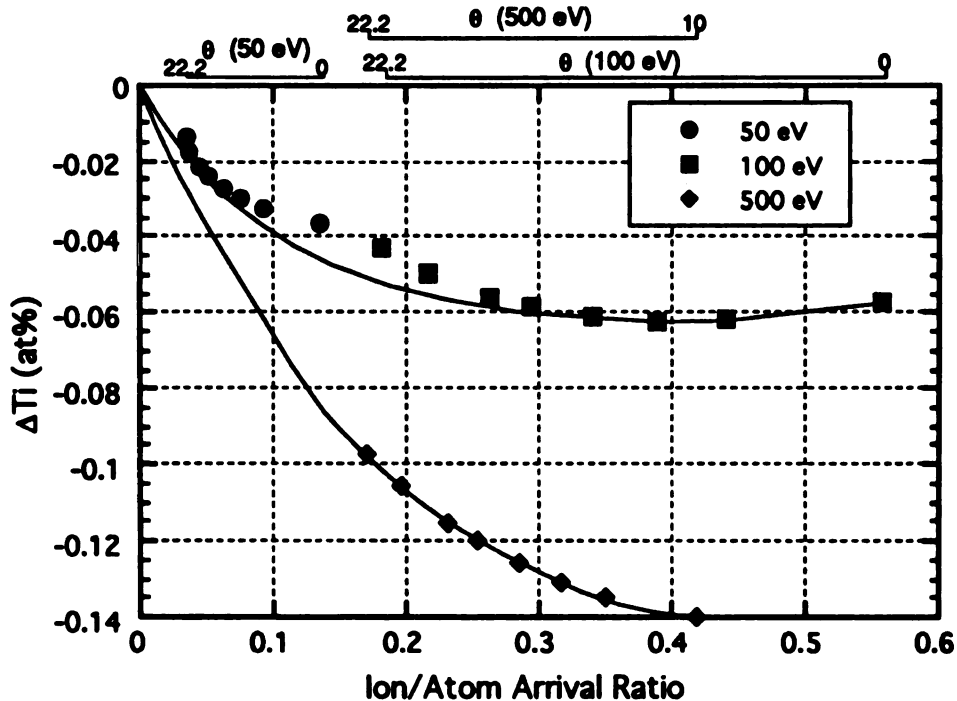


Figure 4-8: The change of titanium concentration of the IBAD processed Ti-Ni films as a function of I/A ratio, relative to the expected composition of the film in the absence of an assist-beam. Data are shown for 50, 100 and 500 eV beam.

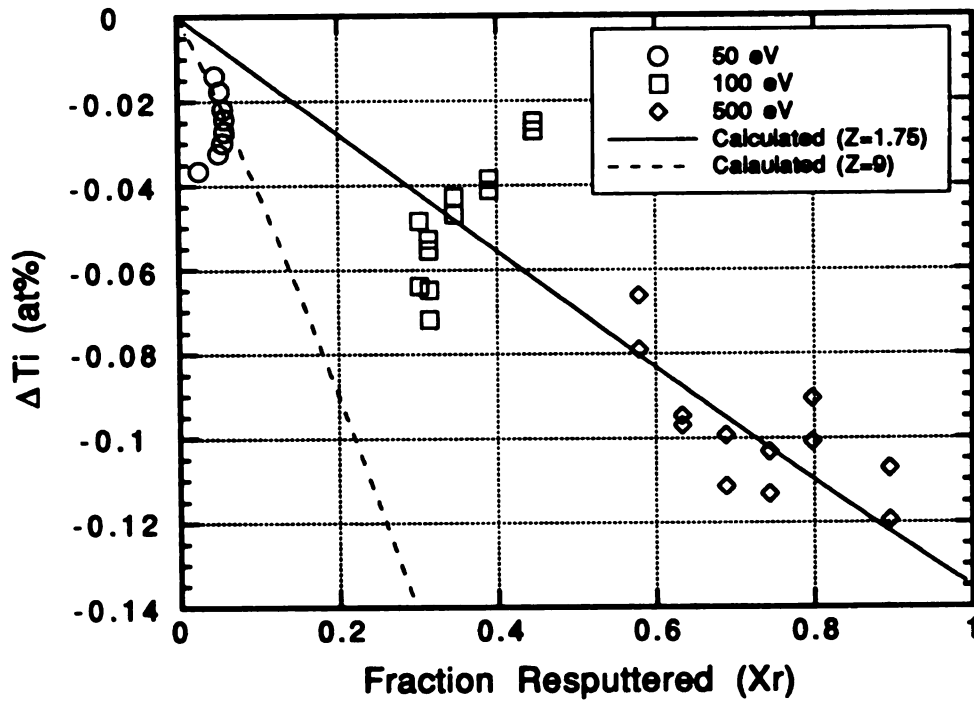


Figure 4-9: The change in titanium content for IBAD processed Ti-Ni films as a function of the total fraction of the film resputtered by the assist-beam, relative to the expected composition of the film in the absence of an assist-beam. Data are shown for 50, 100 and 500 eV beams.

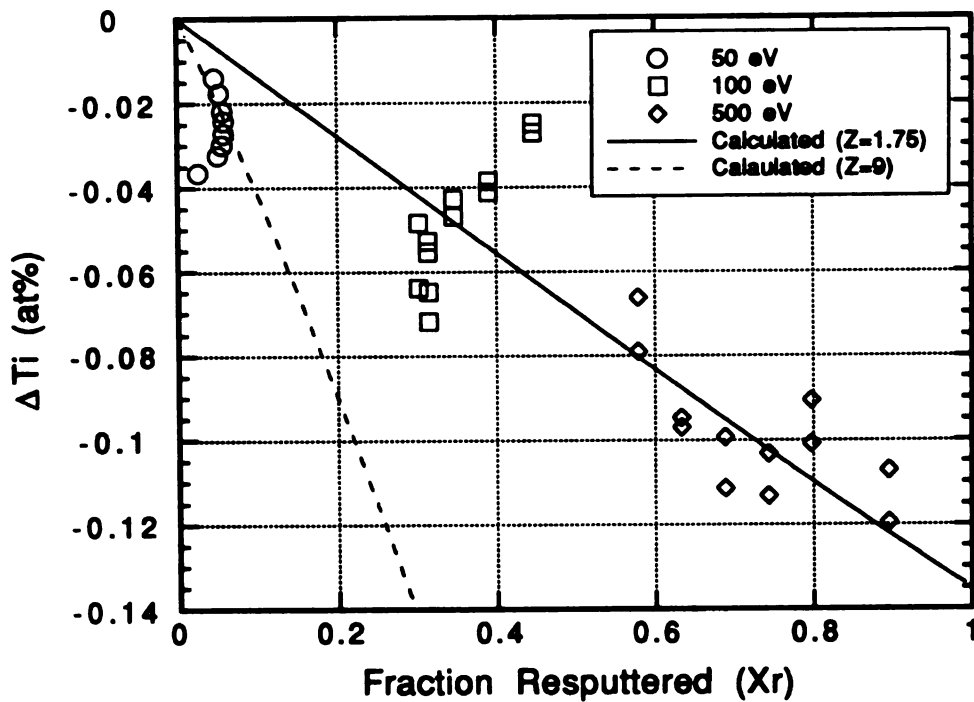


Figure 4-9: The change in titanium content for IBAD processed Ti-Ni films as a function of the total fraction of the film resputtered by the assist-beam, relative to the expected composition of the film in the absence of an assist-beam. Data are shown for 50, 100 and 500 eV beams.

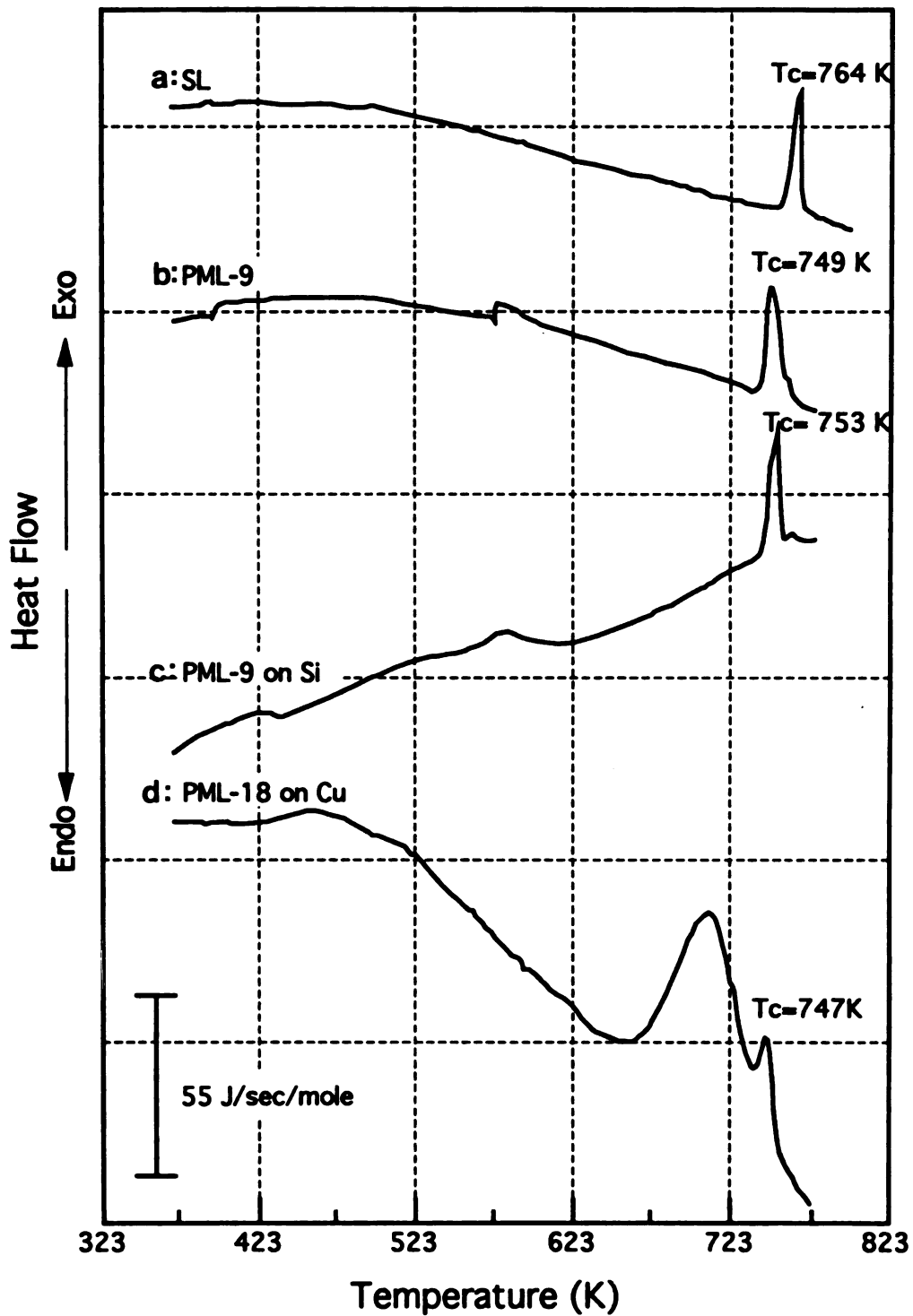


Figure 4-10: Differential scanning calorimetry data: (a) free-standing SL film; (b) free-standing PML-9 film; (c) PML-9 film on Si (100) substrate and (d) PML-18 film on Cu substrate at a heating rate of 10 K/min.

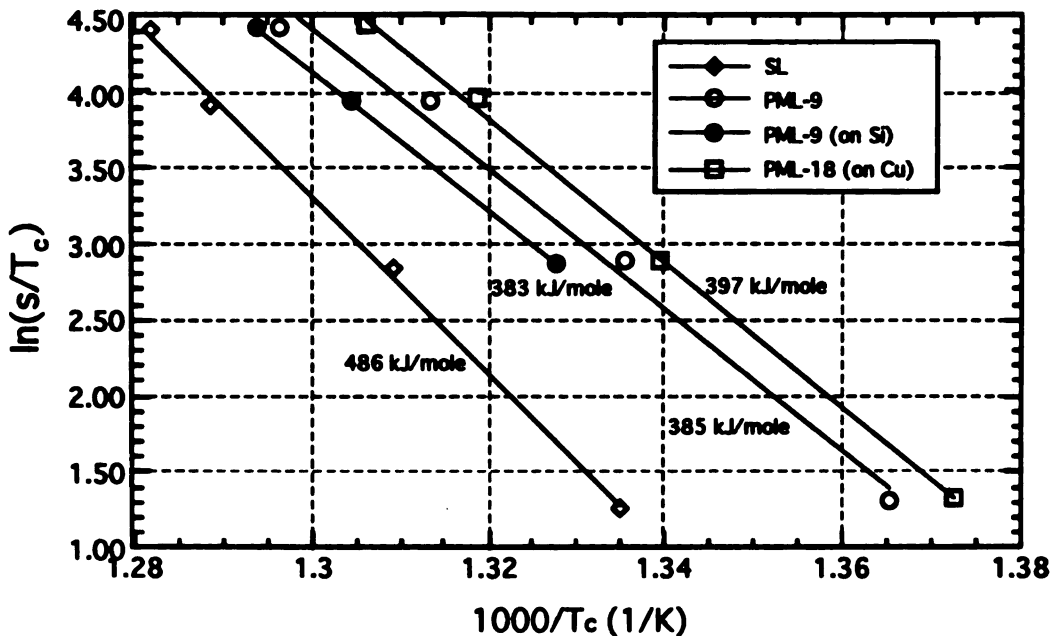


Figure 4-11: Plot of  $\ln(s/T_c^2)$  versus the inverse of crystallization temperature yielding the activation energies of crystallization for a number of magnetron sputter-deposited films.

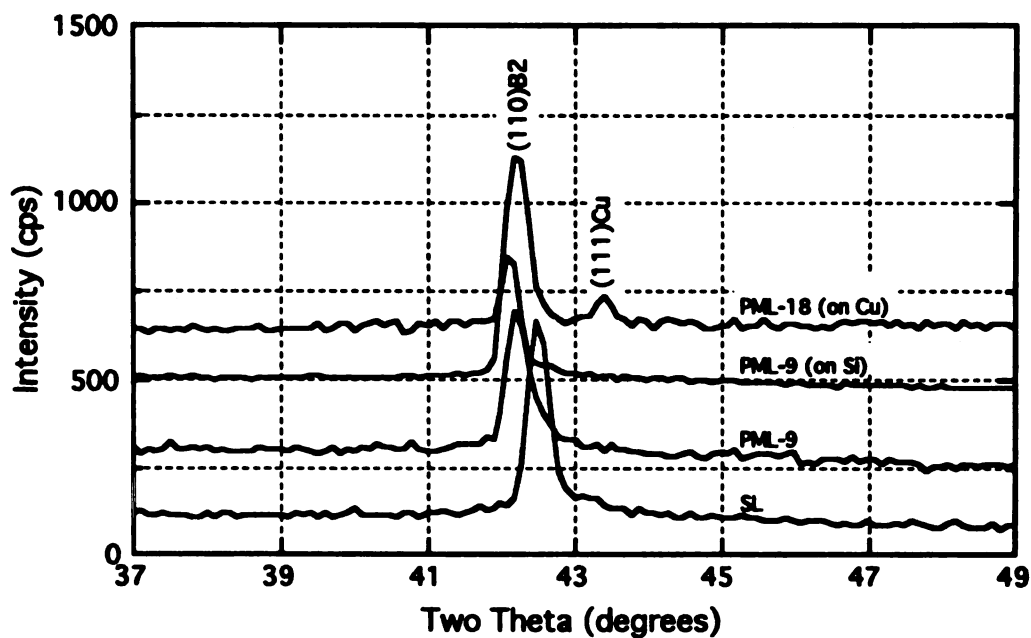


Figure 4-12: X-ray diffraction patterns of a number of magnetron sputter-deposited films after an isotropic anneal in the DSC cell.

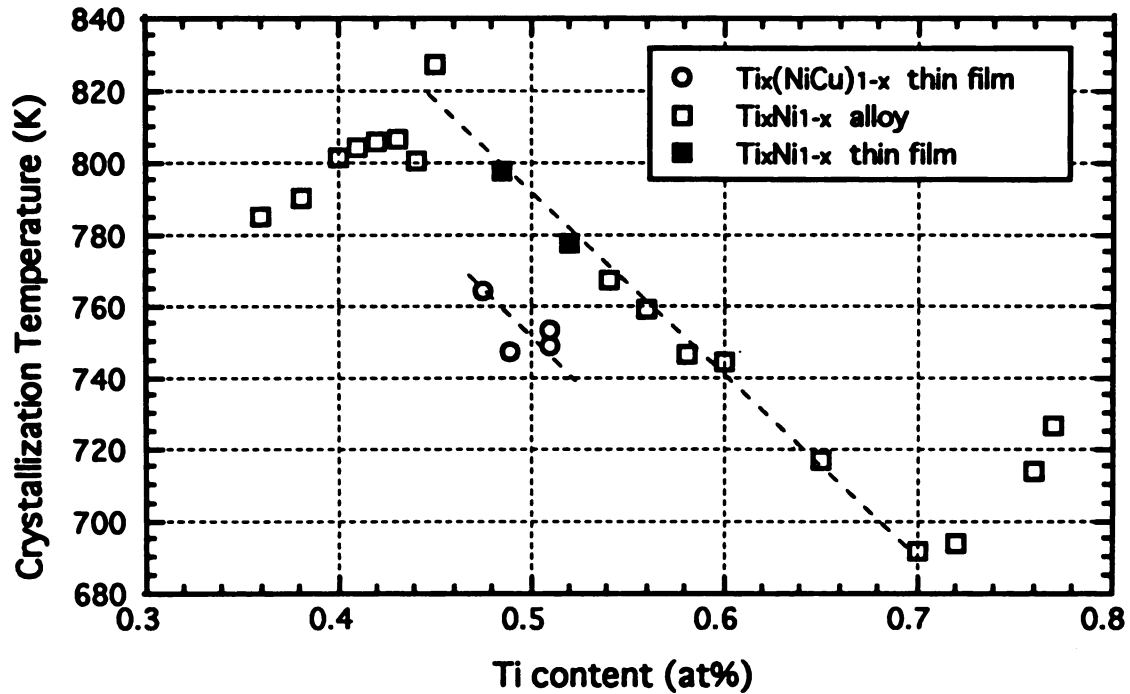


Figure 4-13: Comparison of the crystallization temperatures of ion sputter-deposited and magnetron sputter-deposited films, and melt-quenched ribbons. (Both ion sputter-deposited films and ribbons are binary Ti-Ni alloys.)

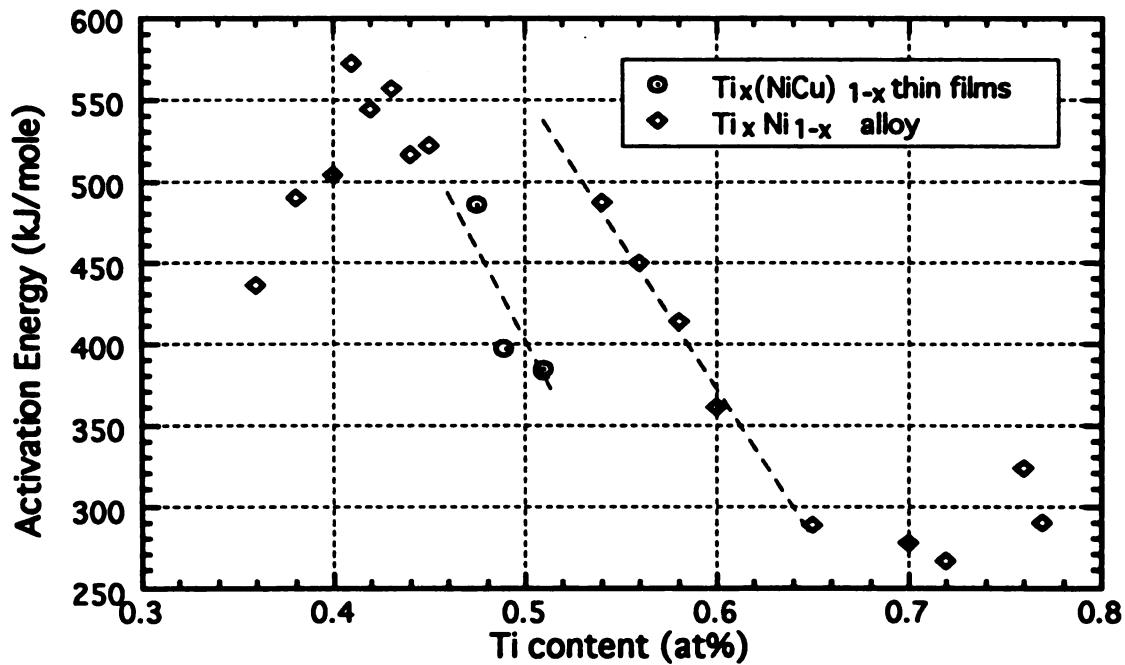


Figure 4-14: Comparison of the activation energies of crystallization of magnetron sputter-deposited films and melt-quenched ribbons.

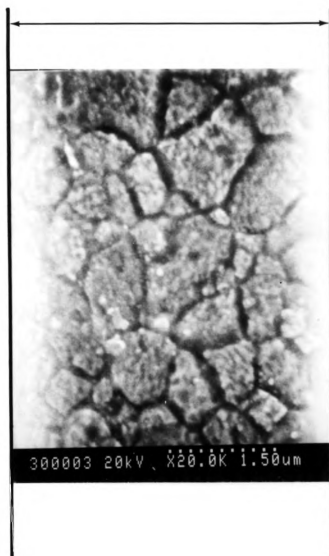


Figure 4-15: Cross-section secondary electron micrograph for the SL film annealed at 923 K for one hour showing grain size and grain morphology.

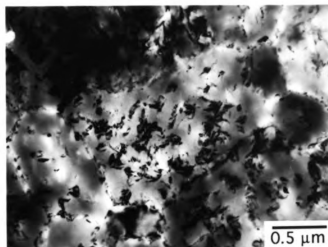


Figure 4-16: In-plane TEM micrograph for the SL film annealed at 923 K for one hour showing grain size and microstructure.

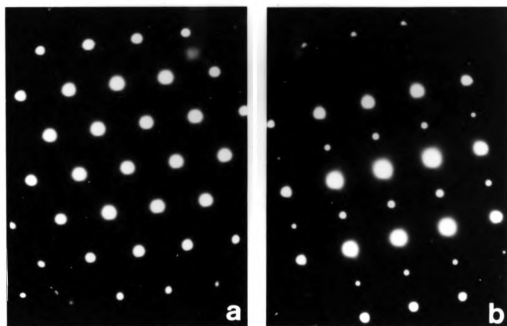


Figure 4-17: Electron diffraction patterns acquired from the matrix phase of the 923 K annealed SL films at room temperature in (a)  $\langle 111 \rangle_{B_2}$  and (b)  $\langle 110 \rangle_{B_2}$  zone axes showing streaks in  $\langle 110 \rangle$  and  $\langle 112 \rangle$  reciprocal directions respectively.

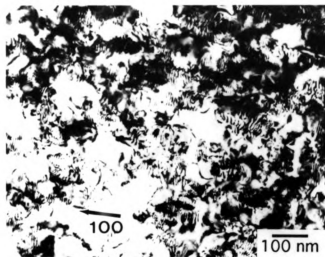


Figure 4-18: A room temperature bright field image of the SL film annealed at 923 K for one hour showing small precipitates with distorted Moiré fringes roughly perpendicular to the [100] B2 direction.

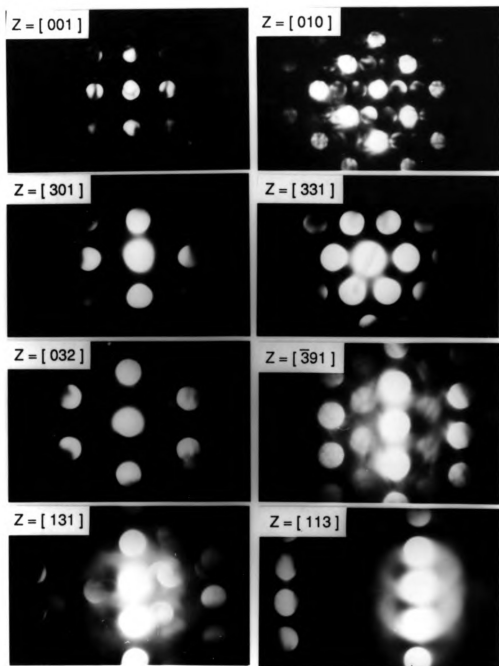


Figure 4-19: Convergent beam diffraction patterns taken from small precipitates in a 923 K annealed SL film. A tetragonal cell with  $a = 0.31$  nm and  $c = 0.80$  nm is evident from the diffraction patterns and the rotation angles between them.

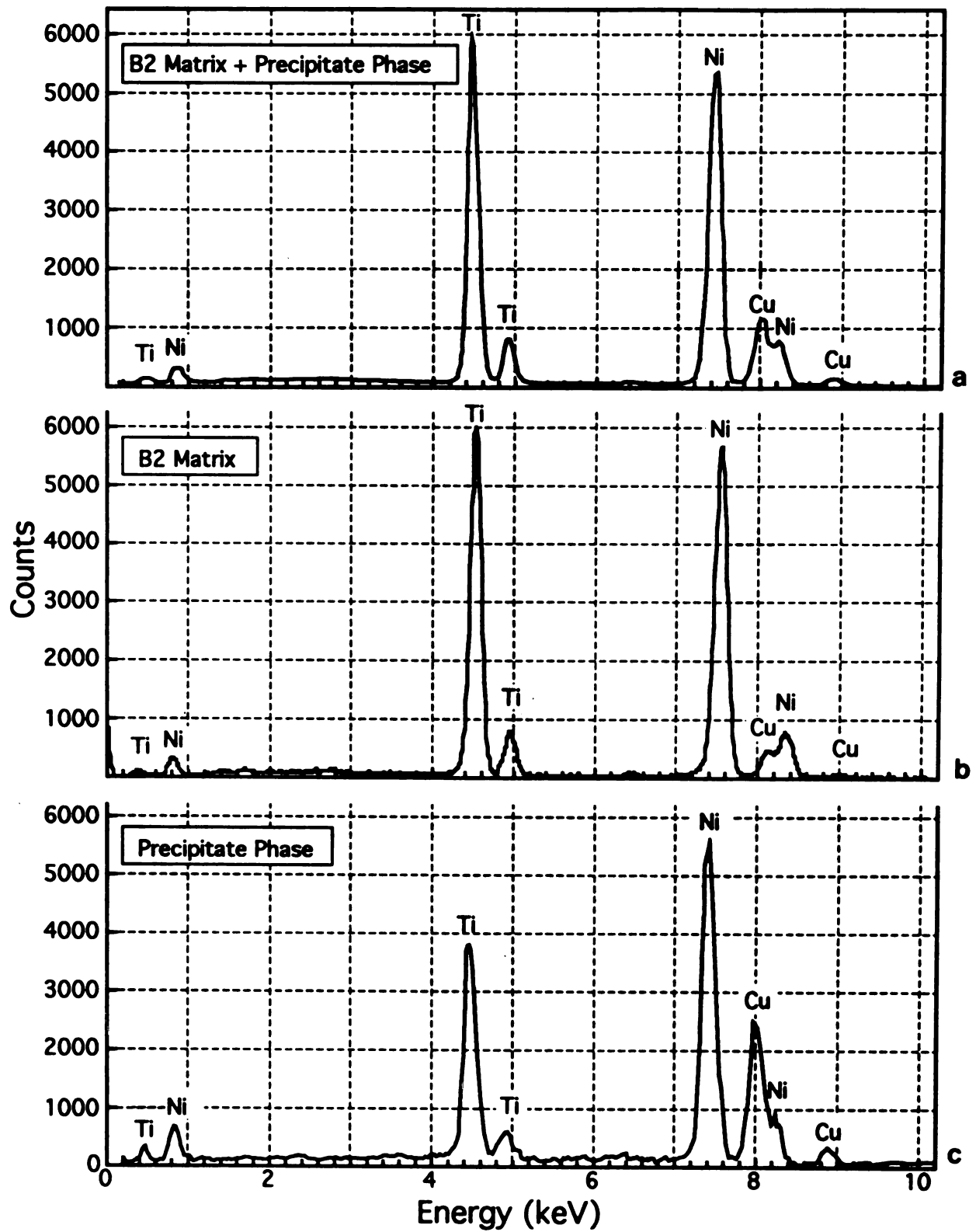


Figure 4-20: Energy dispersive X-ray fluorescence spectra of matrix and precipitates of a SL film annealed at 923 K for four hour.

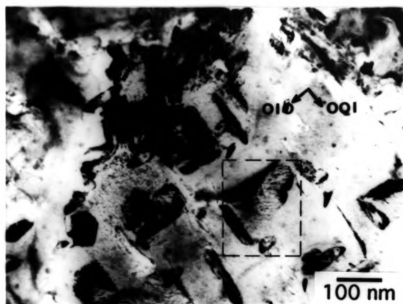


Figure 4-21: A bright field micrograph of the  $(\text{NiCu})_2\text{Ti}$  precipitates taken almost parallel to  $\langle 100 \rangle_{\text{B2}}$  direction showing the morphology and habit plane of the precipitates. The misfit dislocation network (see enclosed rectangular area) lies on the (001) precipitates interface.

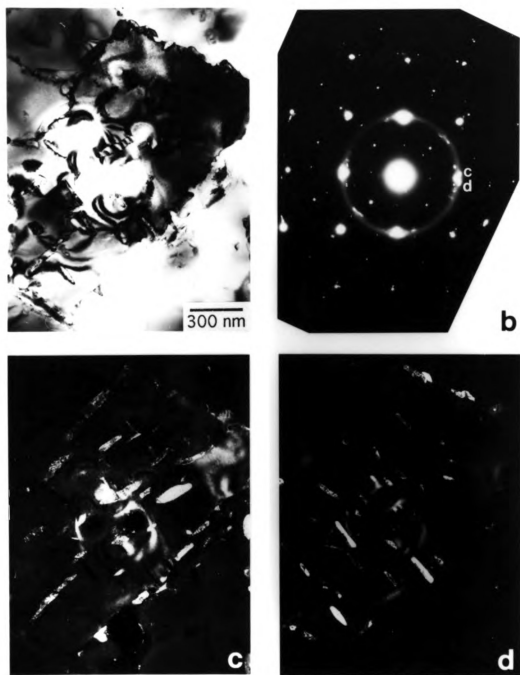


Figure 4-22: (a) Bright field micrograph of the annealed SL film showing three precipitate variants in matrix; (b) corresponding diffraction pattern showing [100] and [010]  $(\text{NiCu})_2\text{Ti}$  zone axes parallel to  $\langle 100 \rangle_{\text{B}_2}$ , and (c-d) dark field images taken from spot c and d in (b) respectively.

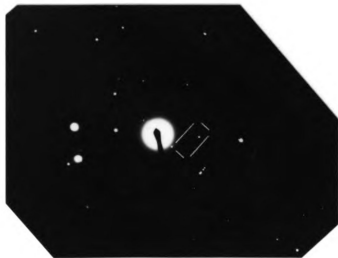
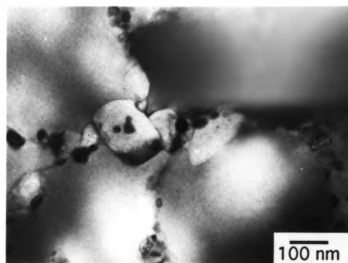


Figure 4-23: A bright field image of the annealed SL film showing grain boundary precipitates. The associated diffraction pattern is in an  $\langle 112 \rangle$  zone axis of  $\text{Ti}_2\text{Ni}$  phase.

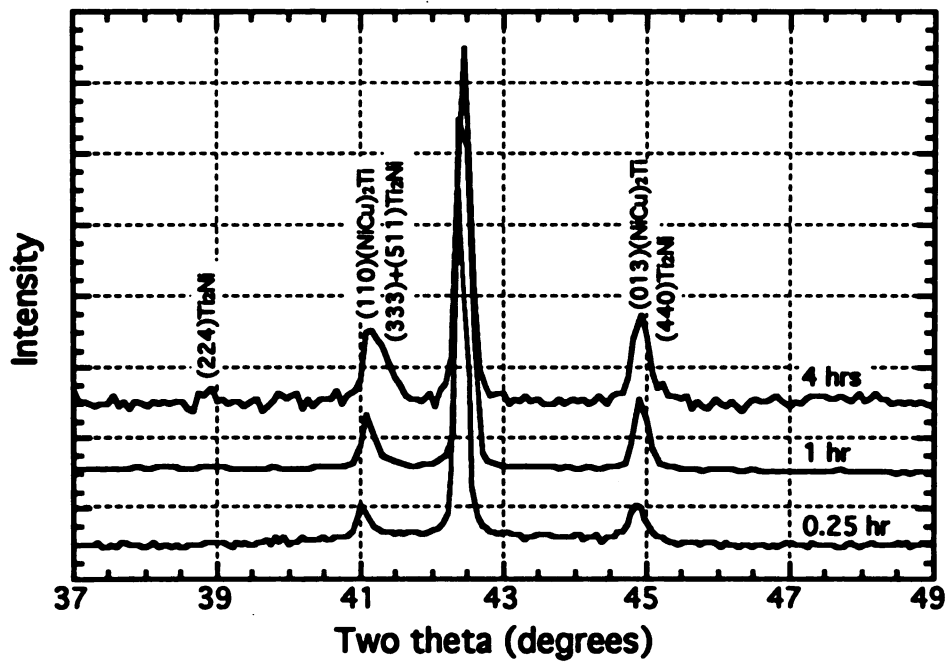


Figure 4-24: X-ray diffraction patterns of the SL films annealed at 923 K for (a) 0.25 hour; (b) 1 hour; and (c) 4 hours.

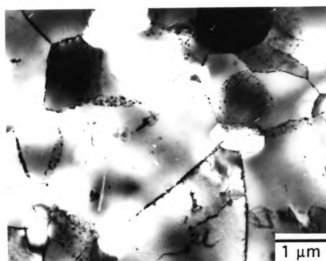


Figure 4-25: Electron micrograph showing the grain size and microstructure of a PML-16 film annealed at 923 K for one hour .

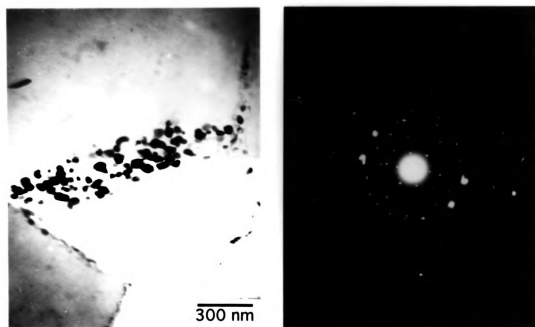


Figure 4-26: Electron micrograph of the grain boundary precipitates for a PML-16 film annealed at 923 K for one hour. The associated diffraction pattern is in an  $\langle 110 \rangle$  zone axis of  $\text{Ti}_2\text{Ni}$  phase.

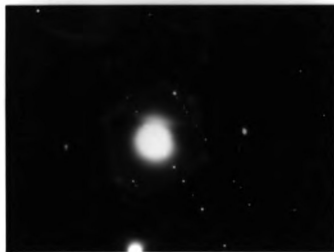
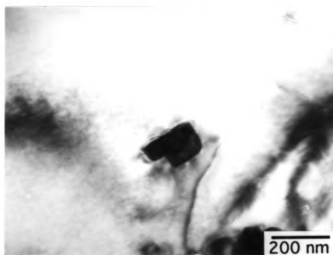


Figure 4-27: Electron micrograph of a PML-16 film annealed at 923 K for one hour showing  $\text{Ti}_2\text{Ni}$  precipitates observed in the grain interior. The associated diffraction pattern corresponds to two (111) twin-related  $\langle 123 \rangle$  zones of  $\text{Ti}_2\text{Ni}$  phase.



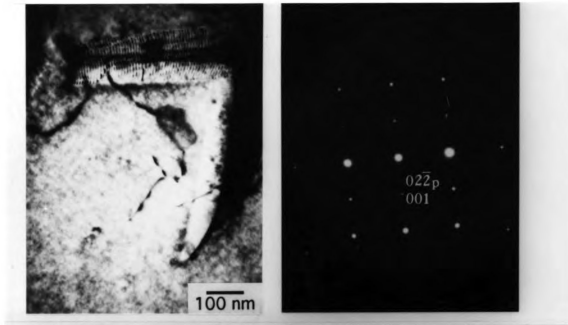


Figure 4-28: Electron micrograph of a PML-16 film annealed at 923 K for one hour showing blade-like precipitates. The corresponding diffraction patterns are in an  $\langle 110 \rangle_{B2}$  zone axis and a  $[011]$  precipitate zone axis, indexed using an orthorhombic unit cell with  $a = 0.441$  nm,  $b = 0.882$  nm and  $c = 1.35$  nm.

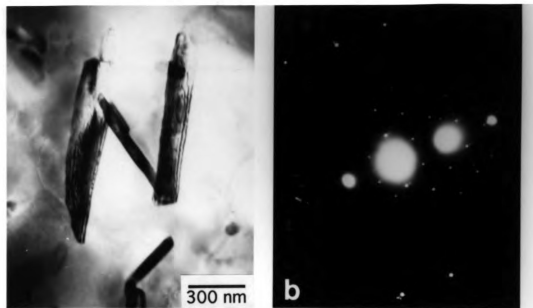


Figure 4-29: (a) Bright field micrograph of a PML-16 film annealed at 923 K for one hour showing misfit dislocations lying on the interface of  $Ni_3Ti_2$  type precipitates. (b) The corresponding diffraction pattern, taken from a rod-like precipitate located between two  $Ni_3Ti_2$  particles, corresponds to an  $\langle 110 \rangle$  zone axis of  $Ti_2Ni$  phase.

Figure 4-30: X-ray diffraction spectra for the PML-16 films annealed at 923 K for (a) 5 minutes; (b) 1 hour and (c) 6 hours.

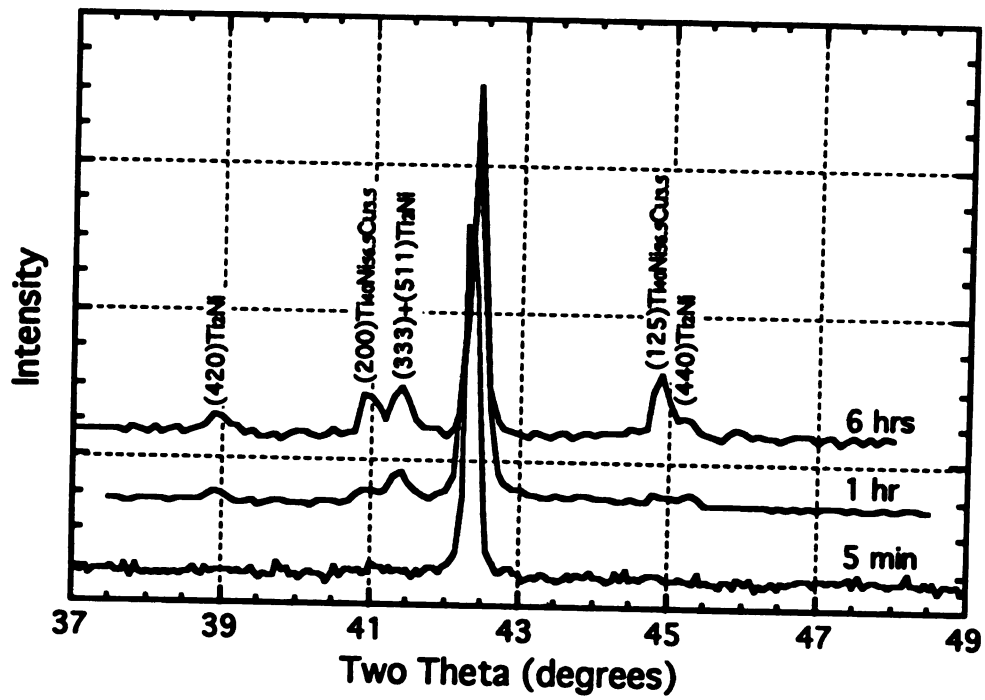


Figure 4-30: X-ray diffraction spectra for the PML-16 films annealed at 923 K for (a) 5 minutes; (b) 1 hour and (c) 6 hours.

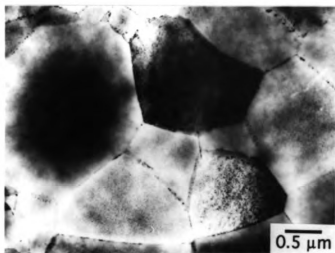


Figure 4-31: Electron micrograph of a PML-9 film annealed at 923 K for one hour showing the grain size and microstructure.

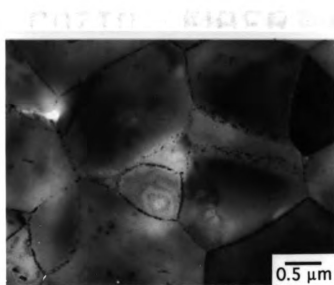


Figure 4-32: Electron micrograph of a PML-9 film annealed at 823 K for one hour showing the grain size and microstructure.

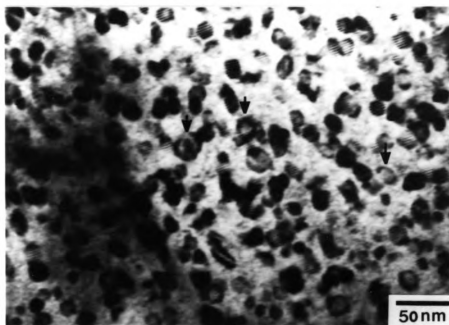


Figure 4-33: Bright field micrograph of a PML-9 film annealed at 923 K for one hour showing the size and morphology of second phase particles in the grain interiors.

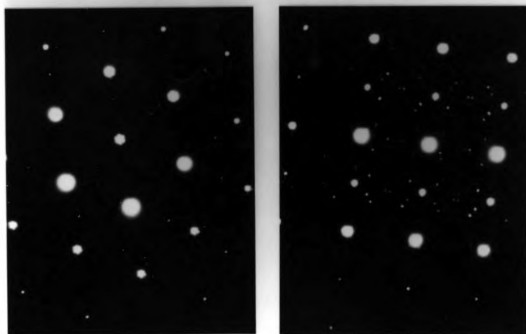


Figure 4-34: Selected area diffraction patterns in (a)  $[110]_{B_2}$  and (b)  $[111]_{B_2}$  zone axes showing that the precipitates have an fcc unit cell with  $a = 1.132$  nm with  $(100)_{\text{precipitate}} // (100)_{B_2}$  and  $[010]_{\text{precipitate}} // [010]_{B_2}$ .

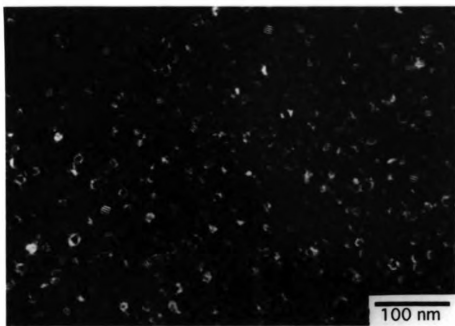


Figure 4-35: 3 g dark field electron micrograph showing strain contrast around the precipitates.

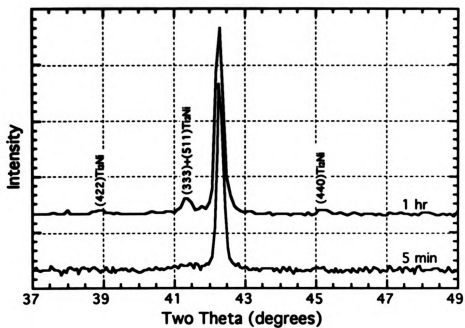


Figure 4-36: X-ray diffraction spectra for the PML-9 films annealed at 923 K for (a) 5 minutes and (b) one hour.

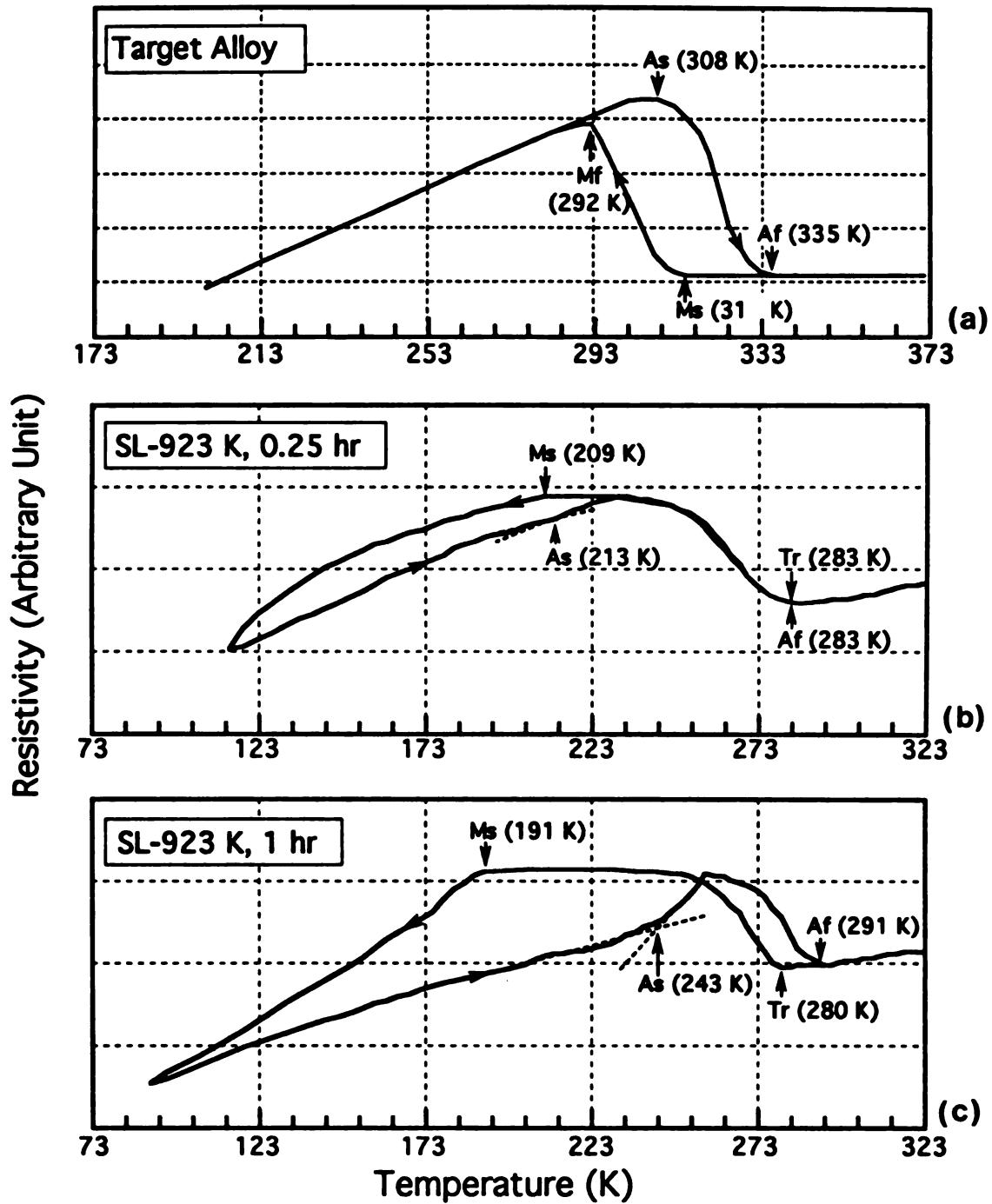


Figure 4-37: Electrical resistivity as a function of temperature for (a) the target alloy, (b) the SL film annealed at 923 K for 0.25 hour and (c) the SL film annealed at 923 K for one hour.

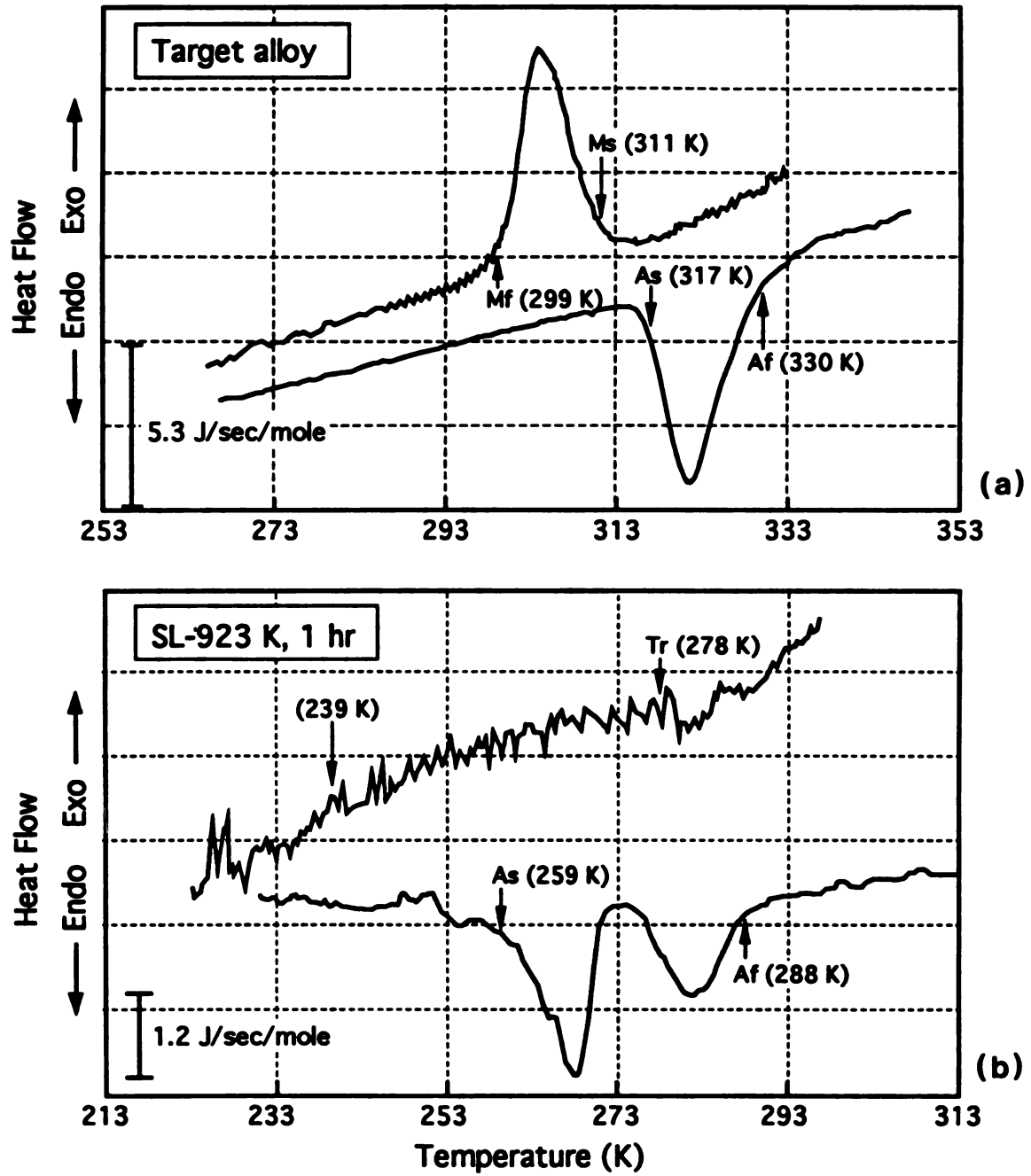


Figure 4-38: Differential scanning calorimetry data for (a) the target alloy and (b) the SL film annealed at 923 K for one hour.

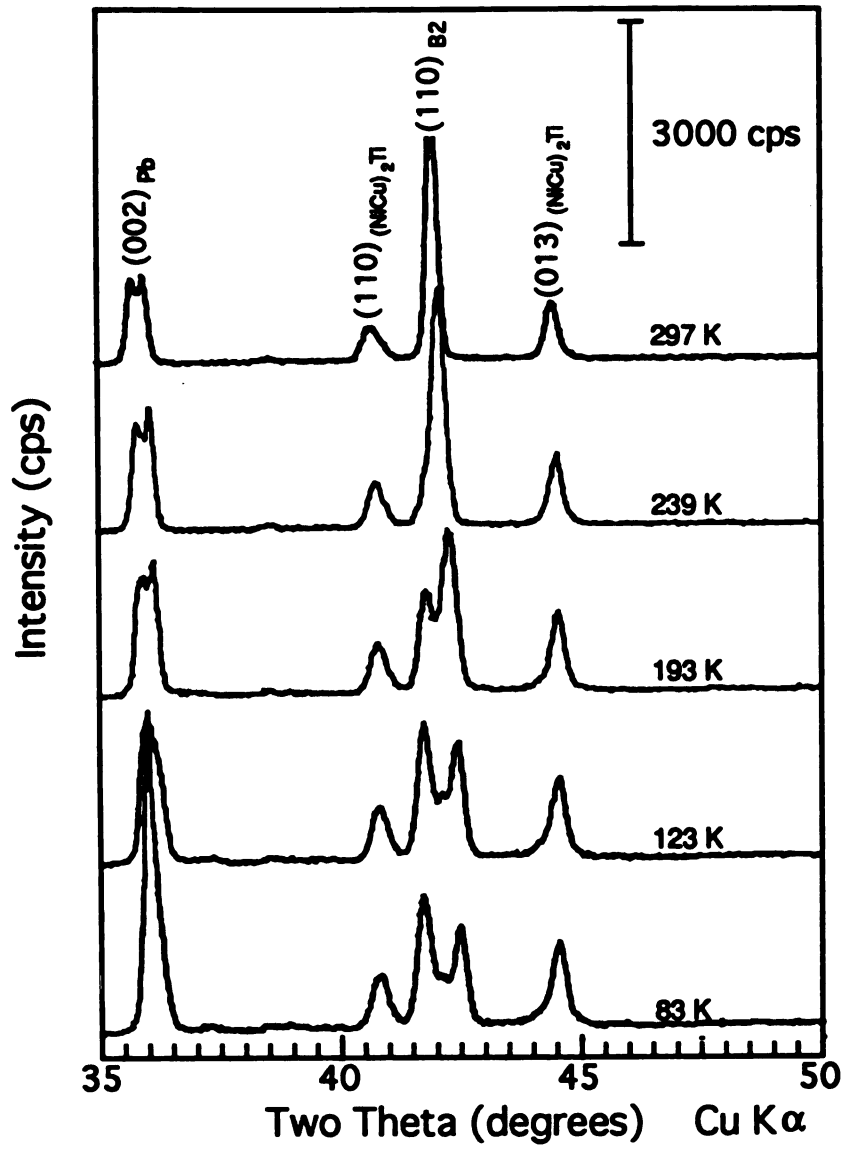


Figure 4-39: X-ray diffraction spectra for the SL film annealed at 923 K for 0.25 hour acquired at various temperature.

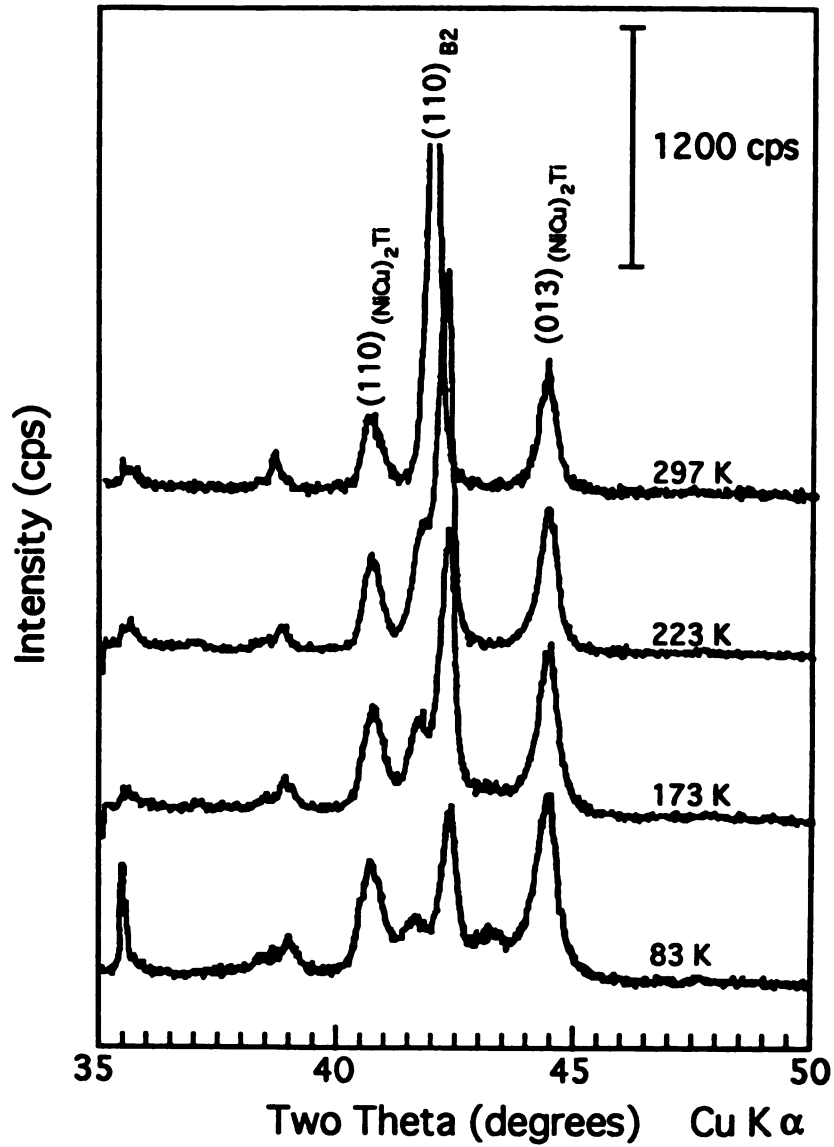


Figure 4-40: X-ray diffraction spectra for the SL film annealed at 923 K for one hour acquired at various temperature.

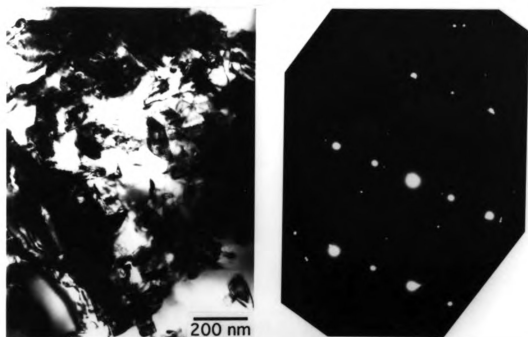


Figure 4-41: TEM micrograph of an one-hour annealed SL film taken at 255 K. The associated  $[012]_{B2}$  diffraction pattern shows well defined  $1/3$  spots in the  $\langle 321 \rangle_{B2}$  direction.

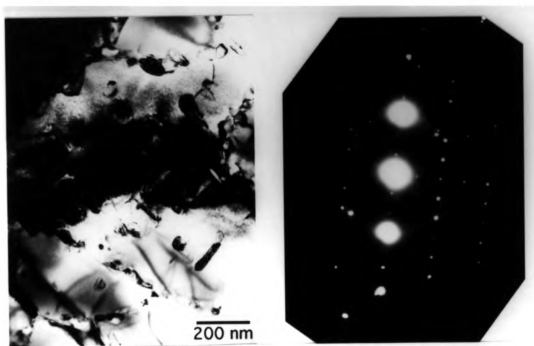


Figure 4-42: Electron micrograph of one-hour annealed SL film taken at 255 K. The associated diffraction pattern which can be identified as an  $[11\bar{2}0]_R$  zone axis using a hexagonal unit cell with  $a = 0.738$  nm and  $c = 0.532$  nm.



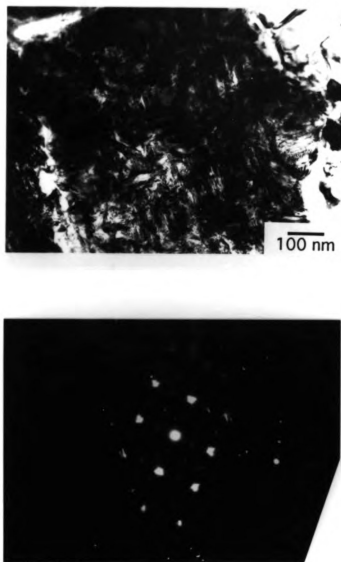
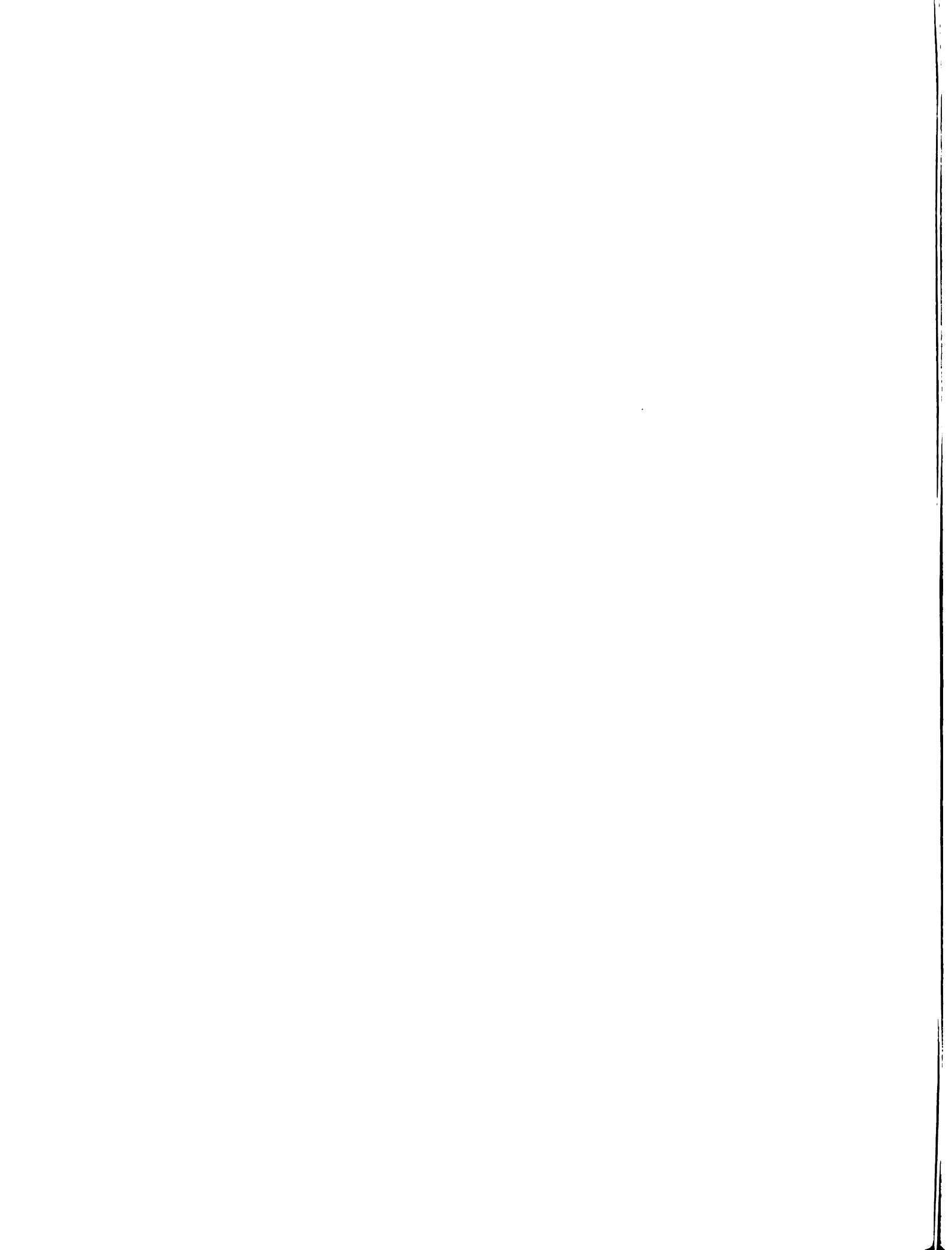


Figure 4-43: Bright field image of an one-hour annealed SL film taken at 160 K. The corresponding diffraction pattern showing [100] zone of martensite.



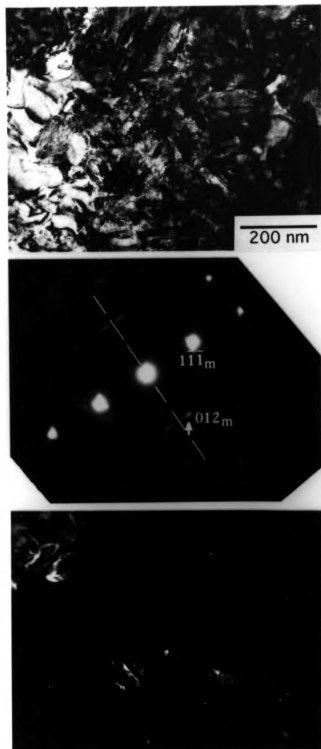


Figure 4-44: Electron micrograph of a one-hour annealed SL film taken at 160 K showing small martensite variants. The associated  $[3\bar{1}]$  diffraction patterns and dark filed micrograph showing  $(11\bar{2})$  twin relation between neighboring variants.

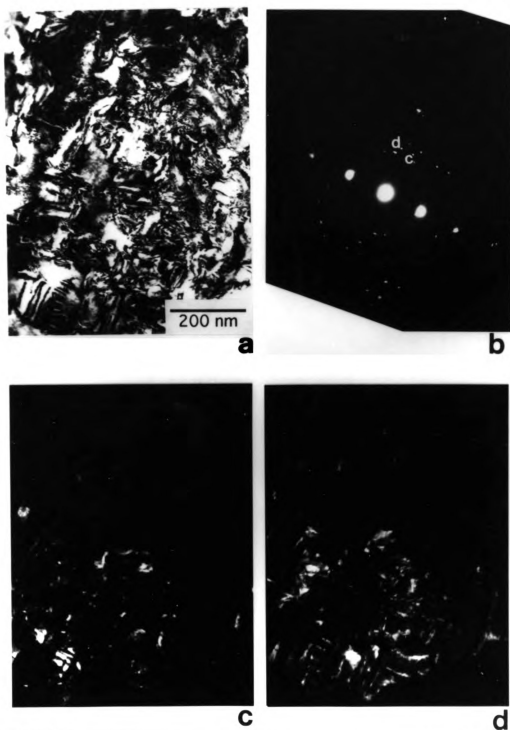


Figure 4-45: (a) Bright field micrograph showing plate-like R-phase variants; (b) associated diffraction pattern revealing the R-phase variants oriented perpendicular or parallel to  $[110]B_2$  reciprocal direction and (c-d) dark field images taken from spots c and d in (b) respectively showing labyrinth-like R-phase domains.

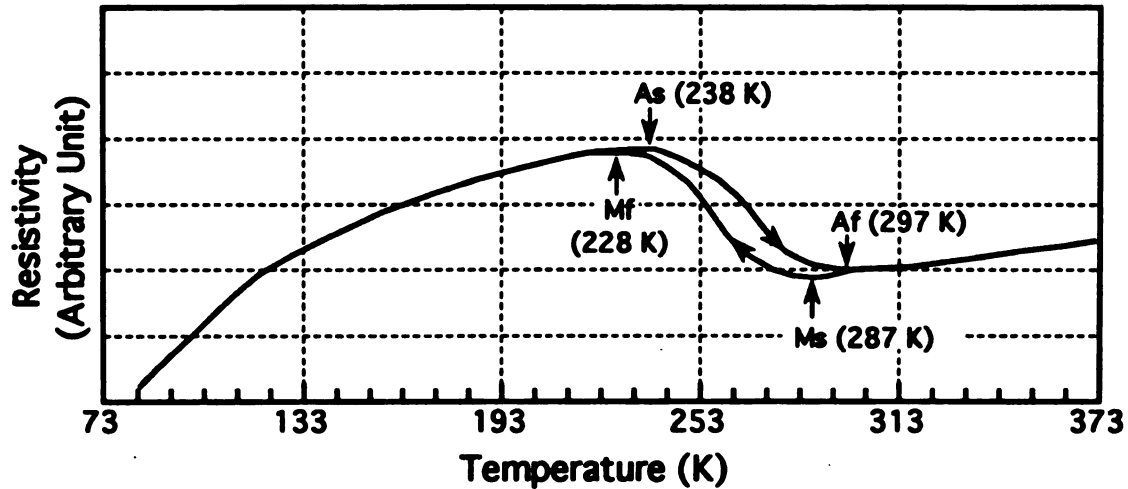


Figure 4-46: Electrical resistivity as a function of temperature of a PML-16 film annealed at 923 K for one hour in a vacuum of  $2.6 \times 10^{-3}$  Pa.

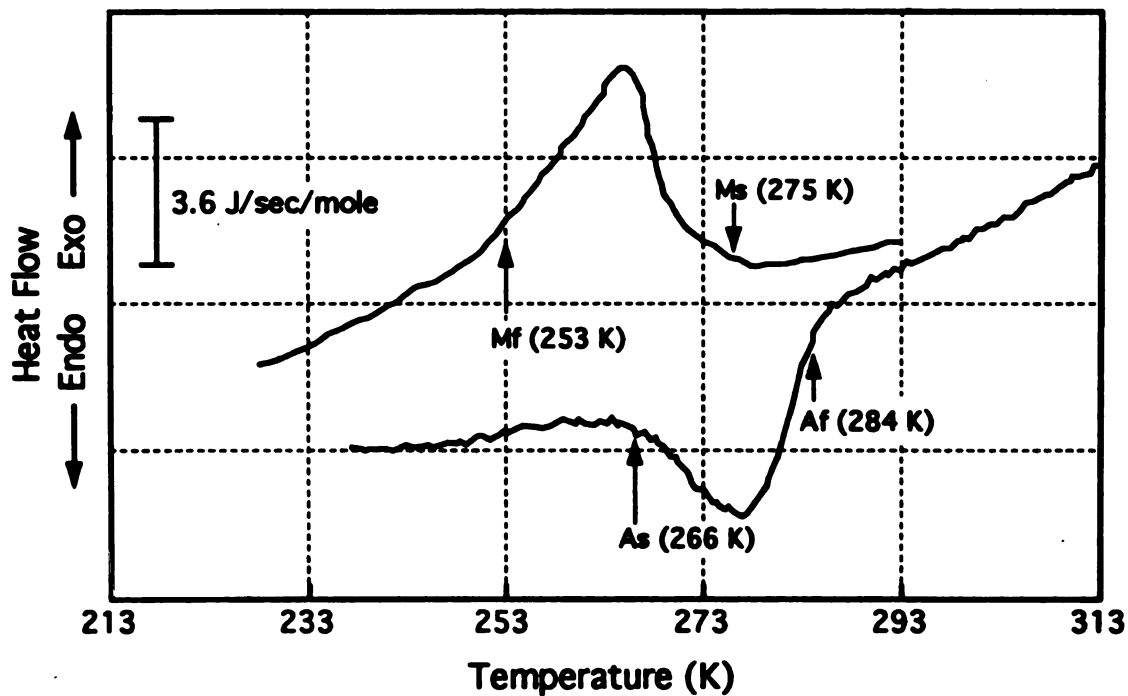


Figure 4-47. Differential scanning calorimetry data for a PML-16 film annealed at 923 K for one hour in a vacuum of  $2.6 \times 10^{-3}$  Pa.

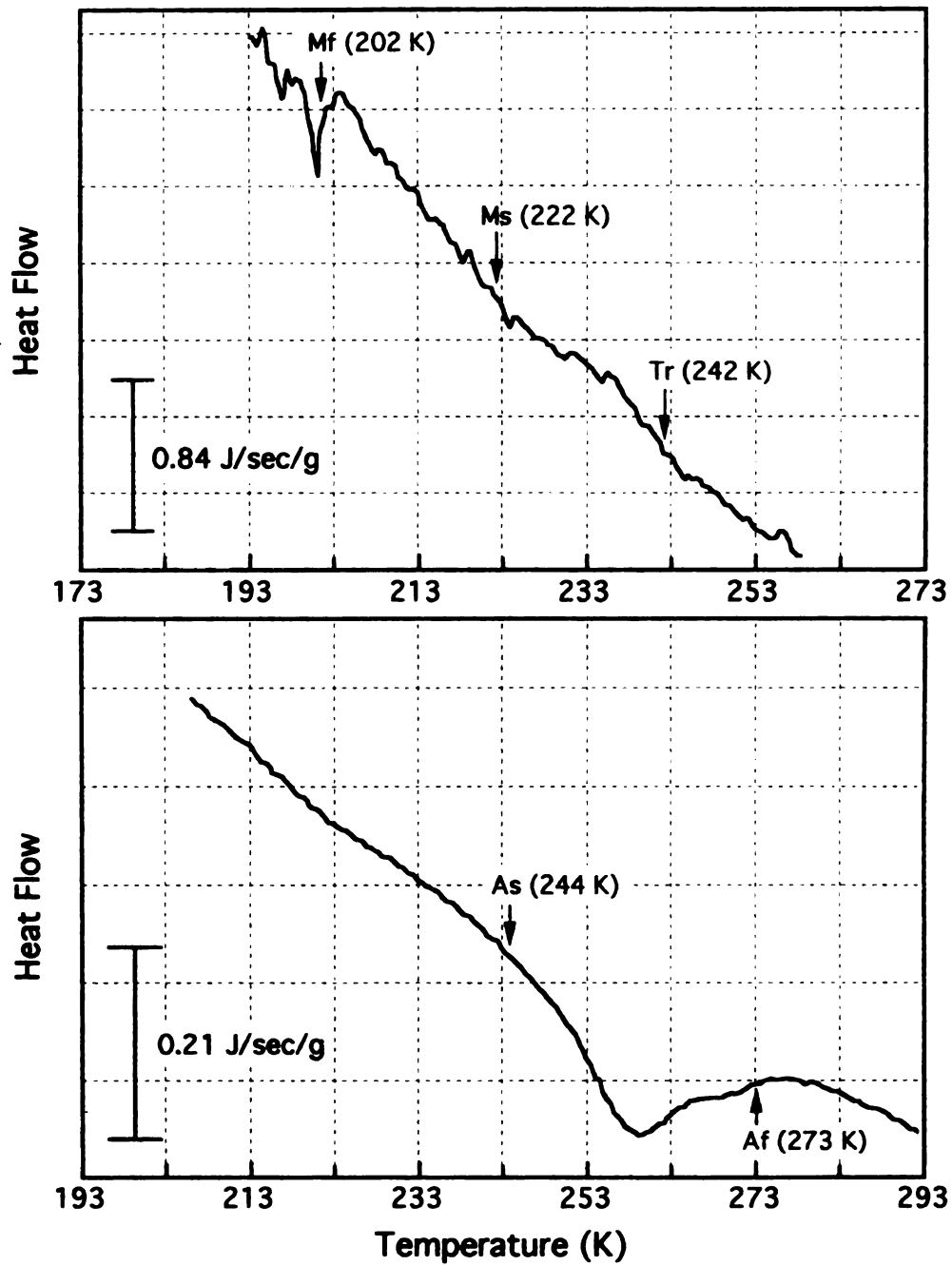


Figure 4-48: Differential scanning calorimetry data for a PML-16 film annealed at 823 K for one hour in a vacuum of  $2.6 \times 10^{-4}$  Pa.

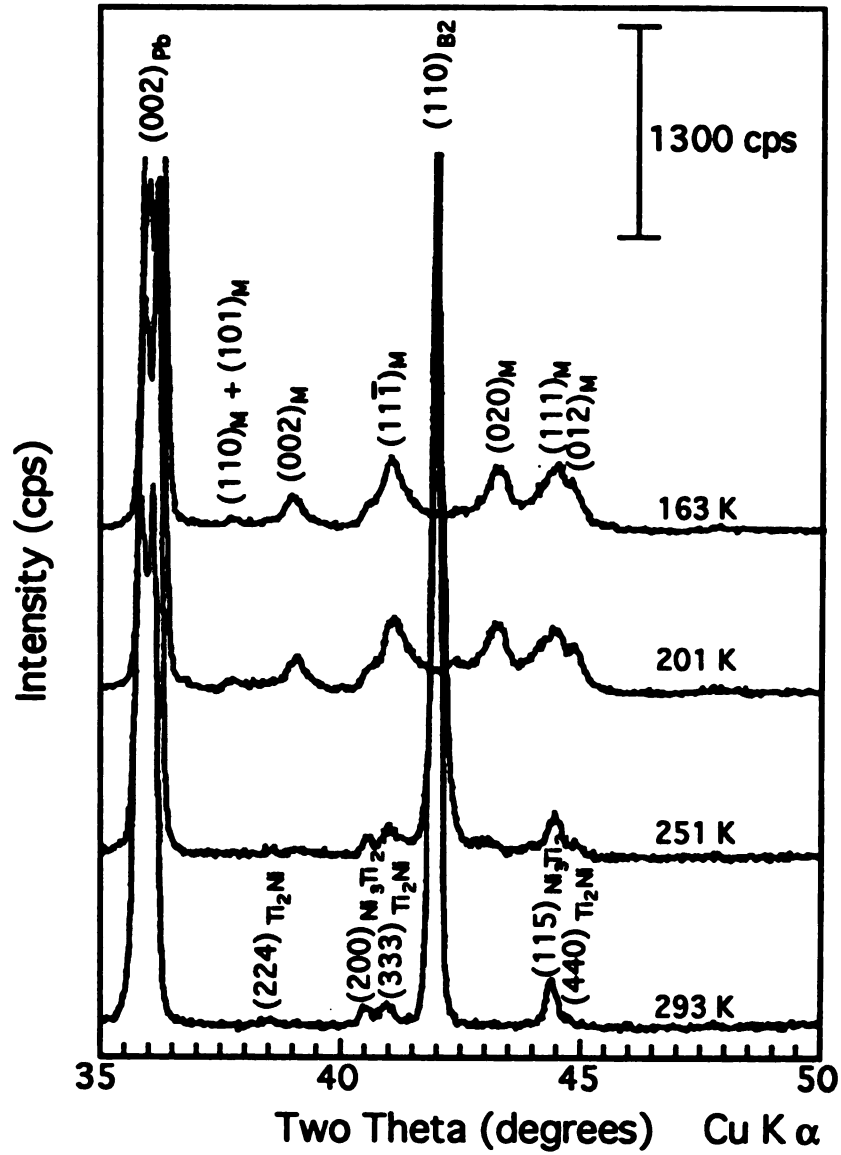


Figure 4-49: Cold-stage X-ray diffraction patterns of a PML-16 film annealed at 923 K in a vacuum of  $2.6 \times 10^{-4}$  Pa.

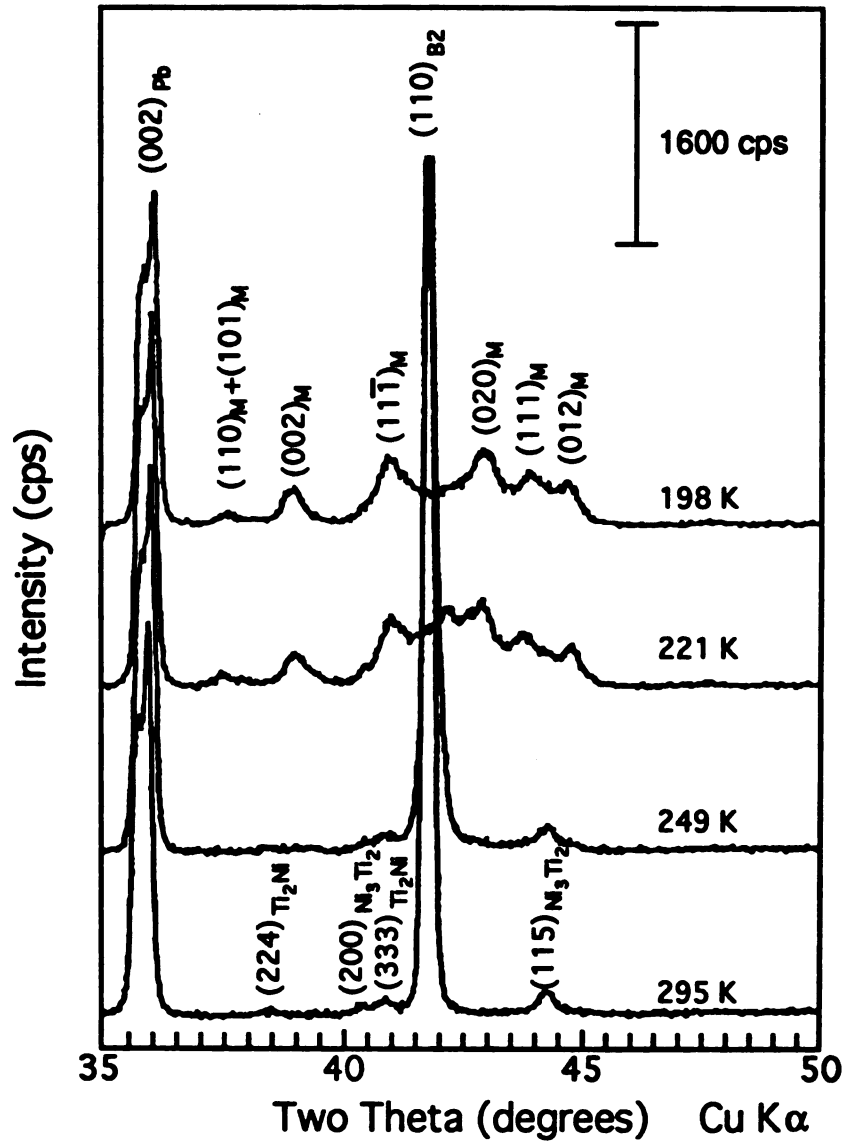


Figure 4-50: Cold-stage X-ray diffraction patterns of the PML-16 film annealed at 823 K in a vacuum of  $2.6 \times 10^{-4}$  Pa.

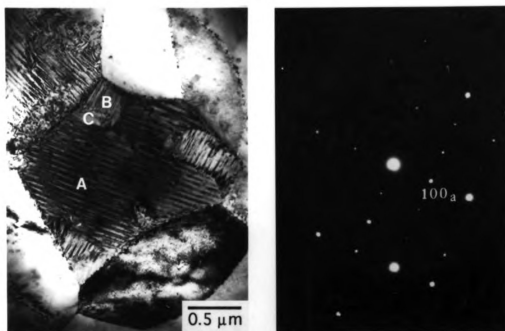


Figure 4-51: Electron micrograph and corresponding  $[1\bar{5}43]_R$  diffraction pattern of 823 K annealed PML-16 film taken at 215 K showing R-phase variants with plate-like variants.

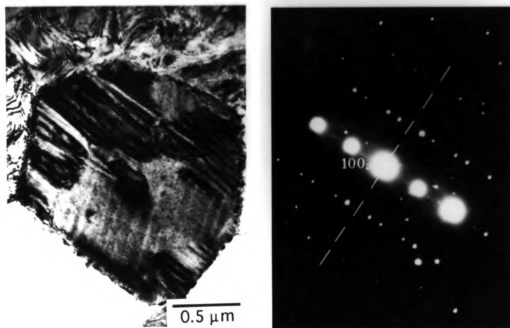


Figure 4-52: Electron micrograph and corresponding  $[023]_{B2}$  diffraction pattern of 823 K annealed PML-16 film taken at 215 K showing plate-like R-phase variants. The  $[023]_{B2}$  diffraction patterns is superimposed with two (100) twin-related  $[\bar{5}14\bar{2}5]_R$  diffraction patterns.

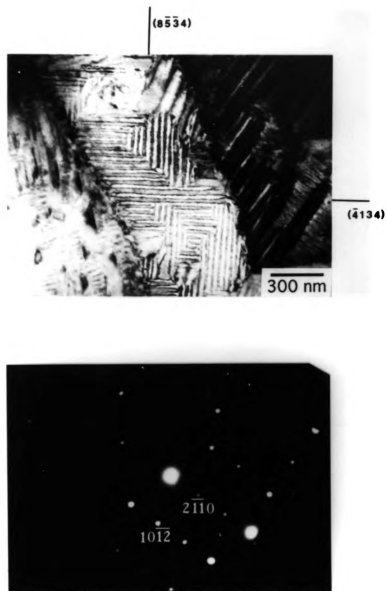


Figure 4-53: Electron micrograph and corresponding  $[0\bar{2}21]_R$  diffraction pattern of 823 K annealed PML-16 film taken at 215 K showing labyrinth-like variant-combination of the R-phase.

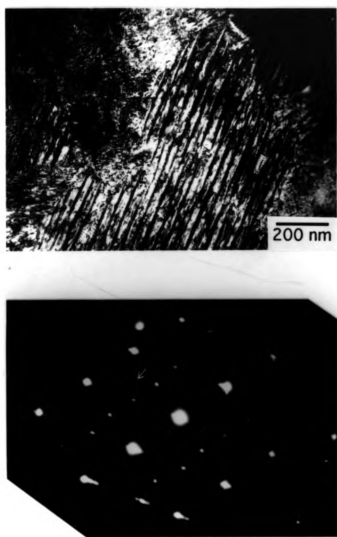
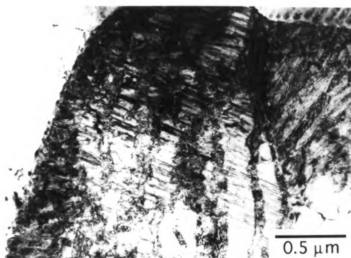
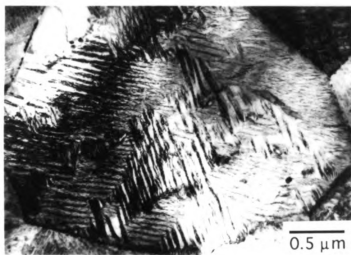


Figure 4-54: Electron micrograph of 823 K annealed film taken at 215 K showing martensite plates in R-phase matrix. The corresponding diffraction pattern shows a  $[010]_M$  pattern and a  $[011]_{B2}$  pattern with  $1/3$  spots in  $\langle 111 \rangle$  reciprocal directions.

**a****b**

**Figure 4-55:** Microstructure of monoclinic martensite in annealed PML-16 films taken at 170 K: (a) band-like variants and (b) zigzagged variants.

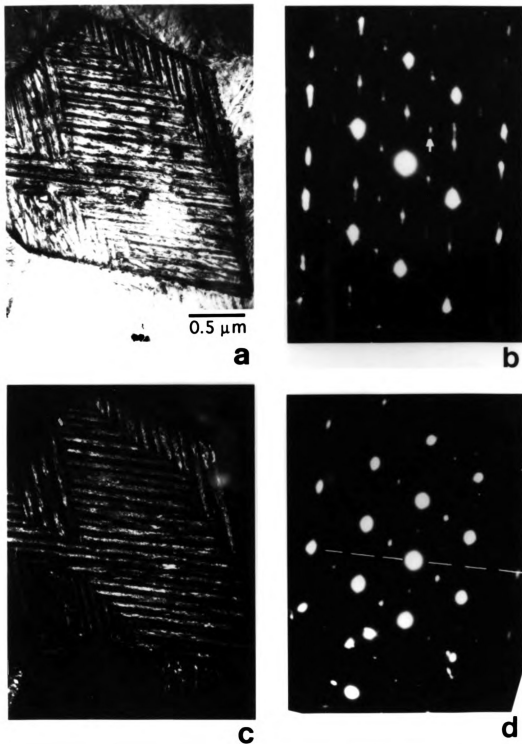


Figure 4-56: TEM micrographs of self-accommodated monoclinic martensite taken at 170 K: (a) bright field image; (b) [010] and  $[2\bar{1}\bar{1}]$  diffraction patterns; (c) dark field image taken from  $(100)+(01\bar{1})$  spots labeled in (b); and (d)  $[110]$  and  $[101]$  diffraction patterns.

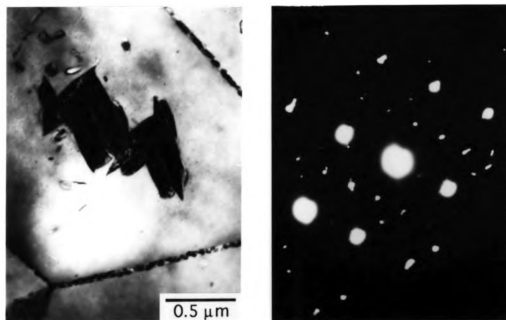


Figure 4-57: An electron micrograph of the 823 K annealed film illuminated by converged electron beam showing zigzagged martensite plates retained in the B2 matrix. The associated diffraction pattern are in  $[001]_M$  and  $[011]_{B2}$  zone axes.

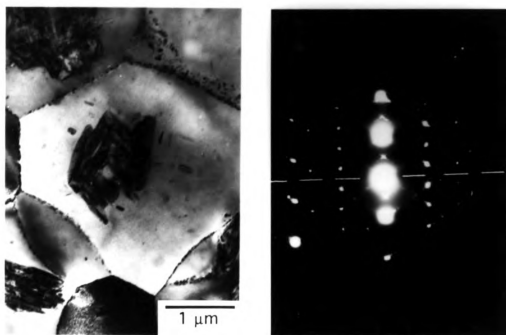


Figure 4-58: An electron micrograph of the 823 K annealed film illuminated by converged electron beam showing zigzagged martensite plates retained in B2 matrix. The associated diffraction pattern shows two  $(111)$  twin-related  $[3\bar{1}2]_M$  zone, corresponding to two sets of martensite plates.

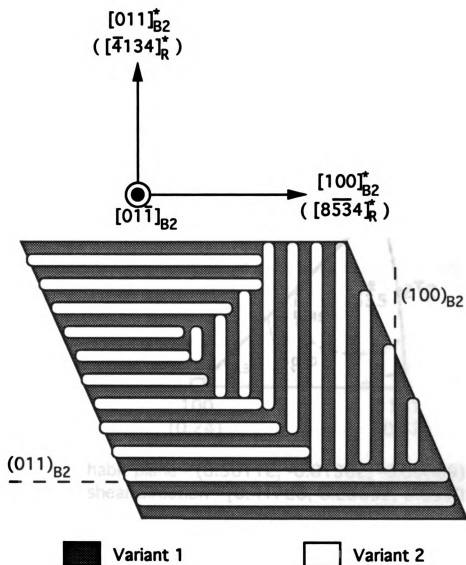
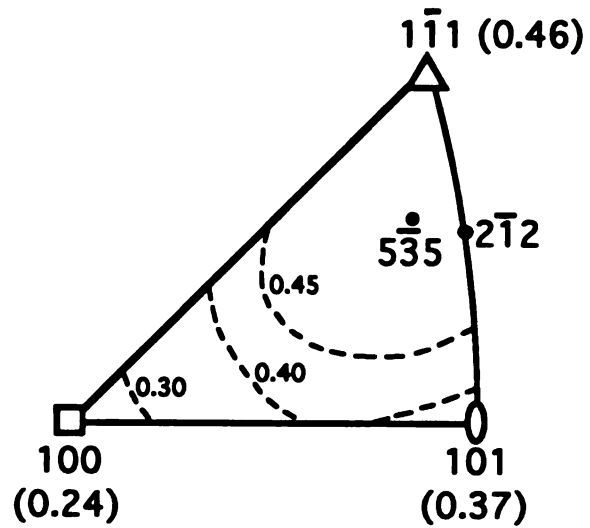


Figure 4-59: Schematic drawing showing the labyrinth-like morphology of R-phase.



habit plane -  $(0.58112, -0.81382, -0.00089)$   
 shear direction -  $[0.41720, 0.29652, 0.85908]$

**Figure 4-60:** Orientation dependence of the shape strain for Type-I twinning derived from solution 1 listed in Table 4-5.

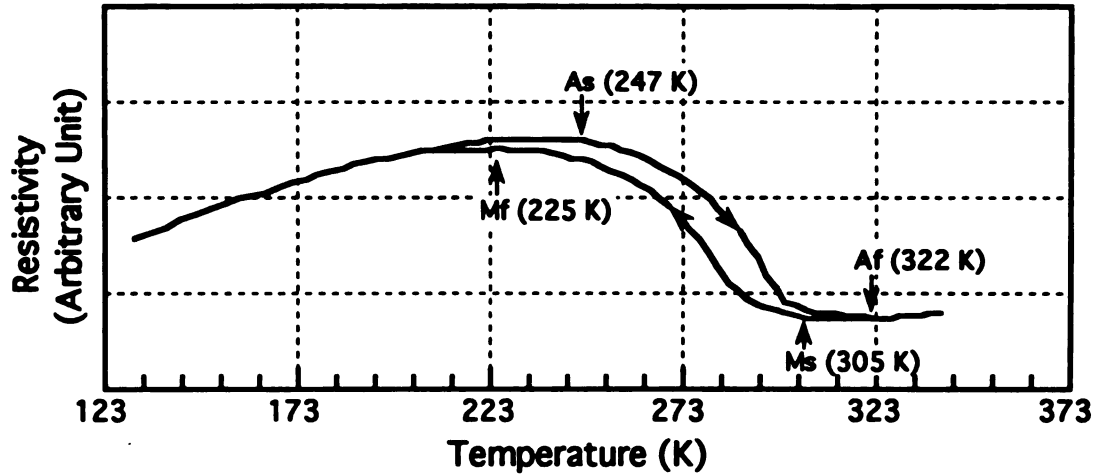


Figure 4-61: Electrical resistivity as a function of temperature of the PML-9 film annealed at 923 K for one hour in a vacuum of  $2.6 \times 10^{-3}$  Pa.

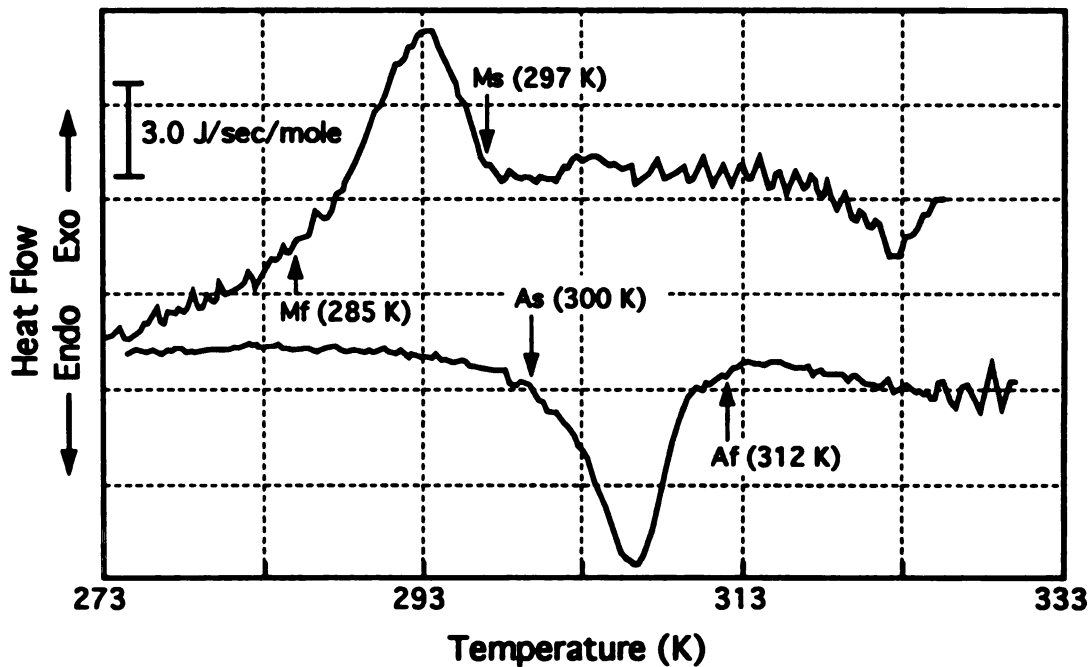


Figure 4-62: Differential scanning calorimetry data for the PML-9 film annealed at 923 K for one hour in a vacuum of  $2.6 \times 10^{-3}$  Pa.

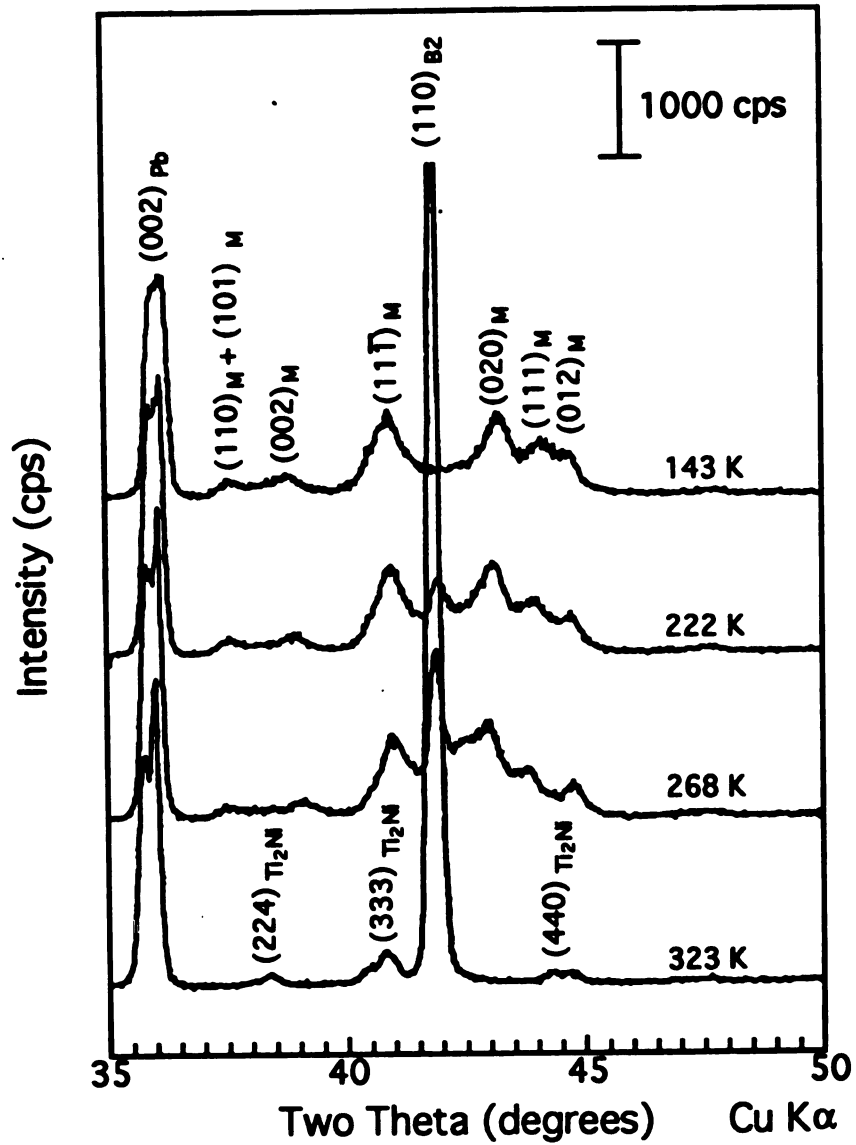


Figure 4-63: Cold-stage X-ray diffraction patterns of the PML-9 film annealed at 923 K in a vacuum of  $2.6 \times 10^{-3}$  Pa.

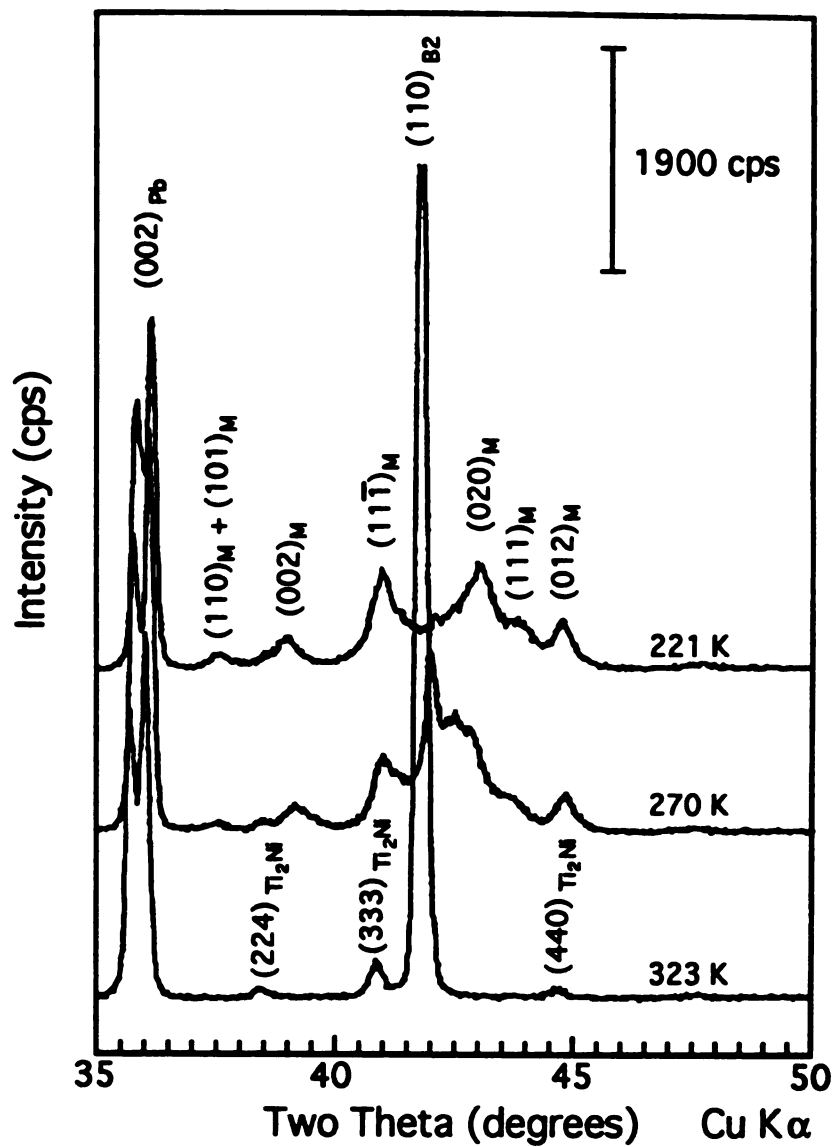


Figure 4-64: Cold-stage X-ray diffraction patterns of the PML-9 film annealed at 923 K in a vacuum of  $2.6 \times 10^{-4}$  Pa.

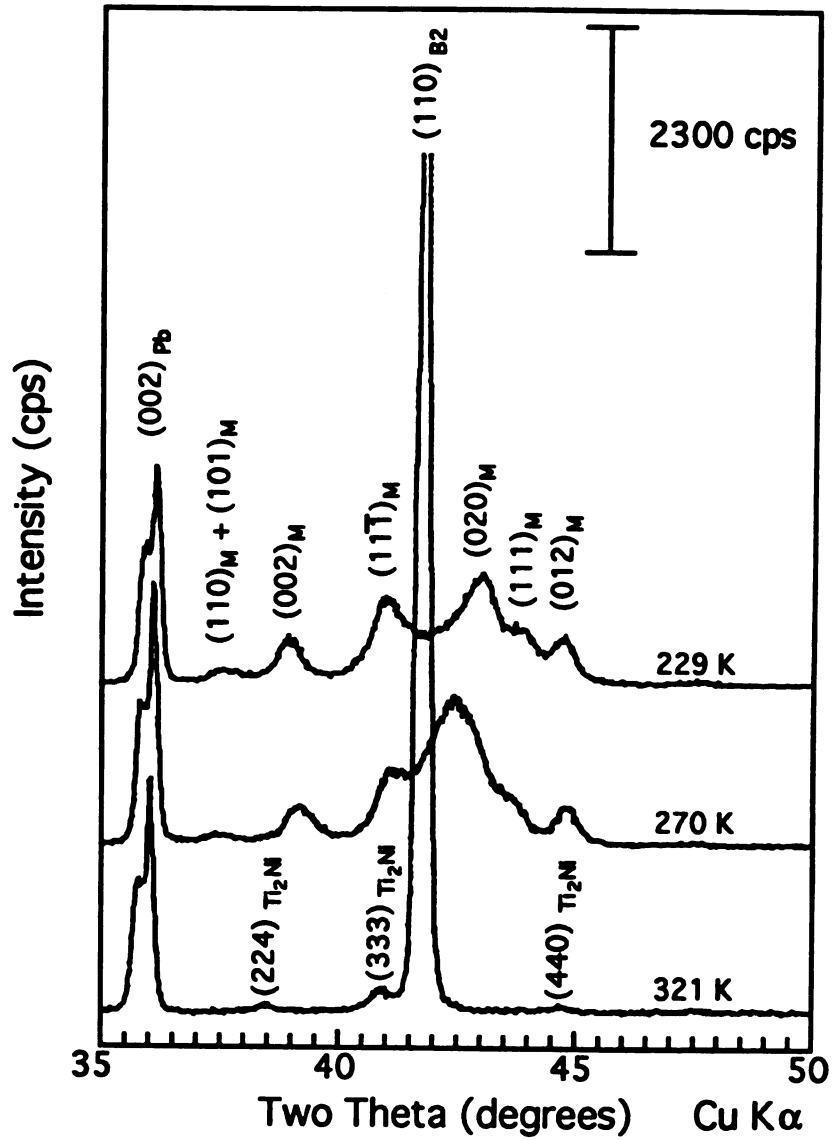


Figure 4-65: Cold-stage X-ray diffraction patterns of the PML-9 film annealed at 823 K in a vacuum of  $2.6 \times 10^{-4}$  Pa.

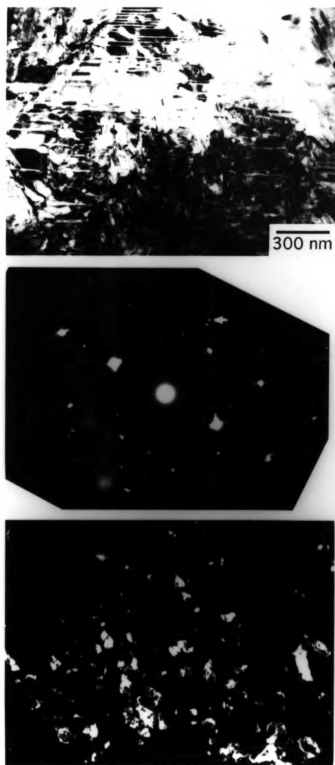


Figure 4-66: Retained austenite observed at 160 K: (a) bright field micrograph; (b) corresponding [110] diffraction pattern and (c) dark field image from (200)<sub>B2</sub> spot labeled in (b).

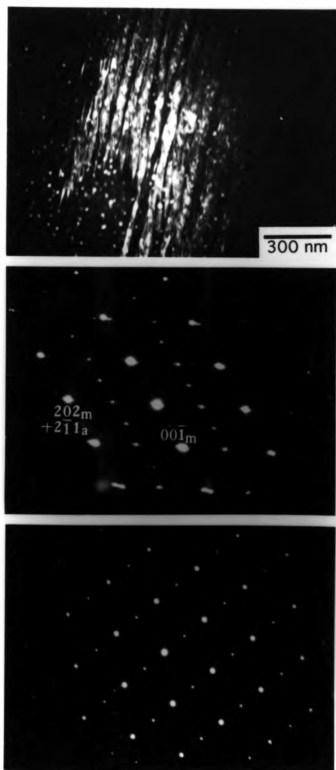
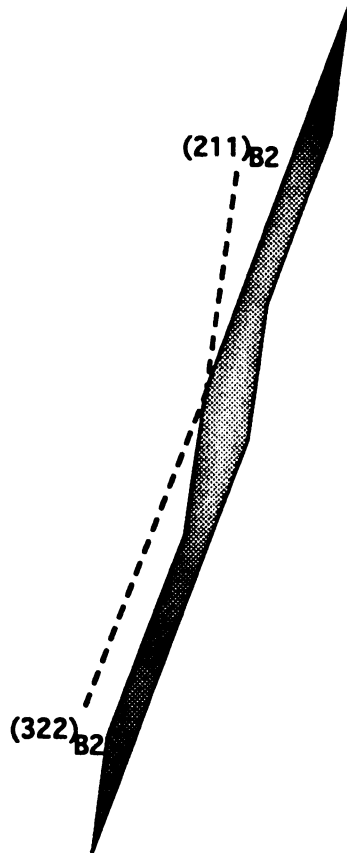


Figure 4-67: Orthorhombic martensite at ambient temperature: (a) dark field image; (b) corresponding diffraction pattern in the  $[010]_{\text{orth}}$  and  $[011]_{B_2}$  zone axes; (c) diffraction pattern in a  $[101]_{\text{orth}}$  zone axis.



3

d

Figure 4-67 (cont'd)

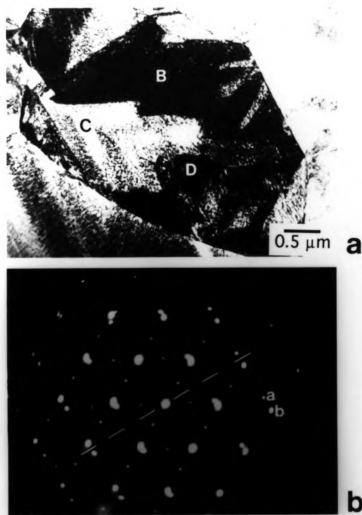


Figure 4-68: TEM micrographs of self accommodated orthorhombic martensite taken at room temperature: (a) bright field micrograph; (b) [110] diffraction pattern taken from area B; (c) [110] diffraction patterns taken from area C; (d) [101] diffraction pattern taken from area D; (e) dark field image taken from spot a in (b) showing four martensite variants a, b, c and d; (f) dark field image taken from spot g in (d) at higher magnification showing three martensite variants e, g and f; and (g) schematic drawing showing the variant distribution.

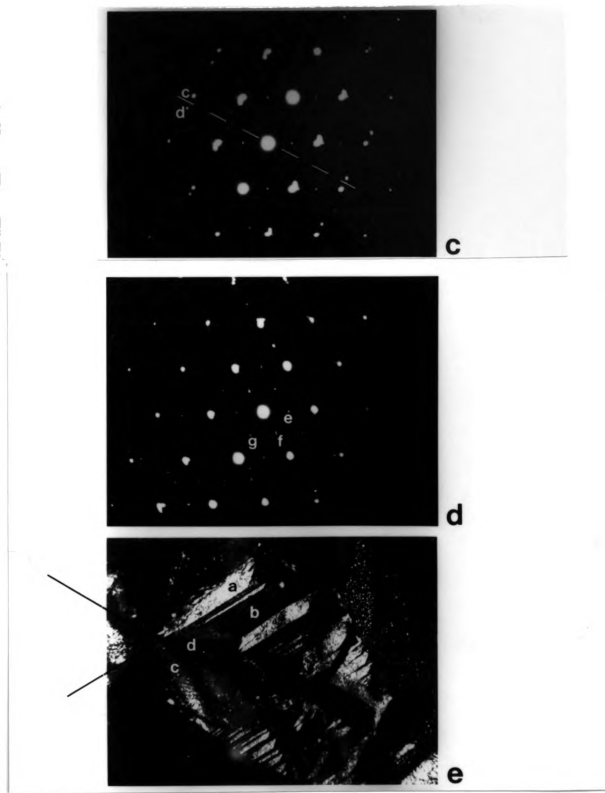


Figure 4-68 (cont'd)

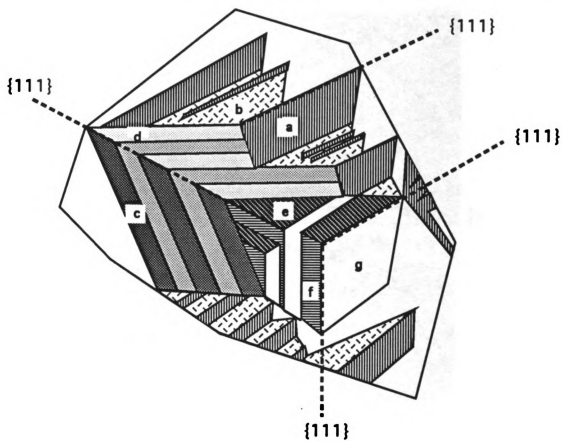
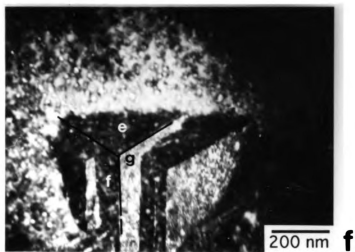


Figure 4-68 (cont'd)

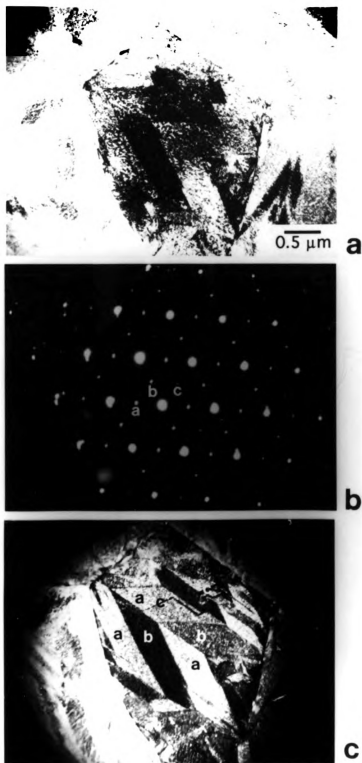


Figure 4-69: Self accommodated orthorhombic martensite taken at room temperature: (a) bright field micrograph; (b) corresponding diffraction pattern showing three (111) twin-related [101] patterns and (c) dark field image taken from spot a in (b) showing three martensite variants a, b and c.

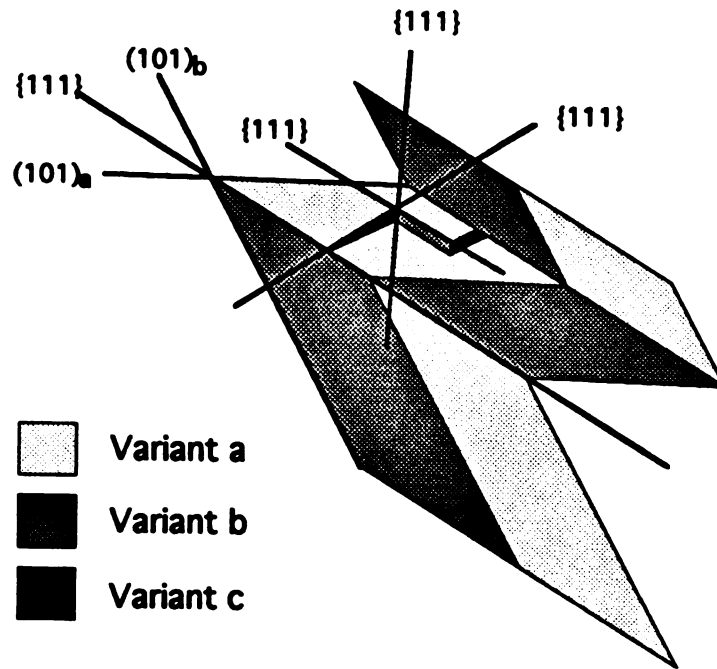
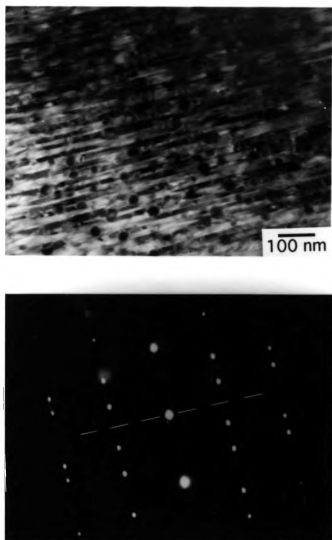


Figure 4-70: Crystallographic nature of the martensite variants shown in Figure 4-69.



**Figure 4-71:** Electron micrograph and corresponding [121] diffraction pattern showing (111) twins in a thin-plate form of orthorhombic martensite taken at room temperature.

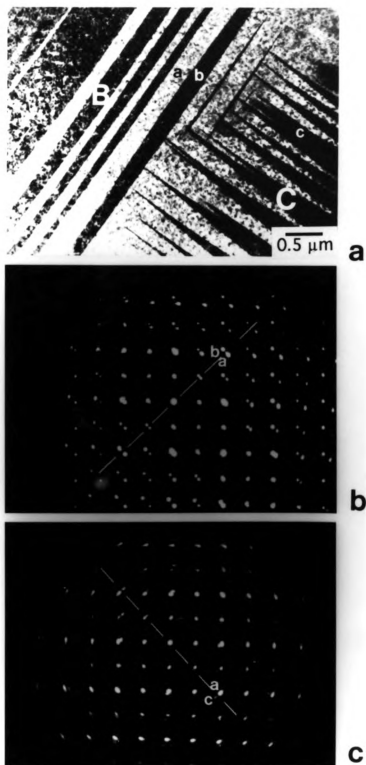


Figure 4-72: TEM micrographs of self accommodated orthorhombic martensite taken at room temperature: (a) bright field micrograph; (b) [100] diffraction pattern taken from area B showing one set of (011) twins and (c) [100] diffraction pattern taken from area C showing another set of (011) twins.

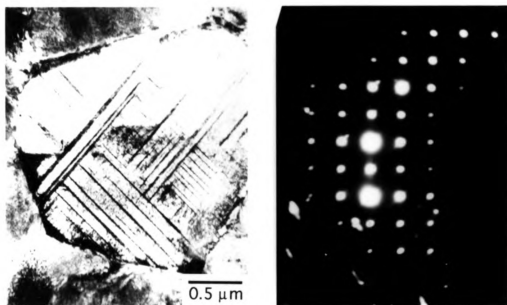


Figure 4-73: Electron micrograph taken at 123 K showing the monoclinic martensite inherits (011) twin-related orthorhombic variants. The associated diffraction pattern showing the electron beam is almost parallel to  $[100]_{\text{mono}}$ .

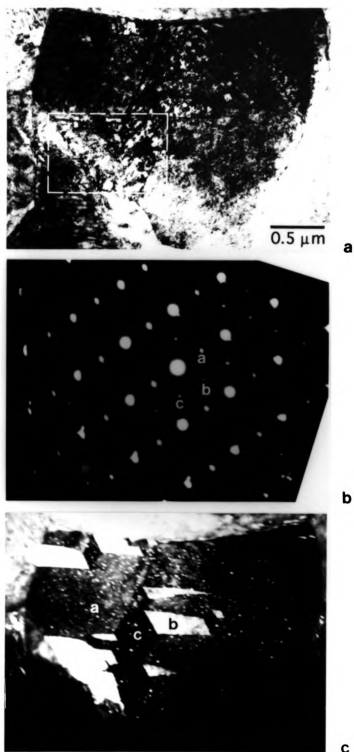


Figure 4-74: Self accommodated monoclinic martensite at 140 K: (a) bright field image; (b) diffraction patterns of martensite variants a, b and c in [101] zone axes; (c) dark field image shows variant a, b and c. Fine striations were observed inside the martensite variants.

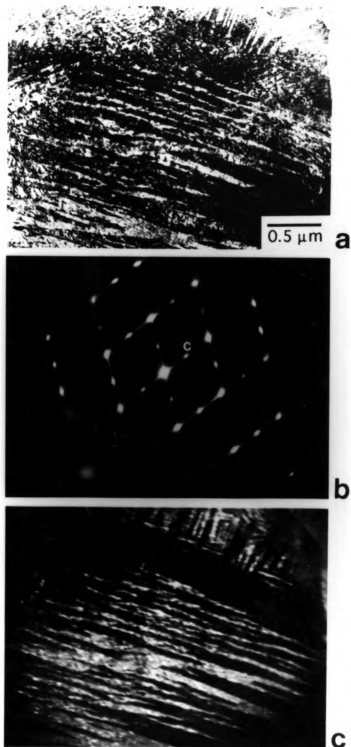


Figure 4-75: Self-accommodated monoclinic martensite at 123 K: (a) bright field micrograph; (b) corresponding  $[110]$  diffraction patterns and (c) dark field image taken from spot c in (b). The streaks of diffraction spots in  $[001]$  reciprocal directions result from  $(001)$  twins.

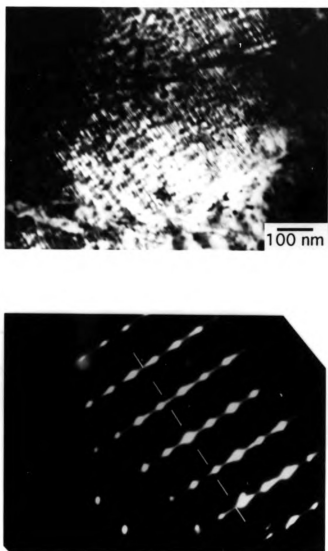


Figure 4-76: Electron micrograph and corresponding  $[110]_M$  diffraction pattern taken at 123 K showing (001) twins with an average spacing of 4 nm.

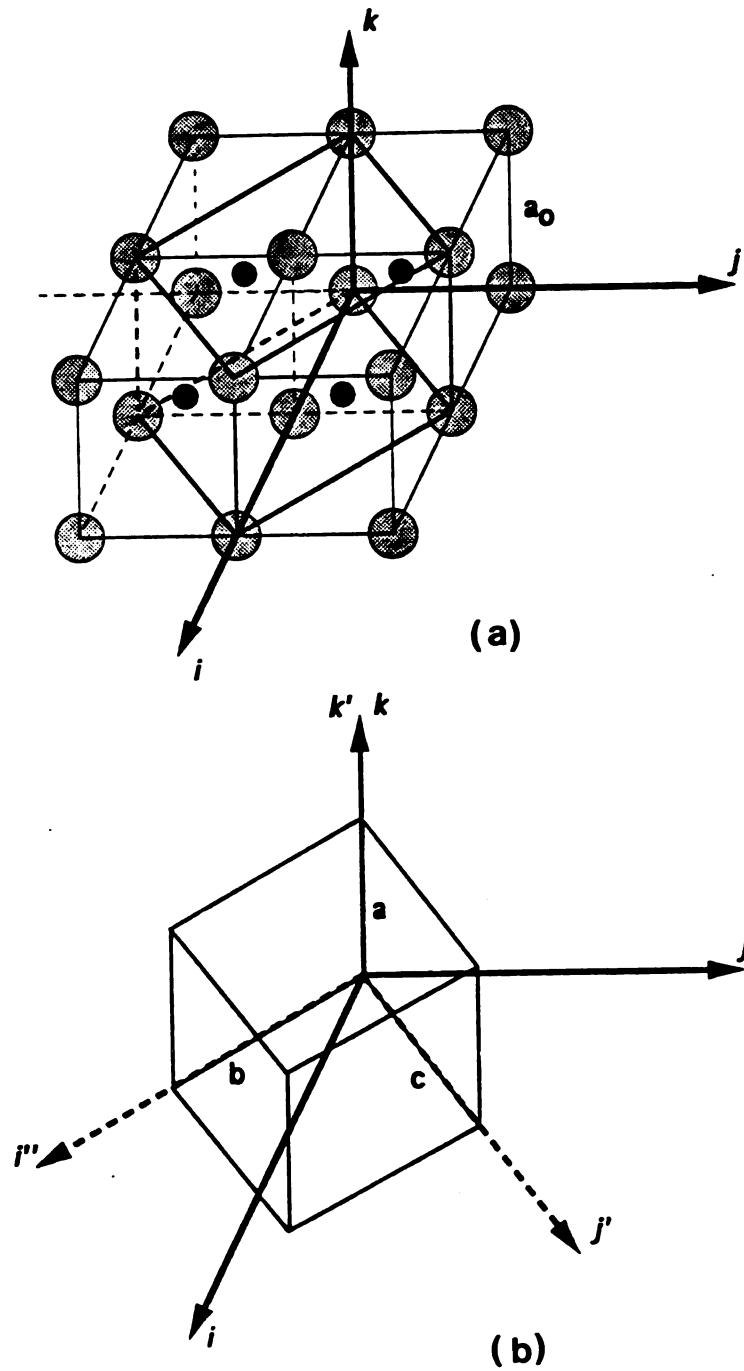


Figure 4-77: (a) Untransformed B2 structure in which a fct cell is delineated. (b) orthorhombic cell transformed from the fct cell. Principle axes ( $i'$ ,  $j'$ ,  $k'$ ) are obtained by 45° rotation about the  $k$  axis.



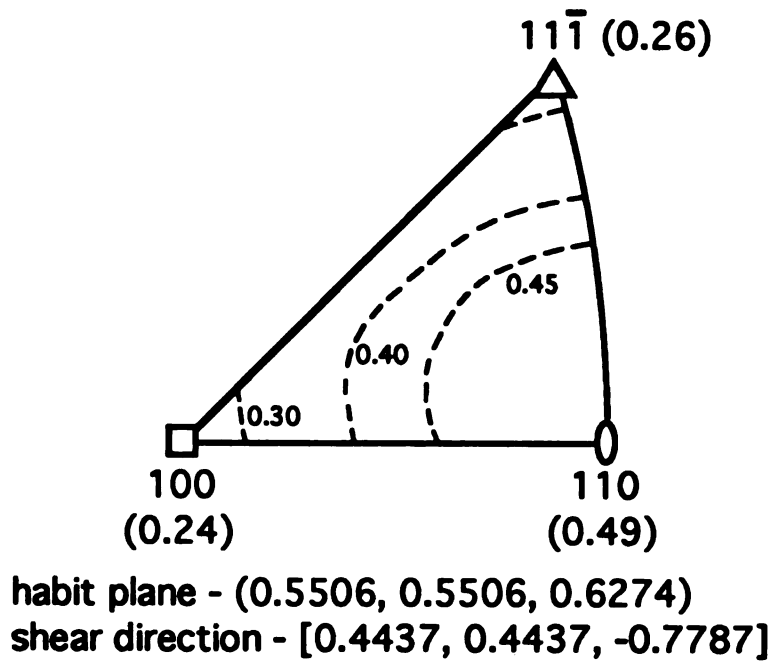


Figure 4-79: Orientation dependence of the shape strain for orthorhombic martensite.

## BIBLIOGRAPHY

1. W. J. Buehler and F. E. Wang, *Ocean Eng.*, **1** (1968) 105.
2. C. M. Jackson, H. J. Wagner and R. J. Wasilewski, NASA-SP 5110 (1972).
3. M. H. Wu in "Engineering Aspects of Shape Memory Alloys", eds. T. W. Duerig, K. N. Melton, D. Stockel and C. M. Wayman, 69 (1990), Butterworth-Heinemann, London.
4. K. N. Melton in "Engineering Aspects of Shape Memory Alloys", eds. T. W. Duerig, K. N. Melton, D. Stockel and C. M. Wayman, 21 (1990), Butterworth-Heinemann, London.
5. D. S. Grummon, S. Nam and L. Chang in "Shape Memory Materials and Phenomena", eds. C. T. Liu, H. Kunsmann, K. Otsuka and M. Wuttig, 259 (1991), Materials Research Society Symposium Proceedings, Vol. 246.
6. D. Johnson, *J. Micromech. Microeng.*, **1** (1991) 34.
7. W. J. Moberly and K. N. Melton in "Engineering Aspects of Shape Memory Alloys", eds. T. W. Duerig, K. N. Melton, D. Stockel and C. M. Wayman, 46 (1990), Butterworth-Heinemann, London.
8. O. Mercier and K. N. Melton, *Metall. Trans.*, **10A** (1979) 387.
9. R. E. Reed-Hill, *Physical Metallurgy Principles*, 611 (1973), Van Nostrand Reinhold Company, New York.
10. Z. Nishiyama, "Martensitic Transformation", 276 (1978), Academic Press, New York.
11. M. W. Burkart and T. A. Read, *Trans. AIME*, **197** (1953) 1516.
12. D. S. Lieberman, M. S. Wechsler and T. A. Read, *J. Appl. Phys.*, **26** (1955) 473.
13. C. M. Wayman in "Engineering Aspects of Shape Memory Alloys", eds. T. W. Duerig, K. N. Melton, D. Stockel and C. M. Wayman, 3 (1990), Butterworth-Heinemann, London.
14. H. C. Tong and C. M. Wayman, *Acta Metall.*, **22** (1974) 887.
15. K. Shimizu and K. Otsuka in "Shape Memory Effects in Alloys", ed. J. Perkins, 59 (1975), Plenum, New York.
16. K. N. Melton and O. Mercier, *Metall. Trans.*, **9A** (1978) 1487.
17. W. J. Buehler and R. C. Wiley: Nickel-Base Alloy, U. S. Patent 3174851, Mar. 23, 1965.
18. R. G. de Lange and J. A. Zijderfeld, *J. Appl. Phys.*, **39** (1968) 2195.
19. K. Otsuka, T. Sawamura, K. Shimizu and C. M. Wayman, *Metall. Trans.*, **5** (1971) 2583.

20. K. Otsuka and K. Shimizu, *Scripta Metall.*, **4** (1970) 469.
21. R. A. Swalin, "Thermodynamics of Solid", 33 (1972), John Wiley & Sons, Inc, New York.
22. H. Warlimont, L. Delaey, R. V. Krishnan and H. Tas, *J Mater. Sci.*, **9** (1974) 1545.
23. S. Miyizaki, K. Otsuka and C. M. Wayman, *Acta Metall.*, **37** (1989) 1873.
24. J. S. Bowles and J. K. Mackenzie, *Acta Metall.*, **2** (1954) 129.
25. M. S. Wechsler, D. S. Leiberman and T. A. Read, *Trans. AIME*, **197** (1953) 1503.
26. D. S. Lieberman, M. S. Wechsler and T. A. Read, *J. Appl. Phys.*, **26** (1955) 473.
27. Z. Nishiyama, "Martensitic Transformation", 355 (1978), Academic Press, New York.
28. E. C. Bain, *Trans AIME*, **70** (1924) 25.
29. Binary Alloy Phase Diagrams, vol. 2, ed. T. B. Massalski, 1768 (1987), American Metals Society, Metals Park.
30. P. Duwez and J. L. Taylor, *Trans, AIME*, **188** (1950), 173 .
31. D. M. Pool and W. Hume-Rothery, *J. Inst. Met.*, **83** (1954-1955), 473.
32. D. Koskimaki, M. J. Marcinkowski and A. Sastri, *Trans AIME*, **245** (1969), 1880.
33. S. P. Gupta, K. Mukherjee and A. A. Johnson, *Mater. Sci. Eng.*, **11** (1973), 283.
34. H. Margolin, E. Ence and J. P. Nielsen, *Trans. AIME*, **197** (1953), 243.
35. G. R. Purdy and J. G. Parr, *Trans. AIME*, **221** (1961), 636.
36. R. J. Wasilewski, S. R. Butler, J. E. Hanlon and D. Worden, *Metall. Trans.*, **2** (1971), 229.
37. G. F. Bastin and G. D. Rieck, *Metall. Trans.*, **5** (1974), 1817.
38. M. Nishida, C. M. Wayman and T. Honma, *Metall. Trans.*, **17A** (1986) 1505.
39. T. Saburi, S. Nenno and T. Fukuda, *J. Less-com. Met*, **125** (1986) 157.
40. J. Beyer, R. A. V. D. Brakel and J. R. T. Lloyd, *Proc. Int. Conf. on Martensitic Transformation* (1986) 703.
41. M. V. Nevitt, *Trans. AIME*, **218** (1960), 327.
42. G. Chattopadhyay and H. Kleykamp, *Z Metallkd.* **74** (1983), 182.
43. R. Kainuma, M. Matsumoto and T. Honma, *Proc. Int. Conf. on Martensitic Transformation* (1986) 717.
44. F. J. J. van Loo, G. F. Bastin and A. J. H. Leenen, *J. Less-com. Met.*, **57** (1978) 11.
45. R. H. Brickell, K. N. Melton and O. Mercier, *Metall. Trans.*, **10A** (1979) 693.
46. A. R. Pelton, P. H. Adler, W. Yu, R. Holt and R. McConville, *Proc. XII th Int. Cong. Electron Microscopy* (1990).
47. L. Chang and D. S. Grummon, *Scripta Metall. Mater.*, **25** (1991) 2079.
48. G. D. Sandrock, A J. Perkins and R. F. Hehemann, *Metall. Trans.*, **2** (1971) 2769.
49. H. C. Ling and R. Kaplow, *Metall. Trans.*, **11A** (1980) 77.

50. C. M. Hwang, M. Meichle, M. B. Salamon and C. M. Wayman, *Phil. Mag.* **47** (1983) 9.
51. E. Goo and R. Sinclair, *Acta Metall.*, **33** (1985) 1717.
52. S. K. Wu and C. M. Wayman, *Acta Metall.*, **37** (1989) 2805.
53. S. Miyazaki and C. M. Wayman, *Acta Metall.*, **36** (1988) 181.
54. K. Otsuka, T. Sawamura and K. Shimizu, *Phys. Stat. Sol.(a)*, **5** (1971) 457.
55. G. M. Michal and R. Sinclair, *Acta Cryst.*, **B37** (1981) 1803.
56. W. Buhner, R. Gotthardt, A. Kulik, O. Mercier and F. Staub, *J. Phys. F: Met. Phys.*, **13** (1983) L77.
57. Y. Kudoh, M. Tokonami, S. Miyazaki and K. Otsuka, *Acta Metall.*, **33** (1985) 2049.
58. C. M. Hwang, M. B. Salamon and C. M. Wayman, *Phil. Mag. A*, **47** (1983) 177.
59. S. K. Wu and C. M. Wayman, *Mater. Sci. Eng.*, **96** (1987) 295.
60. K. M. Knowles and D. A. Smith, *Acta Metall.*, **29** (1981) 101.
61. C. Y. Xie, L. C. Zhao and T. C. Lei, *Scripta Metall. Mater.*, **24** (1990) 1753.
62. R. Sinclair, *AIP conf. Proc.*, **53** (1979) 269.
63. O. Matsumoto, S. Miyazaki, K. Otsuka and H. Tamura, *Acta Metall.*, **35** (1987) 2137.
64. Y. Shugo, S. Hanada and T. Honma, *Bull. Res. Inst. Min. Met., Tohoku Univ.*, **41** (1985) 23.
65. S. Miyazaki and K. Otsuka, *Metall. Trans.*, **17A** (1986) 53.
66. J. L. Proft, K. N. Melton and T. W. Duerig, *Proc. of the Inter. MRS Conf., Tokyo* (1987).
67. K. Otsuka in *Engineering Aspects of Shape Memory Alloys*, eds. T. W. Duerig, K. N. Melton, D. Stockel and C. M. Wayman, **36** (1990), Butterworth-Heinemann, London.
68. M. Nishida and T. Honma, *Scripta Metall.*, **18** (1984) 1299.
69. R. H. Bricknell, K. N. Melton and O. Mercier, *Metall. Trans.*, **10A** (1979) 693.
70. R. H. Bricknell and K. N. Melton, *Metall. Trans.*, **11A** (1980) 1541.
71. T. Tadaki and Wayman, *Metallography*, **15** (1982) 233.
72. Y. Shugo, F. Hasegawa and T. Honma, *Bull. Res. Inst. Min. Met., Tohoku Univ.*, **37** (1981) 79.
73. Y. Shugo and T. Honma, *Bull. Res. Inst. Min. Met., Tohoku Univ.*, **43** (1987) 117.
- 73a. K. Tsuji and K. Nomura, *Scripta Metall. Mater.*, **24** (1990) 2037.
74. K. H. Buschow, *J. Phys. F: Met. Phys.*, **13** (1983) 563.
75. K. H. Buschow, *J. Appl. Phys.*, **56** (1984) 304.
76. K. Ikuta, H. Fujita, M. Ikeda and S. Yamashita, *IEEE CH2832-4* (1990) 38.
77. L. Battezzati, G. Cocco, L. Schiffini and S. Enzo, *Mater. Sci. Eng.*, **97** (1988) 121.

78. R. B. Schwarz, R. R. Petrich and C. K. Saw, *J. Non-Cryst. Solids*, **76** (1985) 281.
79. J. D. Busch, A. D. Johnson, C. H. Lee and D. A. Stevenson, *J. Appl. Phys.*, **68** (1990) 6224.
80. G. F. Bastin and G. D. Rieck, *Metall. Trans*, **5** (1974) 1827.
81. W. L. Johnson, *Mater. Sci. Eng.*, **97** (1988) 1.
82. E. D. McClanadhan and N. Laegreid in "Sputtering by Particle Bombardment III", eds. R. Behrisch and K. Wittmaack, 339 (1991), Springer-Verlag, Berlin.
83. P. Sigmund in "Sputtering by Particle Bombardment I", eds. R. Behrisch, 9 (1981), Springer-Verlag, Berlin.
84. H.H. Anderson and H. L. Bay in "Sputtering by Particle Bombardment I", eds. R. Behrisch, 145 (1981), Springer-Verlag, Berlin.
85. R. Kelly in "Ion Bombardment Modification of Surfaces", eds. O. Auciello and R. Kelly, 101 (1984), Elsevier Science, Amsterdam.
86. J. Bohdansky, J. Roth and H. L. Bay, *J. Appl. Phys.*, **51** (1980) 2861.
87. J. A. Thronton in "Deposition Technologies for Films and Coatings", ed. R. F. Bunshah, 170 (1982), Noyes Publications, Park Ridge.
88. B. M. Clemens, *J. Appl. Phys.*, **61** (1987) 4525.
89. D. Henderson, M. H. Brokdsky and P. Chaudhari, *Appl. Phys. Lett.*, **25** (1974) 641.
90. G. Betz and G. K. Wehner in "Sputtering by Particle Bombardment II", eds. R. Behrisch, 11 (1983), Springer-Verlag, Berlin.
91. P. Ziemann and E. Kay, *J. Vac. Sci. Technol.*, **A1** (1983) 512.
92. J. M. E. Harper in "Thin Film Processes", ed. J. L. Vossen and W. Kern 175 (1978), Academic Press, Inc., New York.
93. H. F. Winters and D. Horne, *Phys Rev. B*, **10** (1974) 55.
94. F. A. Smidt, *Intern. Mat. Rev.*, **35** (1990) 61.
95. J. K. Hirvonen, *Mat. Sci. Reports*, **6** (1991) 215.
96. J. M. E. Harper and R. J. Gambino, *J. Vac. Sci. Technol.*, **16** (1979) 1901.
97. J. J. Cuomo and R. J. Gambino, *J. Vac. Sci. Technol.*, **14** (1977) 152.
98. M. Marinov, *Thin Solid Films*, **46** (1977) 267.
99. L. Pranevicius, *Thin Solid Films*, **63** (1979) 77.
100. G. E. Lane and J. C. Anderson, *Thin Solid Films*, **26** (1975) 5.
101. T. C. Huang, G. Lim, F. Parmigiani and E. Kay, *J. Vac. Sci. Technol.*, **A3** (1985) 2161.
102. B. H. Hirsch and I. K. Varga, *Thin Solid Films*, **69** (1980) 99.
103. R. W. Knoll and E. D. McClanahan, *J. Vac. Sci. Technol.*, **A1** (1983) 271.
104. P. J. Martin, R. P. Netterfield and W. G. Sainty, *J. Appl. Phys.*, **55** (1983) 235.
105. M. L. Tarng and G. K. Wehner, *J. Appl. Phys.*, **42** (1971) 2449.
106. E. V. Kornelsen, *Can. J. Phys.*, **42** (1964) 364.

107. C. M. Gilmore, A. Haeri and J. A. Sprague, *Thin Solid Films*, **165** (1988) 359.
108. S. M. Rossnagel, R. S. Robinson and H. R. Kaufman, *Surf. Sci.*, **123** (1982) 89.
109. B. M. Clemens, *Phys Rev. B*, **33** (1986) 7615.
110. R. J. Gaboriaud and J. Delage, *Thin Solid Films*, **200** (1991) 275.
111. X. C. Zheng and R. A. Dodd, *Nuclear Instr. Meth.*(in press)
112. J. J. Kim, P. Moine and D. A. Stevenson, *Scripta Metall.*, **20** (1986) 243.
113. A. K. Rai and R. S. Bhattacharya, *Mat. Sci. Engr.*, **85** (1987) 139.
114. J. D. Busch, A. D. Johnson, D. E. Hodgson, C. H. Lee and D. A. Stevenson presented in ICOMAT (1989).
115. J. D. Busch, A. D. Johnson, C. H. Lee and D. A. Stevenson, *J. Appl. Phys.*, **68** (1990) 6224.
116. J. D. Busch, M. H. Berkson and A. D. Johnson, presented in Mat. Res. Soc. Meeting at Anaheim (1991).
117. K. Kuribayashi, M. Yosaaki and S. Ogawa, *IEEE CH2832-4/90* (1990) 217.
118. J. A. Walker, K. J. Gabriel and M. Mehregany, *The 5th Int. Conf. on Solid State Sensors and Actuators*, Switzerland, June 8, 1989, 123.
119. J. A. Walker, K. J. Gabriel and M. Mehregany, *Sensors and Actuators*, **A21-A23** (1990) 243.
120. J. G. Miller and D. I. Bolef, *J. Appl. Phys.*, **39** (1968) 5815.
121. J. C. M. Li in "Ultrarapid Quenching of Liquid Alloys", ed. H. Herman, 326 (1981), Academic Press, New York.
122. H. E. Kissinger, *Analytical Chemistry*, **29** (1957) 1702.
123. D. W. Henderson, *J. Non-Crystalline Solids*, **30** (1979) 301.
124. K. Matusita and S. Sakka, *Physics and Chemistry of Glasses*, **20** (1979) 81.
125. J. A. Thornton, *J. Vac. Sci. Technol.*, **11** (1974) 666.
126. J. L. Vossen and J. J. Cuomo in "Thin film processes", eds. J. L. Vossen and W. Kern, 59 (1978), Academic Press, New York.
127. H. S. Chen and K. A. Jackson in "Ultrarapid Quenching of Liquid Alloys", ed. H. Herman, 215 (1981), Academic Press, New York.
128. R. Murri, F. Gozzo, N. Pinto and L. Schiavulli, *J. Non-Crys. Solids*, **127** (1991) 12.
129. JCPDS file 38-1420.
130. H. S. Chen, *Rep. Prog. Phys.*, **43** (1980) 353.
131. E. Balanzat and J. Hillairet, *J. Phys F: Met. Phys.*, **12** (1982) 2907.
132. H. S. Chen, *Appl. Phys. Lett.*, **29** (1976) 12.
133. H. A. Davies, J. Aucote and J. B. Hull, *Scripta Metall.*, **8** (1974) 1179.
134. R. B. Schwarz, *Mater. Sci. Eng.*, **97** (1988)
135. I. O. Popoola, J. P. Villain and P. Moine, *Mater. Sci. Eng.*, **A115** (1989) 133.

136. R. A. Kant, S. A. Dillich, B. D. Sartwell and J. A. Sprague, *Mater. Res. Soc. Symp. Proc.*, **128** (1989) 79.
137. R. A. Kant and B. D. Sartwell, *J. Vac. Sci. Technol.*, **A6** (1988) 2945.
138. *Vacuum Technology: Its Foundation, Formulae and Tables*, Leybold-Heraeus Inc. (1987).
139. R. Behrisch in "Sputtering by Particle Bombardment I", ed. I. R. Behrisch, **1** (1981), Springer-Verlag, Berlin.
140. H. L. Bay and J. Bohdanský, *Appl. Phys.*, **19** (1979) 421.
141. Y. Yamamura and J. Bohdanský, *Vacuum*, **35** (1985) 561.
142. J. L. Vossen, *J. Vac. Sci. Technol.*, **8** (1971) s12.
143. R. Bruning, Z. Altounian J. O. Strom-Olsen, *Mater. Sci. Eng.*, **97** (1988) 317.
144. L. Chang, unpublished data.
145. U. Koster, *Z. Metallkd.*, **75** (1984) 691.
146. M. Nishida and C. M. Wayman, *Metall. Trans.*, **18A** (1987) 785.
147. D. A. Porter and K. E. Easterling, "Phase Transformations in Metals and Alloys", **159** (1981), Van Nostrand Reinhold Company, New York.
148. O. Mercier, E. Torok and B. Tirbonod, *Proc. Inter. Conf. on Martensitic Transformation*, (1979) 702.
149. J. Rao, Y. He and R. Ma, *Metall. Trans.*, **21A** (1990) 1322.
150. C. M. Hwang and C. M. Wayman, *Scripta Metall.*, **17** (1983) 1449.
151. C. Kim and C. M. Hwang, *Scripta Metall.*, **21** (1987) 959.
152. S. K. Wu and H. C. Lin, *Scripta Metall. Mater.*, **25** (1991) 1529.
153. C. M. Hwang, M. Meichle, M. B. Salamon and C. M. Wayman, *Phil. Mag.* **47** (1983) 31.
154. T. Saburi, M. Yoshida and S. Nenno, *Scripta Metall.*, **18** (1984) 363.
155. P. L. Ferraglio and K. Mukherjee, *Acta Metall.*, **22** (1974) 835.
156. A. G. Rozner, E. F. Heintzelman, W. J. Buehler and J. V. Gilfrich, *Trans. ASM*, **58** (1965) 415.
157. A. Hedayat, J. Rechien and K. Mukerjee, *J. Mater. Sci.*, **27** (1992) 5306.
158. T. Saburi, T. Komatsu, S. Nenno and Y. Watanabe, *J. Less-Com. Met.*, **118** (1986) 217.
159. B. J. Walles, *Master Theses*, Michigan State University, (1993).
160. N. Afify, *J. Non-crystalline Solid* **126** (1990), 130.

MICHIGAN STATE UNIV. LIBRARIES



31293009103627